Efficient Solvers for the
Phase-Field Crystal Equation

Development and Analysis of a Block-Preconditioner

Dissertation

zur Erlangung des akademischen Grades
Doctor rerum naturalium (Dr. rer. nat.)

vorgelegt an der

Technischen Universität Dresden
Fakultät Mathematik und Naturwissenschaften
Fachbereich Mathematik

von

Simon Praetorius

geboren am 20. September 1985
in Nordhausen, Deutschland

Tag der Einreichung:	05. November 2015
Tag der Verteidigung:	08. Dezember 2015

Gutachter: Prof. Dr. rer. nat. habil. A. Voigt
Technische Universität Dresden
Prof. Dr. S. M. Wise
The University of Tennessee

Zusammenfassung

In dieser Arbeit wird ein Vorkonditionierer zur Verbesserung der Konvergenzeigenschaften von Krylov-Unterraum-Verfahren hergeleitet und analysiert. Der Vorkonitionierer ist angepasst an Gleichungssysteme, die aus der Diskretisierung der Phase-Field Crystal (PFC) Gleichung entstehen.

Das PFC Modell wurde entwickelt, um das Verhalten von Festkörpern auf atomaren Längenskalen und deren Dynamik auf diffusiven Zeitskalen zu beschreiben. Dazu wurde eine Evolutionsgleichung in einem Ordnungsparameter, der Teilchendichte, hergeleitet. Stationäre Lösungen dieser Gleichung beschreiben die Anordnung kolloidaler Teilchen in regelmäßigen Gittern, wie beispielsweise kubisch innenzentrierte Gitter und kubisch flächenzentrierte Gitter in 3D, sowie hexagonale Anordnungen in 2D. Neben den statischen kristallinen Strukturen beschreibt das PFC Modell die Entwicklung hin zu diesen Zuständen. Schmelz- und Kristallisationsprozesse, Dynamik von Korngrenzen, Nukleationsprozesse und Dendritenwachstum sind nur eine kleine Auswahl von Phänomenen die analysiert und beobachtet werden können. Dabei ordnet man das PFC Modell zwischen mikroskopischen Beschreibungen der Bewegung und Interaktion individueller Partikel und einer makroskopischen Evolution eines vergröberten Phasenfeldes ein. Der mikroskopische Ansatz basiert typischerweise auf einer Newton'schen Bewegungsgleichung für alle Teilchen. In der Phasenfeldbeschreibung, andererseits, sind atomistische Details verloren gegangen und es werden nur makroskopische Phänomene in einer effektiven Art und Weise beschrieben. In den Phase-Field Crystal Modellen versucht man nun die Vorteile beider Grenzmodelle zu kombinieren. Es werden individuelle Partikel und deren Interaktion in einem kontinuierlichen Modell beschrieben. Damit erlaubt es dieses Modell das Langzeitverhalten einer großen Anzahl an Teilchen zu studieren.

Der Entwicklungsprozess der Teilchendichte im PFC Modell wird beschrieben durch eine partielle Differentialgleichung, die sich aus einem H^{-1}-Gradientenfluss einer Approximation der helmholtzschen freien Energie des Teilchensystems ableitet. Wachstumsprozesse von Korngrenzen und Langzeitstudien erfordern einerseits die feine Auflösung von Zeitskalen, z.B. während einzelne Teilchen sich umordnen, bei der Keimbildung in einem Phasenübergang, oder dem Zusammenstoßen/-wachsen von Teilchenclustern. Auf der anderen Seite werden Wachstumsprozesse immer langsamer, was eine Zeitschrittänderung von mehreren Größenordnungen, während eines Entwicklungsprozesses, verlangt. Große örtliche Gebiete müssen aufgelöst werden, um beispielsweise Korngrenzen und das Wachstum von Dendriten zu beobachten. Dabei entstehen Teilgebiete, in denen die Teilchendichte weitestgehend konstante Werte annimmt und andere Teilgebiete, in denen sich periodische, regelmäßig oszillierende Strukturen bilden. Zur effizienten Behandlung beider Anteile sind dazu angepasste Gitter in einer Diskretisierung notwendig. In dieser Arbeit wird eine Finite-Elemente Diskretisierung, kombiniert mit einer Rosenbrock Zeitdiskretisierung, auf die PFC Gleichung angewendet. Der entwickelte Vorkonditionierer erlaubt es die resultierenden Gleichungssysteme effizient – auch in parallelen Rechnungen mit mehreren tausend Prozessoren – zu lösen. Darüber hinaus wird untersucht wie sich der Vorkonditionierer verhält, wenn man die PFC Gleichung in verschiedene Richtungen modifiziert und auch die Orts- und Zeitauflösung variiert. Dies führt letztendlich auf eine Verallgemeinerung des Ansatzes für eine große Klasse von Evolutionsgleichungen, auch für Modelle höherer Ordnung, wie eine erhaltende Lifshitz-Petrich Gleichung, die am Ende dieser Arbeit betrachtet wird.

iv

Summary

In this thesis a preconditioner for the linear system arising from a finite-element discretization of the Phase-Field Crystal (PFC) equation is developed and analyzed.

The PFC model is established as a phenomenological model for solid state phenomena on an atomistic scale with dynamics acting on diffusive time scales. It predicts various static patterns of the arrangement of colloidal particles. Appart from this, it describes the dynamical formation of these structures. Freezing and crystallization processes, grain-boundary dynamics, nucleation processes, (dendritic) growth, and grain growth are just a small selection of dynamical phenomena that were analyzed.

The evolution process in the PFC model is described by a partial differential equation arising as a H^{-1}-gradient flow of an approximation of the Helmholtz free-energy of the particle system. For growth phenomena and long-time studies, on the one hand, a detailed resolution of time scales must be provided, e.g., when particles rearrange, during nucleation of the crystal, or in the freezing transition. On the other hand, the evolution process gets slower and slower. An adaptive timestepping scheme must be provided that allows for timestep changes of orders of magnitude during the evolution. Large spatial scales must be resolved, to study grain-boundaries and dendritic growth phenomena in the Phase-field Crystal model. There, regions with nearly constant particle density can be found next to regions with periodic oscillating patterns. Adaptive grids in the spatial discretization of the equation are necessary, to allow for an efficient solution of the problem. In this work a finite-element discretization in space, combined with a Rosenbrock time-discretization is formulated and an efficient preconditioner for the linear system is developed and analyzed. Variations in the model formulation, and in temporal and spatial resolutions, may influence the properties of the developed preconditioner. Thus, a numerical study in various directions is provided.

The developed preconditioner additionally is generalized to a class of higher order equations in the expansion of the Helholtz free-energy. This allows to construct a preconditioner for the Cahn-Hilliard, Phase-Field Crystal, and Lifshitz-Petrich equation in the same framework.

Contents

Ⅱ N the last four years of my research at the Institute of Scientific Computing at the Technische Universität Dresden my focus was on problems involving the Phase-Field Crystal (PFC) equation. Starting from an initial work on this topic in my Diploma thesis [199], I have extended the classical PFC model from passive systems in equilibrium to flowing systems and finally to active systems; from systems described by one order-parameter – translational order – to systems involving many order-parameters, i.e., orientational order, translational order, and a particle polarization; from the pure Phase-Field Crystal equation to coupled systems involving the Navier-Stokes equations for flow contributions, Q-tensor equations for liquid crystals, phase-field models – based on Cahn-Hilliard equations – for geometric restrictions, and many more. Finally, this has led to a Navier-Stokes Cahn-Hilliard Vacancy PFC model and a Polar Liquid-Crystal PFC model. The arising equations were solved, using finite-element methods or Fourier Spectral methods in 2D, 3D and on surfaces, which are implicitly or explicitly described. Thus, I have gained a broad view on the Phase-Field Crystal topic.

I did not do this work all by myself, but in cooperation with many researchers. Many ideas of the classical PFC equation were discussed with Rainer Backofen; the coupling to the Navier-Stokes equations and to the Cahn-Hilliard equation has incorporated ideas from Sebastian Aland; the work on the Liquid-Crystal PFC model was done together with Raphael Wittkowski and Hartmut Löwen from Heinrich Heine Universität Düsseldorf; applications of a polar PFC model were discussed with Wieland Marth and Francesco Alaimo; a direct solver approach was analyzed in cooperation with AmirHossein Aminfar from Stanford University, and the basic idea for the developed preconditioner was initiated by Thomas Witkowski. All the ideas and results were discussed and mirrored with Axel Voigt. Thus, I have decided not to use the singular "I" in the following sections of this thesis, but the plural "we" instead, to indicate that the research was (and is) always influenced and stimulated by a group of people.

Fractions of the results in the individual chapters of this thesis were already published in international journals or have motivated further studies related to the considered topics:

Chapter 1:

[201] S. PRAETORIUS AND A. VOIGT, *Development and Analysis of a Block-Preconditioner for the Phase-Field Crystal Equation*, SIAM Journal on Scientific Computing, 37 (2015), pp. B425–B451.

x

Chapter 2:

[200] S. PRAETORIUS AND A. VOIGT, *A Phase Field Crystal Approach for Particles in a Flowing Solvent*, Macromolecular Theory and Simulations, 20 (2011), pp. 541–547.

[202] S. PRAETORIUS AND A. VOIGT, *A Navier-Stokes Phase-Field Crystal Model for Colloidal Suspensions*, The Journal of Chemical Physics, 142 (2015), p. 154904.

Chapter 3:

[203] S. PRAETORIUS, A. VOIGT, R. WITTKOWSKI, AND H. LÖWEN, *Structure and Dynamics of Interfaces between two Coexisting Liquid-Crystalline Phases*, Physical Review E, 87 (2013), p. 052406.

[250] S. TANG, S. PRAETORIUS, R. BACKOFEN, A. VOIGT, Y.-M. YU, AND J. WANG, *Two-dimensional Liquid Crystalline Growth within a Phase-Field-Crystal Model*, Physical Review E, 92 (2015), p. 012504.

Chapter 4:

[28] R. BACKOFEN, M. GRÄF, D. POTTS, S. PRAETORIUS, A. VOIGT, AND T. WITKOWSKI, *A Continuous Approach to Discrete Ordering on $\mathbb{S}^2$*, Multiscale Modeling & Simulation, 9 (2011), pp. 314–334.

Various model extensions are discussed in Chapter 3 and Chapter 4. A a generalization of the preconditioner is proposed in Chapter 5. New projects are planned including a hydrodynamic model for active colloidal particles and the analysis of structures and dynamics of liquid crystalline phases on curved surfaces.

Introduction

$\mathbb{T}$HE Phase-Field Crystal (PFC) model was introduced as a phenomenological model for solid state phenomena on an atomistic scale [78, 79] with dynamics acting on diffusive time-scales. It is formulated in terms of one order-parameter, namely a one-particle number density. This either leads to a homogeneous field, to describe an isotropic liquid phase, or provides rich non-constant periodic or symmetric patterns that give rise to various molecular/colloidal crystalline phases, such as face centered cubic phase (FCC), body centered cubic phase (BCC), hexagonal close packed phase (HCP), and columnar phases in three spatial dimensions; and a triangular phase, honeycomb phase and stripe phase in two spatial dimensions. Apart from the static patterns, the Phase-Field Crystal model describes the dynamical formation of these structures. Freezing and crystallization processes, grain-boundary dynamics [79, 39, 174], nucleation processes [29, 26, 107, 30], (dendritic) growth [90, 289, 249], and grain growth [27] are just a small selection of dynamical phenomena that are analyzed using the PFC model. Also topics in biology were viewed in the context of the Phase-Field Crystal model (see, e.g., [8, 10]). An overview about various applications can be found in the recently published review papers [85, 23].

The PFC model can be ranged in between microscopic models, which describe the motion and interaction of individual particles, and mesoscopic/macroscopic models, which describe the evolution of a coarse-grained phase-field variable. The microscopic approach, thereby, implements Newton's equations of motion, the Langevin equations or stochastically equivalent the Fokker–Planck or Smoluchowski equation, respectively, for the time evolution of an N-body probability density. The phase-field description, on the other hand, looses the atomistic details and can describe only macroscopic phenomena in an effective manner. Apart from the difference in detailedness of the models, there is a big disparity in the level of numerical complexity of the approaches. Where the stochastic models have to resolve not only the individual particles by few to many degrees of freedom, it also needs to resolve temporal scales, ranging from the motion due to stochastic collisions with solvent molecules to macroscopic motion and arrangement of thousands of individual items. The phase-field models are advantageous in this context, since they describe a large number of particles in a coarse-grained continuous field variable. The evolution of macroscopic structures, which would involve millions to billions of particles, can thus easily be examined [58]. In Phase-Field Crystal models one tries to combine the advantages of both ends of the range, i.e., resolve individual particles and its interactions in a continuum model on coarse-grained time-scales, that allows not only to handle a big number of particles

but also to describe the long-time behavior of the system.

Dynamic density functional theory

Basis for PFC models is the dynamic density functional theory (DDFT) [165, 195, 215, 20, 101] that describes the evolution of a one-particle number density $\varrho(\mathbf{x}, t)$ by a generalized diffusion equation

$$\partial_t \varrho(\mathbf{x}, t) = M_0 \nabla \cdot \left(\varrho(\mathbf{x}, t) \nabla \frac{\delta F_{\mathrm{H}}[\varrho(\mathbf{x}, t)]}{\delta \varrho(\mathbf{x}, t)} \right) \tag{1}$$

with M_0 a diffusion coefficient and F_{H} the Helmholtz free-energy. Mathematically, this evolution equation is equivalent to a conserved Wasserstein gradient flow [130, 131, 4, 194] to minimize the functional F_{H}. A classical result of static density functional theory (DFT) states the existence of a grand canonical free-energy $\Omega[\mu, \varrho(\mathbf{x})]$, whose minimizer corresponds to the equilibrium one-particle density $\varrho(\mathbf{x})$ and, evaluated at this ϱ, the energy represents the corresponding equilibrium grand canonical free-energy of the inhomogeneous system [85]. Although the existence is stated, the form of the functional is unknown. Nevertheless, we have the relation

$$\Omega[\mu, \varrho] = F_{\mathrm{H}}[\varrho] - \mu V \bar{\varrho}$$

with V the volume of the system, μ chemical potential as the thermodynamic conjugate to ϱ, i.e., $\mu = \frac{\delta F_{\mathrm{H}}[\varrho]}{\delta \varrho}$, with the mean density $\bar{\varrho}$, and a representation of F_{H} in terms of three contributions,

$$F_{\mathrm{H}}[\varrho] = F_{\mathrm{id}}[\varrho] + F_{\mathrm{exc}}[\varrho] + F_{\mathrm{ext}}[\varrho].$$

The ideal solution part $F_{\mathrm{id}}[\varrho]$ and an external energy part $F_{\mathrm{ext}}[\varrho]$ may be given explicitly, whereas the excess free-energy contribution $F_{\mathrm{exc}}[\varrho]$, which describes the individual particle interactions, is not known in general. $F_{\mathrm{ext}}[\varrho]$ may include external contributions such as a gravitational potential or wall potentials.

In the DDFT the excess free-energy part is approximated by various expansion. An approximation that leads to the Phase-Field Crystal model basically is a functional Taylor expansion of the energy with the second variation further expanded in powers of the density gradient. Details about the expansion can be found, e.g., in [85, 268] and in shortened form in Section 2.1. Instead of evolving the one-particle density ϱ directly, a reparametrization in terms of a shifted density variation ψ is used (see Section 2.2.5) that finally leads to a dimensionless approximate form of the functional F_{H}:

$$F_{\mathrm{H}}[\varrho(\psi)] \simeq F_{\mathrm{sh}}[\psi] = \int \frac{1}{4} \psi^4 + \frac{1}{2} \psi (r + (1 + \Delta)^2) \psi \, \mathrm{d}\mathbf{x} \tag{2}$$

with a phenomenological expansion coefficient r. The functional $F_{\mathrm{sh}}[\psi]$ is also known as Swift-Hohenberg energy [247]. Minimizing this functional with respect to variations in ψ, using a constant mobility approximation of the dynamical equation (1), results in the classical PFC equation formulated by Elder and Grant [78]

$$\partial_t \psi = M_0 \Delta \left(\psi^3 + (r + (1 + \Delta)^2) \psi \right). \tag{3}$$

Solution methods for this 6th order nonlinear parabolic partial differential equation are developed and analyzed on this work.

Discretization of the classical PFC equation

The common spatial discretization methods for the PFC equation (3) used in literature are finite-difference discretizations [59, 113, 119, 35, 291, 54] and spectral methods [251, 83], which are combined with a semi-implicit time-discretization.

The spectral methods, based on a fast Fourier transform in the plane two-dimensional and three-dimensional domain [112], or based on a spherical harmonics transform, when discretized on a spherical surface [179, 28], are basically restricted to periodic geometries. Nonlinearities in the equation are difficult to handle and are often simply taken explicitly in the time-discretization, i.e., an implementation of a pseudo-spectral method. Nonlinear Galerkin schemes [111, 136] and advanced operator splitting techniques [251], combined with additional stabilization techniques [83], might be an improvement to the classical pseudo-spectral approach. However, the geometric restrictions limit the applicability of these approaches. We will show simulations in nonperiodic and nonrectangular domains, such as a circular disc (see Section 4.2.4), a triangular sector of a larger domain (see Section 5.2), the surface of a ball (see Section 4.1), or on a complicated manifold such as a Schwarz-P surface [189] (see Section 4.1.2).

Finite-difference discretizations are very common to discretize PDEs like equation (3) because of its simplicity in the implementation. Apart from this, efficient linear solvers, like Multi-Grid methods [119, 51, 261], can easily be adopted to these discretization or arise naturally. Although easily implementable for simple geometries, complex boundaries make this method also more complex. Partial differential equations living on surfaces can be implemented [223, 261] but need special techniques and a discretization of the neighborhood of the surface. We here follow a different approach.

We consider a discretization in space using the finite-element method and a discretization in time using either a semi-implicit Euler discretization or a Rosenbrock discretization. The advantage of finite-element schemes is that complex geometries, local refinement, and surface PDEs can be implemented with little or no modifications of the basic scheme.

Recently, the PFC model has been coupled to other field variables, such as flow [200, 202, 258], orientational order [3, 203], and mesoscopic phase-field parameters [138]. This limits the applicability of spectral methods due to the lack of periodic boundary conditions in these applications. On the other hand, simulations in complex geometries have been considered, e.g., colloids in confinements motivated by studies of DDFT [14], crystallization on embedded manifolds [31, 28, 12, 228], or particle-stabilized emulsions, where the PFC model is considered at fluid-fluid interfaces [10, 11]. These applicabilities also limit the use of spectral and finite-difference methods or make them sometimes even impossible. The finite-element method provides high flexibility concerning complex geometries and coupling to other partial differential equations.

Solving the linear systems

Basic steps of finite-element methods include refinement and coarsening of a mesh, error estimation, assembling of a linear system and solving the linear system. Most previous finite-element simulations for the PFC model [29, 31, 200] have implemented direct solvers for the last step, which however restrict the system size due to the high memory requirements and allow only computations in 2D and small systems in 3D. Well-established solution methods for linear systems, such as iterative Krylov-subspace solvers, like CG, MINRES, GMRES, TFQMR, BiCGStab, are

not directly applicable for the PFC equation, do not converge, or converge very slowly, if used without or with standard preconditioners, like Jacobi or ILU preconditioners.

In this thesis, we propose a block-preconditioner for the discretized PFC equations (3) and its variants/modifications. The preconditioner is analyzed with respect to convergence of a GMRES method. Additionally the influence of modifications of the classical equation is investigated.

Structure of the thesis

This thesis is organized as follows: In Chapter 1 the classical PFC equation, as introduced by Elder et al. [78], is discretized using finite-elements in space and a Rosenbrock method in time. A preconditioner for the block linear system is formulated and two variants of its implementation are discussed. The analysis, based on a spectral transform of the continuous PDE system, is given and timestep restrictions for the time-discrete equations are found. Numerically, the preconditioner is analyzed for crystallization processes and a study of parallel scalability is shown.

In Chapter 2 a modification of the classical PFC model is introduced. An advected Phase-Field Crystal model, coupled to the Navier-Stokes equations, is formulated and analyzed. The influence of the coupling to the flow to the preconditioner is discussed and numerically examined. A further modification is motivated by the work of [55], i.e., to allow the description of individual particles by a Vacancy PFC model. An advected Vacancy PFC model is numerically solved and applied to test cases examining the sedimentation process of colloidal particles. The arising linear systems can again be solved using a preconditioned Krylov-subspace method. Numerical studies on the stability of the preconditioner with respect to the modification of the PFC system are performed.

Chapter 3 considers a further modification of the classical PFC model. The coupling of translational density to an orientational order-parameter is developed and numerical simulations are performed. This coupling introduces a liquid crystal PFC model. The stability of liquid crystalline phases and coexistences between those phases are numerically investigated. For two classes of time-discretizations of the coupled nonlinear PDE system the developed PFC preconditioner can be applied. The last section of this chapter extends the apolar liquid crystal PFC model to include a particle polarization, to describe polar liquid crystals. The system of coupled equations is numerically solved and classical phases are visualized.

The following Chapter 4 restricts the classical and modified PFC equations to an explicitly or implicitly described surface and to a complex geometry, which additionally can evolve. The implicit geometric restriction introduces nonconstant factors in all the terms of the PFC equation. This modification complicates the solution process of the linear system. The preconditioner is modified accordingly and numerical simulations are carried out. A final formulation of a hydrodynamic model incorporates the advected Vacancy PFC model, a Cahn-Hilliard equation to describe the evolving domain, and a diffuse-domain approach.

In Chapter 5 we recapitulate the PFC preconditioner and extend the approach to a larger class of equations. The Cahn-Hilliard and Phase-Field Crystal preconditioner can be found as special cases of a generalized formulation. To test the approach, a higher order equation is examined, the Quasi-Crystal PFC model, and the general preconditioner is applied and numerically investigated.

Finally, in Chapter 6 alternative solution method for the Phase-Field Crystal equation are highlighted and explained. In cooperation with the developed preconditioner or as a separate

solution approach these methods may be reasonable extensions of current solver methods. Currently, the developed problem-dependent PFC preconditioner shows higher efficiency and is thus the method of choice.

The thesis is completed with a conclusion and outlook to further developments in the direction of PFC preconditioners and alternative solver approaches.

Solving the Phase-Field Crystal equation

$\mathbb{W}$E *develop a preconditioner for the linear system arising from a finite-element discretization of the Phase-Field Crystal (PFC) equation. This has been published in [201]. The PFC model serves as an atomic description of crystalline materials on diffusive time scales and thus offers the opportunity to study long time behavior of materials with atomic details. This requires adaptive time stepping and efficient time discretization schemes, for which we use an embedded Rosenbrock method.*

To resolve spatial scales of practical relevance, parallel algorithms are also required, which scale to a large number of processors. The developed preconditioner provides such a tool. It is based on an approximate factorization of the system matrix and can be implemented efficiently. The preconditioner is analyzed in detail and has shown to speed up the computation drastically.

1.1   Modelling

We consider the original model introduced in [78], which is a conserved gradient flow of a Swift-Hohenberg energy and serves as a model system for a regular periodic wave-like order-parameter field that can be interpreted as particle density. Here, the Swift-Hohenberg energy is given in a simplified form:

$$F_{\mathrm{sh}}[\psi] = \int_\Omega \frac{1}{4}\psi^4 + \frac{1}{2}\psi(r + (1+\Delta)^2)\psi \, \mathrm{d}\mathbf{x}\,, \tag{1.1}$$

where the order-parameter field ψ describes the deviation from a reference density. The parameter r can be related to the temperature of the system, and $\Omega \subset \mathbb{R}^m$, $m = 1, 2, 3$ corresponds to the spatial domain. According to the notation in [268] we consider the H^{-1}-gradient flow of F_{sh}, the PFC2-model,

$$\partial_t\psi = \Delta\frac{\delta F_{\mathrm{sh}}[\psi]}{\delta\psi} \tag{1.2}$$

and a Wasserstein gradient flow [130] of F_{sh}, the PFC1-model, as a generalization of (1.2),

$$\partial_t \psi = \nabla \cdot \left(M(\psi) \nabla \frac{\delta F_{\text{sh}}[\psi]}{\delta \psi} \right) \tag{1.3}$$

with a mobility function $M(\psi) = \psi - \psi_{\min} \geq 0$ with the lower bound [1] $\psi_{\min} = -1.5$. By calculus of variations and splitting of higher order derivatives, we find a set of second order equations, which will be analyzed in the subsequent sections:

$$
\begin{aligned}
\psi^{\natural} &= \psi^3 + (1+r)\psi + 2\Delta\psi + \Delta\psi^{\flat}\,, \\
\partial_t \psi &= \nabla \cdot (M(\psi)\nabla\psi^{\natural})\,, && \text{in } \Omega \times [0, T] \\
\psi^{\flat} &= \Delta\psi\,,
\end{aligned}
\tag{1.4}
$$

for a time interval $[0, T]$. To close the problem formulation we require an initial condition $\psi(t = 0) = \psi_0$ in $\bar{\Omega}$ and boundary conditions on $\partial\Omega$, e.g., homogeneous Neumann boundary conditions

$$\partial_n \psi = \partial_n \psi^{\flat} = M(\psi)\partial_n \psi^{\natural} = 0 \quad \text{on } \partial\Omega.$$

The H^{-1}-gradient flow as well as the Wasserstein gradient flow lead to conserved dynamics of the field ψ, in contrast to the non-conserved Swift-Hohenberg equation $\partial_t \psi = -\delta F_{\text{sh}}[\psi]/\delta\psi$. This also explains the name *conserved Swift-Hohenberg equation*, which is often used in the literature, cf. [247, 254].

1.2 Discrete equations

To transform the partial differential equations (1.4) into a system of linear equations, we discretize in space using finite-elements and in time using a backward Euler discretization as well as a Rosenbrock discretization scheme.

Let $\Omega \subset \mathbb{R}^m$ be a regular domain ($m = 1, 2, 3$) with a conforming triangulation $\mathcal{T}_h(\Omega)$ with $h = \max_{T \in \mathcal{T}_h}(h_T)$ a discretization parameter describing the maximal element size[2] in the triangulation. We consider simplicial meshes, i.e., made of line segments in 1D, triangles in 2D, and tetrahedra in 3D. Let

$$V_h := \{v \in H^1(\Omega)\,;\ v|_T \in \mathbb{P}_p(T),\ \forall T \in \mathcal{T}_h(\Omega)\}$$

be the corresponding finite-element space, with $\mathbb{P}_p(T)$ the space of local polynomials of degree $\leq p$, where we have chosen $p = 1, 2$ in our simulations. In the following we use the notation P^1, P^2 for the Lagrange finite-element spaces with $p = 1$ and $p = 2$, respectively. The problem (1.4) in discrete variational form can be stated as follows: Find $\psi_h^{\natural}, \psi_h, \psi_h^{\flat} \in L_2(0, T; V_h)$ with $\psi_h(t = 0) = \psi_0 \in L_2(\Omega)$, s.t.

$$
\begin{aligned}
(\psi_h^{\natural} - \psi_h^3 - (1+r)\psi_h, \vartheta_h)_\Omega &+ (2\nabla\psi_h + \nabla\psi_h^{\flat}, \nabla\vartheta_h)_\Omega \\
&+ (\partial_t \psi_h, \vartheta_h')_\Omega + (M(\psi_h)\nabla\psi_h^{\natural}, \nabla\vartheta_h')_\Omega \\
&+ (\psi_h^{\flat}, \vartheta_h'')_\Omega + (\nabla\psi_h, \nabla\vartheta_h'')_\Omega = 0\,, && \forall \vartheta_h, \vartheta_h', \vartheta_h'' \in V_h\,,
\end{aligned}
\tag{1.5}
$$

---

[1] The lower bound $\psi_{\min} = -1.5$ is due to the scaling and shifting of the order-parameter from a physical density with lower bound 0. See also Section 2.2.5 for a detailed derivation of this value.

[2] The element size h_T of a simplex T corresponds to the length of the longest edge in the element.

with $(u, v)_\Omega := \int_\Omega u \cdot v \, \mathrm{d}\mathbf{x}$.

In the following let $0 = t_0 < t_1 < \ldots < t_N = T$ be a discretization of the time interval $[0, T]$. Let $\tau_k := t_{k+1} - t_k$ be the timestep width in the k-th iteration, and $\psi_k \equiv \psi_h(t_k)$, $\psi_k^\natural \equiv \psi_h^\natural(t_k)$, and $\psi_k^\flat \equiv \psi_h^\flat(t_k)$ the discrete functions at time t_k. Applying a semi-implicit Euler discretization to (1.5) results in a time and space discrete system of equations as follows.

Let $\psi_0 \in L_2(\Omega)$ be given. For $k = 0, 1, \ldots, N - 1$ find $\psi_{k+1}^\natural, \psi_{k+1}, \psi_{k+1}^\flat \in V_h$, s.t.

$$
\begin{aligned}
a^{(e)}&\big((\psi_{k+1}^\natural, \psi_{k+1}, \psi_{k+1}^\flat), (\vartheta_h, \vartheta_h', \vartheta_h'')\big) \\
&:= (\psi_{k+1}^\natural - (1 + r)\psi_{k+1}, \vartheta_h)_\Omega + (2\nabla\psi_{k+1} + \nabla\psi_{k+1}^\flat, \nabla\vartheta_h)_\Omega \\
&\quad + \big(\psi_{k+1}, \vartheta_h'\big)_\Omega + (\tau_k M(\psi_k)\nabla\psi_{k+1}^\natural, \nabla\vartheta_h')_\Omega \\
&\quad + (\psi_{k+1}^\flat, \vartheta_h'')_\Omega + (\nabla\psi_{k+1}, \nabla\vartheta_h'')_\Omega \\
&= (\psi_k^3, \vartheta_h)_\Omega + \big(\psi_k, \vartheta_h'\big)_\Omega =: \big\langle F^{(e)}, (\vartheta_h, \vartheta_h', \vartheta_h'') \big\rangle \qquad \forall \vartheta_h, \vartheta_h', \vartheta_h'' \in V_h.
\end{aligned}
\tag{1.6}
$$

Instead of taking ψ_k^3 explicitly, it is pointed out in [29] that a linearization of this nonlinear term stabilizes the system and allows for larger timestep widths. Therefore, we replace $(\psi_k^3, \vartheta_h)_\Omega$ by $(3\psi_k^2\psi_{k+1} - 2\psi_k^3, \vartheta_h)_\Omega$. Thus, (1.6) is transformed into

$$
\begin{aligned}
a&\big((\psi_{k+1}^\natural, \psi_{k+1}, \psi_{k+1}^\flat), (\vartheta_h, \vartheta_h', \vartheta_h'')\big) \\
&:= (\psi_{k+1}^\natural - (1 + r)\psi_{k+1} - 3\psi_k^2\psi_{k+1}, \vartheta_h)_\Omega + (2\nabla\psi_{k+1} + \nabla\psi_{k+1}^\flat, \nabla\vartheta_h)_\Omega \\
&\quad + \big(\psi_{k+1}, \vartheta_h'\big)_\Omega + (\tau_k M(\psi_k)\nabla\psi_{k+1}^\natural, \nabla\vartheta_h')_\Omega \\
&\quad + (\psi_{k+1}^\flat, \vartheta_h'')_\Omega + (\nabla\psi_{k+1}, \nabla\vartheta_h'')_\Omega \\
&= (-2\psi_k^3, \vartheta_h)_\Omega + \big(\psi_k, \vartheta_h'\big)_\Omega =: \big\langle F, (\vartheta_h, \vartheta_h', \vartheta_h'') \big\rangle, \qquad \forall \vartheta_h, \vartheta_h', \vartheta_h'' \in V_h.
\end{aligned}
\tag{1.7}
$$

Let $\{\theta_i\}$ be a basis of V_h, then we can define the system matrix $\mathbf{A}$ and the right-hand-side vector $\mathbf{b}$, for the linear system $\mathbf{A}\mathbf{x} = \mathbf{b}$, as

$$
\mathbf{A} = \begin{bmatrix} \mathbf{A}^{00} & \mathbf{A}^{01} & \mathbf{A}^{02} \\ \mathbf{A}^{10} & \mathbf{A}^{11} & \mathbf{A}^{12} \\ \mathbf{A}^{20} & \mathbf{A}^{21} & \mathbf{A}^{22} \end{bmatrix}, \quad \mathbf{b} = \begin{pmatrix} \mathbf{b}^0 \\ \mathbf{b}^1 \\ \mathbf{b}^2 \end{pmatrix},
$$

with each block defined via

$$
[\mathbf{A}^{ij}]_{kl} = a\big(\mathbf{e}_j\theta_l, \mathbf{e}_i\theta_k\big), \quad [\mathbf{b}^i]_j = \big\langle F, \mathbf{e}_i\theta_j \big\rangle,
$$

where $\mathbf{e}_i$ is the ith Cartesian unit vector.

Introducing the shortcuts $\mathbf{M} := \big((\theta_j, \theta_i)_\Omega\big)_{ij}$ and $\mathbf{K} := \big((\nabla\theta_j, \nabla\theta_i)_\Omega\big)_{ij}$ for mass and stiffness-matrix, $\mathbf{K}_\mathrm{M}(\psi) := \big((M(\psi)\nabla\theta_j, \nabla\theta_i)_\Omega\big)_{ij}$ for the mobility matrix, and for the nonlinear term $\mathbf{N}(\psi) := \big((-3\psi^2\theta_j, \theta_i)_\Omega\big)_{ij}$, we can express $\mathbf{A}$ as

$$
\mathbf{A} = \begin{bmatrix} \mathbf{M} & -(1+r)\mathbf{M} + \mathbf{N}(\psi_k) + 2\mathbf{K} & \mathbf{K} \\ \tau_k\mathbf{K}_\mathrm{M}(\psi_k) & \mathbf{M} & 0 \\ 0 & \mathbf{K} & \mathbf{M} \end{bmatrix}.
\tag{1.8}
$$

We the same way we find that $\mathbf{b}^0 = \left((-2\psi_k^3, \theta_j)_\Omega \right)_j$, $\mathbf{b}^1 = \mathbf{M}\boldsymbol{\psi}_k$, and $\mathbf{b}^2 = 0$. Using this, we define a new matrix $\mathbf{B} := \mathbf{K}\mathbf{M}^{-1}\mathbf{K}$ to decouple the first two equations from the last equation, i.e.,

$$\mathbf{A}' = \begin{bmatrix} \mathbf{M} & -(1+r)\mathbf{M} + \mathbf{N}(\psi_k) + 2\mathbf{K} - \mathbf{B} \\ \tau_k \mathbf{K}_{\mathrm{M}}(\psi_k) & \mathbf{M} \end{bmatrix}. \tag{1.9}$$

With $\mathbf{x} = (\boldsymbol{\psi}_{k+1}^\natural, \boldsymbol{\psi}_{k+1}, \boldsymbol{\psi}_{k+1}^\flat)^\top$, $\mathbf{x}' = (\boldsymbol{\psi}_{k+1}^\natural, \boldsymbol{\psi}_{k+1})^\top$, and $\mathbf{b}' = (\mathbf{b}^0, \mathbf{b}^1)^\top$, where the discrete coefficient vectors correspond to a discretization with the same basis functions as the matrices, i.e.,

$$\psi_h = \sum_i \boldsymbol{\psi}_i \theta_i \quad \text{with coefficients} \quad \boldsymbol{\psi} = (\boldsymbol{\psi}_i)_i\,,$$

and $\boldsymbol{\psi}^\natural, \boldsymbol{\psi}^\flat$ in a same manner, we have

$$(1.7) \;\Leftrightarrow\; \mathbf{A}\mathbf{x} = \mathbf{b} \;\Leftrightarrow\; \mathbf{A}'\mathbf{x}' = \mathbf{b}',\; \mathbf{M}\boldsymbol{\psi}_{k+1}^\flat = -\mathbf{K}\boldsymbol{\psi}_{k+1}.$$

The reduced system (1.9) can be seen as a discretization of a partial differential equation including the bi-Laplacian, i.e.,

$$\partial_t \psi = \nabla \cdot (M(\psi)\nabla\psi^\natural), \quad \text{with} \quad \psi^\natural = \psi^3 + (1+r)\psi + 2\Delta\psi + \Delta^2\psi.$$

1.2.1 Rosenbrock time-discretization

In several publications higher order time-stepping schemes for the PFC equation were proposed, considering energy stability and adaptive step-size control, cf. [59, 119, 102, 83, 36, 294, 97]. Here we apply a more general framework to obtain a time discretization with high accuracy and stability with an easy step size control. Therefore, we replace the discretization (1.6) and (1.7) respectively, by an (embedded) Rosenbrock time-discretization scheme, cf. [219, 160, 109, 190, 142, 141, 207, 128, 129].

Consider the abstract general form of a differential algebraic equation, $\mathbb{M}\partial_t\mathbf{x} = \mathbb{F}[\mathbf{x}]$, with a linear (mass-)operator $\mathbb{M}$, possibly singular, and a (nonlinear) differential operator $\mathbb{F}$. Using the notation $\mathbb{J}_\mathbb{F}(\mathbf{x})[\mathbf{y}] := \frac{\mathrm{d}}{\mathrm{d}\epsilon}\mathbb{F}[\mathbf{x} + \epsilon\mathbf{y}]\big|_{\epsilon=0}$ for the Gâteaux derivative of $\mathbb{F}$ at $\mathbf{x}$ in the direction $\mathbf{y}$, we can write a general Rosenbrock scheme

$$\frac{1}{\tau_k c}\mathbb{M}\mathbf{y}_i^k - \mathbb{J}_\mathbb{F}(\mathbf{x}^k)[\mathbf{y}_i^k] = \mathbb{F}[\mathbf{x}_i^k] + \sum_{j=1}^{i-1}\frac{c_{ij}}{\tau_k}\mathbb{M}\mathbf{y}_j^k\,, \qquad \text{for } i = 1, \ldots, s \tag{1.10}$$

$$\mathbf{x}_i^k = \mathbf{x}^k + \sum_{j=1}^{i-1} a_{ij}\mathbf{y}_j^k\,, \qquad (i\text{th stage solution})$$

$$\mathbf{x}^{k+1} = \mathbf{x}^k + \sum_{j=1}^{s} m_j\mathbf{y}_j^k\,, \qquad (\text{timestep update}) \tag{1.11}$$

$$\hat{\mathbf{x}}^{k+1} = \mathbf{x}^k + \sum_{j=1}^{s} \hat{m}_j\mathbf{y}_j^k$$

with coefficients $c, a_{ij}, c_{ij}, m_i, \hat{m}_i$, and timestep width τ_k. The coefficients m_i and $\hat{m}_i$ build up linear-combinations of the intermediate solutions of two different orders. This can be used to

estimate the timestep error and control the timestep width. Details about step-size control can be found in [109, 141]. The coefficients used for the PFC equation are based on the *Ros3Pw* scheme [207] and are listed in Table 1.1. This W-method has three internal stages, i.e., $s = 3$, and is strongly A-stable. Interpreted as Rosenbrock-method, it is of order three. It avoids order reduction when applied to semidiscretized parabolic PDEs and is thus applicable to our equations.

$c = 0.78867513459481287$	$c_{11} = -c_{22} = c$
$a_{21} = 2$	$c_{21} = -2.53589838486225$
$a_{22} = 1.57735026918963$	$c_{31} = -1.62740473580836$
$a_{31} = 0.633974596215561$	$c_{32} = -0.274519052838329$
$a_{33} = 0.5$	$c_{33} = -0.0528312163512967$
$m_1 = 1.63397459621556$	$\hat{m}_1 = 1.99444650053487$
$m_2 = 0.294228634059948$	$\hat{m}_2 = 0.654700538379252$
$m_3 = 1.07179676972449$	$\hat{m}_3 = m_3$

Table 1.1 – *A set of coefficients for the Ros3Pw Rosenbrock scheme translated into the modified form of the Rosenbrock method used in* (1.10). *All coefficients not given explicitly are set to zero.*

In the case of the PFC system (1.4) we have $\mathbf{x} = (\psi^\natural, \psi, \psi^\flat)^\top$ and $\mathbb{M} = \mathrm{diag}(0, 1, 0)$. The functional $\mathbb{F}$ applied to $\mathbf{x}$ is given by

$$\mathbb{F}[\mathbf{x}] = \underbrace{\begin{bmatrix} -\psi^\natural + (1 + r)\psi + 2\Delta\psi + \Delta\psi^\flat \\ 0 \\ -\psi^\flat + \Delta\psi \end{bmatrix}}_{\mathbb{F}_{\mathrm{Lin}}[\mathbf{x}]} + \begin{bmatrix} \psi^3 \\ \nabla \cdot (M(\psi)\nabla\psi^\natural) \\ 0 \end{bmatrix}. \tag{1.12}$$

For the Jacobian of $\mathbb{F}$ in the direction $\mathbf{y} = (d\psi^\natural, d\psi, d\psi^\flat)^\top$ we find

$$\mathbb{J}_\mathbb{F}(\mathbf{x})[\mathbf{y}] = \mathbb{F}_{\mathrm{Lin}}[\mathbf{y}] + \begin{bmatrix} 3\psi^2 d\psi \\ \nabla \cdot (M(\psi)\nabla d\psi^\natural) + \nabla \cdot (d\psi\partial_\psi(M(\psi))\nabla\psi^\natural) \\ 0 \end{bmatrix}$$

$$(\text{assuming } M(\psi) = \psi - \psi_{\min})$$

$$= \mathbb{F}_{\mathrm{Lin}}[\mathbf{y}] + \begin{bmatrix} 3\psi^2 d\psi \\ \nabla \cdot (M(\psi)\nabla d\psi^\natural) + \nabla \cdot (d\psi\nabla\psi^\natural) \\ 0 \end{bmatrix}.$$

By multiplying with test functions $\boldsymbol{\vartheta} = (\vartheta, \vartheta', \vartheta'')^\top$ and integrating over Ω, we derive the weak form of (1.10): For $i = 1, \dots, s$ find $\mathbf{y}_i^k \in \left(L_2(0, T; V_h)\right)^3$, s.t.

$$\frac{1}{\tau_k c}(\mathbb{M}\mathbf{y}_i^k, \boldsymbol{\vartheta})_\Omega - \mathbb{J}_\mathbb{F}(\mathbf{x}^k)[\mathbf{y}_i^k, \boldsymbol{\vartheta}] = \mathbb{F}(\mathbf{x}_i^k)[\boldsymbol{\vartheta}] + \sum_{j=1}^{i-1} \frac{c_{ij}}{\tau_k}(\mathbb{M}\mathbf{y}_j^k, \boldsymbol{\vartheta})_\Omega, \qquad \forall \boldsymbol{\vartheta} \in (V_h)^3 \tag{1.13}$$

with the linear form $\mathbb{F}(\cdot)[\cdot]$,

$$
\begin{aligned}
\mathbb{F}(\mathbf{x})[\boldsymbol{\vartheta}] &= \Big[(-\psi^{\natural} + (1+r)\psi, \vartheta)_{\Omega} - (2\nabla\psi + \nabla\psi^{\flat}, \nabla\vartheta)_{\Omega} - (\psi^{\flat}, \vartheta'')_{\Omega} - (\nabla\psi, \nabla\vartheta'')_{\Omega} \Big] \\
&\quad + (\psi^3, \vartheta)_{\Omega} - (M(\psi)\nabla\psi^{\natural}, \nabla\vartheta')_{\Omega} \\
&=: \mathbb{F}_{\mathrm{Lin}}(\mathbf{x})[\boldsymbol{\vartheta}] + (\psi^3, \vartheta)_{\Omega} - (M(\psi)\nabla\psi^{\natural}, \nabla\vartheta')_{\Omega}
\end{aligned}
$$

and the bi-linear form $\mathbb{J}_{\mathbb{F}}(\cdot)[\cdot,\cdot]$,

$$
\mathbb{J}_{\mathbb{F}}(\mathbf{x})[\mathbf{y}, \boldsymbol{\vartheta}] = \mathbb{F}_{\mathrm{Lin}}(\mathbf{y})[\boldsymbol{\vartheta}] + (3\psi^2 d\psi, \vartheta)_{\Omega} - (M(\psi)\nabla d\psi^{\natural} + d\psi\nabla\psi^{\natural}, \nabla\vartheta')_{\Omega}.
$$

Using the definitions of the elementary matrices $\mathbf{M}, \mathbf{K}, \mathbf{K}_{\mathrm{M}}$, and $\mathbf{N}$, from above, and introducing $\mathbf{F}(\psi^{\natural}) := \big((\theta_j \nabla\psi^{\natural}, \nabla\theta_i)_{\Omega}\big)_{ij}$, we obtain the Rosenbrock discretization in matrix form for the ith stage iteration:

$$
\underbrace{\begin{bmatrix} \mathbf{M} & -(1+r)\mathbf{M} + 2\mathbf{K} + \mathbf{N}(\psi_k) & \mathbf{K} \\ \tau_k \mathbf{K}_{\mathrm{M}}(\psi_k) & \frac{1}{c}\mathbf{M} + \tau_k \mathbf{F}(\psi_k^{\natural}) & 0 \\ 0 & \mathbf{K} & \mathbf{M} \end{bmatrix}}_{\mathbf{A}^R} \mathbf{y}_i^k = \mathbf{b}_i^R, \tag{1.14}
$$

with $\mathbf{b}_i^R$ the assembled right-hand-side vector of (1.13), with a factor τ_k multiplied to the second component. The system matrix $\mathbf{A}^R$ in each stage of one Rosenbrock time iteration is very similar to the matrix derived for the simple backward Euler discretization in (1.8), up to a factor $\frac{1}{c}$ in front of a mass-matrix and the derivative of the mobility term $\mathbf{F}$. The latter can be removed in the case of the PFC2 model (1.2), where $\mathbf{F} = 0$ and $\mathbf{K}_{\mathrm{M}} = \mathbf{K}$.

1.3 Precondition the linear systems

To solve the linear system $\mathbf{A}\mathbf{x} = \mathbf{b}$, or $\mathbf{A}^R\mathbf{y} = \mathbf{b}^R$, linear solvers must be applied. Since direct solvers, like UMFPACK [65], MUMPS [16], or SuplerLU_DIST [146], suffer from fast increase of memory requirements and bad scaling properties for massively parallel problems[3], iterative solution methods are required. The system matrix $\mathbf{A}$, or $\mathbf{A}^R$ respectively, is non-symmetric, non-positive definite and non-normal, which restricts the choice of applicable solvers. We here use a GMRES algorithm [226] or its flexible variant FGMRES [224], to allow for preconditioners with (nonlinear) iterative inner solvers, like a CG method. In [236] on overview about recent developments in Krylov-subspace methods was given that highlights the necessity of flexible variants of various solvers.

Instead of solving the linear system $\mathbf{A}\mathbf{x} = \mathbf{b}$ directly, we consider the modified system $\mathbf{A}\mathbf{P}^{-1}(\mathbf{P}\mathbf{x}) = \mathbf{b}$, i.e.,a right preconditioning of the matrix $\mathbf{A}$. A natural requirement for the preconditioner $\mathbf{P}$ is that it should be simple and fast to solve $\mathbf{P}^{-1}\mathbf{v}$ for arbitrary vectors $\mathbf{v}$, since it is applied to the Krylov basis-vectors in each iteration of the (F)GMRES method.

We propose a block-preconditioner $\mathbf{P}$ for the 2×2 upper left block matrix $\mathbf{A}'$ of $\mathbf{A}$ based on an approach similar to a preconditioner developed for the Cahn-Hilliard equation [49]. Therefore, we first simplify the matrix $\mathbf{A}'$ and the corresponding reduced system $\mathbf{A}^{R'}$ of $\mathbf{A}^R$, respectively,

---

[3]In Section 6.1 an alternative direct approach is explained, which reduces the amount of required memory.

by considering a fixed timestep width $\tau_k = \tau$ and using a constant mobility approximation, i.e., $\mathbf{K}_M \approx M_0 \mathbf{K}$, with $M_0 = \langle M(\psi) \rangle$ the mean of the mobility coefficient $M(\psi)$, and $\mathbf{F} = 0$. For simplicity, we develop the preconditioner for the case $M_0 = 1$ and $c = 1$ only[4]. For small timestep widths τ the semi-implicit Euler time-discretization (1.6) is a good approximation of (1.14), so we neglect the non-linear term $\mathbf{N}(\psi)$. What remains is the reduced system

$$\mathbf{A}'' := \begin{bmatrix} \mathbf{M} & -(1+r)\mathbf{M} + 2\mathbf{K} - \mathbf{B} \\ \tau\mathbf{K} & \mathbf{M} \end{bmatrix}.$$

By adding a small perturbation to the diagonal of $\mathbf{A}''$, we find a matrix having an explicit triangular block-factorization. This matrix, proposed as a preconditioner for the original matrix $\mathbf{A}'$, reads

$$\mathbf{P} := \begin{bmatrix} \mathbf{M} & 2\mathbf{K} - \mathbf{B} \\ \tau\mathbf{K} & \mathbf{M} - \delta\mathbf{K} + \delta\mathbf{B} \end{bmatrix} = \begin{bmatrix} \mathbf{M} & 0 \\ \tau\mathbf{K} & \mathbf{M} + \delta\mathbf{K} \end{bmatrix} \begin{bmatrix} \mathbf{I} & \mathbf{M}^{-1}(2\mathbf{K} - \mathbf{B}) \\ 0 & \mathbf{M}^{-1}(\mathbf{M} - 2\delta\mathbf{K} + \delta\mathbf{B}) \end{bmatrix} \quad (1.15)$$

with $\delta := \sqrt{\tau}$. In each (F)GMRES iteration, the preconditioner is applied to a vector $(\mathbf{b}_0, \mathbf{b}_1)^\top$, which means solving the linear system $\mathbf{P}\mathbf{x} = \mathbf{b}$, in four steps:

$\quad$ (1) $\mathbf{M}\mathbf{y}_0 = \mathbf{b}_0$, $\qquad\qquad\qquad\qquad$ (2) $(\mathbf{M} + \delta\mathbf{K})\mathbf{y}_1 = \mathbf{b}_1 - \tau\mathbf{K}\mathbf{y}_1$,

$\quad$ (3) $(\mathbf{M} - 2\delta\mathbf{K} + \delta\mathbf{B})\mathbf{x}_1 = \mathbf{M}\mathbf{y}_1$, $\qquad$ (4) $\mathbf{x}_0 = \mathbf{y}_0 + \dfrac{1}{\delta}(\mathbf{y}_1 - \mathbf{x}_1)$.

Since the overall system matrix $\mathbf{A}$ has a third component, which was removed for the construction of the preconditioner, the third component $\mathbf{b}_2$ of the vector has to be preconditioned as well. This can be performed by solving:

$$(5) \ \mathbf{M}\mathbf{x}_2 = \mathbf{b}_2 - \mathbf{K}\mathbf{x}_1.$$

In step (3) we have to solve

$$\mathbf{S}\mathbf{x}_1 := (\mathbf{M} - 2\delta\mathbf{K} + \delta\mathbf{K}\mathbf{M}^{-1}\mathbf{K})\mathbf{x}_1 = \mathbf{M}\mathbf{y}_1, \quad (1.16)$$

which requires special care, as forming the matrix $\mathbf{S}$ explicitly is no option, as the inverse of the mass-matrix $\mathbf{M}$ is dense and thus the matrix $\mathbf{S}$, as well. In the following subsections we give two approximations to solve this problem.

1.3.1 Diagonal approximation of the mass matrix

Approximating the mass-matrix by a diagonal matrix leads to a sparse approximation of $\mathbf{S}$. Using the ansatz $\mathbf{M}^{-1} \approx \text{diag}(\mathbf{M})^{-1} =: \mathbf{M}_D^{-1}$ the matrix $\mathbf{S}$ can be approximated by

$$\mathbf{S}_D := (\mathbf{M} - 2\delta\mathbf{K} + \delta\mathbf{K}\mathbf{M}_D^{-1}\mathbf{K}).$$

By estimating the eigenvalues of the generalized eigenvalue problem $\lambda\mathbf{S}_D\mathbf{x} = \mathbf{S}\mathbf{x}$ we show, similarly as in [48], that the proposed matrix is a good approximation.

---

[4]In Section 4.2.4 a variant of the preconditioner is analyzed that includes a non-trivial mobility.

Theorem 1. *The eigenvalues λ of the generalized eigenvalue problem $\lambda \mathbf{S}_D \mathbf{x} = \mathbf{S}\mathbf{x}$ are bounded by bounds of the eigenvalues μ of the generalized eigenvalue problem $\mu \mathbf{M}_D \mathbf{y} = \mathbf{M}\mathbf{y}$ for mass-matrix and diagonal approximation of the mass-matrix.*

Proof. We follow the argumentation of [48, Section 3.2].

Using the matrices $\widehat{\mathbf{D}} := \mathbf{M}^{\frac{1}{2}} \mathbf{M}_D^{-1} \mathbf{M}^{\frac{1}{2}}$ and $\widehat{\mathbf{K}} := \mathbf{M}^{-\frac{1}{2}} \mathbf{K} \mathbf{M}^{-\frac{1}{2}}$ we reformulate the eigenvalue problem $\lambda \mathbf{S}_D \mathbf{x} = \mathbf{S}\mathbf{x}$ as

$$\lambda \mathbf{M}^{\frac{1}{2}}(\mathbf{I} - 2\delta\widehat{\mathbf{K}} + \delta\widehat{\mathbf{K}}\widehat{\mathbf{D}}\widehat{\mathbf{K}})\mathbf{M}^{\frac{1}{2}}\mathbf{x} = \mathbf{M}^{\frac{1}{2}}(\mathbf{I} - 2\delta\widehat{\mathbf{K}} + \delta\widehat{\mathbf{K}}\widehat{\mathbf{K}})\mathbf{M}^{\frac{1}{2}}\mathbf{x}. \tag{1.17}$$

Multiplying from the left with $\mathbf{x}^\top$, dividing by $\|\mathbf{M}^{\frac{1}{2}}\mathbf{x}\|^2$ and defining the normalized vector $\mathbf{y} := \mathbf{M}^{\frac{1}{2}}\mathbf{x}/\|\mathbf{M}^{\frac{1}{2}}\mathbf{x}\|$ results in a scalar equation for λ:

$$\lambda(1 - 2\delta k + \delta k^2 d) = 1 - 2\delta k + \delta k^2$$

with the Rayleigh quotients $k = \mathbf{y}^\top \widehat{\mathbf{K}}\mathbf{y}/(\mathbf{y}^\top \mathbf{y})$ and $d = \mathbf{y}^\top \widehat{\mathbf{D}}\mathbf{y}/(\mathbf{y}^\top \mathbf{y})$. Assuming that $(1 - 2\delta k + \delta k^2 d) \neq 0$ we arrive at

$$\lambda = \frac{1 - 2\delta k + \delta k^2}{1 - 2\delta k + \delta k^2 d},$$

where the difference in the highest order terms of the rational function is the factor d. From the definition of d and $\widehat{\mathbf{D}}$, bounds are given by the bounds of the eigenvalues of $\mu \mathbf{M}_D v = \mathbf{M}v$. $\square$

In [278] concrete values are provided for linear and quadratic Lagrangian finite-elements on triangles and linear Lagrangian elements on tetrahedra. For the latter, the bound $d \in [0.3924, 2.5]$ translates directly to the bound for λ, i.e., $\lambda \in [0.3924, 2.5]$, and thus $\mathbf{S}_D$ provides a reasonable approximation of $\mathbf{S}$.

Remark 1. *Other diagonal approximations based on lumped mass-matrices could also be used, which however would lead to different eigenvalue bounds.* $\triangleleft$

1.3.2   Relation to a Cahn-Hilliard system

An alternative to the diagonal approximation can be achieved by using the similarity of step (3) in the preconditioning with the discretization of a Cahn-Hilliard equation [52, 49]. This equation can be written using higher order derivatives:

$$\partial_t c = \Delta(c^3) - \Delta c - \eta \Delta^2 c,$$

with η a parameter related to the interface thickness. For an Euler discretization in time with timestep width τ' and finite-element discretization in space as above, we find the discrete equation

$$\big(\mathbf{M} - \tau'\mathbf{K} + \tau'\eta\mathbf{B} - \tau'\mathbf{N}'(c_k)\big)c_{k+1} = \mathbf{M}c_k.$$

Setting $\eta := \frac{1}{2}$ and $\tau' := 2\delta$, and neglecting the Jacobian operator $\mathbf{N}'$, we recover (1.16). A preconditioner for the Cahn-Hilliard equation (see [49, 48, 24]) thus might help to solve the equation in step (3), which we rewrite as a block system

$$\begin{bmatrix} \mathbf{M} & \mathbf{M} - \eta\mathbf{K} \\ \tau'\mathbf{K} & \mathbf{M} \end{bmatrix} \begin{pmatrix} * \\ x_1 \end{pmatrix} = \begin{pmatrix} 0 \\ \mathbf{M}y_1 \end{pmatrix}, \tag{1.18}$$

with Schur complement $\mathbf{S}$. Using the proposed inner preconditioner $\widehat{\mathbf{A}}_0$ of [49, p. 13]:

$$\widehat{\mathbf{A}}_0 := \begin{bmatrix} \mathbf{M} & -\eta\mathbf{K} \\ \tau'\mathbf{K} & \mathbf{M} + 2\sqrt{\tau'\eta}\mathbf{K} \end{bmatrix},$$

with Schur complement $\mathbf{S}_{\mathrm{CH}} := \mathbf{M} + 2\sqrt{\tau'\eta}\mathbf{K} + \tau'\eta\mathbf{K}\mathbf{M}^{-1}\mathbf{K}$ as a direct approximation of (1.18) and (1.16), i.e.,

$$\mathbf{S}_{\mathrm{CH}}\mathbf{x}_1 = (\mathbf{M} + 2\sqrt{\delta}\mathbf{K} + \delta\mathbf{K}\mathbf{M}^{-1}\mathbf{K})\mathbf{x}_1 = \mathbf{M}\mathbf{y}_1, \tag{1.19}$$

we arrive at a simple two step procedure for step (3):

$$(3.1)\ (\mathbf{M} + \sqrt{\delta}\mathbf{K})\mathbf{z} = \mathbf{M}\mathbf{y}_1, \qquad (3.2)\ (\mathbf{M} + \sqrt{\delta}\mathbf{K})\mathbf{x}_1 = \mathbf{M}\mathbf{z}.$$

With the following theorem it is shown that for small timestep widths τ the matrix $\mathbf{S}_{\mathrm{CH}}$ is indead a good approximation of $\mathbf{S}$.

Theorem 2. *The eigenvalues λ of the generalized eigenvalue problem $\lambda\mathbf{S}_{CH}\mathbf{x} = \mathbf{S}\mathbf{x}$ satisfy*

$$\lambda \in [(1 - \sqrt{\delta})/2, 1].$$

Proof. We follow the proof of [193, Theorem 4] and denote by λ the eigenvalue of $\mathbf{S}_{\mathrm{CH}}^{-1}\mathbf{S}$ with the corresponding eigenvector $\mathbf{x}$. We have $\mathbf{M}$ symmetric and positive definite and hence $\mathbf{I} + \sqrt{\delta}\mathbf{M}^{-1}\mathbf{K}$ positive definite and thus invertible.

$$\mathbf{S}_{\mathrm{CH}}^{-1}\mathbf{S}\mathbf{x} = \lambda\mathbf{x}$$
$$\Rightarrow \qquad (\mathbf{M} + 2\sqrt{\delta}\mathbf{K} + \delta\mathbf{K}\mathbf{M}^{-1}\mathbf{K})^{-1}(\mathbf{M} - 2\delta\mathbf{K} + \delta\mathbf{K}\mathbf{M}^{-1}\mathbf{K})\mathbf{x} = \lambda\mathbf{x}$$
$$\Rightarrow \qquad (\mathbf{I} + \sqrt{\delta}\mathbf{M}^{-1}\mathbf{K})^{-2}(\mathbf{I} - 2\delta\mathbf{M}^{-1}\mathbf{K} + \delta(\mathbf{M}^{-1}\mathbf{K})^2)\mathbf{x} = \lambda\mathbf{x}.$$

Thus, for each eigenvalue μ of $\mathbf{M}^{-1}\mathbf{K}$ we have $\mu \in \mathbb{R}_{\geq 0}$ and

$$\lambda(\mu) := (\mu^2 + 2\delta\mu + \delta)(\mu + \sqrt{\delta})^{-2}$$

an eigenvalue of $\mathbf{S}_{\mathrm{CH}}^{-1}\mathbf{S}$ and since $\mathbf{M}^{-1}\mathbf{K}$ is similar to $\mathbf{M}^{1/2}\mathbf{M}^{-1}\mathbf{K}\mathbf{M}^{-1/2}$, which is symmetric, all eigenvalues are determined.

With algebraic arguments and $\sqrt{\delta} > 0$ we find

$$\lambda(\mu) \leq \frac{\mu^2 + (\sqrt{\delta})^2}{(\mu + \sqrt{\delta})^2} \leq 1$$

and $\nabla\lambda = 0$ for $\mu, \delta \searrow 0$. This leads to the lower bound $\frac{1-\sqrt{\delta}}{2} \leq \lambda(\mu)$. $\qquad\square$

We can write the matrix $\mathbf{P} = \mathbf{P}(\mathbf{S})$ in terms of the Schur complement matrix $\mathbf{S}$:

$$\mathbf{P}(\mathbf{S}) = \begin{bmatrix} \mathbf{M} & \delta^{-1}(\mathbf{M} - \mathbf{S}) \\ \tau\mathbf{K} & \delta\mathbf{K} + \mathbf{S} \end{bmatrix}. \tag{1.20}$$

Inserting $\mathbf{S}_{\mathrm{CH}}$ instead of $\mathbf{S}$ gives the precondition-matrix for the Cahn-Hilliard approximation

$$\mathbf{P}_{\mathrm{CH}} := \mathbf{P}(\mathbf{S}_{\mathrm{CH}}) = \begin{bmatrix} \mathbf{M} & -2\sqrt{\delta}\mathbf{K} - \mathbf{B} \\ \tau\mathbf{K} & \mathbf{M} + (\delta + 2\sqrt{\delta})\mathbf{K} + \delta\mathbf{B} \end{bmatrix}.$$

1.4   Convergence analysis of the Krylov-subspace method

To analyze the proposed preconditioners for the GMRES algorithm, we have a look at the norm of the residuals $\mathbf{r}_k(\mathbf{A}) = \mathbf{b} - \mathbf{A}\mathbf{x}_k$ of the approximate solution $\mathbf{x}_k$ obtained in the k-th step of the GMRES algorithm. In our studies, we are interested in estimates of the residual norm of the form

$$\frac{\|\mathbf{r}_k\|}{\|\mathbf{r}_0\|} = \min_{p \in \Pi_k} \frac{\|p(\mathbf{A})\mathbf{r}_0\|}{\|\mathbf{r}_0\|} \leq \min_{p \in \Pi_k} \|p(\mathbf{A})\|_2 \tag{1.21}$$

with $\Pi_k := \{p \in \mathbb{P}_k \,:\, p(0) = 1\}$ and $\mathbf{r}_0$ the initial residual. The right-hand side corresponds to an ideal-GMRES bound that excludes the influence of the initial residual. In order to get an idea of the convergence behavior, we have to estimate/approximate the right-hand-side term by values that are attainable by analysis of $\mathbf{A}$. Replacing $\mathbf{A}$ by $\mathbf{A}\mathbf{P}^{-1}$ we hope to get an improvement in the residuals.

A lower bound for the right-hand side of (1.21) can be found by using the spectral mapping theorem $p(\sigma(\mathbf{A})) = \sigma(p(\mathbf{A}))$, as

$$\min_{p \in \Pi_k} \max_{\lambda \in \sigma(\mathbf{A})} |p(\lambda)| \leq \min_{p \in \Pi_k} \|p(\mathbf{A})\|_2 \tag{1.22}$$

(see [260, 71]) and an upper bound can be stated by finding a set $\mathcal{S}(\mathbf{A}) \subset \mathbb{C}$ associated with $\mathbf{A}$, so that

$$\min_{p \in \Pi_k} \|p(\mathbf{A})\|_2 \leq C \min_{p \in \Pi_k} \max_{\lambda \in \mathcal{S}(\mathbf{A})} |p(\lambda)|\,, \tag{1.23}$$

where C is a constant that depends on the condition number of the eigenvector matrix, the ϵ-pseudospectra of $\mathbf{A}$, or on the fields of values of $\mathbf{A}$.

Both estimates contain the min-max value of $p(\lambda)$ on some set $\mathcal{S}$. In [209, 71] it is shown that the limit

$$\lim_{k \to \infty} \left[\min_{p \in \Pi_k} \max_{\lambda \in \mathcal{S}} |p(\lambda)| \right]^{1/k} =: \rho_{\mathcal{S}}$$

exists, where $\rho_{\mathcal{S}}$ is called the estimated asymptotic convergence factor related to the set $\mathcal{S}$. Thus, for large k we expect a behavior for the right-hand side of (1.21) like

$$\rho_{\sigma(\mathbf{A})}^k \lesssim \min_{p \in \Pi_k} \|p(\mathbf{A})\|_2 \lesssim C \rho_{\mathcal{S}(\mathbf{A})}^k.$$

The tilde indicates that this estimate only holds in the limit $k \to \infty$.

In the next two sections, we will summarize known results on how to obtain the asymptotic convergence factors $\rho_{\mathcal{S}}$ and the constant C in the approximation of the relative residual bound.

1.4.1   The convergence prefactor

The constant C plays an important role in the case of non-normal matrices, as pointed out by [84, 260], and can dominate the convergence in the first iterations. It is shown in Section 1.5 that the linear part of the operator matrix related to $\mathbf{A}$ is non-normal and also the preconditioned operator related to $\mathbf{Q} := \mathbf{A}\mathbf{P}^{-1}$ is non-normal. Thus, we have to take a look at this constant.

Let $\mathbf{V}$ be the matrix of normalized right eigenvectors of $\mathbf{A}$ and $\mathbf{\Lambda}$ a diagonal matrix containing the eigenvalues on its diagonal. If $\mathbf{A}$ is diagonalizable, i.e., $\mathbf{A} = \mathbf{V}\mathbf{\Lambda}\mathbf{V}^{-1}$, then

$$\min_{p \in \Pi_k} \|p(\mathbf{A})\|_2 \leq \kappa(\mathbf{V}) \min_{p \in \Pi_k} \max_{\lambda \in \sigma(\mathbf{A})} |p(\lambda)| \tag{1.24}$$

holds true, with the condition number $\kappa(\mathbf{V}) = \|\mathbf{V}\|_2 \|\mathbf{V}^{-1}\|_2$ of the eigenvector matrix (see, e.g., [84]). Thus the constant is given by $C \equiv \kappa(\mathbf{V})$. If the matrix is not diagonalizable this estimate is not applicable.

As can be seen in Figure 1.1 the convexification of $\sigma(\mathbf{A})$ contains the origin. It follows that

$$0 \in W(\mathbf{A}) := \left\{ \frac{\mathbf{x}^* \mathbf{A} \mathbf{x}}{\mathbf{x}^* \mathbf{x}} \ \middle| \ \mathbf{x} \in \mathbb{C}^3, \mathbf{x} \neq 0 \right\}$$

with $W(\mathbf{A})$ the field of values of $\mathbf{A}$. This set is convex and contains $\sigma(\mathbf{A})$. So known convergence bounds related to the field of values can not be used.

An estimate of the convergence constant, applicable for general non-normal matrices, is related to the ϵ-pseudospectrum $\sigma_\epsilon(\mathbf{A})$ of the matrix $\mathbf{A}$. This can be defined by the spectrum of a perturbed matrix [260, 84]

$$\sigma_\epsilon(\mathbf{A}) := \left\{ z \in \mathbb{C} \,\middle|\, z \in \sigma(\mathbf{A} + \mathbf{E}), \ \|\mathbf{E}\|_2 \leq \epsilon \right\}.$$

Let $\Gamma_\epsilon := \partial \sigma_\epsilon$ be an union of Jordan curves approximating the boundary of σ_ϵ, then

$$\min_{p \in \Pi_k} \|p(\mathbf{A})\|_2 \leq \frac{|\Gamma_\epsilon|}{2\pi\epsilon} \min_{p \in \Pi_k} \max_{\lambda \in \Gamma_\epsilon} |p(\lambda)| \leq \frac{|\Gamma_\epsilon|}{2\pi\epsilon} \min_{p \in \Pi_k} \max_{\lambda \in \sigma_\epsilon(\mathbf{A})} |p(\lambda)|, \tag{1.25}$$

and thus $C \equiv \frac{|\Gamma_\epsilon|}{2\pi\epsilon}$, with $|\Gamma_\epsilon|$ the length of the curve Γ_ϵ [260]. This estimate is approximated, using the asymptotic convergence factor for large k, by

$$\min_{p \in \Pi_k} \|p(\mathbf{A})\|_2 \lesssim \frac{|\Gamma_\epsilon|}{2\pi\epsilon} \rho_{\Gamma_\epsilon}^k \leq \frac{|\Gamma_\epsilon|}{2\pi\epsilon} \rho_{\sigma_\epsilon(\mathbf{A})}^k. \tag{1.26}$$

This constant gives a first insight into the convergence behavior of the GMRES method for the PFC matrix $\mathbf{A}$ and the preconditioned matrix $\mathbf{Q}$.

1.4.2 The asymptotic convergence factor

The asymptotic convergence factor $\rho_{\mathcal{S}}$, where $\mathcal{S}$ is a set in the complex plane, e.g., $\mathcal{S} = \sigma(\mathbf{A})$, or $\mathcal{S} = \sigma_\epsilon(\mathbf{A})$, can be estimated by means of potential theory [71, 137]. Therefore, we have to construct a conformal mapping $\Phi : \mathbb{C} \to \mathbb{C}$ of the exterior of $\mathcal{S}$ to the exterior of the unit disk with $\Phi(\infty) = \infty$. We assume that $\mathcal{S}$ is connected. Otherwise, we will take a slightly larger connected set. Having $\mathcal{S} \subset \mathbb{C} \setminus \{0\}$ the convergence factor is then given by

$$\rho_{\mathcal{S}} = \frac{1}{|\Phi(0)|}. \tag{1.27}$$

Let $\mathcal{S} = [\alpha, \beta]$ be a real interval with $0 < \alpha < \beta$ and $\kappa := \frac{\beta}{\alpha}$, then a conformal mapping from the exterior of the interval to the exterior of the unit circle is given by

$$\Phi(z) = \frac{2z - \kappa - 1 - 2\sqrt{z^2 - (\kappa + 1)z + \kappa}}{\kappa - 1}, \tag{1.28}$$

(see [71][5]), and gives the asymptotic convergence factor

$$\rho_{[\alpha,\beta]} = \frac{\sqrt{\kappa} - 1}{\sqrt{\kappa} + 1}, \tag{1.29}$$

which is a well known convergence bound for the CG method for symmetric positive definite matrices with $\kappa = \frac{\lambda_{\max}}{\lambda_{\min}}$ the spectral condition number of the matrix $\mathbf{A}$.

By using Chebyshev polynomials an exact representation of the min-max value in the case of intervals can be formulated (see [225]),

$$\min_{p \in \Pi_k} \max_{\lambda \in \mathcal{S}_0} |p(\lambda)| = 2\frac{\rho_{[\alpha,\beta]}^k}{1 + \rho_{[\alpha,\beta]}^{2k}} < 2\rho_{[\alpha,\beta]}^k,$$

where the difference is of order $\mathcal{O}(\rho_{[\alpha,\beta]}^{2k})$.

In the next section, we will apply the given estimates for the asymptotic convergence factor and for the constant C to the Fourier transform of the operators that define the PFC equation, in order to get an estimate of the behavior of the GMRES solver.

1.5   Spectral analysis of the preconditioner

We analyze the properties and quality of the proposed preconditioner by means of a Fourier analysis, following the approach of [98]. We therefore consider an unbounded or periodic domain Ω, respectively and introduce continuous operators $\mathbb{A}$, $\mathbb{A}_0$, and $\mathbb{P}$ associated with the linear part $\mathbb{F}_{\mathrm{Lin}}$ of (1.12), the linear part of the 6th order non-splitted version of (1.2), and the preconditioner, respectively, for $M(\psi) \equiv 1$:

$$\mathbb{A}[\mathbf{x}] := \begin{bmatrix} \psi^\natural - (1+r)\psi - 2\Delta\psi - \Delta\psi^\flat \\ -\tau\Delta\psi^\natural + \psi \\ \psi^\flat - \Delta\psi \end{bmatrix},$$

$$\mathbb{A}_0[\psi] := \psi - \tau\Delta\big((1+r)\psi + 2\Delta\psi + \Delta^2\psi\big)$$

with $\mathbf{x} = (\psi^\natural, \psi, \psi^\flat)$. The operator that represents the preconditioner reads

$$\mathbb{P}[\mathbf{x}] := \begin{bmatrix} \psi^\natural - 2\Delta\psi - \Delta^2\psi \\ -\tau\Delta\psi^\natural + \psi - \delta\Delta\psi + \delta\Delta^2\psi \\ \psi^\flat - \Delta\psi \end{bmatrix}.$$

Using the representation of $\mathbf{P}(\mathbf{S})$ in (1.20), we can also formulate the operator that determines the Cahn-Hilliard approximation of $\mathbf{P}$ by inserting $\mathbf{S}_{\mathrm{CH}}$:

$$\mathbb{P}_{\mathrm{CH}}[\mathbf{x}] := \begin{bmatrix} \psi^\natural + 2\sqrt{\delta}\Delta\psi - \Delta^2\psi \\ -\tau\Delta\psi^\natural + \psi + (\delta + 2\sqrt{\delta})\Delta\psi + \delta\Delta^2\psi \\ \psi^\flat - \Delta\psi \end{bmatrix}.$$

---

[5]In [71] the sign of the square root is wrong and thus the exterior of the interval is mapped to the interior of the unit circle. In formula (1.28) this has been corrected.

We denote by $\mathbf{k} = (k_1, k_2, k_3)$ the wave vector with $\mathbf{k}^2 = k_1^2 + k_2^2 + k_3^2$. The Fourier transform of a function $u = u(\mathbf{r})$ will be denoted by $\widehat{u} = \widehat{u}(\mathbf{k})$ and is defined as

$$\mathcal{F} : u(\mathbf{r}) \mapsto \widehat{u}(\mathbf{k}) = \int_{\mathbb{R}^3} e^{-\mathrm{i}(\mathbf{k} \cdot \mathbf{r})} u(\mathbf{r}) \, \mathrm{d}\mathbf{r}.$$

Using the inverse Fourier transform, the operators $\mathbb{A}, \mathbb{A}_0, \mathbb{P}$, and $\mathbb{P}_{\mathrm{CH}}$, applied to $\mathbf{x}$ and ψ respectively, can be expressed as

$$\mathbb{A}[\mathbf{x}] = \mathcal{F}^{-1}(\mathcal{A}\widehat{\mathbf{x}}), \ \mathbb{A}_0[\psi] = \mathcal{F}^{-1}(\mathcal{A}_0\widehat{\psi}), \ \mathbb{P}[\mathbf{x}] = \mathcal{F}^{-1}(\mathcal{P}\widehat{\mathbf{x}}), \ \text{and} \ \mathbb{P}_{\mathrm{CH}}[\mathbf{x}] = \mathcal{F}^{-1}(\mathcal{P}_{\mathrm{CH}}\widehat{\mathbf{x}})$$

with $\widehat{\mathbf{x}} = (\widehat{\psi^\natural}, \widehat{\psi}, \widehat{\psi^\flat})$ and $\mathcal{A}_0, \mathcal{A}, \mathcal{P}$, and $\mathcal{P}_{\mathrm{CH}}$ the symbols of $\mathbb{A}_0, \mathbb{A}, \mathbb{P}$, and $\mathbb{P}_{\mathrm{CH}}$, respectively. These symbols are written in terms of the wave vector $\mathbf{k}$:

$$\mathcal{A}\widehat{\mathbf{x}} = \begin{bmatrix} 1 & -(1+r) + 2\mathbf{k}^2 & \mathbf{k}^2 \\ \tau\mathbf{k}^2 & 1 & 0 \\ 0 & \mathbf{k}^2 & 1 \end{bmatrix} \begin{pmatrix} \widehat{\psi^\natural} \\ \widehat{\psi} \\ \widehat{\psi^\flat} \end{pmatrix}, \tag{1.30}$$

$$\mathcal{A}_0\widehat{\psi} = \left(1 + \tau[(1+r)\mathbf{k}^2 - 2\mathbf{k}^4 + \mathbf{k}^6] \right)\widehat{\psi}, \tag{1.31}$$

$$\mathcal{P}\widehat{\mathbf{x}} = \begin{bmatrix} 1 & 2\mathbf{k}^2 - \mathbf{k}^4 & 0 \\ \tau\mathbf{k}^2 & 1 - \delta\mathbf{k}^2 + \delta\mathbf{k}^4 & 0 \\ 0 & \mathbf{k}^2 & 1 \end{bmatrix} \begin{pmatrix} \widehat{\psi^\natural} \\ \widehat{\psi} \\ \widehat{\psi^\flat} \end{pmatrix}, \tag{1.32}$$

$$\mathcal{P}_{\mathrm{CH}}\widehat{\mathbf{x}} = \begin{bmatrix} 1 & -2\sqrt{\delta}\mathbf{k}^2 - \mathbf{k}^4 & 0 \\ \tau\mathbf{k}^2 & 1 + (\delta + 2\sqrt{\delta})\mathbf{k}^2 + \delta\mathbf{k}^4 & 0 \\ 0 & \mathbf{k}^2 & 1 \end{bmatrix} \begin{pmatrix} \widehat{\psi^\natural} \\ \widehat{\psi} \\ \widehat{\psi^\flat} \end{pmatrix}. \tag{1.33}$$

In Figure 1.1 the eigenvalue symbol curves of $\mathcal{A}$ restricted to a bounded range of frequencies, together with the distribution of eigenvalues of an assembled matrix[6] $\mathbf{A}$, using quadratic finite-elements on a periodic tetrahedral mesh with grid size $h = \pi/4$, is shown. The qualitative distribution of the eigenvalues is similar for symbol curves and assembled matrices and changes as the timestep width increases.

For small τ, the origin is excluded by the Y-shape profile of the spectrum. Increasing τ leads to a surrounding of the origin. This does not necessarily imply a bad convergence behavior.

1.5.1 Critical timestep width

For larger timestep widths τ we can even get the eigenvalue zero in the continuous spectrum, i.e., the time-discretization gets unstable. In the following theorem this is analyzed in detail and a modification is proposed that shifts this critical timestep width limit. This modification will be used in the rest of the paper

---

[6]Since a finite-element mass-matrix has eigenvalues far from the continuous eigenvalue 1, depending on the finite-elements used, the grid size and the connectivity of the mesh, the overall spectrum of $\mathbf{A}$ (which contains mass-matrices on the diagonal) is shifted on the real axis. In order to compare the continuous and the discrete spectrum, we have therefore considered the diagonal preconditioned matrix $\widehat{\mathbf{A}} = \mathrm{diag}(\mathbf{A})^{-1}\mathbf{A}$ that is a blockwise diagonal scaling by the inverse of the diagonal of mass-matrices.
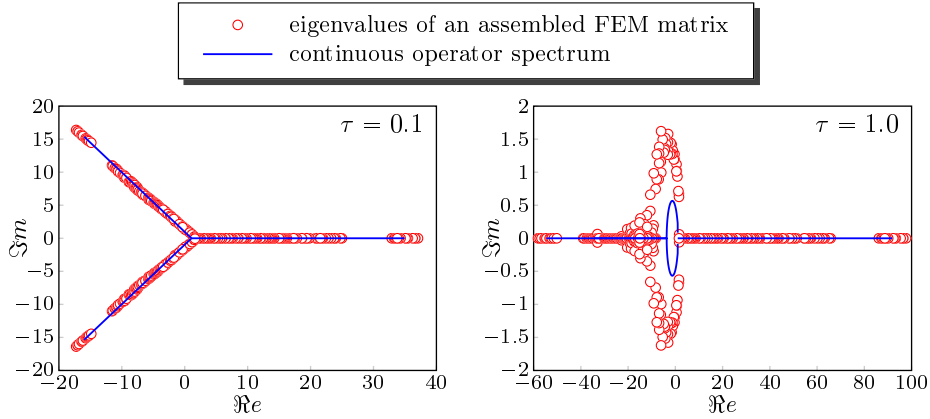
Figure 1.1 – Eigenvalues of the diagonally preconditioned finite-element matrix $\widehat{\mathbf{A}} = \mathrm{diag}(\mathbf{A})^{-1}\mathbf{A}$, i.e., a discretization of the continuous operator $\mathbb{A}$ multiplied with the inverse of its diagonal, and the three eigenvalues of the symbol $\mathcal{A}$ visualized as restricted symbol curves. Left: Spectrum for timestep width $\tau = 0.1$, Right: Spectrum for timestep width $\tau = 1$.

Theorem 3. *Let $\mathcal{A}_0$ be given as in* (1.31) *and $r < 0$ then the spectrum $\sigma(\mathcal{A}_0)$ contains zero in case of the critical timestep width*

$$\tau \geq \tau^* := \frac{27}{2(\sqrt{\alpha}-1)(\sqrt{\alpha}+2)^2} \tag{1.34}$$

with $\alpha = 1 - 3r$.

Let $\bar{\psi} \in \mathbb{R}$. The spectrum of the modified operator $\hat{\mathcal{A}}_0$, given by

$$\hat{\mathcal{A}}_0 := \left(1 + \tau[(3\bar{\psi}^2 + 1 + r)\mathbf{k}^2 - 2\mathbf{k}^4 + \mathbf{k}^6]\right), \tag{1.35}$$

contains zero only in the case of $\bar{\psi}^2 < \frac{-r}{3}$. Then the critical timestep width is given by (1.34) *with $\alpha = 1 - 3r - 9\bar{\psi}^2$.*

Remark 2. *The modified operator $\hat{\mathcal{A}}_0$ can be derived by linearizing ψ^3 around a constant reference density $\bar{\psi}$:*

$$\psi^3 \approx 3\bar{\psi}^2\psi - 2\bar{\psi}^3.$$

Adding this as an approximation of the nonlinear term to the system (1.31) *leads to the operator symbol* (1.35). ◁

Remark 3. *If we take $\bar{\psi}$ as the constant mean value of ψ over Ω, where r has the physical meaning of an undercooling of the system, then the relation $|\bar{\psi}| = \sqrt{-r/3}$ is related to the solid-liquid transition in the phase-diagram of the PFC model, i.e., $|\bar{\psi}| > \sqrt{-r/3}$ leads to stable constant solutions, interpreted as a liquid phase, and $|\bar{\psi}| < \sqrt{-r/3}$ leads to an instability of the constant phase, interpreted as a crystalline state. An analysis of the stability condition can be found in* [59, 79] *among others.* ◁

Remark 4. *In [279, 119] an unconditionally stable discretization is provided that changes the structure of the matrix, i.e., the negative $2\mathbf{k}^4$ term is moved to the right-hand side of the equation. In order to analyze also the Rosenbrock scheme we cannot take the same modification into account. The modification shown here is a bit similar to the stabilization proposed in [83], but the authors have added a higher order term $C\mathbf{k}^4$ instead of the lower order term $C'\mathbf{k}^2$ in (1.35).* ◁

Proof. (of Theorem 3). We analyze the eigenvalues of $\hat{\mathcal{A}}_0$ and get the eigenvalues of $\mathcal{A}_0$ as a special case for $\bar{\psi} = 0$. The eigenvalue symbol $\hat{\mathcal{A}}_0$ gets zero whenever

$$\hat{\mathcal{A}}_0 = 0 \iff \tau = \frac{-1}{(3\bar{\psi}^2 + 1 + r)\mathbf{k}^2 - 2\mathbf{k}^4 + \mathbf{k}^6}.$$

The minimal $\tau \in \mathbb{R}_{>0}$, denoted by τ^*, that fulfills this equality is reached at

$$\mathbf{k}^2 = \frac{2}{3} + \frac{1}{3}\sqrt{1 - 3r - 9\bar{\psi}^2} =: \frac{2}{3} + \frac{1}{3}\sqrt{\alpha}.$$

Inserting this into τ gives

$$\tau^* := \frac{27}{2(\sqrt{\alpha} - 1)(\sqrt{\alpha} + 2)^2}.$$

We have $\alpha \geq 0$ for $|\bar{\psi}| \geq \frac{1}{3}\sqrt{1 - 3r}$ and $\tau^* > 0 \iff \alpha > 1 \iff \bar{\psi}^2 > \frac{-r}{3}$ by simple algebraic calculations. □

On account of this zero eigenvalue, we restrict the spectral analysis to small timestep widths τ. For $r = -0.35$, as in the numerical examples below, we get the timestep width bound $0 < \tau < \tau^* \approx 2.6548$ for the operator $\mathcal{A}_0$ and with $\bar{\psi} = -0.34$ we have $0 < \tau < \tau^* \approx 312.25$ for $\hat{\mathcal{A}}_0$, hence a much larger upper bound. In the following, we will use the modified symbols for all further calculations, i.e.,

$$\hat{\mathcal{A}} = \begin{bmatrix} 1 & -(3\bar{\psi}^2 + 1 + r) + 2\mathbf{k}^2 & \mathbf{k}^2 \\ \tau\mathbf{k}^2 & 1 & 0 \\ 0 & \mathbf{k}^2 & 1 \end{bmatrix}, \tag{1.36}$$

and remove the hat symbol for simplicity, i.e., $\hat{\mathcal{A}} \to \mathcal{A}$, $\hat{\mathcal{A}}_0 \to \mathcal{A}_0$.

Calculating the eigenvalues of the preconditioner symbol $\mathcal{Q} := \mathcal{A}\mathcal{P}^{-1}$ and $\mathcal{Q}_{\text{CH}} := \mathcal{A}\mathcal{P}_{\text{CH}}^{-1}$ directly gives the sets

$$\sigma(\mathcal{Q}) = \left\{ 1, 1, \frac{\tau(\mathbf{k}^6 - 2\mathbf{k}^4 + (3\bar{\psi}^2 + 1 + r)\mathbf{k}^2) + 1}{\tau\mathbf{k}^6 + (\sqrt{\tau} - 2\tau)\mathbf{k}^4 - \sqrt{\tau}\mathbf{k}^2 + 1} \,\Big|\, \mathbf{k} \in \mathbb{R}^m \right\} \tag{1.37}$$

$$\sigma(\mathcal{Q}_{\text{CH}}) = \left\{ 1, 1, \frac{\tau(\mathbf{k}^6 - 2\mathbf{k}^4 + (3\bar{\psi}^2 + 1 + r)\mathbf{k}^2) + 1}{\tau\mathbf{k}^6 + (\sqrt{\tau} + 2\tau^{3/4})\mathbf{k}^4 + (\sqrt{\tau} + 2\tau^{1/4})\mathbf{k}^2 + 1} \,\Big|\, \mathbf{k} \in \mathbb{R}^m \right\} \tag{1.38}$$

with values all on the real axis (for $\tau > 0$). Similar to the analysis of $\mathcal{A}_0$ we get a critical timestep width, i.e., eigenvalues zero, for $\tau \geq \tau^*$. The denominator of the third eigenvalue of $\sigma(\mathcal{Q}_{\text{CH}})$ is strictly positive, but the denominator of $\sigma(\mathcal{Q})$ can reach zero. This would lead to bad convergence behavior, since divergence of this eigenvalue would lead to divergence of the asymptotic convergence factor in (1.29).

The critical timestep width, denoted by $\tau^\natural$, that allows a denominator with value zero is given by $\tau = (-\mathbf{k}^4 + 2\mathbf{k}^2)^{-2}$, which is minimal positive for $\mathbf{k}^2 = 1$ and gives $\tau^\natural = 1$. Thus, for the preconditioner $\mathcal{P}$ we have to restrict the timestep width to $\tau \in (0, \min(\tau^\natural, \tau^*))$. This restriction is not necessary for the preconditioner $\mathcal{P}_{\mathrm{CH}}$.

1.5.2 The asymptotic convergence factor

Since the third eigenvalue of $\mathcal{Q}$ in (1.37) and $\mathcal{Q}_{\mathrm{CH}}$ in (1.38) is a real interval $\subset \mathbb{R}_+$, for τ in the feasible range $(0, \min(\tau^\natural, \tau^*))$, we can use formula (1.29) to estimate an asymptotic convergence factor for the lower bound on $\min_{p \in \Pi_k} \|p(\mathcal{Q}_*)\|_2$. For fixed $r = -0.35$ and various values of $\bar{\psi}$ minimum and maximum of (1.37) and (1.38) are calculated numerically. Formula (1.29) thus gives the corresponding estimated asymptotic convergence factor (see the left plot of Figure 1.2). For step widths τ less than 1 we have the lowest convergence factor for the operator $\mathcal{Q}$ and the largest for the original operator $\mathcal{A}_0$. The operator $\mathcal{Q}_{\mathrm{CH}}$ has slightly greater convergence factor than $\mathcal{Q}$ but is more stable with respect to an increase in timestep width.

The stabilization term $3\bar{\psi}^2$ added to $\mathcal{A}_0$ and $\mathcal{A}$ in (1.35) and (1.36) respective, influences the convergence factor of $\mathcal{A}_0$ and $\mathcal{Q}$ only slightly, but the convergence factor of $\mathcal{Q}_{\mathrm{CH}}$ is improved a lot, i.e. the critical timestep width is shifted toward positive infinity.

The upper bounds on the convergence factor are analyzed in the next section.
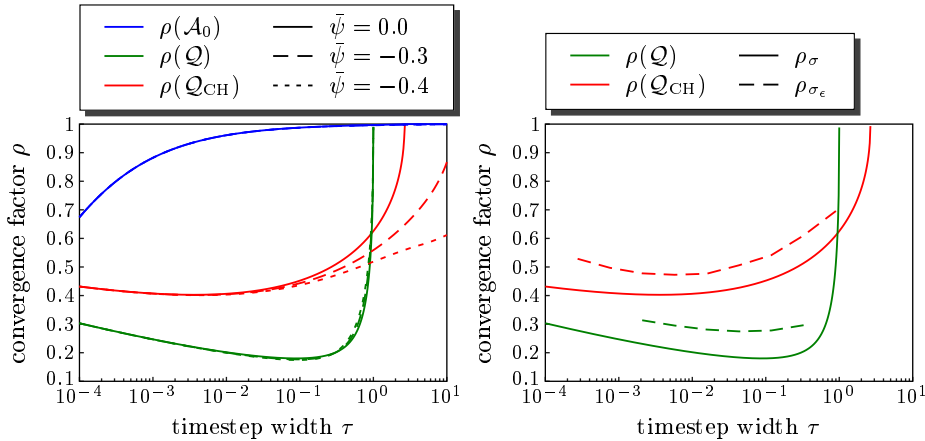
Figure 1.2 – *Left: Asymptotic convergence factor for operators $\mathcal{A}_0, \mathcal{Q}$, and $\mathcal{Q}_{\mathrm{CH}}$. In dashed lines, the dependence on the mean density $\bar{\psi}$-modification (1.35) is shown. Right: Comparison of the convergence factor related to the spectrum and ϵ-pseudospectrum is shown. This corresponds to lower and upper bounds of the actual asymptotic convergence factor.*

1.5.3 Analysis of the pseudospectrum

As can be seen by simple calculations, the symbol $\mathcal{A}$ is non-normal:

$$\left(\mathcal{A}^\top \mathcal{A} - \mathcal{A}\mathcal{A}^\top\right)_{2,0} = \mathbf{k}^2\big((3\bar{\psi}^2 + 1 + r) - 2\mathbf{k}^2\big) \neq 0$$

for a matrix entry at row 2 and column 0. For slightly more complex calculations it can be shown that also $\mathcal{Q} := \mathcal{AP}^{-1}$ and $\mathcal{Q}_{\mathrm{CH}} := \mathcal{AP}_{\mathrm{CH}}^{-1}$ are non-normal:

$$\left(\mathcal{Q}^{\top}\mathcal{Q} - \mathcal{Q}\mathcal{Q}^{\top}\right)_{2,2} = \left(\mathcal{Q}_{\mathrm{CH}}^{\top}\mathcal{Q}_{\mathrm{CH}} - \mathcal{Q}_{\mathrm{CH}}\mathcal{Q}_{\mathrm{CH}}^{\top}\right)_{2,2} = \mathbf{k}^4 \neq 0.$$

For non-normal matrices we have to analyze the ϵ-pseudospectrum in order to get an estimate of convergence bounds for the GMRES method, as pointed out in Section 1.4.1.

Using the MATLAB toolbox `Eigtool` provided by [288], we can calculate the pseudospectra σ_ϵ and approximations Γ_ϵ of its boundaries with single closed Jordan curves for all wave-numbers $k_i \in [0, k_{\max}]$. The maximal frequency used in the calculations is related to the grid size h of the corresponding triangulation, $k_{\max} = \frac{\pi}{h}$. In all the numerical examples below, we have used a grid size $h = \frac{\pi}{4}$ that can resolve all the structures sufficiently well, and thus we get $k_{\max} = 4$, which leads to $\|\mathbf{k}\|_{\max} = \sqrt{m}k_{\max}$.

The ϵ-pseudospectrum of $\mathcal{Q}$ and $\mathcal{Q}_{\mathrm{CH}}$ can be seen in Figure 1.3 for various values of ϵ. The pseudospectrum of $\mathcal{Q}_{\mathrm{CH}}$ gets closer to the origin than that of $\mathcal{Q}$, since the eigenvalues get closer to the origin as well. The overall structure of the pseudospectra is very similar.
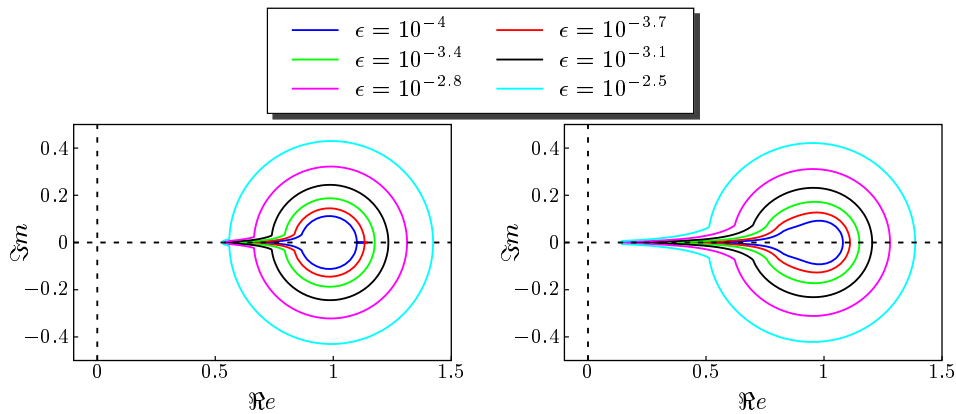
Figure 1.3 – *ϵ-pseudospectra of the preconditioned matrices for various values of ϵ. Left: $\sigma_\epsilon(\mathcal{Q})$, Right: $\sigma_\epsilon(\mathcal{Q}_{CH})$, for $\tau = 0.1$ and $\mathbf{k}$ in the restricted range $[0, |\mathbf{k}|_{\max}]$. The dashed lines correspond to the zero-axis and indicate the origin.*

For the convergence factor corresponding to the pseudospectra, we compute the inverse conformal map $\Psi = \Phi^{-1}$ of the exterior of the unit disk to the exterior of a polygon $\mathcal{S}_0$ approximating the set $\mathcal{S} = \sigma_\epsilon$, by the Schwarz-Christoffel formula, using the SC MATLAB toolbox [73, 72]. A visualization of the inverse map Ψ for the pseudospectrum of $\mathcal{A}$ and $\mathcal{Q}$ can be found in Figure 1.4.

Evaluating the asymptotic convergence factor depending on the ϵ-pseudospectrum of the matrices is visualized in Figure 1.5. The calculation is performed for fixed timestep width $\tau = 0.1$ and parameters $r = -0.35$ and $\bar{\psi} = 0$.

Increasing ϵ increases the radius of the sphere like shape around point 1. For a simple disc the convergence factor is proportional to the radius (see [71]), thus we find increasing convergence factors also for our disc with the tooth. When ϵ gets too large the pseudospectrum may contain the origin that would lead to useless convergence bounds, since then $\rho_{\sigma_\epsilon} > 1$ in (1.27). If ϵ gets
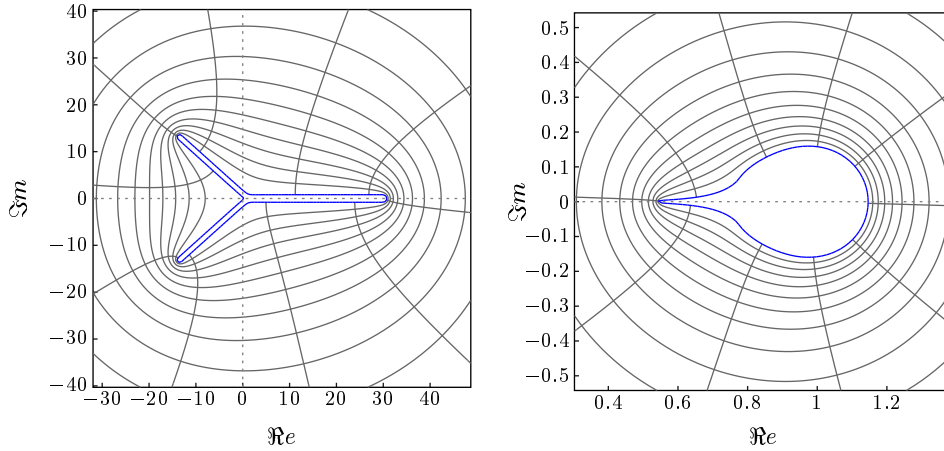
Figure 1.4 – *Inverse conformal map Ψ of the unit disk to the exterior of a polygon enclosing the ϵ-pseudospectrum of $\mathcal{A}$ and $\mathcal{Q}$ for one ϵ and a restricted range of frequencies. For both plots the ϵ value is chosen small enough to have 0 in the exterior of the peudospectrum.*

too small, the convergence constant C in (1.25) is growing rapidly, since $|\Gamma_\epsilon|$ is bounded from below by the eigenvalue interval length, i.e., $|\Gamma_\epsilon| \leq 2(\beta - \alpha) = 2\big(\max(\sigma(\mathcal{Q})) - \min(\sigma(\mathcal{Q}))\big)$, and we divide by ϵ. Thus, the estimates also are not meaningful in the limit $\epsilon \to 0$.

An evaluation of the constant C for various values ϵ can be found in the left plot of Figure 1.5. It is a log-log plot with constants in the range $[10^2, 10^4]$.

For all $\epsilon > 0$ the upper bound (1.25) is valid, so we have chosen $\epsilon = 10^{-3}$ and plotted the resulting estimated asymptotic convergence factor in relation to the lower bound, i.e., the convergence factor corresponding to the spectrum of the matrices, in the right plot of Figure 1.2. The upper bound is just slightly above the lower bound. Thus, we have a convergence factor for $\mathcal{Q}$ that is in the range $0.2 - 0.3$ (for $\tau = 0.1$ and $r = -0.35$) and for the matrix $\mathcal{Q}_{\text{CH}}$ in the range $0.45 - 0.55$, that is much lower than the lower bound of the convergence factor of $\mathcal{A}_0$ (approximately 0.99).

So both the preconditioner $\mathcal{P}$ and $\mathcal{P}_{\text{CH}}$ improve the asymptotic convergence factor a lot and we expect fast convergence also in the case of discretized matrices.

1.6 Numerical studies

We now demonstrate the properties of the preconditioner numerically. We consider a simple crystallization problem in 2D and 3D, starting with an initial grain in a corner of a rectangular domain. The solution of the PFC equation in the crystalline phase is a periodic wave-like field with specific wave length and amplitude. In [79, 124] a single mode approximation for the PFC equation in 2D and 3D is provided. These approximations show a wave length of $d := 4\pi/\sqrt{3}$, corresponding to a lattice spacing in a hexagonal crystal in 2D and a body-centered cubic crystal in 3D. We define the domain Ω as a rectangle/cube with edge length, a multiple of the lattice spacing: $\Omega = [N \cdot d]^{2,3}$, with $N \in \mathbb{N}_{>0}$. Discretizing one wave with 10 gridpoints leads to a sufficient resolution. Our grid size therefore is $h = \frac{d}{10} \approx \frac{\pi}{4}$ throughout the numerical calculations.
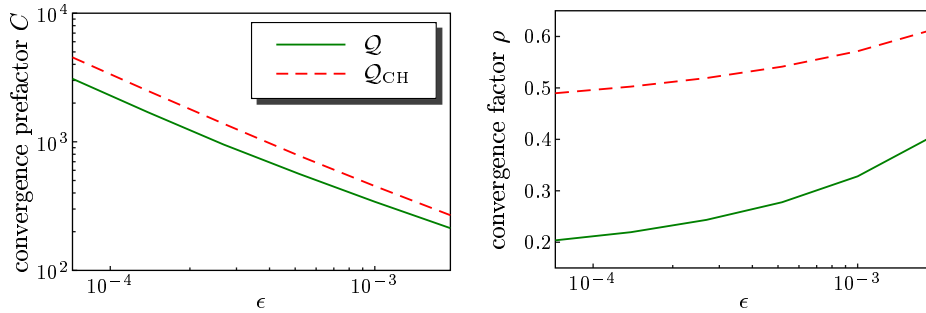
Figure 1.5 – *Left: Estimated convergence prefactor $C := \frac{|\Gamma_\epsilon|}{2\pi\epsilon}$ for the matrix $\mathcal{Q} = \mathcal{AP}^{-1}$ and $\mathcal{Q}_{CH} = \mathcal{AP}_{CH}^{-1}$ with $r = -0.35$ and $\tau = 0.12$, plotted in logarithmic scale for ϵ and C. Right: Estimated asymptotic convergence factor $\rho_{\sigma_\epsilon(\mathcal{Q})} = |\Phi_{\sigma_\epsilon(\mathcal{Q})}(0)|^{-1}$ and $\rho_{\sigma_\epsilon(\mathcal{Q}_{CH})}$ analogously. The legend in the left plot is valid also for the right plot.*

We use regular simplicial meshes, with h corresponding to the length of an edge of a simplex for linear elements and twice its length for quadratic elements, to guarantee the same number of degrees of freedom (DOFs) within one wave.

1.6.1 General problem setting and results

As system parameters we have chosen values corresponding to a coexistence of liquid and crystalline phases: 2D ($\bar{\psi} = -0.35$, $r = -0.35$), 3D ($\bar{\psi} = -0.34$, $r = -0.3$). Both parameter sets are stable for large timestep widths, with respect to Theorem 3. Figure 1.6 shows snapshots of the coexistence regime of liquid and crystal is shown for 2D and 3D calculations.
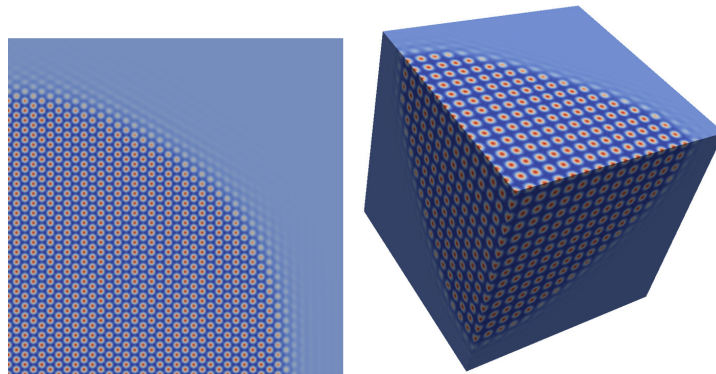
Figure 1.6 – *Intermediate state of growing crystal, starting from one corner of the domain. Shown is the order parameter field ψ. Left: $\Omega = [20d]^2$, number of DOFs: 263,169, calculated on 1 processor; Right: $\Omega = [12d]^3$, number of DOFs: 101,255,427, calculated on 3,456 processors.*

In steps (1), (2), (3), and (5) of the preconditioner solution procedure, linear systems have to be solved. For this task we have chosen iterative solvers with standard preconditioners and parameters as listed in Table 1.2. The PFC equation is implemented in the finite-element frame-

work AMDiS [273, 216] using the linear algebra backend MTL4 [103, 67, 104] in sequential calculations and PETSc [32] for parallel calculation for the block-preconditioner (1.15) and the inner iterative solvers. As an outer solver, a FGMRES method is used with restart parameter 30 and modified Gram-Schmidt orthogonalization procedure. The spatial discretization is done using Lagrange elements of polynomial degree $p = 1, 2$ and as time discretization the implicit Euler or the described Rosenbrock scheme is used.

| precon. steps	matrix	solver	precond.	rel. tolerance
(1),(5)	$\mathbf{M}$	PCG	diag	10^{-3}
(2)	$\mathbf{M} + \delta\mathbf{K}$	PCG	diag	10^{-3}
(3.1), (3.2)	$\mathbf{M} + \sqrt{\delta}\mathbf{K}$	PCG	diag	10^{-3}
(3)	$\mathbf{M} - 2\delta\mathbf{K} + \delta\mathbf{K}\mathbf{M}_D^{-1}\mathbf{K}$	PCG	diag	20 (iter.)

Table 1.2 – *Parameters for the inner solvers of the preconditioner with Cahn-Hilliard approximation $\mathbf{S}_{CH}$ and in the last line for the diagonal approximation $\mathbf{S}_D$ of the matrix $\mathbf{S}$. The preconditioner named 'diag' indicates a Jacobi preconditioner. We have solved each inner system up to a relative solver tolerance given in the last column of the table. Only in the case of the matrix $\mathbf{S}_D$ it is more efficient to use a fixed number of iteration.*

The first numerical test compares a PFC system solved without a preconditioner to a system solved with the developed preconditioner. In Figure 1.7 the relative residual in the first timestep of a small 2D system is visualized. For increasing timestep widths the FGMRES solver without preconditioner (dashed lines) shows a dramatic increase of the number of iterations up to a nearly stagnating curve for timestep widths greater than 0.5. On the other hand, we see in solid lines the preconditioned solution procedure that is much less influenced by the timestep widths and reaches the final residual within 20 to 30 iterations. A detailed study of the influence of the timestep width can be found below. For larger systems, respective systems in 3D, we get nearly no convergence for the non-preconditioned iterations.

Next, we consider the solution procedure of the sub-problems in detail. Table 1.3 shows a comparison between an iterative *preconditioned conjugate gradient* method (PCG) and a direct solver, where the factorization is calculated once for each sub-problem matrix per timestep. The number of outer iterations increases when we use iterative inner solvers, but the overall solution time decreases since a few PCG steps are faster than the application of an LU-factorization to the Krylov vectors. This holds true in 2D and 3D for polynomial degree 1 and 2 of the Lagrange basis functions.

We now compare the two proposed preconditioners regarding the same problem. Table 1.4 shows a comparison of the approximation of the sub-problem (3) by either the diagonal mass-matrix approximation $\mathbf{S}_D$ or the Cahn-Hilliard preconditioner approximation $\mathbf{S}_{CH}$. In all cases, the number of outer solver iterations needed to reach the relative tolerance and also the time for one outer iteration is lower for the $\mathbf{S}_{CH}$ approximation than for the $\mathbf{S}_D$ approximation.

In the following, we thus use the preconditioned solution method with $\mathbf{S}_{CH}$ and PCG for the sub-problems. We analyze the dependence on the timestep width in detail and compare it with the theoretical predictions and show parallel scaling properties.
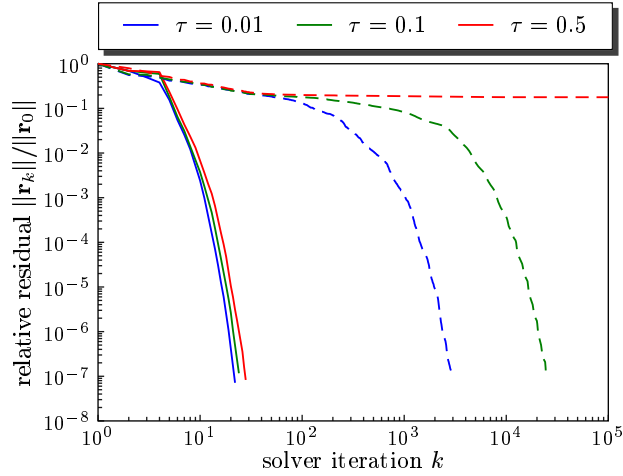
Figure 1.7 – *Relative residual of the solver iterations. Solid lines show preconditioned solver iterations and dashed lines iterations without a preconditioner. The systems is $\Omega = [d]^2$, $h = \frac{\pi}{4}$.*

dim. m	poly. degree p	direct		iterative	
		time [sec]	#iterations	time [sec]	#iterations
2D	1	6.11	14	1.65	14
	2	5.89	14	3.04	15
3D	1	41.72	17	3.36	18
	2	35.24	17	9.62	19

Table 1.3 – *Comparison of the number of iterations and time to solve the linear system averaged over 20 timesteps for the preconditioner matrix $\mathbf{S}_{CH}$ with timestep width $\tau = 0.1$. Sub-problems of the preconditioner are solved with iterative solvers as in Table 1.2 or with the direct solver UMFPACK. The benchmark configuration is a problem with approximately 66,000 DOFs and grid size $h = \pi/4$.*

1.6.2 Influence of timestep width

In Table 1.5 the time to solve the linear system averaged over 20 timesteps is listed for various timestep widths τ. All simulations are started from the same initial condition that is far from the stationary solution. It can be found that the solution time increases and also the number of outer solver iterations increases. In Figure 1.9, this increase in solution time is visualized for various parameter sets for polynomial degree and space dimension. The behavior corresponds to the increase in the asymptotic convergence factor (see Figure 1.2) for increasing timestep widths.

We have analyzed whether a critical timestep width occurs in the two approximations of $\mathbf{S}$ (see Figure 1.8). The diagonal approximation $\mathbf{S}_D$ is spectrally similar to the original preconditioner $\mathbf{S}$ that has shown the critical timestep width $\tau^{\natural} = 1$. In the numerical calculations, $\mathbf{S}_D$ shows a critical value around the analytical value, but it varies depending on the finite-element approximation of the operators. For linear Lagrange elements we see $\tau^{\natural} \approx 2$ and for quadratic element $\tau^{\natural} \approx 0.6$. The Cahn-Hilliard approximation $\mathbf{S}_{CH}$ does not show a timestep width, where

dim. m	poly. degree p	$\mathbf{S}_{\mathrm{CH}}$ time [sec]	#iterations	$\mathbf{S}_D$ time [sec]	#iterations
2D	1	1.65	14	2.72	16
	2	3.04	15	7.03	20
3D	1	3.36	18	8.14	21
	2	9.62	19	81.49	55

Table 1.4 – *Comparison of the number of iterations and time to solve the linear system averaged over 20 timesteps for the preconditioner with diagonal approximation $\mathbf{S}_D$ of $\mathbf{S}$, and Cahn-Hilliard approximation $\mathbf{S}_{CH}$. Sub-problems of the preconditioner are solved with iterative solvers as in Table 1.2. The benchmark configuration is a problem with approximately 66,000 DOFs, timestep width $\tau = 0.1$ and grid size of $h = \pi/4$.*

| timestep width τ	2D time [sec]	#iterations	3D time [sec]	#iterations
0.01	2.50	13	8.01	17
0.1	3.05	15	9.62	19
1.0	4.53	19	14.29	24
10.0	10.81	47	34.94	58

Table 1.5 – *Comparison of time to solve the linear system averaged over 20 timesteps for various timestep widths τ for a 2D and a 3D system. The benchmark configuration is a problem with polynomial degree $p = 2$ with approximately 66,000 DOFs.*

the number of outer iterations explodes, at least in the analyzed interval $\tau \in [10^{-3}, 10^1]$. The difference in the finite-element approximations is also not so pronounced as in the case of $\mathbf{S}_{\mathrm{D}}$.

While in all previous simulations an implicit Euler discretization was used, we now will demonstrate the benefit of the described Rosenbrock scheme, for which the same preconditioner is used. Adaptive time stepping becomes of relevance, especially close to the stationary solution, where the timestep width needs to be increased rapidly to reduce the energy $F_{\mathrm{sh}}[\psi]$ further. In order to allow for large timestep widths the iterative solver and preconditioner, must be stable with respect to an increase in this parameter.

In Figure 1.10 the system setup and evolution for the Rosenbrock benchmark are shown. We use 10 initial grains randomly distributed and oriented in the domain and let the grains grow until a stable configuration emerges. When growing grains touch each other, they build grain boundaries with crystalline defects. The orientation of the final grain configuration is shown in the right plot of Figure 1.10 with a color coding with respect to an angle of the crystal cells relative to a reference orientation.

The time evolution of the timestep width obtained by an adaptive step size control and the evolution of the corresponding solver iterations is shown in the left plot of Figure 1.11. Small grains grow until the whole domain is covered by particles. This happens in the time interval $[0, 200]$, where small timestep widths are required. From this time, the timestep width is increased a lot by the step size control since the solution is in a nearly stable state. The number of outer solver iterations increases with increasing timestep width, as expected. Timestep widths up to
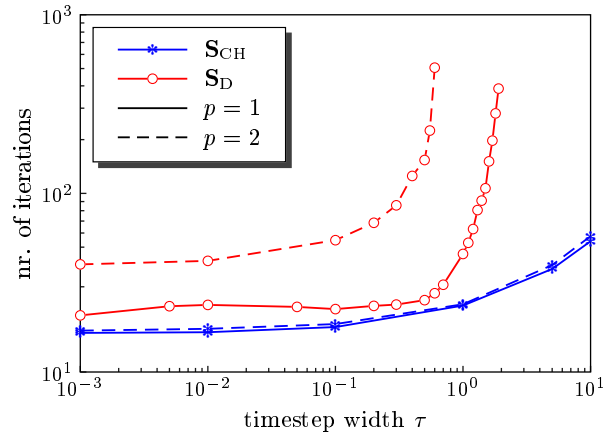
Figure 1.8 – *Increase in number of outer iterations when the timestep width increases. The red curves (curcular dots) correspond to the diagonal approximation $\mathbf{S}_D$ of $\mathbf{S}$ and the blue curves (asterisk dots) to the Cahn-Hilliard approximation $\mathbf{S}_{CH}$. All simulations are performed in 3D in a domain with grid size $h = \pi/4$. The solid lines correspond to simulations with polynomial degree $p = 1$ and the dashed lines with polynomial degree $p = 2$.*

18 in the time evolution are selected by the step size control and work fine with the proposed preconditioner.

In the right plot of Figure 1.11, the relation of the obtained timestep widths to the solution time is given. Increasing the timestep widths increases also the solution time, but the increasing factor is much lower than that of the increase in timestep width, i.e., the slope of the curve is much lower than 1. Thus, it is advantageous to increase the timestep widths as much as possible to obtain an overall fast solution time.

1.6.3   Parallel calculations

We now demonstrate parallel scaling properties. Figure 1.12 shows strong and weak scaling results. All simulations are done in 3D and show results for the time to solve the linear system in comparison with a minimal number of processors that have the same communication and memory access environment. The efficiency of this strong scaling benchmark is about 0.8–0.9 depending on the workload per processing unit. The efficiency of the weak scaling is about 0.9–0.95, slightly better than the strong scaling.

#processors p	total DOFs	time [sec]	#iterations
48	1,245,456	13.62	24
96	2,477,280	13.57	24
192	4,984,512	13.83	25
384	9,976,704	14.97	25

Table 1.6 – *Average number of iterations and solution time for weak scaling computations.*
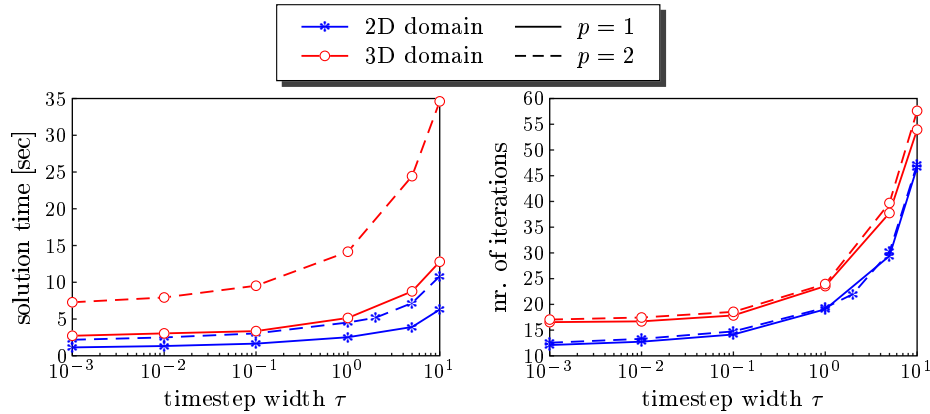
Figure 1.9 – *Left: Solution time per timestep iteration for various timestep widths τ averaged over 20 timesteps. Right: Number of outer iterations per timestep for various timestep widths τ averaged over 20 timesteps. The four curves show the dependence on dimension (2D or 3D) and on polynomial degree p of the Lagrange basis functions.*
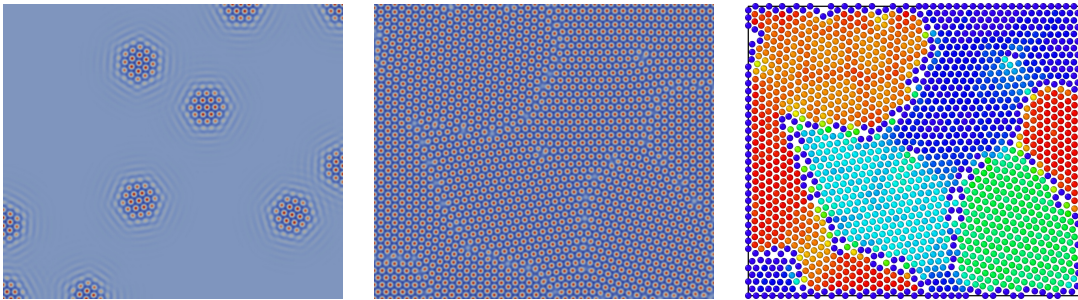
Figure 1.10 – *Grain growth simulation. Left: Initial grains that do not touch each other. Center: Grown grains with different orientation and grain boundaries. Right: Coloring of the different crystal orientations. The coloring fails at the boundary of the domain.*

In Table 1.6 the number of outer solver iterations for various system sizes is given. The calculations are performed in parallel on a mesh with constant grid size but with variable domain size. By increasing the number of processors or the number of DOFs in the system the number of solver iterations remains almost constant. Also the solution time changes only slightly.

Larger systems up to 3,456 processors also show that the preconditioner does not perturb the scaling behavior of the iterative solvers. All parallel computations have been done on JUROPA at JSC.

1.7   Conclusion

In this chapter we have developed a block-preconditioner for the discretized Phase-Field Crystal equation. It leads to a precondition procedure in five steps that can be implemented by compo-
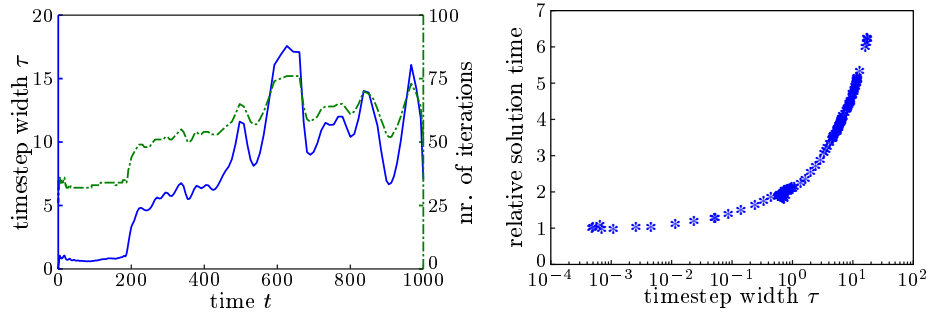
Figure 1.11 – Left: Time series of timestep width (solid line) and outer solver iterations (dashed line) for a simulation using a Rosenbrock scheme with automatic step size selection. Right: Evolution of the solution time for increasing timestep widths. The time is measured relative to the time for the minimal timestep width. The data is extracted from the simulation of the grain growth, see Figure 1.10.

sition of simple iterative solvers. Additionally, we have analyzed the preconditioner in Fourier-space and in numerical experiments. We have found a critical timestep width for the original preconditioner and have proposed a variant with an inner Cahn-Hilliard preconditioner, which does not show this timestep limit. Since most of the calculations were performed in parallel, a scaling study was provided, that shows, that there is no negative influence of the preconditioner on the scaling properties. Thus, large scale calculations in 2D and 3D can be performed.

Modifications of the classical PFC equation, motivated in the introduction, toward liquid crystalline phases [203] and flowing crystals [176, 200, 202], might change the behavior of the preconditioner. Thus, we need to perform studies on the influence of the modifications to the convergence of the iterative solvers. These studies are performed in the next chapters.
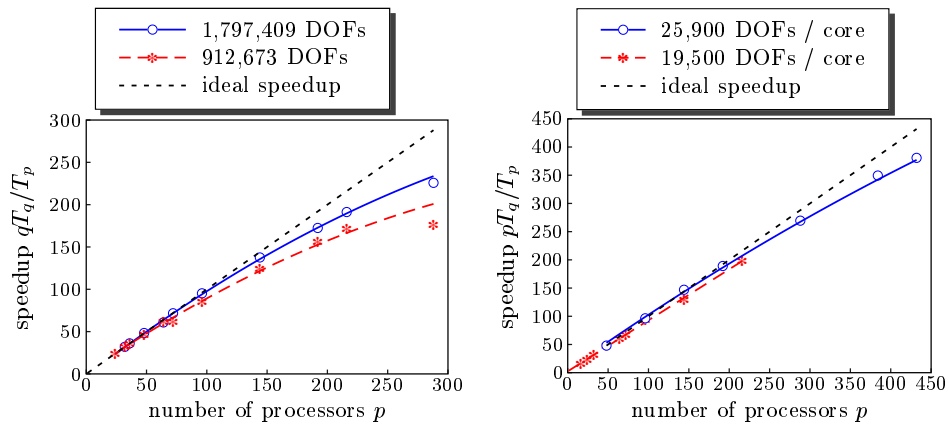
Figure 1.12 – *Speedup of parallel simulation. Left: Strong scaling for fixed overall number of DOFs. Right: Weak scaling for fixed number of DOFs per processor. The parameter q is a reference number of processors, that is, $q = 24/32$ for the calculation in the left plot and $q = 16/48$ for the right plot. The first number corresponds to the dashed lines and the second to the solid lines.*

CHAPTER 2

Hydrodynamics of interacting particles within the PFC model

A number of dynamic density functional theories were developed to describe the dynamics of the one-particle density of atomic fluids. We review an approach that accounts for particle advection by a flowing solvent and make further approximations, using a locally advected Phase-Field Crystal model to describe the particles in a solvent. This model is coupled to the Navier-Stokes equations, which account for the evolution of the surrounding fluid.

In Section 2.1 we apply the approach to Brownian particles, e.g., coarse grained polymer coils, in a solvent flowing around fixed obstacles, e.g., colloidal particles. Results were published in [200]. We compare the bow wave in the particle density in front of the obstacles, as well as the wake behind it. The results qualitatively agree with full dynamic density functional theory results and simulations based on the underlying Brownian dynamics. The much lower computational cost of the Phase-Field Crystal approach provides an efficient way to couple fluid flow around macroscopic fixed or moving objects with interacting particles in the solvent.

Section 2.2 extends this approach towards a coupling of the moving particles to the evolution of the flow field of the surrounding fluid. There, we have developed a fully continuous model for colloidal suspensions with hydrodynamic interactions. Some of the results were published in [202]. The Navier-Stokes Phase-Field Crystal (NS-PFC) model combines ideas of dynamic density functional theory with particulate flow approaches and is related to other dynamic density functional theory approaches with hydrodynamic interactions. The derived system is used to analyze colloidal crystallization in flowing environments, demonstrating a strong coupling in both directions, between the crystal shape and the flow field. We further validate the model against other computational approaches for particulate flow systems for various colloidal sedimentation problems.

The PDE systems arising in both sections are discretized using finite-elements and the resulting linear systems are solved with iterative methods. Therefore, the preconditioner of Chapter 1 is analyzed, with respect to an extension by an advection term in the Phase-Field Crystal equation.

2.1   A Phase-Field Crystal approach for particles in a flowing solvent

Binary mixtures of colloids and non-adsorbing polymer coils are ideal model systems for the study of phase behavior and equilibrium as well as non-equilibrium physics of multicomponent systems.

The generalization of classical density functional theory to the case of non-equilibrium situation, known as dynamic density functional theory (DDFT), was first introduced by Marconi and Tarazona [165], and was recently extended to driven systems [213] in the advected dynamic density functional theory (aDDFT). The authors used this method to model colloidal particles moving through a polymer solution, or conversely, the flow of polymer coils around a fixed macroscopic particle. The colloid deforms the flow field, as its hydrodynamic radius is greater than zero.

Earlier studies of a similar system with conventional density functional theory (DFT) [195] have neglected this deformation and are therefore only valid for small obstacles of radius $R \ll a$, where a is the effective radius of the polymer coils. A full DDFT model including the advection of the solvent particles was analyzed by [213].

In this chapter we present an approximation of the DDFT using a Phase-Field Crystal (PFC) model, motivated by [213] and [195], and extend this approach by a transport term to approximate the generalized aDDFT. In contrast to DDFT equations, the PFC model is given by a local differential equation and can easily be solved in complex geometries.

In the following section the model is derived, starting from the Langevin equation of motion for an ensemble of advected interacting Brownian particles. Using various approximation steps we derive an advected PFC equation. Simulation results for the polymer density around one colloidal particle are shown. For the comparison and relation to the results of Chapter 1 we formulate the corresponding discrete equations and analyze a preconditioner applied to the resulting linear system.

2.1.1   Model derivation

A continuum model considering the particle density in a flowing solvent is derived, starting from an atomistic theory, as motived by [165].

Fokker-Planck equation

We consider the Langevin equation of motion for an ensemble of N advected interacting Brownian particles with position coordinates $\vec{\mathbf{x}} = \{\mathbf{x}_1, \mathbf{x}_2, \ldots, \mathbf{x}_N\}$, and mass m, immersed in an incompressible fluid,

$$
\begin{aligned}
\partial_t \mathbf{x}_i &= \mathbf{u}(\mathbf{x}_i, t) + \frac{1}{\gamma}(\mathbf{F}_i(\vec{\mathbf{x}}, t) + \boldsymbol{f}_i(t)) \\
&\approx \mathbf{u}(\mathbf{x}_i, t) - \frac{1}{\gamma}\left(\nabla_{\mathbf{x}_i}\Big[\sum_i V_1(\mathbf{x}_i, t) + \sum_{i<j} V_2(\|\mathbf{x}_i - \mathbf{x}_j\|) \Big]\right) + \boldsymbol{f}_i(t) \,,
\end{aligned}
\tag{2.1}
$$

with the external potential $V_1(\mathbf{x}_i, t)$, the pair interaction potential $V_2(\|\mathbf{x}_i - \mathbf{x}_j\|)$, flow field $\mathbf{u}(\mathbf{x}_i, t)$, and a white-noise term $\boldsymbol{f}_i(t)$ with homogeneous first moment and the second moment

given by

$$\langle f_{i\alpha}(t) f_{j\beta}(t') \rangle = 2\gamma k_{\mathrm{B}} T \delta_{ij} \delta_{\alpha\beta} \delta(t - t')$$

with Bolzmann's constant k_{B} and temperature T. The parameter γ is related to a friction coefficient. We assume here that the potential terms sum up to approximate the deterministic force $\mathbf{F}_i$ acting on the ith particle.

The corresponding Fokker-Planck equation for a probability density, $W(\vec{\mathbf{x}}, t)$, which determines the probability of finding a set of N particles around the positions $\mathbf{x}_1, \dots, \mathbf{x}_N$ at time t, reads

$$\partial_t W(\vec{\mathbf{x}}, t) = \mathcal{L}_S W(\vec{\mathbf{x}}, t) \quad \text{with} \quad \mathcal{L}_S(\cdot) = \sum_i \nabla_{\mathbf{x}_i} \cdot \left[\left(-\mathbf{u}(\mathbf{x}_i, t) - \frac{1}{\gamma} \mathbf{F}_i(\vec{\mathbf{x}}, t) + k_{\mathrm{B}} T \nabla_{\mathbf{x}_i} \right)(\cdot) \right] \quad (2.2)$$

with initial conditions $W(\vec{\mathbf{x}}, t_0) = \delta(\vec{\mathbf{x}} - \vec{\mathbf{x}}_0)$ and appropriate boundary conditions.

Because we are not interested in the probability distribution of finding particles at all positions, but rather the probability of finding any particle at a given position, we can integrate equation (2.2) over $N - 1$ of the N variables to obtain a one-particle number density. Therefore, we introduce the n-particle density $\varrho^{(n)}$ by integrating the probability density $(N - n)$-times,

$$\varrho^{(n)}(\mathbf{x}_1, \dots, \mathbf{x}_n, t) = \frac{N!}{(N - n)!} \int \cdots \int W(\vec{\mathbf{x}}, t) \, \mathrm{d}\mathbf{x}_{n+1} \dots \mathrm{d}\mathbf{x}_N.$$

Dropping the superscript for the one-particles density $\varrho^{(1)} =: \varrho$ and the subscript in the positions we obtain the continuity equation

$$\partial_t \varrho(\mathbf{x}, t) + \nabla \cdot \big(\varrho(\mathbf{x}, t) \, \mathbf{u}(\mathbf{x}, t) \big) = -\nabla \cdot \mathbf{j}(\mathbf{x}, t) \tag{2.3}$$

with

$$\gamma \, \mathbf{j}(\mathbf{x}, t) = -\varrho(\mathbf{x}, t) \nabla V_1(\mathbf{x}, t) - k_{\mathrm{B}} T \nabla \varrho(\mathbf{x}, t) - \int \varrho^{(2)}(\mathbf{x}, \mathbf{x}', t) \nabla V_2(\|\mathbf{x} - \mathbf{x}'\|) \, \mathrm{d}\mathbf{x}'. \tag{2.4}$$

If we neglect the pair-interaction term containing the two-particle density $\varrho^{(2)}$, equations (2.3) and (2.4) reduce to Fick's diffusion equation in a flowing heat bath

$$\partial_t \varrho(\mathbf{x}, t) + \nabla \cdot \big(\varrho(\mathbf{x}, t) \, \mathbf{u}(\mathbf{x}, t) \big) = -\nabla \cdot \mathbf{j}(\mathbf{x}, t),$$
$$\beta \gamma \, \mathbf{j}(\mathbf{x}, t) = -\varrho(\mathbf{x}, t) \nabla U_1(\mathbf{x}, t) - \nabla \varrho(\mathbf{x}, t) \tag{2.5}$$

with an external potential $U_1 := \beta V_1$ and coefficient $\beta := (k_{\mathrm{B}} T)^{-1}$. This equation models the flow of non-interacting particles.

Dynamic density functional theory

In classical dynamic density functional theory the flux $\mathbf{j}$ is related to the gradient of the variational derivative of an energy functional $F_{\mathrm{H}}[\varrho] := F_{\mathrm{id}}[\varrho] + F_{\mathrm{ext}}[\varrho] + F_{\mathrm{exc}}[\varrho]$. The first term in the functional corresponds to an ideal solution part

$$F_{\mathrm{id}}[\varrho] = k_{\mathrm{B}} T \int \varrho(\mathbf{x}) (\ln(\varrho(\mathbf{x}) \Lambda^m) - 1) \, \mathrm{d}\mathbf{x},$$

where Λ is the thermal wavelength. A contribution for an external potential is

$$F_{\text{ext}}[\varrho] = \int \varrho(\mathbf{x}, t) V_1(\mathbf{x}, t) \, \mathrm{d}\mathbf{x} \,,$$

whereas the excess free-energy for particle interactions $F_{\text{exc}}[\varrho]$ is unknown for general systems. The authors of [213] used this relation for the advected dynamic density functional theory to obtain the evolution equation

$$\partial_t \varrho(\mathbf{x}, t) + \nabla \cdot (\varrho(\mathbf{x}, t) \, \mathbf{u}(\mathbf{x})) = \nabla \cdot \left(\gamma^{-1} \varrho(\mathbf{x}, t) \nabla \frac{\delta F_{\text{H}}[\varrho(\mathbf{x}, t)]}{\delta \varrho(\mathbf{x}, t)} \right). \tag{2.6}$$

Equation (2.6) still contains the unknown free-energy part F_{exc} and further approximations are necessary. One approach to obtain F_{exc} is the mean-field approximation for very soft interactions

$$F_{\text{exc}}[\varrho] \approx \frac{1}{2} \iint \varrho(\mathbf{x}) \varrho(\mathbf{x}') \nabla V_2(\|\mathbf{x} - \mathbf{x}'\|) \, \mathrm{d}\mathbf{x} \, \mathrm{d}\mathbf{x}' \,.$$

In [213] this approach is used to obtain a DDFT for particles in a flowing solvent. Even if the approach is only valid for potential flows, in [195], situations are described where it gives good approximations in cases without detailed balance. This is confirmed in [213] by considering Stokes flows.

We will follow this route and further approximate equation (2.6). To derive more efficient models which allow us to simulate more complex problems we consider a different way to approximate F_{exc}, than the mean field approach. Known approximations for hard and soft particles include those based on the Rosenfeld fundamental measure theory [221], (modified) weighted density approximation [182, 105], and the Rumakrishnan-Yussouff (RY) approximation [204]. In this work we use the RY approximation.

Phase-Field Crystal model

Consider the relative density deviation from a constant reference liquid density: $\delta \varrho(\mathbf{x}) := \varrho(\mathbf{x}) - \varrho_L$. The excess free part of the energy can be approximated in the RY-approximation by expansion around the liquid density ϱ_L up to second order, in the sense of a functional Taylor expansions

$$
\begin{aligned}
F_{\text{exc}}[\varrho] - F_{\text{exc}}[\varrho_L] &=: \triangle F_{\text{exc}}[\varrho] \\
&\approx \int \delta \varrho(\mathbf{x}) \frac{\delta F_{\text{exc}}[\varrho_L]}{\delta \varrho(\mathbf{x})} \, \mathrm{d}\mathbf{x} + \frac{1}{2} \iint \delta \varrho(\mathbf{x}) \, \delta \varrho(\mathbf{x}') \frac{\delta^2 (F_{\text{exc}}[\varrho_L])}{\delta \varrho(\mathbf{x}) \, \delta \varrho(\mathbf{x}')} \, \mathrm{d}\mathbf{x} \, \mathrm{d}\mathbf{x}' \\
&= -k_{\text{B}} T \int \delta \varrho(\mathbf{x}) c^{(1)}(\mathbf{x}, \varrho_L) \, \mathrm{d}\mathbf{x} - \frac{k_{\text{B}} T}{2} \iint \delta \varrho(\mathbf{x}) c^{(2)}(\mathbf{x}, \mathbf{x}', \varrho_L) \, \delta \varrho(\mathbf{x}') \, \mathrm{d}\mathbf{x} \, \mathrm{d}\mathbf{x}' \,,
\end{aligned}
$$

with the direct correlation functions given by

$$c^{(1)}(\mathbf{x}, \varrho) = -\beta \frac{\delta F_{\text{exc}}[\varrho]}{\delta \varrho} \quad \text{and} \quad c^{(2)}(\mathbf{x}_1, \mathbf{x}_2, \varrho) = \frac{\delta c^{(1)}(\mathbf{x}_1, \varrho)}{\delta \varrho(\mathbf{x}_2)} = -\beta \frac{\delta^2 (F_{\text{exc}}[\varrho])}{\delta \varrho(\mathbf{x}_1) \, \delta \varrho(\mathbf{x}_2)} \,.$$

In the liquid reference fluid another form of $c^{(1)}$ can be found: $c^{(1)}(\mathbf{x}, \varrho_L) = \ln(\varrho_L \Lambda^m) - \beta \mu_L$ with μ_L the constant chemical potential of the reference liquid. The ideal gas part F_{id} of the energy can be rewritten as

$$F_{\text{id}}[\varrho] - F_{\text{id}}[\varrho_L] =: \triangle F_{\text{id}}[\varrho] = k_B T \int \delta\varrho \big(\ln(\varrho_L \Lambda^m) - 1 \big) + \varrho(\mathbf{x}) \ln \left(\frac{\varrho(\mathbf{x})}{\varrho_L} \right) d\mathbf{x}.$$

Combining both, the ideal gas and the excess part of the energy (relative to the reference liquid state), results in

$$\triangle F_{\text{id}}[\varrho(\mathbf{x})] + \triangle F_{\text{exc}}[\varrho(\mathbf{x})]$$
$$= k_B T \int \underbrace{\delta\varrho(\mathbf{x})\Big(\beta\mu_L - 1\Big)}_{f_1(\varrho(\mathbf{x}))} + \underbrace{\varrho(\mathbf{x}) \ln \left(\frac{\varrho(\mathbf{x})}{\varrho_L} \right)}_{f_2(\varrho(\mathbf{x}))} - \underbrace{\frac{1}{2} \int \delta\varrho(\mathbf{x}) \bar{c}^{(2)}(\mathbf{x}, \mathbf{x}', \varrho_L) \, \delta\varrho(\mathbf{x}) \, d\mathbf{x}'}_{f_3(\varrho(\mathbf{x}))} \, d\mathbf{x}.$$

Because V_2 depends on the distance $\|\mathbf{x} - \mathbf{x}'\|$ only, this property is assumed to be true also for the direct pair correlation function, especially in the liquid phase. So, we assume that $c^{(2)}(\mathbf{x}, \mathbf{x}', \varrho_L) = \bar{c}^{(2)}(\|\mathbf{x} - \mathbf{x}'\|)$ and the rotational symmetry of $\bar{c}^{(2)}$ follows immediately.

Now consider the Fourier transformed correlation function by rewriting $f_3(\varrho)$ as convolution $f_3(\varrho(\mathbf{x})) = \frac{1}{2} \delta\varrho(\mathbf{x}) \big[\bar{c}^{(2)} * \delta\varrho \big](\mathbf{x})$. The correlation-function is rotationally symmetric. This leads to a simplification of the Fourier-transform of $\bar{c}^{(2)}$, i.e.,

$$\mathcal{F}[\bar{c}^{(2)}] =: \hat{c}(\mathbf{k}) = \int_{\mathbb{R}^n} \bar{c}^{(2)}(\|\mathbf{x}\|) \cos(\mathbf{k} \cdot \mathbf{x}) \, d\mathbf{x}.$$

Expanding $\hat{c}$ around $\mathbf{k}_0 = 0$ [80] leads to

$$\hat{c}(\mathbf{k}) = C_0 + \mathbf{k}^2 C_2 + \mathbf{k}^4 C_4 + \dots$$

with $\mathbf{k}^2 := \sum_i k_i^2$ the square of the wave vector $\mathbf{k}$. The coefficients with odd derivatives vanish due to the choice of the expansion point. We can now write the Fourier transform of f_3 as

$$\mathcal{F}[f_3(\varrho)](\mathbf{k}) = \frac{1}{2 \cdot (2\pi)^n} \Big[\hat{\delta\varrho} * (\hat{c} \cdot \hat{\delta\varrho}) \Big](\mathbf{k})$$
$$= \frac{1}{2 \cdot (2\pi)^n} \Big[\hat{\delta\varrho} * \big((C_0 + C_2(\cdot)^2 + C_4(\cdot)^4 + \dots) \cdot \hat{\delta\varrho} \big) \Big](\mathbf{k}) =: \hat{f}_3(\varrho).$$

The inverse Fourier transform leads to the real space approximation, by truncating the expansion at fourth order,

$$\mathcal{F}^{-1}[\hat{f}_3(\varrho)](\mathbf{x}) \approx \frac{1}{2} \delta\varrho(\mathbf{x})(C_0 - C_2\Delta(\cdot) + C_4\Delta^2(\cdot)) \, \delta\varrho(\mathbf{x}).$$

To relate the parameters C_i to those of other models, which assume constant mobility in equation (2.6) on the right-hand side (e.g., the PFC2-model in [268]), the ideal gas term in the energy is expanded around the mean density $\bar{\varrho}$. We introduce a new variable $\varphi(\mathbf{x}, t) := (\varrho(\mathbf{x}, t) - \bar{\varrho})/\bar{\varrho} = (\delta\varrho(\mathbf{x}, t) - \bar{\varrho})/\bar{\varrho} + \varrho_L/\bar{\varrho}$, the dimensionless *density modulation*, and truncate the

expansions at fourth order. The expansions of $f_i(\varrho)$ in terms of φ, neglecting all linear terms, because they vanish by differentiation, yield

$$\frac{1}{\bar{\varrho}}\big(f_1(\varrho(\mathbf{x})) - f_1(\bar{\varrho})\big) = \varphi(\mathbf{x},t)\big(\beta\mu_L - 1\big) = \text{ (linear term)},$$

$$\frac{1}{\bar{\varrho}}\big(f_2(\varrho(\mathbf{x})) - f_2(\bar{\varrho})\big) \approx \frac{1}{2}\varphi(\mathbf{x},t)^2 - \frac{1}{6}\varphi(\mathbf{x},t)^3 + \frac{1}{12}\varphi(\mathbf{x},t)^4 + \text{ (linear terms)},$$

$$\frac{1}{\bar{\varrho}}\big(f_3(\varrho(\mathbf{x})) - f_3(\bar{\varrho})\big) \approx \frac{1}{2}\varphi(\mathbf{x},t)(C_0 - C_2\Delta + C_4\Delta^2)\varphi(\mathbf{x},t) + \text{ (linear terms)}.$$

The third term in the energy, $\triangle F_{\text{ext}}[\varrho] = \int \delta\varrho V_1 =: \int f_4(\varrho)$, contains the external potentials and can also be expressed in terms of φ as $\frac{1}{\bar{\varrho}}\big(f_4(\varrho(\mathbf{x})) - f_4(\bar{\varrho})\big) = \varphi(\mathbf{x},t)V_1(\mathbf{x},t)$. Finally, we can define the total free-energy relative to the mean density by summation of the energy parts: $\frac{1}{\bar{\varrho}}\big(\triangle F_{\text{H}}[\varrho] - \triangle F_{\text{H}}[\bar{\varrho}]\big) = \frac{1}{\bar{\varrho}}\big(F_{\text{H}}[\varrho] - F_{\text{H}}[\bar{\varrho}]\big) \approx F_1[\varphi]$ with

$$\begin{aligned}
\beta F_1[\varphi] := & \int \frac{1}{2}\varphi(\mathbf{x})^2 - \frac{1}{6}\varphi(\mathbf{x})^3 + \frac{1}{12}\varphi(\mathbf{x})^4 \, \mathrm{d}\mathbf{x} \\
& - \int \frac{1}{2}\varphi(\mathbf{x})(C_0 - C_2\Delta + C_4\Delta^2)\varphi(\mathbf{x}) \, \mathrm{d}\mathbf{x} \\
& + \int \beta M(\varphi(\mathbf{x}))V_1(\mathbf{x}) \, \mathrm{d}\mathbf{x},
\end{aligned} \tag{2.7}$$

where $M(\varphi) := \varrho = (\varphi + 1)\bar{\varrho}$, and the notation F_1 comes from the original name *PFC1-model* in [268]. Now, the evolution equation with respect to φ can be derived from (2.6) as

$$\begin{aligned}
\partial_t\varphi(\mathbf{x},t) + \nabla \cdot (\varphi(\mathbf{x},t)\,\mathbf{u}(\mathbf{x})) &= \nabla \cdot \left\{ \gamma^{-1}M(\varphi)\nabla\frac{\delta F_1[\varphi(\mathbf{x},t)]}{\delta\varphi(\mathbf{x},t)} \right\} \\
&= \nabla \cdot \left\{ (\beta\gamma)^{-1}M(\varphi)\nabla\big(\varphi(\mathbf{x},t) - \frac{1}{2}\varphi(\mathbf{x},t)^2 + \frac{1}{3}\varphi(\mathbf{x},t)^3 \right. \\
&\qquad\qquad \left. + \beta M'(\varphi)V_1(\mathbf{x}) - (C_0 - C_2\Delta\varphi(\mathbf{x},t) + C_4\Delta^2\varphi(\mathbf{x},t))\big) \right\}.
\end{aligned}$$

This evolution equation is an approximation of the dynamic density functional theory, obtained by expansion of the correlation function. It is related to the classical PFC equation, extended by an advection term and non-constant mobility, and was first derived by Elder and Grant [79] with a slightly different parametrization.

To obtain the original Elder–Grant form of the PFC equation, we introduce a new variable $\psi := \varphi - 0.5$ and perform a re-parametrization to new parameters r and $\bar{\psi}$. The number of parameters is reduced by setting the lattice constant to 1, i.e., to fix the ratio $2|C_4|/C_2 \overset{!}{=} 1$. Stability considerations give the sign of the last parameter, i.e., $\text{sign}(C_4) = -1$. This leads to the parameter relations

$$C_0 := C_2\left(\frac{9}{2} - \frac{1}{2}(1+r)\right), \quad C_2 := \frac{1}{6}, \quad C_4 := -\frac{1}{2}C_2.$$

Inserting this into the energy (2.7) and neglecting linear and constant terms, we arrive at the proposed standard formulation that is the base for our simulations,

$$\beta F_1[\psi(\mathbf{x})] = C\int \frac{1}{2}\psi(\mathbf{x})\big(r + (1+\Delta)^2\big)\psi(\mathbf{x}) + \frac{1}{4}\psi(\mathbf{x})^4 + M(\psi(\mathbf{x}))U(\mathbf{x}) \, \mathrm{d}\mathbf{x} \tag{2.8}$$

with $C = (48/\bar{\varrho})^{-1}$, and $U(\mathbf{x}) = (Ck_\mathrm{B}T)^{-1}V_1(\mathbf{x})$, which is the rescaled external potential, and with $M(\psi) := \varrho = \bar{\varrho}(1.5 + \psi)$. This functional is strongly related to the Swift-Hohenberg functional [247]. The evolution equation of the simplified *advected Phase-Field Crystal model* (aPFC) reads

$$\partial_t \psi + \nabla \cdot (\psi \mathbf{u}) = \nabla \cdot \left\{ \gamma^{-1} M(\psi) \nabla \frac{\delta F_1[\psi]}{\delta \psi} \right\} = \nabla \cdot \left\{ M_0 M(\psi) \nabla \mu \right\},$$
$$\mu = \psi^3 + (r + (1 + \Delta)^2)\psi + M'(\psi)U \tag{2.9}$$

with $M_0 = C/(\beta\gamma)$.

2.1.2 Computational results

Numerical discretization

The evolution equations (2.5) and (2.9) are discretized using finite-elements in space and a semi-implicit discretization in time. For the standard PFC part we follow the approach described in [29] and Section 1.2 and extend the scheme by a transport term and an external potential. The advection-diffusion equation is discretized using a backward Euler scheme.

Following the notation in Chapter 1 we have a sequence of discrete equations. Let $\psi_0, c_0 \in L_2(\Omega)$ be given. Furthermore, let N be the number of timesteps. For $k = 0, 1, \ldots, N-1$, find $\psi_{k+1}, \psi_{k+1}^\natural, \psi_{k+1}^\flat \in V_h$, s.t.

$$(\psi_{k+1}^\natural - ((1+r) + 3\psi_k^2)\psi_{k+1}, \vartheta_h)_\Omega + (2\nabla\psi_{k+1} + \nabla\psi_{k+1}^\flat, \nabla\vartheta_h)_\Omega = (-2\psi_k^3 + M'(\psi_k)U, \vartheta_h)_\Omega,$$
$$\left(\psi_{k+1}, \vartheta_h'\right)_\Omega + \tau_k(M(\psi_k)\nabla\psi_{k+1}^\natural - \psi_{k+1}\mathbf{u}, \nabla\vartheta_h')_\Omega = \left(\psi_k, \vartheta_h'\right)_\Omega, \tag{2.10}$$
$$(\psi_{k+1}^\flat, \vartheta_h'')_\Omega + (\nabla\psi_{k+1}, \nabla\vartheta_h'')_\Omega = 0, \qquad \forall \vartheta_h, \vartheta_h', \vartheta_h'' \in V_h$$

for the advected PFC equation and find $c_{k+1}, c_{k+1}^\natural \in V_h$, s.t.

$$(c_{k+1}^\natural - c_{k+1}, \vartheta_h)_\Omega = (M'(c_k)U, \vartheta_h)_\Omega,$$
$$\left(c_{k+1}, \vartheta_h'\right)_\Omega + \tau_k(M(c_k)\nabla c_{k+1}^\natural - c_{k+1}\mathbf{u}, \nabla\vartheta_h')_\Omega = \left(c_k, \vartheta_h'\right)_\Omega, \qquad \forall \vartheta_h, \vartheta_h' \in V_h \tag{2.11}$$

for the advection-diffusion system.

The equations (2.10) and (2.11) lead to the linear systems $\mathbf{A}_\mathrm{pfc}\mathbf{x} = \mathbf{b}_\mathrm{pfc}$ and $\mathbf{A}_\mathrm{diff}\mathbf{x}' = \mathbf{b}_\mathrm{diff}$ with the solution components $\mathbf{x} = (\boldsymbol{\psi}_{k+1}^\natural, \boldsymbol{\psi}_{k+1}, \boldsymbol{\psi}_{k+1}^\flat)^\top$ and $\mathbf{x}' = (\boldsymbol{c}_{k+1}^\natural, \boldsymbol{c}_{k+1})^\top$ respectively, where the corresponding matrices are given by

$$\mathbf{A}_\mathrm{pfc} = \begin{bmatrix} \mathbf{M} & -(1+r)\mathbf{M} + \mathbf{N}(\psi_k) + 2\mathbf{K} & \mathbf{K} \\ \tau_k\mathbf{K}_\mathrm{M}(\psi_k) & \mathbf{M} - \tau_k\mathbf{W} & 0 \\ 0 & \mathbf{K} & \mathbf{M} \end{bmatrix}, \quad \mathbf{A}_\mathrm{diff} = \begin{bmatrix} \mathbf{M} & -\mathbf{M} \\ \tau_k\mathbf{K}_\mathrm{M}(c_k) & \mathbf{M} - \tau_k\mathbf{W} \end{bmatrix} \tag{2.12}$$

and the right-hand-side vectors by

$$\mathbf{b}_\mathrm{pfc} = \begin{pmatrix} \left((-2\psi_k^3 + M'(\psi_k)U, \theta_j)_\Omega\right)_j \\ \mathbf{M}\boldsymbol{\psi}_k \\ 0 \end{pmatrix}, \qquad \mathbf{b}_\mathrm{diff} = \begin{pmatrix} \left((M'(c_k)U, \theta_j)_\Omega\right)_j \\ \mathbf{M}\mathbf{c}_k \end{pmatrix},$$

where $\mathbf{W}$ is a shortcut for the advection term, i.e., $\mathbf{W} = \left((\theta_j \mathbf{u}, \nabla\theta_i)_\Omega\right)_{ij}$.

Similar to the calculation of [213], an external potential of exponential form is used, i.e., $U(\mathbf{x}) = \omega_1 \cdot \exp\left(-\frac{\|\mathbf{x}\|^q}{\omega_2^q}\right)$, where the parameters ω_1, ω_2 and q are chosen in such a way that the slope and interaction region depend on the colloid and polymer coils. This potential describes a soft colloidal particle in the center of a domain. In the following we have set $\omega_1 = 10, \omega_2 = 11$, and $q = 6$. For simplicity we set the mobility in the evolution equations to $M(\cdot) \equiv 1$.

Validation of the advection scheme

To validate the approach we use a simple configuration with one colloidal particle fixed in the center of a rectangular domain. We assume a steady flow around the particle, where viscous forces dominate over initial forces in the fluid, i.e., we consider the low Reynolds number limit. There are no additional external forces acting on the fluid and no geometric constraints, i.e., walls or other obstacles. Then the flow field around the colloidal particle with radius R is given by the solution of the Stokes equation, which can be expressed analytically by [213, 108]

$$\mathbf{u}(\mathbf{x}) = \mathbf{c} - \frac{3R}{4\|\mathbf{x}\|}\left(1 + \frac{R^2}{3\|\mathbf{x}\|^2}\right)\mathbf{c} + \frac{3R}{4\|\mathbf{x}\|^3}\mathbf{x}(\mathbf{x}\cdot\mathbf{c})\left(\frac{R^2}{\|\mathbf{x}\|^2} - 1\right) \tag{2.13}$$

with $\mathbf{c} = c^\infty\,\mathbf{e}_x$ the velocity at infinity distance from the obstacle. For $R = 0$ this reduces to the uniform flow $\mathbf{u}(\mathbf{x}) = \mathbf{c}$. More complex situations with more colloidal particles could be handled using a superposition principle, or by solving the (non-stationary) Stokes equation numerically. For non-stationary flow fields a direct coupling of the equations of fluid dynamics to the equations of the simulation of interacting polymer particles in the solvent would be necessary. Such coupling is crucial for the inclusion of the hydrodynamic forces between polymer coils exerted on the solvent and s implemented and analyzed in the next major section.

Figure 2.1 shows the density distribution ψ and c of the advected PFC-equation and the advection-diffusion equation respectively, for a fluid flowing through the domain from left to right. The density values are normalized, so that red corresponds to the maximal density in front of the spherical obstacle and dark blue corresponds to the minimal density on the obstacle. The obstacle, i.e., the colloidal particle, is visualized with a spherical ball in the center of the domain. The characteristic first density wave can be seen in both simulations, but in the PFC simulation several fading out waves follow the first one. The studies of [195, 108] indicate that more than one such wave exists in the interacting case, as can be seen in their Brownian dynamics simulations and DDFT calculations. For this reason we assume that in the interacting case the wave like structure in front of the obstacle is more realistic than the single peak observed in the simple diffusion case.

Proceeding from the qualitative comparison we now follow [213] and analyze the dependency of the density distribution on both, the radius of the colloid and the velocity of the fluid, for the case of interacting and non-interacting particles. We use the same analytic Stokes flow (2.13) with a far-field velocity depending on the reference value $c^* := c^\infty D\bar{\psi}/r$. First the radius of the obstacle is fixed at $R/D =: R^* = 0.6$, thus the colloid is bigger than the polymer coils. The size D represents the interaction radius of the colloid, i.e., how close particles can approach the obstacle boundary. The value can be approximated by $D = R + d/2$, where $d = 4\pi/\sqrt{3}$ is the mean distance between the center of mass of polymer coils in the one-mode approximation [79, 268].
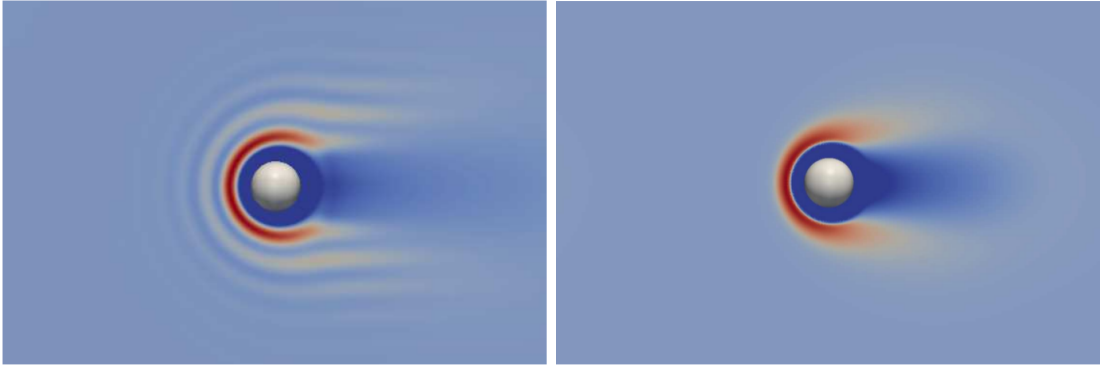
Figure 2.1 – *Polymer density around a colloidal particle. Left: Phase-Field Crystal simulation with $R^* = 0.6, c = 0.8, r = -0.1$, and $\bar{\psi} = -0.3$. Right: Advection-diffusion simulation with $R^* = 0.6, c = 1.0$, and $\bar{\psi} = -0.3$. Red indicates high density, whereas blue indicates low density. The colloid in the center is visualized as a gray ball.*

Figure 2.2 shows the density profile with non-interacting and interacting particles for a fixed obstacle radius. The difference between the left and right plot of Figure 2.2 is the formation behavior of the first wave depending on the reference velocity. Where the non-interacting simulation shows a big increase of the first maximum for higher values c^*, in the interacting case this is far less pronounced.

For the interacting case the maximum increases slightly with increasing c^* and the change is negligible on further increase of c^*. Behind the colloid, i.e., to the right of the obstacle, the wave structure is also found. Because of the compressibility of the polymer coils in the solvent, the distance of the maxima in front of the colloid shrinks slightly. Thus, the mean particle distance d of the one-mode approximation is only an approximation of the Phase-Field Crystal particle distance and is not constant over the domain.

The dependency of the density structure to the radius of the obstacle is plotted in Figure 2.3, again for non-interacting and interacting particles. There, the reference velocity is fixed at $c^* = 12$. For radii bigger than the polymer coil radius, i.e., $R^* > 0.5$, the density shows an additional wave behind the obstacle, whereas for smaller radii one cannot see such an effect. For higher velocities, i.e., lower values of R^*, the first maximum rises much more in the case of non-interacting particles than in the case of interacting ones. The interesting observation is the structure behind the colloid. For radii R^* less than 0.5, i.e., the colloidal radius is less than the interaction radius of the polymers, the bow wave does not show the oscillating structure, which can be seen for larger radii. The wave is similar to the non-interacting case.

Preconditioner for the PFC-system

For the numerical validation we first apply the direct solver UMFPACK [65] to the PFC system directly, since the problems are small enough. The diffusion problem can be solved by simple iterative Krylov-subspace methods, either in the 2x2 block system, or by rewriting the system as a one component scalar equation, as it is done as part of the PFC preconditioner. Larger problems with more than one obstacle need more efficient linear solvers for the PFC equation.
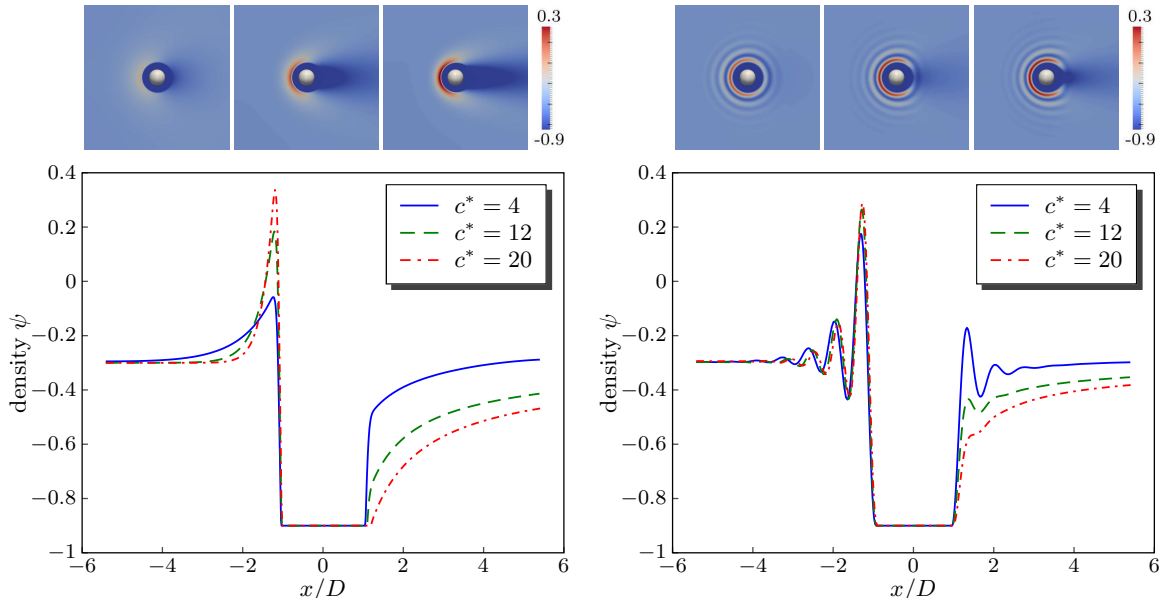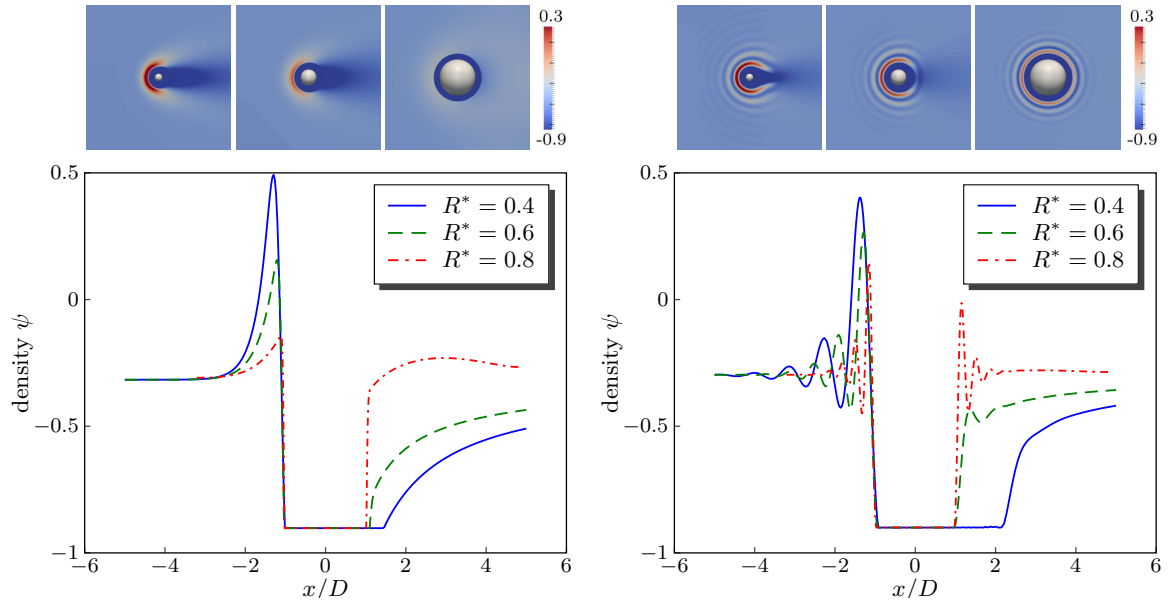
Figure 2.2 – *Density-profile of the solution for different reference velocities c^* of the fluid, at fixed radius $R^* = 0.6$ of the obstacle. Left: Snapshots of the advection-diffusion equations for three different reference velocities c^*. Right: For the same three reference velocities the corresponding PFC solution, that represents the density profile in the interacting case.*

Therefore, a preconditioned Krylov-subspace method is applied. Similar to the classical PFC system the system-matrix $\mathbf{A}_{\mathrm{pfc}}$ can be simplified and approximated by a matrix $\mathbf{P}$ that can easily be factorized in a product of two triangular matrices.

In [49] a convective Cahn-Hilliard equation is analyzed with respect to the influence of the advection term to the preconditioner. Assuming $\tau_k \in \mathcal{O}(h^2)$ and $\mathbf{u} \in \mathcal{O}(1)$, the convection term does not dominate the other terms in the diagonal block and can thus be neglected in the preconditioner. We follow this approach and study the properties of the preconditioner with increasing velocity c^*. The preconditioner matrix is chosen equal to $\mathbf{P}$ of equation (1.15) for the classical PFC system.

In the validation of the advected PFC equation we have considered one spherical obstacle with dimensionless radius R^* in a flow field given by equation (2.13). Analyzing the developed density waves around the obstacle, we have found steep gradients within a length scale d. The finite-element discretization allows to use adaptive grids with fine resolution around the obstacle and a coarse resolution far away from the obstacle. This may influence the properties of the preconditioner, as well.

The influence of the velocity to the number of solver iterations of a FGMRES solver [224] is studied in Figure 2.4. The same setup as for the validation is used and the number of solver iterations is averaged over the first 20 timesteps for various refinement levels used to resolve the obstacle. It shows that with increasing reference velocity c^* the number of iterations also increases, but this increase is nearly linear. Changing the mesh resolution around the obstacle does not influence the solver significantly.

Figure 2.3 – *Density-profile of the solution for different radii R^* of the obstacle, at fixed reference velocity $c^* = 12$ of the fluid. Left: Snapshots of the advection-diffusion equations for three different radii R^*. Right: For the same three radii the corresponding PFC solution, that represents the density profile in the interacting case.*

2.1.3 Conclusion

We have proposed a local approximation to the DDFT formulation in [213]. The formulation provides an efficient way to treat interacting Brownian particles in a flowing solvent. Neglecting the hydrodynamic interactions between the solute particles and between the solute and colloid particles allows for an efficient coupling, in which only the time derivative in the PFC model is replaced by the total (material) time derivative. The obtained equation thus provides an advected PFC model, which is then solved in a domain excluding the spherical obstacles.

A quantitative comparison with the full aDDFT simulations in [213, 195] was not possible. Qualitatively the aPFC simulations show wave structures similar to the results of the authors above, but significantly more pronounced. The influence of both, the reference velocity of the fluid, and the radius of the colloidal particle, was investigated, and comparisons were made between the Phase-Field Crystal and diffusion-advection model, for interacting and non-interacting polymer coils in the solvent.

The aPFC model requires much less computational effort than full aDDFT simulations, due to the locality of the approach. Furthermore, coupling to the Navier-Stokes equations could be done easily. This is encouraging for an extension of the approach to include colloid-colloid interactions in more complex configurations. The calculation of depletion forces between two colloids that are close to each other, so that polymer particles do not fit between them, is appealing and easily realizable with the aPFC approach. Hydrodynamic interactions between the polymer particles is often neglected but could also be included in the model. In the next section such a model is explained and validated.
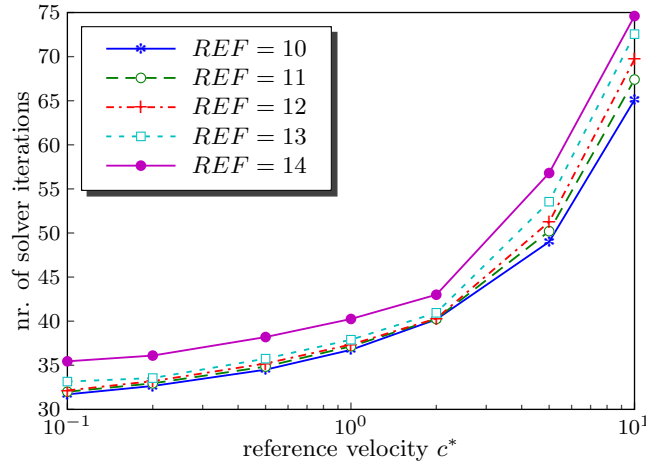
Figure 2.4 – *Number of solver iteration when a preconditioner is applied. The setup is a flow of polymer coils around a spherical obstacle with various reference flow velocities c^*. PFC parameters: $r = -0.1$, $\psi = -0.3$, mobility $M(\psi) \equiv 1$, obstacle radius $R^* = 0.6$, polynomial degree $p = 2$ in 2D, and boundary potential with $\omega_1 = 10$, averaged over 20 timesteps with timestep width $\tau = 0.1$. Various adaptive refinements of the obstacle are compared. The minimal grid size for refinement $REF = (10, 11, 12, 13, 14)$ corresponds to $h = (0.6413, 0.4535, 0.3206, 0.2267, 0.1603)$.*

For the development of an efficient solver for the advected PFC equation, we have followed the approach of [49] and have used the originally proposed preconditioner (1.15), neglecting the advection term. This approximation seems reasonable, since numerical experiments show only a little influence on the number of solver iterations in a FGMRES method, for increasing velocity term. Also an adaptive refinement of the grid around the spherical obstacle is investigated with respect to the properties of the preconditioner. It is found that the grid refinement in this setup does not increase the solver iterations a lot.

The good preconditioner properties for the advected PFC equations may also be explained due to the PFC setup in the liquid phase. In Remark 3 in Section 1.5.1 about the critical timestep width in the preconditioner, we have seen that the preconditioner, for parameters in the liquid phase, is very stable with respect to the influence of τ and thus is more stable than the preconditioner in the crystalline parameter regime. In the next section we have analyzed a setup of crystallization in a flowing environment and study the influence of the reference velocity there.

2.2 A Navier-Stokes Phase-Field Crystal model for colloidal suspensions

Simple fluids can be coarse grained, considered as a continuum and very well described by the Navier-Stokes equations. A quantitative description can be achieved down to the nanometer scale. For colloidal suspensions, this simple treatment is not necessarily valid any more. Here, colloidal particles, with a typical size range of nanometers to a few microns, move due to collisions with the solvent molecules, interact with each other, and induce flow fields due to their motion. It is shown that these hydrodynamic interactions are of relevance in various practical applications, e.g., colloidal gelation [96] or coagulation of colloidal dispersions [170]. To calculate non-equilibrium properties of such systems, it is required to resolve the different time and length scales arising from thermal Brownian motion and hydrodynamic interactions. Various approaches have been developed to consider these interactions in an effective way. An overview about proposed coarse-graining descriptions can be found in [191].

One of the most popular approaches is Stokesian dynamics (SD) within the low Reynolds number limit [50]. The hydrodynamic interaction is thereby incorporated in an approximate analytical form, assuming to result as the sum of two-body interactions. The approach is difficult to implement for complex boundary conditions and is relatively expensive. As an alternative, direct numerical simulations are proposed, which involve determining fluid motion simultaneously with particle motion. In these methods, the colloidal particles are fully resolved and coupled with the Navier-Stokes equations, leading to coupled discrete-continuous descriptions. Other discrete and hybrid models are, e.g., the (smoothed) dissipative particle dynamics model [116, 88, 152], the fictitious domain/immersed boundary method [198, 99], and the Lattice Boltzmann-Molecular Dynamics method [187, 132, 186]. A short review and comparison of such models is given in [95].

Our aim is to derive a fully continuous system of equations from such hybrid models. This has the advantage of an efficient numerical treatment, the possibility of a detailed numerical analysis, and it offers a straightforward coupling with other fields. Moreover, continuous models often allow to formulate analytical predictions for the behavior of some reference systems and provide mathematical tools to derive coarse grained descriptions. The model will serve as a general continuum model for colloidal suspensions, providing a quantitative approach down to the length scale set by the colloidal particles and it is operating on diffusive time scales. The approach will be derived by combining ideas from: (a) dynamic density functional theory (DDFT), and (b) hybrid discrete-continuous particulate flow models. We will test the derived system for colloidal crystallization in flowing environments and for colloidal sedimentation.

2.2.1 Overview about existing approaches

Dynamic density functional theory approach

The aim of the dynamic density functional theory (DDFT) approach is to provide a reduced model that describes the local state of a colloidal fluid by the time averaged one-particle density. The evolution of this density is driven by a gradient-flow of the equilibrium Helmholtz free-energy functional. A first realization of a DDFT for colloidal fluids was presented in the work of Marconi and Tarazona [165] with colloids modeled as Brownian particles. Later, this theory

was extended by Archer [20] and has been connected to the equations of motion from continuum fluid mechanics. Rauscher [213] has described an advected DDFT, to model colloids in a flowing environment that do not interact via hydrodynamic interactions. The work of Goddard et al. [101] has incorporated the effect of inertia and hydrodynamic interactions between the colloidal particles and recently Gránásy et al. [258] have explored a coarse-grained density coupling of DDFT and the Navier-Stokes equations.

We start the derivation of our model with the dynamical equations derived by Archer [20]. Therefore, we introduce the one-particle (number) density $\varrho(\mathbf{x}, t)$ and the average local velocity $\mathbf{v}(\mathbf{x}, t)$ of the colloidal particles. The density is driven by a continuity equation

$$\partial_t \varrho + \nabla \cdot (\varrho \mathbf{v}) = 0 \tag{2.14}$$

with the current $\varrho \mathbf{v}$ evolving via the dynamical equation

$$m\varrho \left(\partial_t \mathbf{v} + (\mathbf{v} \cdot \nabla) \mathbf{v} + \gamma \mathbf{v} \right) = -\varrho \nabla \frac{\delta F_{\mathrm{H}}[\varrho]}{\delta \varrho} + \eta \Delta \mathbf{v}, \tag{2.15}$$

where m represents the mass of the particles, γ a dumping coefficient, $F_{\mathrm{H}}[\varrho]$ the equilibrium Helmholtz free-energy functional and η a viscosity coefficient.

We use a minimal expression for the free-energy, the Swift-Hohenberg (SH) energy [247, 78], in a dimensionless form

$$F_{\mathrm{H}}[\varrho(\psi)] \simeq F_{\mathrm{sh}}[\psi] = \int \frac{1}{4}\psi^4 + \frac{1}{2}\psi(r + (q_0^2 + \Delta)^2)\psi \, \mathrm{d}\hat{\mathbf{x}}, \tag{2.16}$$

with $\varrho = \bar{\varrho}(1 + (\psi + 0.5))$ a parametrization of the one-particle density with respect to a reference density $\bar{\varrho}$. The phenomenological parameter r is related to the undercooling of the system and the constant q_0 is related to the lattice spacing. This functional arises by splitting the energy in an ideal gas contribution and an excess free energy $F_{\mathrm{H}} = F_{\mathrm{id}} + F_{\mathrm{exc}}$, rescaling and shifting of the order-parameter ϱ, expanding ideal gas contributions in real-space, and the excess free-energy in Fourier space and simplification, by removing constant and linear terms that would vanish in the dynamical equations. A detailed derivation of the energy can be found in [268, 124, 200] and in Section 2.1.1.

Inserting the density expansion and the free-energy (2.16) into (2.15), we get a system of dynamic equations for the density deviation ψ and the related non-dimensionalized averaged velocity $\hat{\mathbf{v}}$:

$$\partial_t \psi + \nabla \cdot \big((1.5 + \psi)\hat{\mathbf{v}}\big) = 0, \tag{2.17}$$

$$(1.5 + \psi)\left(\partial_t \hat{\mathbf{v}} + (\hat{\mathbf{v}} \cdot \nabla)\hat{\mathbf{v}} + \Gamma\hat{\mathbf{v}}\right) = \frac{1}{\mathrm{Re}}\Delta\hat{\mathbf{v}} - \frac{1}{\mathrm{Pe}}(1.5 + \psi)\nabla\frac{\delta F_{\mathrm{sh}}[\psi]}{\delta\psi}. \tag{2.18}$$

With respect to a length scale L and time scale L/V_0 we have the dimensionless variable $\hat{\mathbf{v}} = \mathbf{v}/V_0$ and Peclet number Pe, Reynolds number Re and friction coefficient Γ given by

$$\mathrm{Pe} = \frac{3mV_0^2}{k_{\mathrm{B}}T}, \quad \mathrm{Re} = \frac{m\bar{\varrho}LV_0}{\eta}, \quad \Gamma = \frac{\gamma L}{V_0}$$

with Boltzmann's constant k_{B} and temperature T. In Section 2.2.5, a detailed derivation of this dimensionless form of the dynamical equations can be found.

In the overdamped limit, $\Gamma \gg 1$, the velocity equation reduces to an explicit expression that relates the velocity to the chemical potential by

$$(1.5 + \psi)\hat{\mathbf{v}} = -\frac{1}{\Gamma \mathrm{Pe}}(1.5 + \psi)\nabla \frac{\delta F_{\mathrm{sh}}[\psi]}{\delta \psi}. \tag{2.19}$$

Inserting (2.19) into (2.17) results in the PFC equation [78]

$$\partial_t \psi = \frac{1}{\Gamma \mathrm{Pe}}\nabla \cdot \left((1.5 + \psi)\nabla \frac{\delta F_{\mathrm{sh}}[\psi]}{\delta \psi}\right), \tag{2.20}$$

referred to as PFC1 model in [268].

Particulate flows

Typical approaches to simulate particulate flows on larger length scales consider a Newton-Euler equation for each particle. This system of equations describes the motion as a rigid body and it can be combine with the Navier-Stokes equations for the flow around these particles. Various numerical approaches have been proposed to model this flow, including fictitious domain approach and the immersed boundary method, which incorporate a no-slip boundary condition on the particles surface (see, e.g., [100, 264, 19, 134]). All these approaches use the general idea to consider the particles as a highly viscous fluid, which allows the flow computation to be done on a fixed space region. The no-slip boundary condition on the particle surface is thereby enforced directly or implicitly, depending on the numerical approach. All these methods combine a continuous description of the flow field with a discrete off-lattice simulation for the particles.

Considering an incompressible fluid with viscosity η_f and constant fluid density ρ_f, we can write the Navier-Stokes equations for velocity $\mathbf{u}$ and pressure p of a pure fluid in a dimensionless form,

$$\partial_t \hat{\mathbf{u}} + (\hat{\mathbf{u}} \cdot \nabla)\hat{\mathbf{u}} = -\nabla \hat{p} + \frac{1}{\mathrm{Re}_f}\nabla \cdot \left(2(1 + \tilde{\eta})\mathbf{D}(\hat{\mathbf{u}})\right) + \mathbf{F}, \tag{2.21}$$

$$\nabla \cdot \hat{\mathbf{u}} = 0 \tag{2.22}$$

with length and time scale as above and the dimensionless velocity field $\hat{\mathbf{u}} = \mathbf{u}/V_0$, the viscosity perturbation $\tilde{\eta}$ from the expansion $\eta_f = \bar{\eta}_f(1 + \tilde{\eta})$, the fluid Reynolds number Re_f, and the dimensionless pressure $\hat{p}$ given by

$$\mathrm{Re}_f = \frac{\rho_f L V_0}{\bar{\eta}_f}, \quad \hat{p} = \frac{p}{\rho_f V_0^2},$$

respectively. The expression $\mathbf{D}(\hat{\mathbf{u}})$ gives the symmetric part of the velocity gradient, i.e.,

$$\mathbf{D}(\hat{\mathbf{u}}) = \frac{1}{2}(\nabla \hat{\mathbf{u}} + \nabla \hat{\mathbf{u}}^\top)$$

and $\mathbf{F}$ defines a volume force.

As a reference model for colloidal suspensions, we consider the fluid particle dynamics model (FPD) by [248]. Here, the particles are considered as a highly viscous fluid and the velocities of

the particles are extracted from the fluid velocity $\mathbf{u}$. The shape of the particles is constructed using a tanh-profile with a specified radius and interface thickness and their centers of mass interacting via an interparticle potential. The approach can also be seen as a modification of a classical "Model H" [235, 114] with a fluid and a particle phase and the driving force in the Navier-Stokes equations governed by the interatomic potential. The approach again combines continuous and discrete descriptions.

The motion of colloidal particles with positions $\mathbf{x}_i(t)$ are governed by the velocities $\mathbf{v}_i(t)$ and the evolution of a flow field $\mathbf{u}$, where the colloidal particles are suspended in. The basic idea is to introduce concentration fields $\phi_i(\mathbf{x}, t) \in [0, 1]$ for each particle and to average the fluid velocity over regions with high concentration, i.e.,

$$\mathbf{v}_i(t) = \frac{\int \phi_i(\mathbf{x}, t)\mathbf{u}(\mathbf{x}, t)\,\mathrm{d}\mathbf{x}}{\int \phi_i(\mathbf{x}, t)\,\mathrm{d}\mathbf{x}}.$$

Thus, the motion of the particles can be described by $\mathbf{x}_i(t + \Delta t) := \mathbf{x}_i(t) + \Delta t \cdot \mathbf{v}_i(t)$, with Δt the simulation time step.

A space-dependent fluid viscosity η_f, as a function of ϕ_i, is introduced to describe the rigidity of the particles and a force term $\mathbf{F} := \mathbf{F}^{[\mathrm{ta}]}$, to account for the particle interactions in the flow equation (2.21). This force is chosen as the negative gradient of an interaction potential V_2 multiplied with the particle-concentration fields ϕ_i,

$$\mathbf{F}^{[\mathrm{ta}]}(\mathbf{x}) \stackrel{\mathrm{def}}{=} -\sum_i \nabla_{\mathbf{x}_i} \big(\sum_{j \neq i} V_2(\|\mathbf{x}_i - \mathbf{x}_j\|) \big) \phi_i(\mathbf{x}). \tag{2.23}$$

The fluid viscosity $\eta_f = \bar{\eta}_f(1 + \tilde{\eta})$ is modeled, by describing the viscosity perturbation $\tilde{\eta}$, as

$$\tilde{\eta}(\mathbf{x}) = \sum_i \big(\frac{\bar{\eta}_p}{\bar{\eta}_f} - 1 \big) \phi_i(\mathbf{x}) \tag{2.24}$$

with $\bar{\eta}_f < \bar{\eta}_p$ the liquid and particle viscosity respectively. In [180] it is argued that the artificial diffusivity $\bar{\eta}_p/\bar{\eta}_f$ must go to ∞ for the particles to become rigid. In their method, they have introduced a different body force to guarantee this rigidity without taking large values of the viscosity ratio. However, we will here only consider the original FPD approach.

Towards a fully continuous description

Our aim is to derive a fully continuous model by combining the FPD model with the PFC approach. A first step in this direction has already been done in [176], where the interaction potential has already been replaced by the PFC approach. The discrete off-lattice simulation for the particles is no longer needed, the particle positions and velocities result from the advected PFC model. However, the forcing term in the Navier-Stokes equations still requires the identification of the position and velocity of each particle and thus, the approach still has a discrete component. To derive a fully continuous model we will first clarify the relation of the different approaches in [200, 248, 176] and will show that all the discrete coupling terms can be approximated with a simple continuous expression.

To allow for a description of the flow of individual particles, we consider a variant of the PFC model, the vacancy PFC model, introduced in [55, 40]. Instead of minimizing the Swift-Hohenberg functional directly, we consider a density field with positive density deviation ψ only,

which leads to a modification of the particle-interaction and allows to handle single particles as well as many individual particles embedded in the fluid.

2.2.2 Derivation of a fully continuous model

In [176] the PFC model and the FPD model are combined, by letting the density field influence the flow field. The interatomic potential is encoded in the Swift-Hohenberg energy (2.16) and the particle positions evolve according to the advective PFC equation (see below). The forcing term $\mathbf{F} := \mathbf{F}^{[ml]}$ in the Navier-Stokes equations now ensures the fluid velocity $\mathbf{u}$ to be equal to the particle velocity $\mathbf{v}_i$ at the particle position $\mathbf{x}_i$, i.e.,

$$\mathbf{F}^{[ml]}(\mathbf{x}) \stackrel{\text{def}}{=} \omega \sum_i (\hat{\mathbf{v}}_i - \hat{\mathbf{u}}(\mathbf{x}))\delta(\mathbf{x} - \mathbf{x}_i) \tag{2.25}$$

with $\omega \gg 1$ a penalty parameter and $\delta(\cdot)$ the pointwise delta-function. Thereby, position and velocity of each individual particle must be extracted from the density field ψ by tracking the maxima of the density, which are interpreted as average particle positions. These quantities are then explicitly inserted into the expression of the forcing term. The fluid viscosity η_f can be modeled as before in (2.24), but now ψ can directly be used to distinguish between the background fluid and the particles.

The force term (2.25) constrains the fluid velocity to be equal to the particle velocity at the center-of-mass position of the particle. In order to implement a no-slip boundary condition at the particle surfaces, the delta function needs to be replaced by the concentration fields $\phi_i(\mathbf{x})$:

$$\mathbf{F}^{[dd]}(\mathbf{x}) \stackrel{\text{def}}{=} \omega \sum_i (\hat{\mathbf{v}}_i - \hat{\mathbf{u}}(\mathbf{x}))\phi_i(\mathbf{x}). \tag{2.26}$$

This ansatz is highly related to the diffuse domain approach [145], where this force is shown to converge to the no-slip boundary condition $\mathbf{u} = \mathbf{v}_i$ at the ith particle surface, if the interface width goes to zero. Thereby ω has to be related to the interface thickness, see [93] for a detailed convergence study.

In the following, we give a new formulation of a continuous force term that can be evaluated without extracting individual particle positions and velocities. At first, we relate the density field ψ, described in (2.20), to a delta function $\delta(\mathbf{x})$ and to a concentration field $\phi(\mathbf{x}) = \sum_i \phi_i(\mathbf{x})$. In a second step, the particle velocities are shown to arise directly from the evolution equations (2.20) and (2.19).

Approximation of a delta-function

For the classical PFC equation in 1D, a one-mode approximation of the density ψ is given by [79]

$$\psi_{\text{om}}(\mathbf{x}) = A\cos(q_0\mathbf{x}) + \bar{\psi}, \tag{2.27}$$

where A, q_0, and $\bar{\psi}$ are constants that define the amplitude, lattice constant, and mean density of the field, respectively. We introduce

$$\psi_{(0)} = \frac{1}{2}\Big(1 + \frac{\psi_{\text{om}} - \bar{\psi}}{A}\Big), \quad \psi_{(k)} = (\psi_{(k-1)})^2, \tag{2.28}$$

for $k > 0$, or in explicit form $\psi_{(k)} = [\psi_{(0)}]^{2^k}$ for $k \in \mathbb{N}$. After appropriate normalization, we obtain

$$\delta_{(k)}(\mathbf{x}) := N_k \psi_{(k)}(\mathbf{x}) \tag{2.29}$$

with N_k normalization constants, which ensure the property $\int \delta_{(k)}(\mathbf{x}) \, \mathrm{d}\mathbf{x} = 1$. Values for various indices k can be found in Table 2.1. In Section 2.2.7 we show that $\delta_{(k)}$ forms a sequence of nascent delta functions. Figure 2.5 shows the first three elements of this sequence in comparison with the classical Gaussians $\delta_\epsilon^{\mathrm{exp}}(\mathbf{x}) \cong e^{[(q_0\|\mathbf{x}\|)^2/(-4\epsilon)]}$, visualizing the convergence qualitatively. As a consequence of this property, the shifted and scaled density field $\psi_{(0)}$ can be seen as a first-order approximation of a delta function. The approach can be generalized to 2D and 3D and will be used for ψ instead of ψ_{om}.

k	0	1	2	3
$N_k \cdot \dfrac{\pi}{q_0}$	1	$\dfrac{4}{3}$	$\dfrac{64}{35}$	$\dfrac{16384}{6435}$

Table 2.1 – *The first four elements of the sequence N_k, the normalization constants for the nascent delta function $\delta_{(k)}$.*
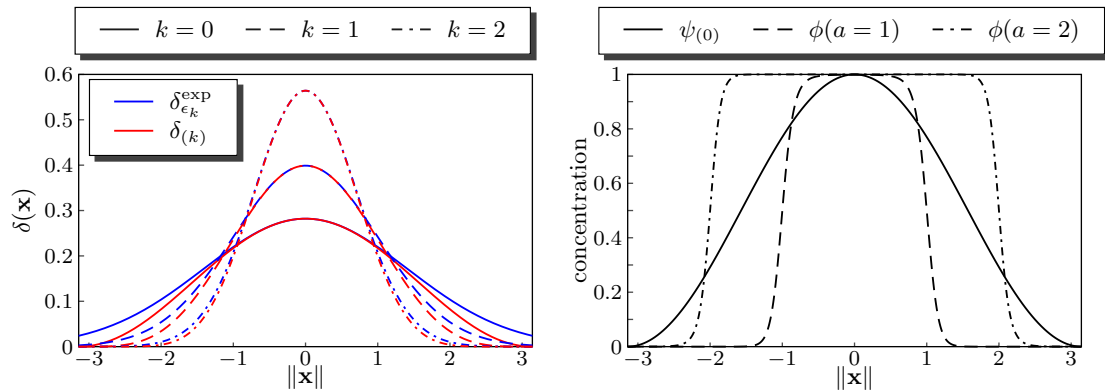
Figure 2.5 – *Left: The first three elements of the sequences $\delta_{\epsilon_k}^{\mathrm{exp}}$ (normalized), with $\epsilon_k = 2^{-k}$, in blue (upper curves) and $\delta_{(k)}$ in red (lower curves). The lattice constant is $q_0 = 1$. Right: Transformation of the density field ψ into a tanh-concentration field, for different particle radii. The lattice constant is $q_0 = 1$ and interface width $\epsilon = 0.1$.*

Approximation of concentration fields

The concentration field ϕ_i in [248], used for the phase-field description of particles, is defined by

$$\phi_i(\mathbf{x}) = \frac{1}{2}\Big(1 - \tanh\big(3(\|\mathbf{x} - \mathbf{x}_i\| - a)/\epsilon\big)\Big) \tag{2.30}$$

with $\mathbf{x}_i$ the center-of-mass position of the ith particle, a the particle radius, and ϵ a small parameter, which defines the width of the smoothing region. We now interpret $\psi_{(0)}$ in (2.28) as

a concentration field. It has the value one at the maxima of the cosine profile and zero in between. The transition is very coarse, but gives an approximation of the tanh-profile of $\phi(\mathbf{x}) = \sum_i \phi_i(\mathbf{x})$, which can be refined with

$$\phi(\psi) = \frac{1}{2}\Big(1 + \tanh\big(3(\psi_{(0)} - \sigma)/\epsilon\big)\Big), \tag{2.31}$$

where $\sigma = \frac{1}{2}\big(1 + \cos(q_0 \cdot a)\big)$ is a shifting parameter, see Figure 2.5 for an example of such an implementation.

In order to define the viscosity field, we adopt the expression (2.24) and insert for $\phi(\mathbf{x})$ the field $\phi(\psi)$. Thus, we introduce a viscosity field depending directly on the PFC density field ψ, using the transformation (2.31) as

$$\tilde{\eta}(\mathbf{x}) = \tilde{\eta}(\psi(\mathbf{x})) = \Big(\frac{\bar{\eta}_p}{\bar{\eta}_f} - 1\Big)\phi(\psi). \tag{2.32}$$

Peak velocities

To approximate the particle velocities $\mathbf{v}_i$ we follow the approach of Rauscher [212] and consider a curl-free velocity field for the derivation. Let $\mathbf{u}$ be given with the property $\nabla \times \mathbf{u} = 0$ and $\nabla \cdot \mathbf{u} = 0$. Then, there exists a potential field Ψ such that

$$\mathbf{u} = -\frac{1}{\gamma m}\nabla\Psi, \quad \Delta\Psi = 0. \tag{2.33}$$

Following the argumentation of [212], the flow potential Ψ acts as an external potential that drives the particle density. In DDFT models, this external potential enters the free-energy by $F^*[\varrho] := F_{\mathrm{H}}[\varrho] + F_{\mathrm{ext}}[\varrho]$, with

$$F_{\mathrm{ext}}[\varrho] = \int \Psi(\mathbf{x})\varrho \,\mathrm{d}\mathbf{x}.$$

Inserting F^* into (2.15) instead of F_{H} leads to

$$m\varrho\left(\partial_t\mathbf{v} + (\mathbf{v}\cdot\nabla)\mathbf{v} + \gamma\mathbf{v}\right) = -\varrho\nabla\frac{\delta F^*[\varrho]}{\delta\varrho} + \eta\Delta\mathbf{v}$$

$$= -\varrho\nabla\frac{\delta F_{\mathrm{H}}[\varrho]}{\delta\varrho} - \varrho\nabla\Psi + \eta\Delta\mathbf{v}$$

$$= -\varrho\nabla\frac{\delta F_{\mathrm{H}}[\varrho]}{\delta\varrho} + \gamma m\varrho\mathbf{u} + \eta\Delta\mathbf{v}$$

and finally we arrive at

$$m\varrho\left(\partial_t\mathbf{v} + (\mathbf{v}\cdot\nabla)\mathbf{v} + \gamma(\mathbf{v} - \mathbf{u})\right) = -\varrho\nabla\frac{\delta F_{\mathrm{H}}[\varrho]}{\delta\varrho} + \eta\Delta\mathbf{v}.$$

Going to the dimensionless form, by introducing length and time scales and inserting F_{sh} for F_{H}, gives

$$\partial_t\psi + \nabla\cdot\big((1.5 + \psi)\hat{\mathbf{v}}\big) = 0, \tag{2.34}$$

$$(1.5 + \psi)\left(\partial_t\hat{\mathbf{v}} + (\hat{\mathbf{v}}\cdot\nabla)\hat{\mathbf{v}} + \Gamma(\hat{\mathbf{v}} - \hat{\mathbf{u}})\right) = \frac{1}{\mathrm{Re}}\Delta\hat{\mathbf{v}} - \frac{1}{\mathrm{Pe}}(1.5 + \psi)\nabla\frac{\delta F_{\mathrm{sh}}[\psi]}{\delta\psi}. \tag{2.35}$$

In the overdamped limit, $\Gamma \gg 1$, the velocity equation (2.35) reduces to a simple expression for the velocity $\hat{\mathbf{v}}$:

$$\Gamma(\hat{\mathbf{v}} - \hat{\mathbf{u}}) \simeq -\frac{1}{\text{Pe}} \nabla \frac{\delta F_{\text{sh}}[\psi]}{\delta \psi}. \tag{2.36}$$

Inserting this into (2.34) results in the advected PFC equation introduced in Section 2.1 and [200] and considered in the context of DDFT in [213],

$$\partial_t \psi + \hat{\mathbf{u}} \cdot \nabla \psi = \frac{1}{\Gamma \text{Pe}} \nabla \cdot \left((1.5 + \psi) \nabla \frac{\delta F_{\text{sh}}[\psi]}{\delta \psi} \right)$$

$$= \nabla \cdot \left(M(\psi) \nabla \frac{\delta F_{\text{sh}}[\psi]}{\delta \psi} \right) \tag{2.37}$$

with a mobility function $M(\psi) = \frac{1}{\Gamma \text{Pe}}(1.5 + \psi)$.

Although this equation can only be derived for potential flows, we will use it as an approximate model for non-potential flows as well. With (2.36) we have found an explicit expression for the mean velocity of the particles, that can be used to formulate the forcing term (2.25) in the continuous form

$$\mathbf{F}^{[\text{ml}]}(\mathbf{x}) = \omega \sum_i (\hat{\mathbf{v}}_i - \hat{\mathbf{u}}(\mathbf{x})) \delta(\mathbf{x} - \mathbf{x}_i)$$

$$\approx -\frac{\omega}{\Gamma \text{Pe}} \nabla \frac{\delta F_{\text{sh}}[\psi]}{\delta \psi} \sum_i \delta(\mathbf{x} - \mathbf{x}_i)$$

$$\approx -\frac{\omega}{\Gamma \text{Pe}} \nabla \frac{\delta F_{\text{sh}}[\psi]}{\delta \psi} \delta_{(k)}, \tag{2.38}$$

with $\delta_{(k)}$ the nascent delta function (2.29) approximating $\delta_\Omega = \sum_i \delta(\mathbf{x} - \mathbf{x}_i)$. The first-order approximation of this force with

$$\delta_{(0)} \approx N_0 \psi_{(0)} = \frac{q_0}{\pi} \psi_{(0)} = \frac{q_0}{2\pi} \left(1 + \frac{1}{A} (\psi - \bar{\psi}) \right),$$

thus reads

$$\mathbf{F}^{[\text{ml}]}_{(0)}(\mathbf{x}) = -(M_0 + M_1 \psi) \nabla \psi^{\natural}(\mathbf{x}). \tag{2.39}$$

The mobility factors are given by $M_0 = (1 - \bar{\psi}/A) \frac{\omega}{\Gamma \text{Pe}} \frac{q_0}{2\pi}$, $M_1 = \frac{\omega}{\Gamma \text{Pe}} \frac{q_0}{2\pi A}$ and the chemical potential reads $\psi^{\natural} := \frac{\delta F_{\text{sh}}[\psi]}{\delta \psi}$, which results in the considered fully continuous description. For $\omega \sim \Gamma$ we have $M_1 = \mathcal{O}(\frac{1}{\text{Pe}})$.

Individual particles and number of particles

In order to allow for particles to move freely, we add a modification introduced by [55]. The authors have argued that by limiting the field ψ from below, the particle interaction can be modified. Therefore, they have introduced the constraint $\psi \geq 0$, which allows to control the volume fraction of particles in the domain by changing the mean density of the system.

To implement the constraint, the free-energy is modified by including a penalty term, i.e., $F_{\text{vpfc}} := F_{\text{sh}} + F_{\text{penalty}}$, with

$$F_{\text{penalty}}[\psi] = \int \omega_2 (|\psi|^n - \psi^n) \, \mathrm{d}\hat{\mathbf{x}}$$

with $\omega_2 \gg 1$ and n an odd integer exponent.

The variational derivative of F_{penalty} can be found to be

$$b(\psi) := \frac{\delta F_{\text{penalty}}[\psi]}{\delta \psi} = n\omega_2 \psi^{n-1}(\text{sign}(\psi) - 1) \tag{2.40}$$

with $\text{sign}(\psi) = \begin{cases} 1 & \text{for } \psi > 0 \\ 0 & \text{for } \psi = 0 \\ -1 & \text{for } \psi < 0. \end{cases}$

While localized states are also observed in the original PFC model for a small range of parameters in the coexistence regime [254], we consider the approach in [55, 40, 218] using the penalty term (2.40). Here, the number of particles can be controlled by choosing the mean density and the area the particles occupy. The initial density field for a collection of N particles located at the positions $\mathbf{x}_i$, $i = 1, \ldots, N$, is a composition of local density peaks

$$\psi_0^{(i)}(\mathbf{x}) = \begin{cases} A \cdot \left(\cos(\frac{\sqrt{3}q_0}{2} \|\mathbf{x} - \mathbf{x}_i\|) + 1 \right) & \text{for } \|\mathbf{x} - \mathbf{x}_i\| < \frac{d}{2} \\ 0 & \text{otherwise}, \end{cases} \tag{2.41}$$

summed up to $\psi(\mathbf{x}, t = 0) = \sum_{i=1}^{N} \psi_0^{(i)}(\mathbf{x})$.

Thus, each particle occupies an area of approximately $B_p := \pi(d/2)^2$ in 2D. Based on the ideas in [55] we set the mean density in the particle domain to $\psi_1 = \sqrt{(-48 - 56r)/133}$, as well as $r = -0.9$ and $q_0 = 1$. The last two parameters define the mean density of the system as

$$\bar{\psi} = \frac{N \cdot B_p}{B_0} \psi_1$$

with $B_0 = |\Omega|$ the area of the computational domain Ω, and with $A = \psi_1$ the parameter for the density scaling.

Navier-Stokes PFC model

Combining all the components, i.e., the Navier-Stokes equation for the solvent (2.21) with viscosity η given by $\eta(\psi)$ in (2.32), and volume force $\mathbf{F}$ by expression (2.39), combined with the density evolution (2.37) with F_{sh} or F_{vpfc}, results in the fully continuous Navier-Stokes PFC (NS-PFC) model

$$\partial_t \hat{\mathbf{u}} + (\hat{\mathbf{u}} \cdot \nabla)\hat{\mathbf{u}} = \nabla \cdot \tilde{\boldsymbol{\sigma}} - M_1 \psi \nabla \psi^{\natural},$$
$$\nabla \cdot \hat{\mathbf{u}} = 0,$$
$$\partial_t \psi + \hat{\mathbf{u}} \cdot \nabla \psi = \nabla \cdot \left(M(\psi) \nabla \psi^{\natural} \right), \tag{2.42}$$
$$\psi^{\natural} = \frac{\delta F_{\text{sh/vpfc}}[\psi]}{\delta \psi}$$

with

$$\tilde{\boldsymbol{\sigma}} = -\tilde{p}\boldsymbol{I} + \frac{1}{\mathrm{Re}_f}\big(1 + \tilde{\eta}(\psi)\big)\big(\nabla\hat{\mathbf{u}} + \nabla\hat{\mathbf{u}}^{\top}\big)\,,$$

$$\frac{\delta F_{\mathrm{sh}}[\psi]}{\delta\psi} = \psi^3 + (r + (1+\Delta)^2)\psi\,,$$

$$\frac{\delta F_{\mathrm{vpfc}}[\psi]}{\delta\psi} = \psi^3 + (r + (1+\Delta)^2)\psi + b(\psi)\,,$$

and $\tilde{p} = \hat{p} + M_0\psi^{\natural}$ a rescaled pressure. Besides the definition of $\psi^{\natural}$, these equations have exactly the form of "Model H" as considered in [125]. In Section 2.2.6, we demonstrate thermodynamic consistency of the derived model.

2.2.3   Numerical studies

We now turn to quantitative properties of the model and compare it with the original PFC model and the FPD approach of [248] for various situations. We rewrite the NS-PFC system as a system of second order equations. Therefore, the variational derivatives are implemented as

$$\frac{\delta F_{\mathrm{sh}}[\psi]}{\delta\psi} = \psi^3 + (r+1)\psi + 2\Delta\psi + \Delta\psi^{\flat},$$

$$\frac{\delta F_{\mathrm{vpfc}}[\psi]}{\delta\psi} = \psi^3 + (r+1)\psi + 2\Delta\psi + \Delta\psi^{\flat} + b(\psi),$$

$$\psi^{\flat} = \Delta\psi.$$

The system (2.42) has to be solved for $\mathbf{u}$, $\tilde{p}$, ψ, $\psi^{\natural}$, and $\psi^{\flat}$ in a domain Ω with boundary conditions depending on the specific example. To numerically solve this system of partial differential equations, we apply here an operator splitting approach [25] with a sequential splitting, where we solve the PFC equations first, using the scheme developed in Section 2.1.2, followed by the Navier-Stokes equations. In time, we use a semi-implicit backward Euler discretization with a linearization of all nonlinear terms, i.e., a one-step Newton iteration. In space, we discretize using a finite-element method, with Lagrange elements, e.g., a P^2/P^1 Taylor-Hood element for the Navier-Stokes equation and a P^2 element for ψ, $\psi^{\natural}$, and $\psi^{\flat}$ in the PFC equation. We further use adaptive mesh refinement, leading to an enhanced resolution along the particles. The system is solved using the parallel adaptive finite-element framework AMDiS [273, 216, 280].

The discretization of the Navier-Stokes equations follows standard approaches (see, e. g., [128, 295, 208]). Let $\mathbf{u}_0 \in \big[L_2(\Omega)\big]^m$ be given and the time-interval $[0,T]$ be discretized using N timesteps t_k with timestep width τ_k as before. The timestep solutions are named $\mathbf{u}_k \equiv \mathbf{u}(\mathbf{x},t_k)$. Let the finite-element space $\mathbf{V}$ be given as a tensor product of P^2 spaces and the space Q as the space P^1 equipped with boundary conditions, i.e.,

$$\mathbf{V_g} := \big\{\mathbf{v} \in \big[P^2\big]^m \,:\, \mathbf{v}\big|_{\partial\Omega} = \mathbf{g}\big\}\,,$$

$$Q := \big\{q \in P^1 \,:\, q(\mathbf{x}_0) = 0\big\}\,, \text{ for } \mathbf{x}_0 \in \Omega.$$

For $k = 0, 1, \ldots, N - 1$, find $\mathbf{u}_{k+1} \in \mathbf{V_g}$ and $p_h \in Q$, s.t.

$$\left(\frac{1}{\tau_k}\mathbf{u}_{k+1} + (\mathbf{u}_k \cdot \nabla)\mathbf{u}_{k+1}, \boldsymbol{v}\right) + \left(\widehat{\mathrm{Re}}_f^{-1}(\psi_h)(\nabla\mathbf{u}_{k+1} + \nabla\mathbf{u}_{k+1}^\top), \nabla\boldsymbol{v}\right) - \left(p_h, \nabla \cdot \boldsymbol{v}\right)$$

$$= \left(\frac{1}{\tau_k}\mathbf{u}_k, \boldsymbol{v}\right) - \left(M_1\psi_h\nabla\psi_h^\natural, \boldsymbol{v}\right), \qquad \forall \boldsymbol{v} \in \mathbf{V}_0, q \in Q$$

$$(\nabla \cdot \mathbf{u}_{k+1}, q) = 0 \qquad\qquad (2.43)$$

with $\widehat{\mathrm{Re}}_f^{-1}(\psi_h) := \mathrm{Re}_f^{-1}\big(1 + \tilde{\eta}(\psi_h)\big)$.

The linear systems in the following small examples are solved using a direct solver UMFPACK [65]. For more complex and involved simulations a more efficient solver, that also scales in parallel calculations, must be applied. In Section 2.2.4 we analyze the preconditioner developed in the previous chapter to solve the advected PFC equation in the crystalline phase and the vacancy PFC equation. Therefore, numerical studies are shown, regarding the influence of the velocity $\hat{\mathbf{u}}$ and the mobility M_0.

Crystallization

The first numerical examples use F_{sh} and consider crystallization processes in flowing environments. Crystallization kinetics during nucleation and growth and crystal orientation during external flow is a problem of wide interest, cf. [241, 240, 115, 271, 192]. Here we study the case of an influence of flow to the crystallization process in an undercooled environment. The fluid is thereby driven by boundary conditions away from the crystal grain. In the first case, we consider a rotating fluid, i.e., a gyre flow, and in the second case, a Poiseuille flow with a parabolic inflow velocity profile.

Rotating crystals A crystal grain is placed in a rotating fluid initially given by

$$\partial_t\mathbf{x} = \mathbf{u}_0(x, y) = \begin{pmatrix} c^\infty \sin(\pi\frac{x}{\dim_x})\cos(\pi\frac{y}{\dim_y}) \\ -c^\infty \cos(\pi\frac{x}{\dim_x})\sin(\pi\frac{y}{\dim_y}) \end{pmatrix} \qquad (2.44)$$

in a domain $(x, y) \in \Omega = [0, \dim_x] \times [0, \dim_y]$. For the numerical experiment we have chosen $\dim_x = \dim_y = 42d$. The boundary conditions for the Navier-Stokes equations are set by $\mathbf{u}_0$.

We start the growth process with an initial grain of radius $2d$ in an undercooled environment with parameters $r = -0.3$ and mean density $\bar{\psi} = -0.35$. The mobility function is set to $M(\psi) = \psi + 1.5$ and the force scaling to $M_1 = 1$. The fluid Reynolds number is set to $\mathrm{Re}_f = 1$ and the viscosity ratio to $\bar{\eta}_p/\bar{\eta}_f = 100$. For the concentration field that defines the profile of the viscosity, we have used an approximation of $\psi_{(0)}$,

$$\phi := \psi_{(0)} \approx \frac{\psi - \min_\Omega(\psi)}{\max_\Omega(\psi) - \min_\Omega(\psi)}.$$

Thus, the fluid viscosity is high in particles, low in between particles and takes an intermediate value in the isotropic phase away from the crystal. However, other definitions of the viscosity parameter are possible as well.

(a)   (b)   (c)
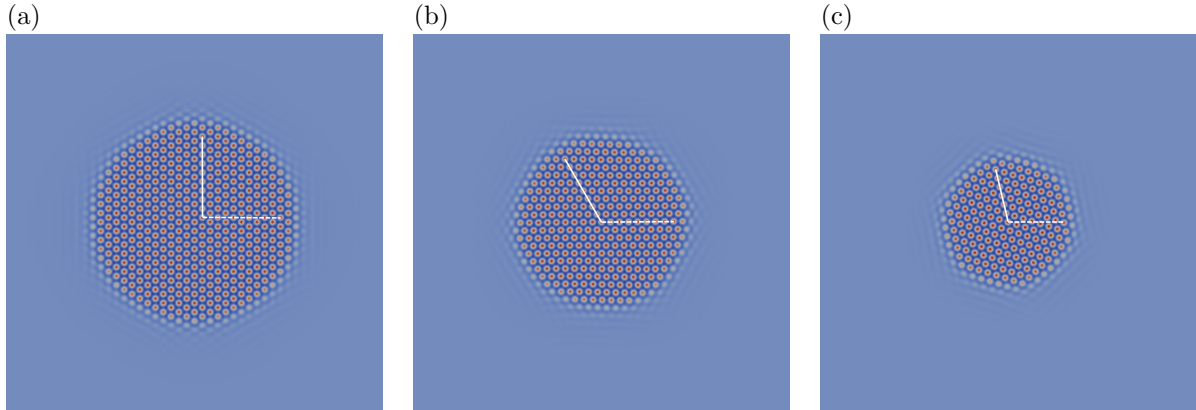
Figure 2.6 – *Final growth-shapes of the crystal in a flowing environment at time $t = 3000$. Shown is the particle density ψ with color red corresponds to high density and blue to low density. The fluid velocity denoted by c^∞: (a) $c^\infty = 0$, (b) $c^\infty = 0.5$, (c) $c^\infty = 1$. The white angles show the crystal orientation and thus, give an indication for crystal rotation.*

In Figure 2.6 the growth shapes for different velocities c^∞ are shown at the same simulation time. For a still fluid ($c^\infty = 0$), i.e., no advection, the final shape is the largest and the size of the crystal decreases for increasing velocity. For the largest considered velocity, $c^\infty = 1$, the faceting of the crystal is also more pronounced than for the case of no induced fluid flow. The stationary images also show that the crystal rotates during the growth process. This can be seen at the varying crystal orientations in (a), (b) and (c) indicated by the white angle.

The growth process is analyzed in Figure 2.7 (left), showing the radius of the growing crystal over simulation time. The growth velocity strongly depends on the induced fluid velocity, as shown in the right plot of Figure 2.7. The crystal grows slower for a larger induced fluid velocity. This clearly shows one direction of the coupling, i.e., the fluid influences the crystallization.

The opposite can be found as well. The crystal also changes the velocity profile of the fluid. At the right side of Figure 2.8, the velocity profiles of two fluids are compared. The left image shows the profile of a fluid with no back-coupling of the density field to the Navier-Stokes equations. This essentially shows the initial profile $\mathbf{u}_0$. The right image shows the velocity profile for the full NS-PFC model with $c^\infty = 1$. We observe different magnitudes of the velocity, whereas the streamlines do not change qualitatively. A more detailed analysis of the velocity profile along the x-axis from the center to the boundary of the domain can be found in Figure 2.8. With fluid coupling, a linear increase of the magnitude in the domain of the crystal is observed, indicated by the black dashed line, which is lower than the prescribed initial profile. The crystal acts as a rotating solid in the fluid, with normalized angular velocity $u_\omega = \|\mathbf{u}\|/(\|\mathbf{x}\|/d) = 0.04$. Away from the crystal, the velocity increases up to the prescribed boundary velocity c^∞.

Translating crystals   In the second case, the crystal grows in a Poiseuille flow. In a narrow channel, we enforce a parabolic velocity at the inflow boundary, i.e.,

$$\mathbf{u}_0(x, y) = (4c^\infty \bar{y}(1 - \bar{y}), 0)^\top , \ \bar{y} := \frac{y}{\dim_y}$$
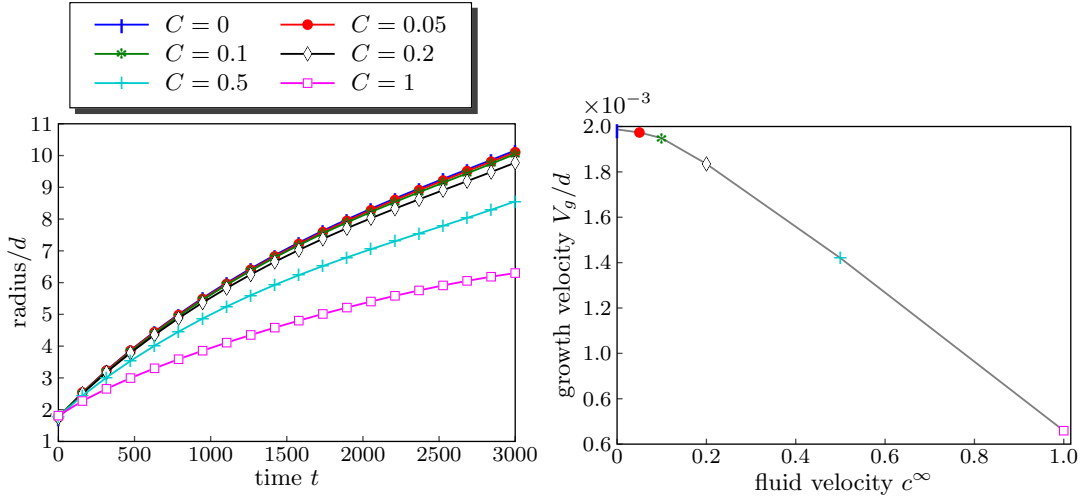
Figure 2.7 – *Left: Radius of the crystal divided by lattice constant over dimensionless time, for various fluid velocities c^∞. Right: The growth velocity of the crystal V_g normalized by the lattice constant is shown for the final time $t = 3000$.*

with a maximal inflow velocity c^∞ and a top/bottom boundary velocity set to zero [1]. Again, we start with an initial grain of radius $2d$ in the center of a box Ω with dimensions $\dim_x = 168d$ and $\dim_y = 42d$. The simulation parameters are the same as above in the case of a rotating fluid.

The shape of the growing crystal is influenced by the fluid, which induces an anisotropy. This can be seen in Figure 2.9, where the shape corresponding to a fluid velocity $c^\infty = 0.15$ is shown in a clipping of the whole domain Ω. The flow direction is from left to right. The particle density ψ is shown in the left image together with the velocity relative to the velocity of the translating crystal, i.e., $\mathbf{v}_{\mathrm{crystal}} = (v_{\mathrm{crystal}}, 0)^\top$ with $v_{\mathrm{crystal}} \approx 0.124$. The right image shows in the upper half the absolute value of the velocity, with a constant value within the crystal, and in the lower half, the flow velocity relative to the initial velocity $\mathbf{u}_0$. This shows an elongated vortex. In the case of no fluid coupling, the crystal grows isotropically to a circular shape, as in the example above.

Thus, also for Poiseuille flow we see a coupling in both directions: the shape of the crystal is influenced by the flowing environment and the fluid velocity is influenced by the crystal.

Sedimentation

In the following, we apply the NS-PFC model to a collection of individual particles to show the applicability as a model for particle dynamics. We therefore consider F_{vpfc}. For the penalty term (2.40) we use the parameters $(n, \omega_2) = (3, 2000)$ in all of the following simulations. The Reynolds number and viscosity ratio are chosen as before, but the viscosity profile is now given

---

[1]Compared to the rotating crystal example, not on all boundaries a velocity profile is prescribed. Thus, the discretization (2.43) must be modified slightly to incorporate the outflow boundary condition. We set $\tilde{\boldsymbol{\sigma}} \cdot \boldsymbol{\nu}\big|_{\partial\Omega_{\mathrm{out}}} = 0$ at the outflow boundary with $\boldsymbol{\nu}$ the outer normal.
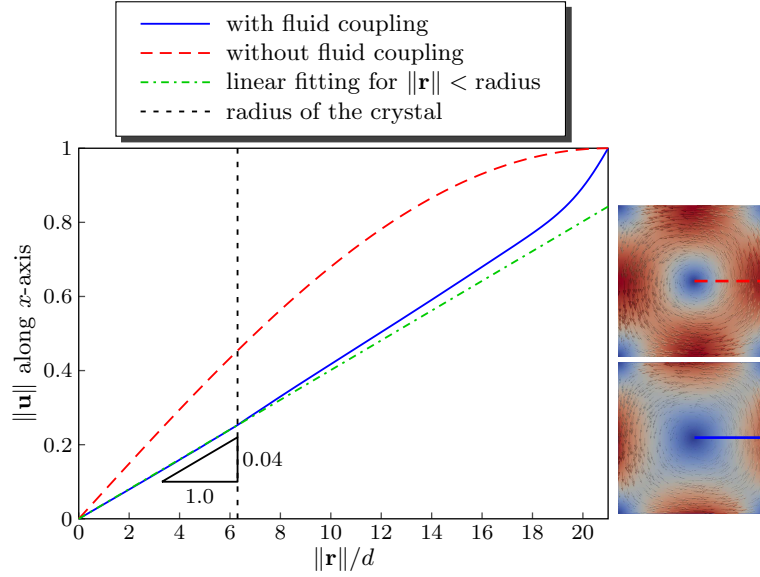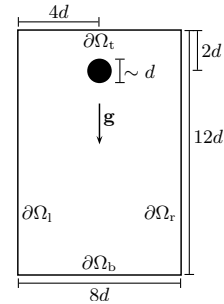
Figure 2.8 – *Fluid velocity at time $t = 3000$ extracted from positive x-axis, as indicated by the lines in the side pictures. The slope 0.04 corresponds to the angular velocity of the fluid in the region with a radius less than the crystal radius. Beside the plot, the magnitude of fluid velocity in the domain Ω for $c^\infty = 1$ is shown. Bottom: Fluid flow not influenced by the crystal. Top: Crystal slows down the fluid due to higher viscosity in the region of particles.*

by $\phi := \psi_{(0)} \approx \psi/\max_\Omega(\psi)$. Thus, we have the lower fluid viscosity away from the particles and a high viscosity on the particles. In order to stabilize the shape of the particles, we increase the diffusional part, i.e. the mobility function $M(\psi)$. We have chosen $M(\psi) \equiv 16$ in the following examples.

One spherical particle in a confinement The objective of this study is to calculate the position and velocity of one spherical particle (circular disk) settling down in an enclosure due to a gravitational force $\mathbf{g}$. In order to include this force, we use a Boussinesq approximation and add the forcing term $\mathbf{F_g} := \phi(\psi)\mathbf{g}$ to the Navier-Stokes equations in (2.42).

The box dimensions are chosen to be multiples of the particle size. All lengths are again normalized by the particle interaction distance $d = 4\pi/\sqrt{3}$, i.e., the lattice constant. We consider the following boundary conditions:

$$\psi = 0 \qquad \text{at } \partial\Omega_\mathrm{l} \cup \partial\Omega_\mathrm{r} \cup \partial\Omega_\mathrm{b},$$
$$\partial_\mathbf{n}\psi = 0 \qquad \text{at } \partial\Omega_\mathrm{t},$$
$$\mathbf{u} = 0 \qquad \text{at } \partial\Omega_\mathrm{l} \cup \partial\Omega_\mathrm{r} \cup \partial\Omega_\mathrm{b},$$
$$\tilde{\boldsymbol{\sigma}} \cdot \mathbf{n}_\Sigma = 0 \qquad \text{at } \partial\Omega_\mathrm{t}$$

with $\mathbf{n}_\Sigma$ the outer normal to $\Sigma := \partial\Omega$.
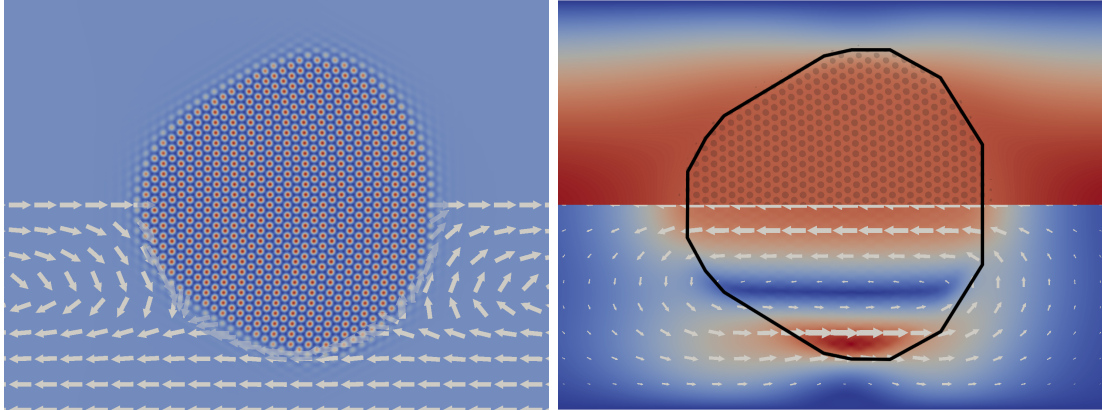
Figure 2.9 – *Crystal shape and corresponding velocity profile at time t=3800 in a narrow channel. Left: Density field ψ, with arrows in the lower half corresponding to $\mathbf{u} - \mathbf{v}_{crystal}$, i.e., fluid velocity relative to the translation velocity of the crystal. Right: Fluid velocity $\mathbf{u}$ with contour line that indicates the shape of the crystal. In the lower half, the velocity relative to the channel flow velocity, i.e., $\mathbf{u} - \mathbf{u}_0$, is shown. Color red corresponds to high values and blue to low values.*

Due to the symmetry of the system, we expect a symmetric trajectory, a straight line in the center of the box with the particle slowing down at the bottom. Figure 2.10 shows the $y(t)$ component of the evolution curve $\big(x(t), y(t)\big)$ compared with FPD simulations. We further show the comparison of the velocity profiles. For both criteria we obtain an excellent agreement.

In the FPD setup, we have used the normalized density field $\psi_{(0)}(\mathbf{x})$ as a concentration field instead of a tanh-profile (2.30) and for treatment of the wall-boundary we have introduced a repulsive potential

$$V_B(k, p)(\mathbf{x}) := k\big(d^{-1} \operatorname{dist}_\Sigma(\mathbf{x})\big)^p$$

with $k = 1, p = 20$ and $\operatorname{dist}_\Sigma(\mathbf{x})$ the distance of $\mathbf{x}$ to the boundary Σ of the domain Ω.

Further care is needed in order to guarantee a symmetric solution. Within both approaches we use a symmetric triangulation of the domain and symmetric quadrature rules. Otherwise we get symmetry breaking in the trajectories, since the motion on a straight line is unstable with respect to small perturbations, as it is also pointed out in the work of [100].

Two interacting particles For two particles sedimenting in a box, additional hydrodynamic interactions are expected to influence the motion of the particles. We expect to see the phenomena of trailing, drafting, kissing and tumbling of the particles, as found in experimental studies [92] and as also observed in several numerical studies with various methods, cf. [118, 217, 100]. Again, we compare it with FPD simulations, where we have to apply direct particle-particle interaction potentials, defined as $V_2(x) := k\big(\big(\frac{x}{d}\big)^{p_1} - 2\big(\frac{x}{d}\big)^{p_2}\big)$ with $(k, p_1, p_2) = (1, 12, 6)$ and a boundary interaction potential V_B as above. Since we do not have a one-to-one mapping between these potentials and their representation in F_{vpfc}, and since the PFC-model introduces additional diffusion due to a non-vanishing mobility function $M(\psi)$, equality of particle trajectories and particle velocities cannot be expected. However, the results qualitatively agree for different fluid viscosities, as can be seen in Figure 2.11. To analyze the dependency of the trajectories on the
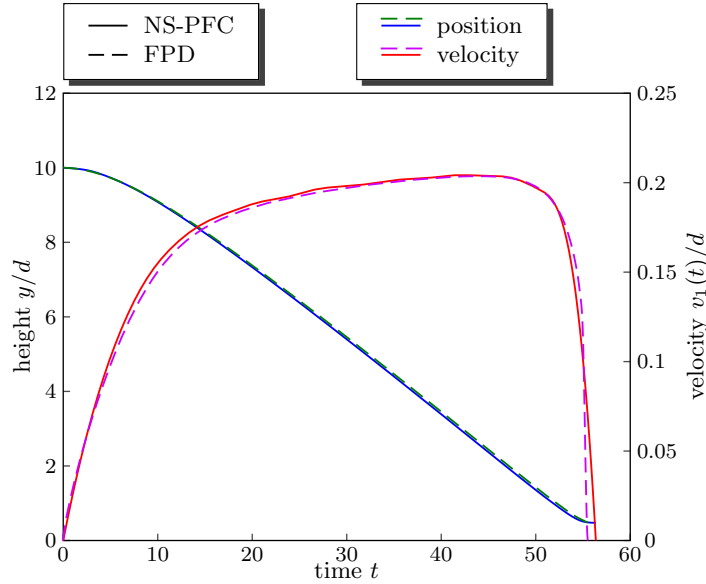
Figure 2.10 – *Trajectory and velocity of one particle settling down in a box filled with a liquid with fluid viscosity $\bar{\eta}_f = 0.1$, particle viscosity $\bar{\eta}_p = 10$ and gravitational force $\mathbf{g} = (0, -1)$. (green and blue) vertical position of the particle, starting from an initial height of $10d$. (red and magenta) effective velocity of the particle, i.e., $v_1(t)^2 = (\dot{x}(t)^2 + \dot{y}(t)^2)/d^2$.*

considered interaction potential V_2, FPD simulations with different potentials, i.e., different parameters in the Lennard-Jones type interaction, and purely repulsive interactions are performed and compared with each other. The obtained differences in the trajectories and the particle velocities are of the same order as the differences if compared with the NS-PFC simulations (results not shown).

The system considered here consists of two particles placed below each other with a small (symmetric) displacement relative to the middle vertical axis. The initial configuration is chosen as $\mathbf{x}_1 = (-0.1d, 9d)$ and $\mathbf{x}_2 = (0.1d, 10d)$ with boundary conditions as for the case of one particle. Compared to the one-particle case, the box size is chosen wider, i.e., a width of $18d$ instead of $8d$, to further reduce boundary effects.

The solution can also be compared qualitatively to the results in [100, 150], where the authors have studied the sedimentation of two hard sphere particles in a narrow enclosure in a similar setup and they have found similar trailing and drafting phenomena. However, they are not as strong as in the FPD or in our simulations. The particles start in close contact and accelerate up to a critical time, when they start moving apart from each other. In the visualized scenarios in Figure 2.11, the particle behind overtakes the other one and reaches the bottom first. Compared with FPD in our simulations, the particles move further away from each other and the velocity decreases in a similar way up to the contact with the lower boundary.

Many particles in an enclosure With three particles already, the interaction and motion of the particles becomes chaotic, as pointed out in [126] and discussed in detail in the review [205].
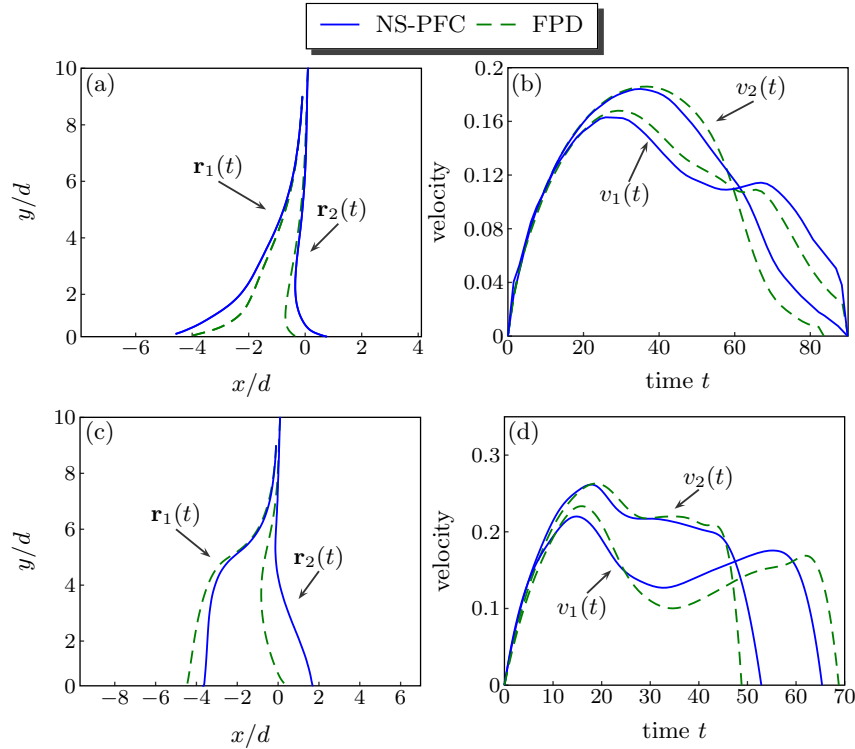
Figure 2.11 – *Two particles settling down in an enclosure. Fluid viscosity is set to $\bar{\eta}_f = 1$ (a,b) and $\bar{\eta}_f = 0.1$ (c,d), particle viscosity to $\bar{\eta}_p = 100$ (a,b) and $\bar{\eta}_p = 10$ (c,d) and mobility of the NS-PFC-model to $M(\psi) \equiv 2$. Left: Trajectories of the particles with coordinates $\mathbf{x}_i(t) = \big(x_i(t), y_i(t)\big)$, $i = 1, 2$. Right: Absolute velocities: $v_i(t)^2 = \big(\dot{x}_i(t)^2 + \dot{y}_i(t)^2\big)/d^2$, $i = 1, 2$.*

Therefore, a direct comparison of trajectories is no longer meaningful. However, considering not only a few, but a larger number of particles in a bounded box under gravity, cause new effects. Particles do not settle down homogeneously, their dynamics strongly depend on the distance to the walls. During the sedimentation process, Rayleigh-Taylor-like instabilities and fingering occur and a compression of the particle lattice at the bottom of the box is seen. To demonstrate the possibility of our approach, to deal with moderate numbers of particles, we aim to observe these phenomena. We have studied a situation of 120 particles arranged in a square lattice in the upper part of a square domain. The initial distance of neighboring particles is set to the lattice constant d. The width of the box is chosen so that 20 particles fit perfectly in one horizontal line, i.e., we have $\dim_x = \dim_y = 20d$. Boundary conditions are similar to the case of one and two particles. For a gravitational force $\mathbf{g} = (0, -2)^\top$ we have simulated the sedimentation process in a fluid with a viscosity ratio $\bar{\eta}_p/\bar{\eta}_f = 100$, as above. The particles close to the side walls start settling down first and due to their motion, an upwards fluid flow in the center of the domain is induced. A visualization of the sedimentation process is shown in Figure 2.12. We have drawn black circular disks to indicate the particle positions. Four snapshots are shown, the initial and final configuration and two intermediate states, i.e., the beginning of the development of the instability and a snapshot with partially sedimented particles.

In Figure 2.13 the mean particle concentration $\langle\psi\rangle(y)$ is shown, which is obtained by averaging over stripes of width d along the particle layers,

$$\langle\psi\rangle(y) := \frac{1}{(x_{\max} - x_{\min}) \cdot d} \int_{x=x_{\min}}^{x_{\max}} \int_{y'=y-0.5d}^{y+0.5d} \psi(x, y') \, \mathrm{d}y' \, \mathrm{d}x.$$

The high-concentration region moves from top to bottom over time and the mean particle density is higher at the bottom of the box than for the initial configuration.
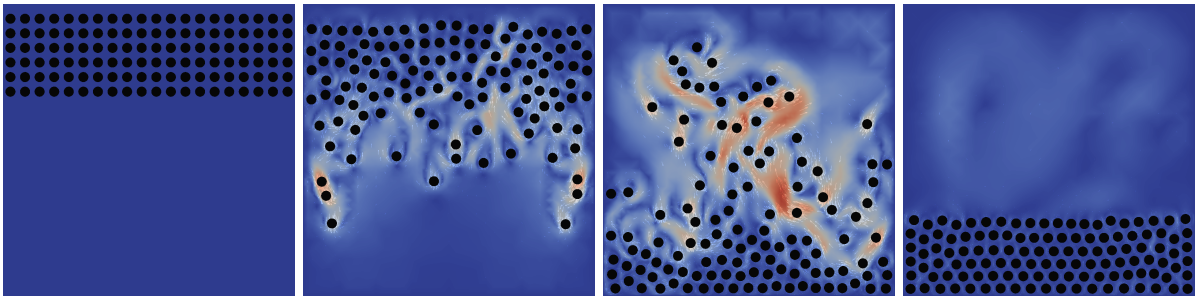

Figure 2.12 – *Four snapshots of the sedimentation simulation for 120 particles in a square box. Color red corresponds to high absolute velocity and blue to low velocity. Left: Initial configuration of particles. Second image: An instability of the particle front, starting from the boundaries. Third image: Particles start to sediment at the bottom. Right: Final compressed sediment of particles.*

2.2.4   Preconditioner for the NS-PFC model

The sedimentation of 120 particles in Section 2.2.3 requires the mesh to be resolved fine near the particles and moderately in the fluid region. This leads to large linear systems with about 60,000 DOFs per component. For a direct solver this system size exceed the size to be efficient in terms of memory requirements and solution time, as it is shown in Section 1.6 and Table 1.3. A setup with about 3,000 particles sedimenting in an enclosure requires approximately 500,000 DOFs per component and is thus out of computational range. More advanced solvers are necessary to handle more particles and finer flow resolution. The developed preconditioner may be a resource to increase the system size of the PFC part. Various preconditioners for the Navier-Stokes equations are developed in literature, based on Schur complement approaches, block factorization, SIMPLE projection schemes and others, cf. [231, 266, 166].

A preconditioner for the advected PFC equation based on the functional $F_{\mathrm{sh}}[\psi]$ is similar to the approach in Section 2.1.2, i.e., the preconditioner matrix $\mathbf{P}$ is the same as in Section 1.3. When including a non-vanishing mobility parameter $M(\psi)$ into the PFC equation a modification of the introduced approach must be formulated. Neglecting the nonlinearity matrix $\mathbf{N}$ and
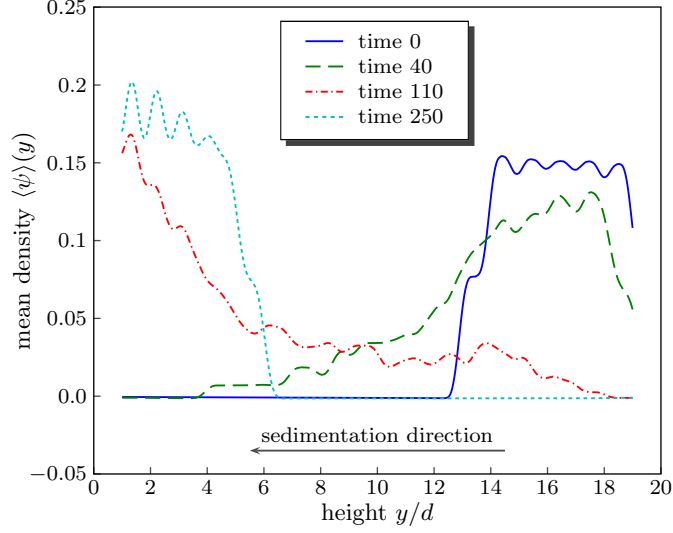
Figure 2.13 – *Evolution of the mean density of particles for four different time steps corresponding to the snapshots in Figure 2.12. The final configuration of particles in a hexagonal lattice has a higher density than the initial configuration in a square lattice.*

perturbing the diagonal entry of $\mathbf{A}_{\mathrm{pfc}}$ in equation (2.12) leads to

$$
\mathbf{P} := \begin{bmatrix} \mathbf{M} & 2\mathbf{K} - \mathbf{K}\mathbf{M}^{-1}\mathbf{K} & 0 \\ \tau_k \mathbf{K}_M(\psi_k) & \mathbf{M} + \sqrt{\tau_k}\big(\mathbf{K}_M(\psi_k) - 2\mathbf{K} + \mathbf{K}\mathbf{M}^{-1}\mathbf{K}\big) & 0 \\ 0 & \mathbf{K} & \mathbf{M} \end{bmatrix} \tag{2.45}
$$

$$
= \begin{bmatrix} \mathbf{M} & 0 & 0 \\ \tau_k \mathbf{K}_M(\psi_k) & \mathbf{M} + \sqrt{\tau_k}\mathbf{K}_M(\psi_k) & 0 \\ 0 & 0 & \mathbf{I} \end{bmatrix} \begin{bmatrix} \mathbf{I} & \mathbf{M}^{-1}\big(2\mathbf{K} - \mathbf{K}\mathbf{M}^{-1}\mathbf{K}\big) & 0 \\ 0 & \mathbf{M}^{-1}\big(\mathbf{M} - 2\sqrt{\tau_k}\mathbf{K} + \sqrt{\tau_k}\mathbf{K}\mathbf{M}^{-1}\mathbf{K}\big) & 0 \\ 0 & \mathbf{K} & \mathbf{M} \end{bmatrix}.
$$

Rewriting the Schur complement form $\mathbf{P(S)}$ of the preconditioner (1.20) in terms of the mobility matrix $\mathbf{K}_M(\psi_k)$, we can construct the expression

$$
\mathbf{P(S)} = \begin{bmatrix} \mathbf{M} & \delta^{-1}(\mathbf{M} - \mathbf{S}) & 0 \\ \tau_k \mathbf{K}_M(\psi_k) & \delta \mathbf{K}_M(\psi_k) + \mathbf{S} & 0 \\ 0 & \mathbf{K} & \mathbf{M} \end{bmatrix}
$$

with $\delta = \sqrt{\tau_k}$. Inserting $\mathbf{S} = \mathbf{M} - 2\delta\mathbf{K} + \delta\mathbf{K}\mathbf{M}^{-1}\mathbf{K}$ from (1.16) into $\mathbf{P(S)}$ leads to (2.45). When using a Cahn-Hilliard inner-preconditioner $\mathbf{S}_{\mathrm{CH}} = \mathbf{M} + 2\sqrt{\delta}\mathbf{K} + \delta\mathbf{K}\mathbf{M}^{-1}\mathbf{K}$ from (1.19) instead, the preconditioner matrix is given by

$$
\mathbf{P}_{\mathrm{CH}} := \begin{bmatrix} \mathbf{M} & -2\delta^{-1/2}\mathbf{K} - \mathbf{K}\mathbf{M}^{-1}\mathbf{K} & 0 \\ \tau_k \mathbf{K}_M(\psi_k) & \mathbf{M} + \delta\big(\mathbf{K}_M(\psi_k) + 2\delta^{-1/2}\mathbf{K} + \mathbf{K}\mathbf{M}^{-1}\mathbf{K}\big) & 0 \\ 0 & \mathbf{K} & \mathbf{M} \end{bmatrix}. \tag{2.46}
$$

In the left plot of Figure 2.14 the setup of the growing rotating crystal (see Section 2.2.3) is analyzed with respect to the influence of the reference velocity c^∞ to the number of FGMRES
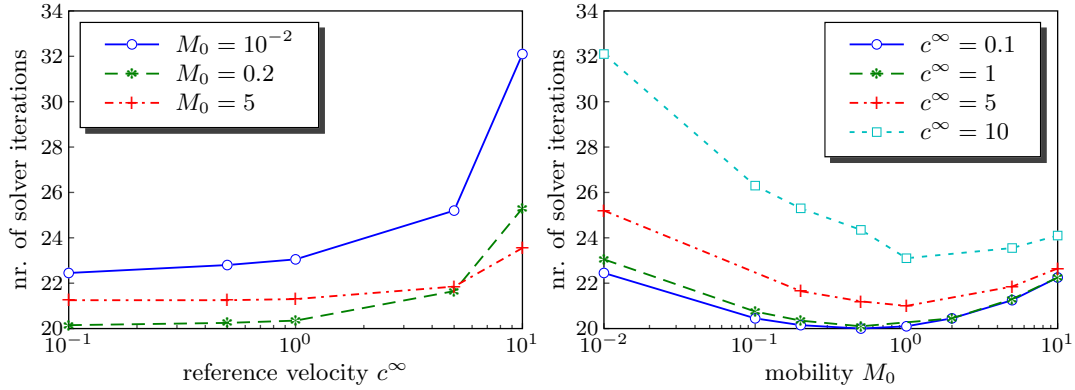
Figure 2.14 – *Number of solver iterations averaged over 20 timesteps, depending on the flow velocity (left) and on the mobility M_0 of the PFC equation (right).*

solver iterations, when the preconditioner (2.46) is applied. Increasing the velocity also increases the number of solver iterations for all mobility parameters M_0. In the right plot of Figure 2.14 the dependence on the mobility is shown. We have set $M(\psi) \equiv M_0$, i.e., a constant mobility for this test. Very small and very large mobility factors lead to an increase in the solver iterations.

A setup that involves the vacancy term, i.e., the PFC equations is based on $F_{\mathrm{vpfc}}[\psi]$, is analyzed in Section 4.2.4 in the context of a diffuse-domain modeling. The boundary of the domain Ω is thereby described implicitly by a phase-field variable, similar to a wall potential as in Section 2.1.2.

2.2.5 Dimensionless form

To get an insight into the derivation of the dimensionless parameters of the model and how they emerge from physical quantities, a dimensionless form of the model is constructed. Therefore, we start with a short sketch of the derivation of the PFC model and finally introduce a scaling of space and time scales.

The one-particle number density ϱ is driven by the variational derivative of the Helmholtz free energy F_{H}. This functional can be decomposed into two contributions $F_{\mathrm{H}} = F_{\mathrm{id}} + F_{\mathrm{exc}}$[2], where the ideal gas part F_{id} is known and the excess free part is unknown for general systems,

$$F_{\mathrm{H}}[\varrho] = k_{\mathrm{B}}T \int \varrho[\ln(\Lambda^m \varrho) - 1]\,\mathrm{d}\mathbf{x} + F_{\mathrm{exc}}[\varrho]$$

with k_{B} Bolzmann's constant, T the temperature, Λ the thermal de-Broglie wave-length and m the space dimension.

Inserting a parametrization $\varrho = \varrho(\varphi) = \bar{\varrho}(1 + \varphi)$ with the density deviation φ and reference density $\bar{\varrho}$, into the energy and expanding the ideal gas part of the energy around $\bar{\varrho}$ leads to a polynomial form of F_{id}. Using a Ramakrishnan-Yussouff approximation [204] of the excess free

---

[2]The external part of the energy F_{ext} is neglected in this derivation of a dimensionless form, but it can easily be included in a similar fashion as the other terms.

part results in an expression of the two-point correlation function $c^{(2)}(\mathbf{x}, \mathbf{x}', \varrho)$,

$$F_{\mathrm{exc}} = C + \iint (\varrho(\mathbf{x}) - \varrho_L) c^{(2)}(\mathbf{x}, \mathbf{x}', \varrho_L)(\varrho(\mathbf{x}') - \varrho_L) \, \mathrm{d}\mathbf{x} \, \mathrm{d}\mathbf{x}'$$

with ϱ_L a reference liquid density. This corresponds to a convolution of $(\varrho - \varrho_L)$ with $c^{(2)}$ and can thus be transformed into a product in Fourier space. Expanding $c^{(2)}$ around the wave-number zero and transforming back leads to a gradient expansion of F_{exc}, that can be written in the variable φ (see Section 2.1.1):

$$\frac{1}{k_{\mathrm{B}} T \bar{\varrho}} (F_{\mathrm{H}}[\varrho(\varphi)] - \bar{F}_{\mathrm{H}}) \approx \int \frac{1}{2} \varphi^2 - \frac{1}{6} \varphi^3 + \frac{1}{12} \varphi^4 \, \mathrm{d}\mathbf{x}$$
$$- \int \frac{1}{2} \varphi (C_0 - C_2 \Delta + C_4 \Delta^2) \varphi \, \mathrm{d}\mathbf{x}$$
$$+ \int D_0 + D_1 \varphi \, \mathrm{d}\mathbf{x},$$

with C_0, C_2, C_4, D_0, D_1 expansion coefficients. For a detailed derivation, see e.g. [268, 124, 200]. Since we take the gradient of the variational derivative in the dynamical equations, all constant and linear terms can be neglected in the energy without changing the dynamics.

Fixing the lattice spacing L, the dimensionless bulk modulus of the crystal B, and introducing parameters r and ψ_0, with

$$\mathrm{sign}(C_4) = -1, \quad L^2 := \frac{2|C_4|}{C_2}, \quad B := \frac{C_2^2}{4|C_4|} = \frac{\psi_0^2}{3}, \quad r := \psi_0^{-2} \left(\frac{9}{4} - 3C_0 \right) - 1,$$

scaling the length by L, i.e., $\hat{\mathbf{x}} = \hat{\mathbf{x}}(\mathbf{x}) := \frac{\mathbf{x}}{L}$, introducing the derivatives $\hat{\nabla} := \partial_{\hat{\mathbf{x}}}$, $\hat{\Delta} = \hat{\nabla} \cdot \hat{\nabla}$ and a new variable $\psi = \psi(\hat{\mathbf{x}})$ as

$$\varrho(\mathbf{x}) = \bar{\varrho}(\psi_0 \cdot (\psi \circ \hat{\mathbf{x}})(\mathbf{x}) + 1.5)$$

with $(\psi \circ \hat{\mathbf{x}})(\mathbf{x}) = \psi(\hat{\mathbf{x}}(\mathbf{x}))$, where $\circ$ acts as a function composition operator, results in the classical PFC energy

$$\frac{3}{k_{\mathrm{B}} T \bar{\varrho} \psi_0^4} (F_{\mathrm{H}}[\varrho(\psi)] - \bar{F}_{\mathrm{H}}) \approx L^n \int \frac{1}{2} (1 + r) \psi^2 + \frac{1}{4} \psi^4 + \psi \hat{\Delta} \psi + \frac{1}{2} \psi \hat{\Delta}^2 \psi \, \mathrm{d}\hat{\mathbf{x}}$$
$$=: L^n F_{\mathrm{sh}}[\psi].$$

We consider the variational derivative of F_{H} and relate it to the variational derivative of F_{sh}:

$$\frac{\delta F_{\mathrm{H}}[\varrho]}{\delta \varrho} = \frac{1}{L^n} \left(\frac{\delta F_{\mathrm{H}}[\varrho \circ \mathbf{x}]}{\delta(\varrho \circ \mathbf{x})} \circ \hat{\mathbf{x}} \right)$$
$$\approx \frac{1}{L^n} \left(\frac{\delta \left(\frac{1}{3} k_{\mathrm{B}} T \bar{\varrho} \psi_0^4 L^n F_{\mathrm{sh}}[\psi] + \bar{F}_{\mathrm{H}} \right)}{\delta(\varrho \circ \mathbf{x})} \circ \hat{\mathbf{x}} \right)$$
$$= \frac{1}{3} k_{\mathrm{B}} T \bar{\varrho} \psi_0^4 \left(\frac{\delta F_{\mathrm{sh}}[\psi]}{\delta \psi} \frac{\delta \psi}{\delta(\varrho \circ \mathbf{x})} \circ \hat{\mathbf{x}} \right)$$
$$= \frac{1}{3} k_{\mathrm{B}} T \psi_0^3 \left(\frac{\delta F_{\mathrm{sh}}[\psi]}{\delta \psi} \circ \hat{\mathbf{x}} \right).$$

Inserting the parametrization of ϱ into the dynamical equations (2.14) and (2.15), fixing $\psi_0 = 1$ for simplicity and using the length scaling $\hat{\mathbf{x}}$, gives

$$(1.5 + \psi)\big(\partial_t\mathbf{v} + \frac{1}{L}(\mathbf{v}\cdot\hat{\nabla})\mathbf{v} + \gamma\mathbf{v}\big) = \frac{k_{\mathrm{B}}T}{3mL}\hat{\nabla}\frac{\delta F_{\mathrm{sh}}[\psi]}{\delta\psi} + \frac{\eta}{m\bar{\varrho}L^2}\hat{\Delta}\mathbf{v},$$

$$\partial_t\psi + \frac{1}{L}\hat{\nabla}\cdot\big((1.5 + \psi)\mathbf{v}\big) = 0.$$

Introducing the dimensionless variables $\hat{t} := tV_0/L$ and $\hat{\mathbf{v}} := \mathbf{v}/V_0$ finally gives the dimensionless dynamical equations

$$(1.5 + \psi)\big(\partial_{\hat{t}}\hat{\mathbf{v}} + (\hat{\mathbf{v}}\cdot\hat{\nabla})\hat{\mathbf{v}} + \frac{\gamma L}{V_0}\hat{\mathbf{v}}\big) = \frac{k_{\mathrm{B}}T}{3mV_0^2}\hat{\nabla}\frac{\delta F_{\mathrm{sh}}}{\delta\psi} + \frac{\eta}{m\bar{\varrho}LV_0}\hat{\Delta}\hat{\mathbf{v}},$$

$$\partial_{\hat{t}}\psi + \hat{\nabla}\cdot\big((1.5 + \psi)\hat{\mathbf{v}}\big) = 0.$$

By defining the dimensionless numbers

$$\mathrm{Pe} = \frac{3mV_0^2}{k_{\mathrm{B}}T}, \ \mathrm{Re} = \frac{m\bar{\varrho}LV_0}{\eta} \ \text{ and } \ \Gamma = \frac{\gamma L}{V_0}$$

as above, we find equations (2.17)–(2.18), where we have neglected the hat symbol on the derivatives for readability.

2.2.6 Energy dissipation

To demonstrate thermodynamic consistency of the model, we assume that the total energy of the system is composed of the Helmholtz free-energy F_{H}, or an appropriate approximation of this functional, and the kinetic energy

$$F_{\mathrm{kin}} = \frac{\rho_f}{2}\int \|\mathbf{u}\|^2 \, \mathrm{d}\mathbf{x}$$

of the surrounding fluid. To be consistent with the dynamical equations (2.42) we focus on the dimensionless energies by introducing length and time scales as above and by defining dimensionless variables denoted by a hat symbol. Additionally, we normalize the energies:

$$\hat{\mathbf{x}} = \mathbf{x}/L, \ \hat{t} = tV_0/L, \ \hat{\mathbf{u}} = \mathbf{u}/V_0, \ \hat{F}_* = F_*/(V_0L^2\bar{\eta}_f).$$

This gives us the dimensionless kinetic energy

$$\hat{F}_{\mathrm{kin}} = \frac{\mathrm{Re}_f}{2}\int \|\hat{\mathbf{u}}\|^2 \, \mathrm{d}\hat{\mathbf{x}}$$

and by considering the correct scaling of the Swift-Hohenberg energy $F_{\mathrm{H}} \approx k_{\mathrm{B}}T\bar{\varrho}\frac{L^3}{3}F_{\mathrm{sh}}$ (see Section 2.2.5) we find

$$\hat{\mathcal{F}}_H = \frac{1}{\mathrm{Sc}}\int \frac{1}{4}\psi^4 + \frac{1}{2}\psi\big(r + (q_0^2 + \Delta)^2\big)\psi \, \mathrm{d}\hat{\mathbf{x}}$$

with the Schmidt number Sc given by

$$\mathrm{Sc} = \frac{\mathrm{Pe}}{\mathrm{Re}_f}\bar{\bar{\varrho}} \quad \text{ with } \bar{\bar{\varrho}} := \frac{\rho_f}{m\bar{\varrho}}.$$

The total dimensionless energy, to be considered, now reads

$$\hat{F}_{\text{tot}} = \hat{F}_{\text{kin}} + \hat{F}_{\text{H}}.$$

In the following, we consider only non-dimensional variables and for readability drop the hat symbols.

We assume that the evolution equations for momentum and mass conservation read

$$\partial_t \mathbf{u} + (\mathbf{u} \cdot \nabla)\mathbf{u} = \nabla \cdot \tilde{\boldsymbol{\sigma}} + \mathbf{F},$$
$$\nabla \cdot \mathbf{u} = 0, \tag{2.47}$$
$$\partial_t \psi + \mathbf{u} \cdot \nabla \psi = -\nabla \cdot \mathbf{j},$$

where the volume force $\mathbf{F}$ and the flux $\mathbf{j}$ need to be determined to justify thermodynamic consistency. Let Ω be a fixed domain with Lipschitz-boundary Σ. The time-evolution of the energy $\partial_t F_{\text{tot}}$ can be split into

$$\partial_t F_{\text{kin}} = \text{Re}_f \int_\Omega \mathbf{u} \cdot \partial_t \mathbf{u} \, d\mathbf{x}$$
$$= \text{Re}_f \int_\Omega \mathbf{u} \cdot (-(\mathbf{u} \cdot \nabla)\mathbf{u} + \nabla \cdot \tilde{\boldsymbol{\sigma}} + \mathbf{F}) \, d\mathbf{x},$$
$$\partial_t F_{\text{H}} = \frac{1}{\text{Sc}} \int_\Omega \frac{\delta F_{\text{sh}}[\psi]}{\delta \psi} \partial_t \psi \, d\mathbf{x}. \tag{2.48}$$

Using incompressibility, integration by parts, and the relations

$$\frac{1}{2} \nabla (\|\mathbf{u}\|^2) = (\mathbf{u} \cdot \nabla)\mathbf{u} - (\nabla \times \mathbf{u}) \times \mathbf{u},$$
$$(f \nabla \mathbf{u}, \mathbf{D}(\mathbf{u}))_\Omega = (f \mathbf{D}(\mathbf{u}), \mathbf{D}(\mathbf{u}))_\Omega,$$

for a scalar field $f = f(\mathbf{x})$ and inner product $(\mathbf{A}, \mathbf{B})_\Omega = \int_\Omega \mathbf{A} : \mathbf{B} \, d\mathbf{x} = \int_\Omega A_{ij}(\mathbf{x})B_{ij}(\mathbf{x}) \, d\mathbf{x},$[3] we get

$$\int_\Omega \mathbf{u} \cdot (\mathbf{u} \cdot \nabla)\mathbf{u} = \int_\Omega \frac{1}{2} \mathbf{u} \cdot \nabla (\|\mathbf{u}\|^2) + \mathbf{u} \cdot [(\nabla \times \mathbf{u}) \times \mathbf{u}] \, d\mathbf{x}$$
$$= \frac{1}{2} \int_\Sigma (\mathbf{u} \cdot \mathbf{n}_\Sigma) \|\mathbf{u}\|^2 \, d\Sigma$$
$$= 0 \text{ for } \begin{cases} \mathbf{u} \cdot \mathbf{n}_\Sigma = 0 & \text{(no-penetration)} \\ \mathbf{u} = 0 & \text{(no-slip)}, \end{cases}$$

$$\int_\Omega \mathbf{u} \cdot \nabla \cdot \tilde{\boldsymbol{\sigma}} \, d\mathbf{x} = \underbrace{\int_\Omega -\nabla \mathbf{u} : \tilde{\boldsymbol{\sigma}} \, d\mathbf{x}}_{\leq 0} + \underbrace{\int_\Sigma \mathbf{u} \cdot \tilde{\boldsymbol{\sigma}} \cdot \mathbf{n}_\Sigma \, d\Sigma}_{(*)}$$
$$(*) = 0 \text{ for } \begin{cases} \tilde{\boldsymbol{\sigma}} \cdot \mathbf{n}_\Sigma = 0 & \text{(no-flux)} \\ \mathbf{u} = 0 & \text{(no-slip)}. \end{cases}$$

---

[3] Here we use the Einstein summation convention.

Thus, we get for the kinetic part of the energy, in the case of no-slip boundary conditions, the estimate

$$\partial_t F_{\mathrm{kin}} \leq \mathrm{Re}_f \int_\Omega \mathbf{u} \cdot \mathbf{F} \ \mathrm{d}\mathbf{x}.$$

The derivative of the PFC-part of the energy evolution reads

$$\partial_t F_{\mathrm{H}} = \frac{1}{\mathrm{Sc}} \int_\Omega \mathbf{j}\nabla \frac{\delta F_{\mathrm{sh}}[\psi]}{\delta\psi} - \mathbf{u} \cdot \frac{\delta F_{\mathrm{sh}}[\psi]}{\delta\psi}\nabla\psi \ \mathrm{d}\mathbf{x}.$$

By choosing the flux $\mathbf{j}$ proportional to $-\nabla \delta F_{\mathrm{sh}}[\psi]/\delta\psi$, e.g.,

$$\mathbf{j} = -M(\psi)\nabla\frac{\delta F_{\mathrm{sh}}[\psi]}{\delta\psi}$$

with $M(\psi)$ any positive definite function, we find for the total energy evolution

$$\partial_t F_{\mathrm{tot}} \leq \int_\Omega \mathbf{u} \cdot \left[\mathrm{Re}_f\mathbf{F} - \frac{1}{\mathrm{Sc}}\frac{\delta F_{\mathrm{sh}}[\psi]}{\delta\psi}\nabla\psi\right] \ \mathrm{d}\mathbf{x}$$

and can choose $\mathbf{F}$ so that this integral vanishes, i.e.,

$$\mathbf{F} = \frac{1}{\mathrm{Re}_f\mathrm{Sc}}\frac{\delta F_{\mathrm{sh}}[\psi]}{\delta\psi}\nabla\psi = \frac{\bar{\bar{\varrho}}}{\mathrm{Pe}}\frac{\delta F_{\mathrm{sh}}[\psi]}{\delta\psi}\nabla\psi.$$

Using incompressibility again, we get the relation to the force and flux terms derived before. For no-slip boundary conditions, we have

$$\int_\Omega -\frac{1}{\mathrm{Sc}}\mathbf{u} \cdot \frac{\delta F_{\mathrm{sh}}[\psi]}{\delta\psi}\nabla\psi \ \mathrm{d}\mathbf{x} = \int_\Omega \frac{1}{\mathrm{Sc}}\mathbf{u} \cdot \psi\nabla\frac{\delta F_{\mathrm{sh}}[\psi]}{\delta\psi} \ \mathrm{d}\mathbf{x}$$

and thus, the force

$$\mathbf{F} = -\frac{\bar{\bar{\varrho}}}{\mathrm{Pe}}\psi\nabla\frac{\delta F_{\mathrm{sh}}[\psi]}{\delta\psi} \tag{2.49}$$

and with $M_1 = \bar{\bar{\varrho}}/\mathrm{Pe}$ the above set of equations (2.42). Our derived continuum model thus fulfills thermodynamic consistency.

2.2.7   Nascent delta functions

To show, that the approximation of a delta-function by powers of a rescaled one-mode density approximation (see equation (2.29)) is reasonable, we show that properties of a nascent delta function hold true.

Let $\mathrm{dist}(\mathbf{x})$ be a distance function that gives the distance of $\mathbf{x}$ to the center-of-mass coordinate of a particle fixed at the coordinate-center. Then, a smeared out delta-function $\delta_\epsilon(\mathbf{x}) \approx \delta(\mathbf{x})$ can be expressed as

$$\delta_\epsilon(\mathbf{x}) := \begin{cases} \frac{1}{2\epsilon}\big(1 + \cos(\pi\,\mathrm{dist}(\mathbf{x})/\epsilon)\big) & \text{for } |\mathrm{dist}(\mathbf{x})| \leq \epsilon \\ 0 & \text{otherwise,} \end{cases} \tag{2.50}$$

where $\epsilon > 0$ is a small parameter that defines the width of the smeared out region of the delta-function (see, e.g., [246, 259, 86]). It can be shown that δ_ϵ converges weakly to δ, i.e.,

$$\delta_\epsilon(\mathbf{x}) \xrightarrow{\epsilon \to 0} \delta(\mathbf{x}) \ :\Leftrightarrow \ (\delta_\epsilon, \xi)_{\mathbb{R}^m} \xrightarrow{\epsilon \to 0} (\delta, \xi)_{\mathbb{R}^m}, \ \forall\xi C_c^\infty.$$

Particularly for the function δ_ϵ one can prove that it is a nascent delta function.

Definition 1. *(Similar to Definition 10.9 in [133]) An integrable function $\delta_\epsilon \in L_1(\mathbb{R}^m)$ is called nascent delta functions if it fulfills the following conditions:*

(i) *For all $\mathbf{x} \in \mathbb{R}^m$ it is positive: $\delta_\epsilon(\mathbf{x}) \geq 0$.*

(ii) *The integral is normalized: $\int_{\mathbb{R}^m} \delta_\epsilon(\mathbf{x})\, d\mathbf{x} = 1$.*

(iii) *The functions δ_ϵ have small support, in the sense that for all $\rho > 0$:*

$$\lim_{\epsilon \to 0} \int_{\mathbb{R}^m \setminus B_\rho(0)} \delta_\epsilon(\mathbf{x})\, d\mathbf{x} = 0$$

with $B_\rho(0)$ a ball around the origin with radius ρ.

Theorem 4. *(Following Theorem 10.11 and Remark 39.6 (b) in [133]) A nascent delta function $\delta_\epsilon(\mathbf{x})$ converges weakly to a delta-function $\delta(\mathbf{x})$ as ϵ goes to zero, in the sense of distributions, i.e.,*

$$\int_{\mathbb{R}^m} \delta_\epsilon(\mathbf{x})\xi(\mathbf{x})\, d\mathbf{x} \xrightarrow{\epsilon \to 0} \xi(0), \qquad \forall \xi \in C_c^\infty.$$

Proof. Since $\delta_\epsilon \in L_1(\mathbb{R}^m)$ is integrable with compact support, there exists $0 < \mu < \infty$ with $\|\delta_\epsilon\|_{L_1} \leq \mu$. Let $\tau > 0$. There exists $d > 0$, such that

$$\|\mathbf{x}\| \leq d \;\Rightarrow\; |\xi(0) - \xi(\mathbf{x})| < \frac{\tau}{\mu}.$$

For $\epsilon < d$ we can write down an estimate of the difference of the integral to $\xi(0)$, that is

$$\left| \xi(0) - \int_{\mathbb{R}^m} \delta_\epsilon(\mathbf{x})\xi(\mathbf{x})\, d\mathbf{x} \right| \overset{(ii)}{=} \left| \int_{\mathbb{R}^m} \delta_\epsilon(\mathbf{x})\big(\xi(0) - \xi(\mathbf{x})\big)\, d\mathbf{x} \right|$$

$$\overset{(iii)}{=} \left| \int_{B_\epsilon} \delta_\epsilon(\mathbf{x})\big(\xi(0) - \xi(\mathbf{x})\big)\, d\mathbf{x} \right| \leq \|\delta_\epsilon\|_{L_1} \frac{\tau}{\mu} \leq \tau.$$

$\square$

Theorem 5. *Let $k \in \mathbb{N}$ and $\psi^{(k)}$ be given by (2.28). Then the function*

$$\delta_{(k)}(\mathbf{x}) := N_k \psi_{(k)}(\mathbf{x}) \tag{2.51}$$

with N_k a normalization factor, is the sum of nascent delta functions and $\delta_{(k)}$ converges weakly to

$$\delta_\Omega(\mathbf{x}) := \sum_i \delta(\mathbf{x} - \mathbf{x}_i), \tag{2.52}$$

as $k \to \infty$, where $\mathbf{x}_i = \frac{2\pi i}{q}$, for $i \in \mathbb{Z}$.

Proof. a) Consider $\psi_{(0)}$ and let $\epsilon := \frac{\pi}{q}$ and $\mathrm{dist}(\mathbf{x}) = \mathbf{x}$ then it follows:

$$\delta_{(0)}(\mathbf{x}) = \frac{N_0}{2}\big(1 + \cos(q\mathbf{x})\big)$$

$$= N_0 \frac{\pi}{q} \delta_\epsilon(\mathbf{x}), \quad \text{for } \|\mathbf{x}\| \leq \frac{\pi}{q}.$$

Setting $N_0 := \frac{q}{\pi}$ we recover the proposed delta function approximation (2.50).

b) Since $\delta_{(0)} \geq 0$ the positivity property (i) of Definition 1 is fulfilled for all $\delta_{(k)}, k \geq 0$.

c) For the integral of $\psi_{(k)}$ we find

$$\frac{\sqrt{\pi}}{\sqrt{2^k}} \frac{2}{q} \int_{-\pi/q}^{\pi/q} \psi_{(k)}(\mathbf{x}) \, d\mathbf{x} = \frac{\Gamma(\frac{1}{2} + 2^k)}{\Gamma(1 + 2^k)\sqrt{2^{-k}}} \xrightarrow{k \to \infty} 1.$$

We set $M_k = \frac{\sqrt{2^k}}{\sqrt{\pi}} \frac{q}{2}$ and $N_k = M_k \frac{\Gamma(1+2^k)}{\Gamma(\frac{1}{2}+2^k)\sqrt{2^k}}$ to provide the normalization condition (ii) of Definition 1 for all $k \geq 0$.

The first values of M_k and N_k are given in table (2.53).

k	0	1	2	3	
M_k	$\frac{q}{2\sqrt{\pi}}$	$\frac{q}{\sqrt{2\pi}}$	$\frac{q}{\sqrt{\pi}}$	$\frac{q\sqrt{2}}{\sqrt{\pi}}$	(2.53)
$N_k \cdot \frac{\pi}{q}$	1	$\frac{4}{3}$	$\frac{64}{35}$	$\frac{16384}{6435}$	

d) Consider now a normalized Gaussian with $\epsilon_k := 2^{-k}$:

$$\delta_{\epsilon_k}^{\exp}(\mathbf{x}) := M_k \psi_{\epsilon_k}^{\exp} = M_k e^{-\frac{(q\mathbf{x})^2}{4\epsilon_k}} \tag{2.54}$$

as a known nascent delta function with weak convergence $\delta_\epsilon^{\exp} \xrightarrow{\epsilon \to 0} \delta$ [133], so particularly the property (iii) of Definition 1 is fulfilled for $\delta_{\epsilon_k}^{\exp}$. Since we have

$$0 \leq \psi_{(0)}(\mathbf{x}) \leq \psi_{\epsilon_0}^{\exp}(\mathbf{x}) \leq 1 \qquad \qquad \text{for } \|\mathbf{x}\| \leq \frac{\pi}{q}$$

and $\psi_{(k)} = \left[\psi_{(0)}\right]^{2^k}$, it follows

$$\forall k \geq 0 : \psi_{(k)}(\mathbf{x}) \leq \psi_{\epsilon_k}^{\exp}(\mathbf{x}) \qquad \qquad \text{for } \|\mathbf{x}\| \leq \frac{\pi}{q},$$

and $\forall \rho > 0$ with $\rho < \frac{\pi}{q}$ it holds

$$M_k \int_\rho^{\pi/q} \psi_{(k)}(\mathbf{x}) \, d\mathbf{x} \leq M_k \int_\rho^{\pi/q} \delta_{\epsilon_k}^{\exp}(\mathbf{x}) \, d\mathbf{x}, \quad \forall k.$$

With $\lim_{k \to \infty} \int_\rho^{\pi/q} \delta_{\epsilon_k}^{\exp}(\mathbf{x}) \, d\mathbf{x} = 0$ it follows

$$\lim_{k \to \infty} \int_\rho^{\pi/q} \delta_{(k)}(\mathbf{x}) \, d\mathbf{x} = \lim_{k \to \infty} N_k \int_\rho^{\pi/q} \psi_{(k)}(\mathbf{x}) \, d\mathbf{x} = 0.$$

This shows property (iii) of Definition 1 for the sequence $\delta_{(k)}$.

All in all we conclude, that $\delta_{(k)}$, restricted to the interval $[-\pi/q, \pi/q]$, is a nascent delta-function and thus converges weakly to $\delta(\mathbf{x})$.

e) We restrict the calculation to single waves of $\delta_{(k)}$, by definition of

$$\delta_{(k)}^i(\mathbf{x}) := \begin{cases} \delta_{(k)}(\mathbf{x} - \mathbf{x}_i), & \text{for } \|\mathbf{x} - \mathbf{x}_i\| \leq \frac{\pi}{q} \\ 0, & \text{otherwise} \end{cases}$$

and can thus provide a partition in the form

$$\sum_i \delta_{(k)}^i = \delta_{(k)}.$$

Since each $\delta_{(k)}^i$ converge weakly to a delta function we have found the property

$$\delta_{(k)}(\mathbf{x}) = \sum_i \delta_{(k)}^i(\mathbf{x}) \xrightarrow{k \to \infty} \sum_i \delta(\mathbf{x} - \mathbf{x}_i) = \delta_\Omega(\mathbf{x}).$$

$\square$

2.2.8 Conclusion

A fully continuous model is developed to simulate colloidal particles in a fluid, interacting via direct particle-particle interaction and via the induced flow fields. The method is based on ideas of dynamic density functional theory and fully resolved direct numerical simulations. The derived NS-PFC system operates on diffusive time scales and provides a qualitative approach down to the particle size.

We have demonstrated the quality of the method in various examples, first in crystallization processes analyzing the influence of a macroscopic flow field and second for three common test cases, namely the sedimentation of one, two, and many particles. For one and two particles, we have quantitatively compared the trajectories and velocities obtained by our simulation to simulations with the FPD method and have found good agreement. For the case of many particles we see the expected instabilities and compression at the bottom. For more quantitative comparisons, the calculation of a hydrodynamic radius would be desirable, as it is done by [191, 186]. However, this requires computations in 3D for the comparison with Stokes drag and drag torque and has thus to be considered in future work. As a preliminary step, we have computed the effective radius of the vacancy NS-PFC model by comparison with the FPD method, using the concentration profile (2.30), for which a radius is given. We have computed the particle velocities obtained by both methods for one particle dragged through a periodic channel. Comparing the result for various radii for the FPD method, we find an effective radius for the NS-PFC model of approximately $0.35d$.

However, in comparison with the other methods mentioned in the introduction, we do not see the advantages of our approach in a more detailed description of the underlying physics on a single particle scale, but in the emergent phenomena on larger scales. Here the formulation as a fully continuous model has several numerical advantages. For the classical PFC equation time step independent stability can be proven for the discrete scheme [29, 279, 202]. Coupling this to the Navier-Stokes equations, as considered e.g. in [7], allows for larger time steps as in the explicit coupling schemes of hybrid methods. As the NS-PFC model only contains local terms, the algorithms are expected to scale independently of the number of particles.

The numerical details of an efficient preconditioner to solve the arising linear systems is described for the advected PFC equation and for the Vacancy PFC model. Larger flow velocities decrease the efficiency of the solver slightly and also large mobility coefficients M_0 lead to slower convergence of the iterative schemes. This must be taken into account when large scale simulations are performed. Nevertheless, in combination with domain-decomposition techniques, as already described in Section 1.6.3, the system size can be increased a lot with an acceptable parallel efficiency.

Liquid crystalline phases within the PFC model

E̲ XTENDING *the classical Phase-Field Crystal model by an additional orientational order-parameter allows to study various liquid-crystalline phases. The corresponding Liquid Crystal PFC (LC-PFC) model was derived and formulated in [154, 282, 284, 283] and later first simulations were performed in [3].*

We use this model to access the structure and thermodynamics of interfaces between two coexisting liquid-crystalline phases in two spatial dimensions. Some results were already published in [203]. Depending on the model parameters, there is a variety of possible coexistences between two liquid-crystalline phases, where one phase is a plastic triangular crystal (PTC). Here, we calculate numerically the profiles for the mean density and the nematic order tensor across the interface for isotropic-PTC and columnar-PTC or smectic A-PTC coexistence. As a general finding, the width of the interface with respect to the nematic order parameter characterizing the orientational order is larger than the width of the mean density interface. In approaching the interface from the PTC side, at first the mean density goes down and then the nematic order parameter follows. The relative shift of the two profiles can be larger than a full lattice constant of the plastic crystal. Finally, we also present numerical results for the dynamic relaxation of an initial order-parameter profile towards its equilibrium interfacial profile. In [250] we have furthermore analyzed the dynamics of topological defects in the orientational director field in the phase transition smectic A-PTC.

Polar order can be incorporated into the Phase-Field Crystal model by introducing furthermore a parameter that describes the colloidal polarization, a vector order-parameter coupled to both fields, the translational and orientational order-parameter. Thermodynamic consistency of the model is shown. A plastic triangular and square phase as well as stripe phases are observed and the structural symmetries are visualized.

3.1   Interfaces between two coexisting liquid-crystalline phases

Liquid crystals build a mesophase with properties of both, a liquid and a crystalline phase [66]. Composed of unsymmetrical molecules or colloidal particles that can be ordered in position and orientation [94, 276], a rich variety of possible arrangements can be observed. In two spatial dimensions we find plastic triangular phases, liquid phases and stripe patterns, i.e., a smectic-A and columnar phase, and orientationally ordered phases, like the nematic phase. An overview about some patterns can be found in Figure 3.1 and Figure 3.2.

Varying the temperature and mean density of a system, not only pure phases can be observed, but also the coexistence of two phases of different ordering. We analyze the structure of the interfaces between those coexisting phases in this chapter, when a plastic triangular phase is involved. Therefore, the transition from liquid to crystalline and from columnar to crystalline is examined. Other phase pairs were already considered in literature, e.g., gas-liquid [89] and solid-liquid [286] interfaces of spherical particles (see also [44, 117, 64, 297, 296, 222, 110]), the isotropic-nematic interface (see, e.g., [172, 269, 43, 274, 267, 285, 214, 265, 270]), the isotropic-smectic (see [173, 239, 45, 70]), and the nematic-smectic interface [188]. However, to the best of our knowledge there is no investigation of an interface, where one of the coexisting phases is plastic or fully crystalline.

We use a variant of the Phase-Field Crystal model that was formulated for anisotropic particles in two [154] and three [282] spatial dimensions allowing for liquid-crystalline phases. It is formulated in terms of three order-parameter fields, namely the (translational) density modulation $\varphi(\mathbf{x})$, the local nematic order parameter $S(\mathbf{x})$, and the nematic director $\hat{\mathbf{n}}(\mathbf{x})$. Numerical studies [3] of the LC-PFC model in two spatial dimensions have shown that a variety of phase coexistences occur as a function of the model parameters. We follow this route and analyze the details about the interfaces between coexisting liquid crystalline phases using the PFC model. Additionally we show the dynamic process of the formation of these interfaces.

The chapter is organized as follows: after the presentation of a suitable PFC model for liquid crystals in Section 3.1.1, we show a numerical discretization in Section 3.1.2 and discuss results obtained by numerical calculations in Section 3.1.4.

3.1.1   PFC model for liquid crystals in two spatial dimensions

A PFC model for apolar[1] liquid crystals in two spatial dimensions[2] was given in [154, 3, 284, 283, 85]. It describes the static properties and dynamical behavior of a liquid-crystalline system in terms of two dimensionless order-parameter fields: the reduced translational density $\varphi(\mathbf{x}, t)$ and the symmetric and traceless nematic tensor $\mathbf{Q}(\mathbf{x}, t)$, with components Q_{ij}, position $\mathbf{x} = (x, y)$ and time t. For liquid-crystalline particles with a symmetry axis, the nematic tensor can be parametrized as

$$Q_{ij}(\mathbf{x}, t) = S(\mathbf{x}, t)\left(n_i(\mathbf{x}, t)n_j(\mathbf{x}, t) - \frac{1}{2}\delta_{ij}\right) \tag{3.1}$$

with the nematic order parameter $S(\mathbf{x}, t)$ and the nematic director $\hat{\mathbf{n}}(\mathbf{x}, t) = (n_1, n_2)$ that corresponds to the eigenvector of $\mathbf{Q}$ with respect to the dominant eigenvalue (see [154, 3, 284]).

---

[1]We neglect a possible macroscopic polarization. A generalization toward polar liquid crystals is formulated in Section 3.2.

[2]An extension toward a 3D model was formulated in [282, 85].
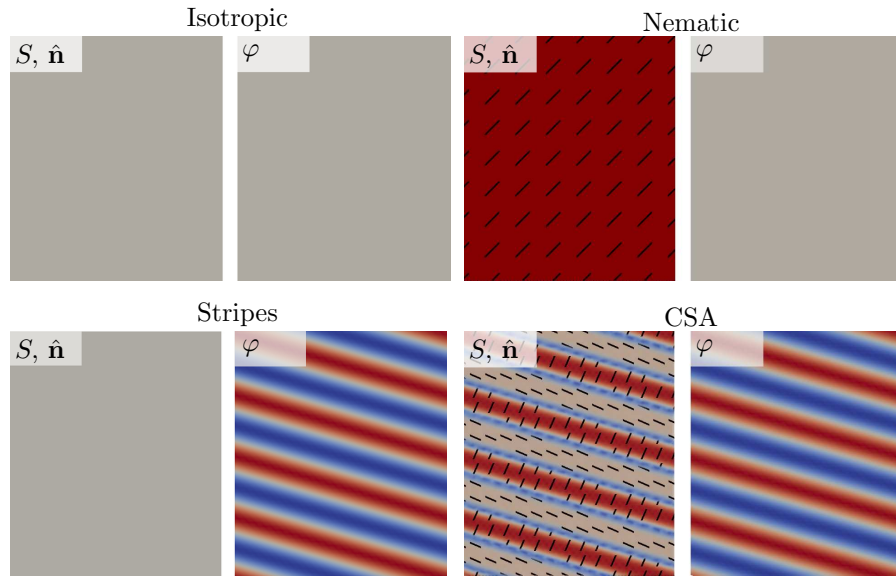
Figure 3.1 – *A collection of some liquid crystalline phases obtained with the Liquid-Crystal PFC (LC-PFC) model. Parameters $(A_1, A_2, B_3, D_1, D_2)$ are given from top-left to bottom-right: isotropic $(4.2, 14, -4, 2, 0.8)$, nematic $(3, 14, -4, -2, 0.8)$, stripes $(1.5, 14, 0, 1, 8)$ and columnar/smectic A (CSA) $(1.5, 14, -4, 2, 0.8)$. All phases with mean density $\bar{\varphi} = 0$.*
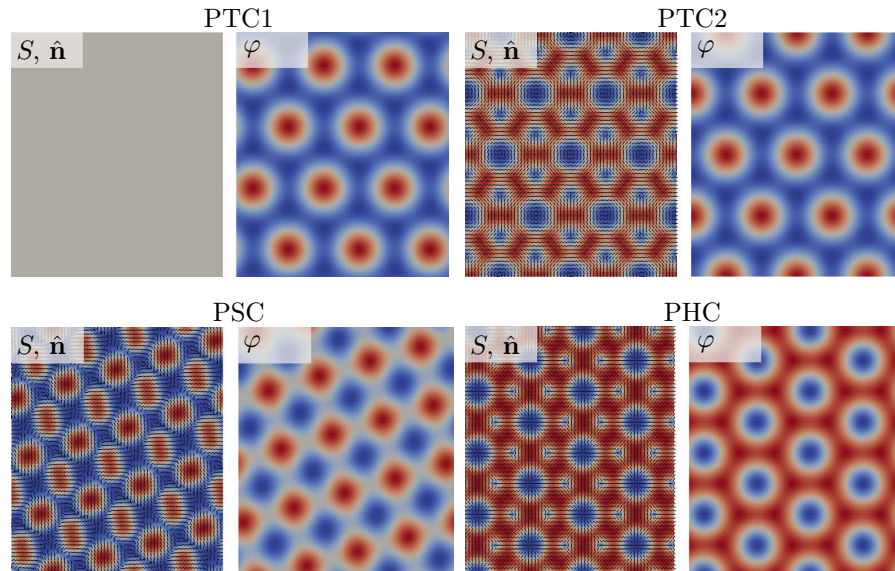
Figure 3.2 – *A collection of some liquid crystalline phases obtained with the Liquid-Crystal PFC (LC-PFC) model. Parameters $(A_1, A_2, B_3, D_1, D_2)$ are given from top-left to bottom-right: plastic triangular crystal 1 (PTC1) $(3, 14, 0, 1, 8)$, plastic triangular crystal 2 (PTC2) $(3, 14, -4, 1, 0.8)$, plastic square crystal (PSC) $(1.5, 14, -4, -0.2, 0.8)$ and plastic honeycomb crystal (PHC) $(4.5, 14, -4, -0.4, 0.8)$. All phases with mean density $\bar{\varphi} = 0$.*

Static free-energy functional

The static properties of a liquid-crystalline system are described by a free-energy functional $F[\varphi, \mathbf{Q}]$, which is minimized with respect to $\varphi(\mathbf{x})$ and $Q_{ij}(\mathbf{x})$ in thermodynamic equilibrium. After an appropriate rescaling of the length and energy scales, this free-energy functional obtains the dimensionless form[3] [283]

$$F[\varphi, \mathbf{Q}] = \int \left\{ -\frac{\varphi^3}{3} + \frac{\varphi^4}{6} + A_1 \varphi^2 + A_2 \varphi (\Delta + \Delta^2) \varphi + (\varphi - 1) \frac{\varphi Q_{kl}^2}{4} \right.$$
$$\left. + B_3 (\partial_k \varphi)(\partial_l Q_{kl}) + \frac{Q_{kl}^2 Q_{mn}^2}{64} + D_1 Q_{kl}^2 + D_2 (\partial_l Q_{kl})^2 \right\} \, \mathrm{d}\mathbf{x} \quad (3.2)$$

with the five dimensionless coupling parameters A_1, A_2, B_3, D_1, and D_2.

Remark 5. *The functional* (3.2) *can be split into a PFC part, an orientational part and a coupling part, i.e.,*

$$F[\varphi, \mathbf{Q}] = \int f_{\mathrm{pfc}}(\varphi) + f_{\mathrm{coupling}}(\varphi, \mathbf{Q}) + f_{\mathrm{Q}}(\mathbf{Q}) \, \mathrm{d}\mathbf{x}$$

with

$$f_{\mathrm{pfc}}(\varphi) = -\frac{\varphi^3}{3} + \frac{\varphi^4}{6} + A_1 \varphi^2 + A_2 \varphi (\Delta + \Delta^2) \varphi \,,$$

$$f_{\mathrm{coupling}}(\varphi, \mathbf{Q}) = \varphi (\varphi - 1) \frac{Q_{kl}^2}{4} + B_3 (\partial_k \varphi)(\partial_l Q_{kl}) \,,$$

$$f_{\mathrm{Q}}(\mathbf{Q}) = \frac{Q_{kl}^2 Q_{mn}^2}{64} + D_1 Q_{kl}^2 + D_2 (\partial_l Q_{kl})^2,$$

where $f_{\mathrm{pfc}}(\varphi)$ is similar to the classical PFC energy density (1.1) *and $f_{\mathrm{Q}}(\mathbf{Q})$ corresponds to the Landau deGennes distorsion and bulk free energy density [66] with fixed quartic term that allows for a stable nematic ordering for $D_1 > 0$.* ◁

Remark 6. *If we relate this free-energy $F[\varphi, \mathbf{Q}]$ to the energy given in Section 2.2.6, we find that the length scale L is fixed to $L = \sqrt{2}$ and the parameters $A_1 = -C_0$ and $A_2 = C_2 = -C_4$. In [283] a slightly different parametrization is used with a parameter A_3 in front of the $\Delta^2 \varphi$ term in the energy.* ◁

Dynamical equations

The corresponding dynamical equations for $\varphi(\mathbf{x}, t)$ and $Q_{ij}(\mathbf{x}, t)$ can be derived from classical dynamical density functional theory [281] and are given in [283], by

$$\partial_t \varphi = -\nabla \cdot \mathbf{J}^\varphi \,, \tag{3.3}$$

$$\partial_t Q = -\Phi^Q \tag{3.4}$$

---

[3]Einstein's sum convention is used throughout this chapter. Notice that powers of indexed quantities involve repeated indices and thus summation, i. e., for example, $Q_{ij}^2 \equiv Q_{ij} Q_{ij} \equiv \sum_{i,j} Q_{ij} Q_{ij}$.

with the dimensionless current $\mathbf{J}^\varphi(\mathbf{x}, t)$ and the dimensionless quasi-current $\Phi^Q(\mathbf{x}, t)$. In constant-mobility approximation, this current and quasi-current are given by [283, 85]

$$\mathbf{J}^\varphi = -2\alpha_1(\nabla\varphi^\natural) - 2\alpha_3(\nabla \cdot \mathbf{Q}^\natural)\,, \tag{3.5}$$

$$\Phi^Q_{ij} = -4\alpha_1(\Delta Q^\natural_{ij}) - 2\alpha_3\big(2(\partial_i\partial_j\varphi^\natural) - \delta_{ij}(\Delta\varphi^\natural)\big) + 8\alpha_4 Q^\natural_{ij}\,, \tag{3.6}$$

with the three dimensionless mobility parameters α_1, α_3, and α_4[4] and the thermodynamic conjugates

$$\varphi^\natural = \frac{\delta\mathcal{F}}{\delta\varphi}\,, \qquad \mathbf{Q}^\natural = \frac{\delta\mathcal{F}}{\delta\mathbf{Q}} \tag{3.7}$$

of $\varphi(\mathbf{x}, t)$ and $\mathbf{Q}(\mathbf{x}, t)$ respectively. The thermodynamic conjugates follow directly from the free-energy functional (3.2) by functional differentiation:

$$\varphi^\natural = -\varphi^2 + \frac{2}{3}\varphi^3 + 2A_1\varphi + 2A_2(\Delta + \Delta^2)\varphi + (2\varphi - 1)\frac{Q^2_{ij}}{4} - B_3(\partial_i\partial_j Q_{ij})\,, \tag{3.8}$$

$$\begin{aligned} Q^\natural_{ij} = {} &\varphi(\varphi - 1)Q_{ij} - B_3\big(2(\partial_i\partial_j\varphi) - \delta_{ij}\Delta\varphi\big) + \frac{Q_{ij}Q^2_{kl}}{8} + 4D_1 Q_{ij} \\ &- 2D_2\partial_k\big(\partial_i Q_{kj} + \partial_j Q_{ki} - \delta_{ij}(\partial_l Q_{kl})\big)\,. \end{aligned} \tag{3.9}$$

For a comparison of the dimensionless rescaled parameters in equations (3.2), (3.5), and (3.6) with the corresponding parameters in the notation of [3, 283, 85], see [203].

The numerical procedure to solve the system of equations is briefly described in the next section.

3.1.2 Numerical solution of the PFC model

By inserting equations (3.8) and (3.9) into equations (3.5) and (3.6), we obtain a system of six coupled nonlinear partial differential equations for the dynamical equations (3.3) and (3.4). In order to solve this system numerically, we decoupled and linearized it. A simplification is possible due to the symmetry and tracelessness of the nematic tensor. Defining the variables $q_i \equiv Q_{i,1}$ and $q^\natural_i \equiv Q^\natural_{i,1}$ allows to write the system of dynamical equations in the compact form

$$\begin{aligned} \partial_t\varphi &= 2\alpha_1\Delta\varphi^\natural + 2\alpha_3\blacktriangle_i q^\natural_i\,, \\ \partial_t q_i &= 4\alpha_1\Delta q^\natural_i + 2\alpha_3\blacktriangle_i\varphi^\natural - 8\alpha_4 q^\natural_i \end{aligned} \tag{3.10}$$

with the operator $\blacktriangle \equiv (\partial_1\partial_1 - \partial_2\partial_2,\ 2\partial_1\partial_2)$ that is related to the Cauchy-Riemann operator. The thermodynamic conjugates reformulated in the new variables read

$$\begin{aligned} \varphi^\natural &= f_\varphi(\varphi, \mathbf{q}) + 2A_1\varphi + 2A_2(\Delta + \Delta^2)\varphi - B_3\blacktriangle_i q_i\,, \\ q^\natural_i &= f_q(\varphi, \mathbf{q})_i + 4D_1 q_i - 2D_2\Delta q_i - B_3\blacktriangle_i\varphi \end{aligned} \tag{3.11}$$

with the polynomials

$$\begin{aligned} f_\varphi(\varphi, \mathbf{q}) &= -\varphi^2 + \frac{2}{3}\varphi^3 + \frac{1}{2}(2\varphi - 1)\|\mathbf{q}\|^2\,, \\ f_q(\varphi, \mathbf{q})_i &= \varphi(\varphi - 1)q_i + \frac{1}{4}q_i\|\mathbf{q}\|^2. \end{aligned} \tag{3.12}$$

---

[4]In Section 3.1.3 a relation of the three mobilities is given that leads to dissipative dynamics.

To discretize the dynamical equations (3.10) in time, let $0 = t_0 < t_1 < t_2 < \ldots < t_N = T$ be a sequence of time steps. Defining $\varphi_k \equiv \varphi(t_k)$, $q_{i,k} \equiv q_i(t_k)$, and $\tau_k = t_{k+1} - t_k$, we obtain the time-discrete systems

$$\frac{\varphi_{k+1}}{\tau_k} - 2\alpha_1\Delta\varphi^\natural = \frac{\varphi_k}{\tau_k} + 2\alpha_3\blacktriangle \cdot \mathbf{q}^\natural\,,$$
$$\varphi^\natural - 2\big(A_1 - A_2\Delta\big)\varphi_{k+1} + A_2\Delta\varphi^\flat = f_\varphi(\varphi_{k+1}, \mathbf{q}_k) - B_3\blacktriangle \cdot \mathbf{q}_k\,, \tag{3.13}$$
$$\varphi^\flat - \Delta\varphi_{k+1} = 0$$

and

$$\frac{1}{\tau_k}\mathbf{q}_{k+1} - 4(\alpha_1\vec{\Delta} - 2\alpha_4)\mathbf{q}^\natural = \frac{1}{\tau_k}\mathbf{q}_k + 2\alpha_3\blacktriangle\varphi^\natural\,, \tag{3.14}$$
$$\mathbf{q}^\natural - 2(2D_1 - D_2\vec{\Delta})\mathbf{q}_{k+1} = f_q(\varphi_{k+1}, \mathbf{q}_{k+1}) - B_3\blacktriangle\varphi_{k+1}\,,$$

by replacing the time-derivative by a backward Euler discretization. We have used a sequential operator splitting approach to separate the dynamical system for φ and $\mathbf{q}$.

Linearizing $f_\varphi(\varphi, \mathbf{q})$ and $f_q(\varphi, \mathbf{q})_i$ around the old time step t_k, two linear systems can be solved one after the other for all k. The linearizations of the polynomials (3.12) read

$$f_\varphi(\varphi_{k+1}, \mathbf{q}) \approx \varphi_{k+1}\big(-2\varphi_k + 2\varphi_k^2 + \|\mathbf{q}\|^2\big) + \varphi_k^2 - \frac{4}{3}\varphi_k^3 - \frac{\|\mathbf{q}\|^2}{2}\,,$$
$$f_q(\varphi, \mathbf{q}_{k+1})_i \approx \frac{1}{4}q_{i,k+1}\big(4\varphi(\varphi - 1) + \|\mathbf{q}_k\|^2\big) + \frac{1}{2}q_{i,k}q_{j,k}q_{j,k+1} - \frac{1}{2}q_{i,k}\|\mathbf{q}_k\|^2. \tag{3.15}$$

Instead of such a simple time-stepping scheme, a higher-order embedded Rosenbrock scheme with an adequate step-size control for the time discretization can be used. Such a scheme is described in more detail in the next section.

Rosenbrock Discretization for the LC-PFC system

We follow the notation $\mathbb{M}\partial_t\mathbf{x} = \mathbb{F}[\mathbf{x}]$ of Section 1.2.1 and introduce the (non-)linear operator $\mathbb{F}$ and Jacobian $\mathbb{J}_\mathbb{F}$ of the right-hand side of system (3.10). We have $\mathbf{x} = (\varphi, \varphi^\natural, \varphi^\flat, \mathbf{q}, \mathbf{q}^\natural)^\top$ and $\mathbb{M} = \mathrm{diag}(0, 1, 0, \mathbf{0}, \mathbf{1})$ with the functional $\mathbb{F}$ applied to $\mathbf{x}$ given by

$$\mathbb{F}[\mathbf{x}] = \underbrace{\begin{bmatrix} -\varphi^\natural + 2A_1\varphi + 2A_2\Delta\varphi + 2A_2\Delta\varphi^\flat - B_3\blacktriangle \cdot \mathbf{q} \\ 2\alpha_1\Delta\varphi^\natural + 2\alpha_3\blacktriangle \cdot \mathbf{q}^\natural \\ -\varphi^\flat + \Delta\varphi \\ -\mathbf{q}^\natural + 4D_1\mathbf{q} - 2D_2\vec{\Delta}\mathbf{q} - B_3\blacktriangle\varphi \\ 4\alpha_1\vec{\Delta}\mathbf{q}^\natural + 2\alpha_3\blacktriangle\varphi^\natural - 8\alpha_4\mathbf{q}^\natural \end{bmatrix}}_{\mathbb{F}_{\mathrm{Lin}}[\mathbf{x}]} + \begin{bmatrix} f_\varphi(\varphi, \mathbf{q}) \\ 0 \\ 0 \\ f_\mathbf{q}(\varphi, \mathbf{q}) \\ \mathbf{0} \end{bmatrix}.$$

The corresponding Jacobian $\mathbb{J}$ of $\mathbb{F}$ in direction $\mathbf{y} = (d\varphi, d\varphi^\natural, d\varphi^\flat, d\mathbf{q}, d\mathbf{q}^\natural)^\top$ reads

$$\mathbb{J}_\mathbb{F}(\mathbf{x})[\mathbf{y}] = \mathbb{F}_{\mathrm{Lin}}[\mathbf{y}] + \begin{bmatrix} \mathbb{J}_{f_\varphi}(\varphi, \mathbf{q})[d\varphi, d\mathbf{q}] \\ 0 \\ 0 \\ \mathbb{J}_{f_\mathbf{q}}(\varphi, \mathbf{q})[d\varphi, d\mathbf{q}] \\ \mathbf{0} \end{bmatrix}$$

with

$$\mathbb{J}_{f_\varphi}(\varphi, \mathbf{q})[d\varphi, d\mathbf{q}] = -2\varphi d\varphi + (2\varphi^2 + \|\mathbf{q}\|^2)d\varphi + (2\varphi - 1)\langle \mathbf{q}, d\mathbf{q}\rangle_2,$$

$$\mathbb{J}_{f_\mathbf{q}}(\varphi, \mathbf{q})[d\varphi, d\mathbf{q}]_i = \left((2\varphi - 1)q_i d\varphi + \varphi(\varphi - 1)dq_i + \frac{1}{4}(2q_i^2 + \|\mathbf{q}\|^2)dq_i, \ \frac{1}{2}q_1 q_2 dq_{j(i)}\right),$$

where $j(i) = 3 - i$ the opposite component of $\mathbf{q}$.

Let $\{\theta_i\}$ be a basis of the finite-element space V_h (see Section 1.2), $\mathbf{M}$ and $\mathbf{K}$ the shortcuts for the assembled mass and stiffness matrices, and the discretized operator matrices defined by

$$\mathbf{M} := \big((\theta_j, \theta_i)_\Omega\big)_{ij}, \quad \mathbf{K} := \big((\nabla\theta_j, \nabla\theta_i)_\Omega\big)_{ij}, \quad \mathbf{K}_{kl} := \big((\partial_l\theta_j, \partial_k\theta_i)_\Omega\big)_{ij}.$$

Using $\mathbf{K} = \mathbf{K}_{11} + \mathbf{K}_{22}$ and $\mathbf{K}^* := \mathbf{K}_{11} - \mathbf{K}_{22}$, we get a structural symmetric representation of the coupled linear system for the ith stage iteration $\mathbf{y}_i^{k+1}$ of the Rosenbrock scheme:

$$\begin{bmatrix} \mathbf{A} & \mathbf{B} \\ \mathbf{B}^\top & \mathbf{C} \end{bmatrix} \mathbf{y}_i^{k+1} = \begin{pmatrix} \mathbf{b}_0 \\ \mathbf{b}_1 \end{pmatrix}, \tag{3.16}$$

where $\mathbf{A}$ corresponds to the PFC part of the equations, $\mathbf{C}$ to the liquid-crystal part of the equations, and $\mathbf{B}$ to a coupling operator. Thereby, the block-diagonal parts of the linear system are given by

$$\mathbf{A} = \begin{bmatrix} \mathbf{H}_{(-2A_1, 2A_2)} - \mathbf{F}^\varphi & \mathbf{M} & 2A_2\mathbf{K} \\ (c\tau_k)^{-1}\mathbf{M} & 2\alpha_1\mathbf{K} & 0 \\ \mathbf{K} & 0 & \mathbf{M} \end{bmatrix}$$

$$\mathbf{C} = \begin{bmatrix} \mathbf{H}_{(-4D_1, -2D_2)} - \mathbf{G}_1^{q_1} & -\mathbf{G}_1^{q_2} & \mathbf{M} & 0 \\ -\mathbf{G}_2^{q_1} & \mathbf{H}_{(-4D_1, -2D_2)} - \mathbf{G}_2^{q_2} & 0 & \mathbf{M} \\ (c\tau_k)^{-1}\mathbf{M} & 0 & \mathbf{H}_{(8\alpha_4, 4\alpha_1)} & 0 \\ 0 & (c\tau_k)^{-1}\mathbf{M} & 0 & \mathbf{H}_{(8\alpha_4, 4\alpha_1)} \end{bmatrix},$$

with the parametrized matrix $\mathbf{H}_{(a,b)} := a\mathbf{M} + b\mathbf{K}$ and c the timestep scaling of the Rosenbrock scheme (see Section 1.2.1). The coupling (off-diagonal) blocks of the system matrix read

$$\mathbf{B} = \begin{bmatrix} -B_3\mathbf{K}^* - \mathbf{F}^{q_1} & -2B_3\mathbf{K}_{12} - \mathbf{F}^{q_2} & 0 & 0 \\ 0 & 0 & 2\alpha_3\mathbf{K}^* & 4\alpha_3\mathbf{K}_{12} \\ 0 & 0 & 0 & 0 \end{bmatrix},$$

$$\mathbf{B}^\top = \begin{bmatrix} -B_3\mathbf{K}^* - \mathbf{G}_1^\varphi & 0 & 0 \\ -2B_3\mathbf{K}_{12} - \mathbf{G}_2^\varphi & 0 & 0 \\ 0 & 2\alpha_3\mathbf{K}^* & 0 \\ 0 & 4\alpha_3\mathbf{K}_{12} & 0 \end{bmatrix}.$$

The matrices corresponding to the non-linear terms are given by

$$\mathbf{F}^\varphi = \big(\big([-2\varphi_k + 2(\varphi_k)^2 + \|\mathbf{q}_k\|^2]\theta_j, \theta_i\big)_\Omega\big)_{ij}, \quad \mathbf{F}^{q_l} = \big(\big([2\varphi_k - 1]q_{l,k}\theta_j, \theta_i\big)_\Omega\big)_{ij},$$

and

$$\mathbf{G}_l^\varphi = \big(\big([2\varphi_k - 1]q_{l,k}\theta_j, \theta_i\big)_\Omega\big)_{ij}, \quad \mathbf{G}_l^{q_m} = \Big(\Big(\big[\delta_{lm}[(\varphi_k)^2 - \varphi_k + \frac{1}{4}\|\mathbf{q}_k\|^2] + \frac{1}{2}q_{l,k}q_{m,k}\big]\theta_j, \theta_i\Big)_\Omega\Big)_{ij}.$$

Especially, one can find $\mathbf{F}^{q_l} = \mathbf{G}_l^\varphi$ and $\mathbf{G}_l^{q_m} = \mathbf{G}_m^{q_l}$ and thus the symmetry of the system.

Solving the LC-PFC system

When using the operator splitting approach (3.13)–(3.14) we have to solve the PFC part and the liquid-crystal part in rotation, where the PFC part (3.13) can be solved using the preconditioner developed in Chapter 1.

In the Rosenbrock scheme (3.16) the Jacobi-matrix can be approximated, by neglecting one or both of the off-diagonal blocks, i.e. by solving the block triangular or block diagonal system

$$
\begin{bmatrix} \mathbf{A} & 0 \\ \mathbf{B}^\top & \mathbf{C} \end{bmatrix} \mathbf{y}_i^{k+1} = \begin{pmatrix} \mathbf{b}_0 \\ \mathbf{b}_1 \end{pmatrix}, \quad \text{or} \quad \begin{bmatrix} \mathbf{A} & 0 \\ 0 & \mathbf{C} \end{bmatrix} \mathbf{y}_i^{k+1} = \begin{pmatrix} \mathbf{b}_0 \\ \mathbf{b}_1 \end{pmatrix},
$$

respectively. This leads to a valid and efficient time-discretization scheme, when using a Rosenbrock W-method (see, e.g., [242, 207]). In the block-diagonal approximation the two systems can be solved in parallel, since the matrices depend on the old timestep solutions only. Also in the operator-splitting approach a parallel splitting could be implemented with the same order of convergence 1, with respect to the timestep width, as a sequential splitting. Both schemes show similar stability in the case of coupling the PFC equation to the Q-tensor equation.

The matrix $\mathbf{A}$ in the Rosenbrock scheme corresponds to the PFC part and can thus be solved using a preconditioned Krylov-subspace method FGMRES with the preconditioner matrix $\mathbf{P}$ of Section 1.3 or the corresponding variant, involving the Cahn-Hilliard subpreconditioner, $\mathbf{P}_{\mathrm{CH}}$.

3.1.3   Thermodynamic consistency

In order to find appropriate parameter regimes for the mobility parameters α_1, α_3, and α_4 we consider the variation of the energy with respect to variations in the order-parameters in time. For dissipative dynamics we have to find mobilities lead to the relation $\partial_t F[\varphi, \mathbf{Q}] \leq 0$.

The static free-energy functional (3.2) can be reformulated in terms of the variable φ and the two components of the Q-tensor, namely $\mathbf{q}$,
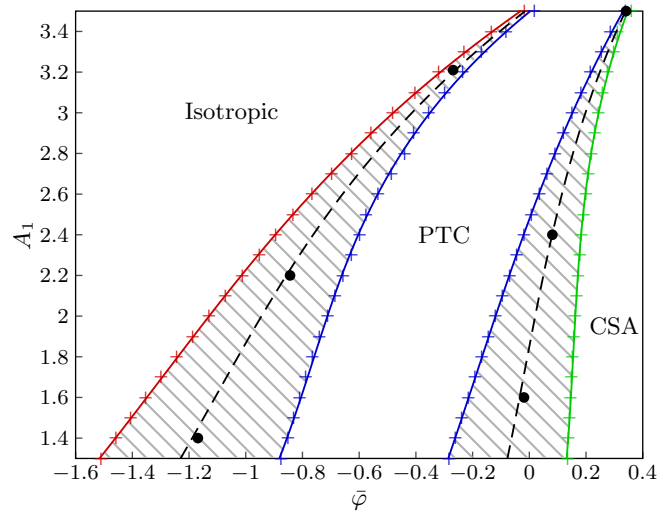
$$
\begin{aligned}
F[\varphi, \mathbf{Q}] = F[\varphi, \mathbf{q}] &= \int A_2 |\Delta \varphi|^2 - A_2 \|\nabla \varphi\|^2 + D_2 \|\nabla \mathbf{q}\|_F^2 + B_3 \langle \nabla \varphi, \vec{\mathbf{\nabla}} \mathbf{q} \rangle_2 + \mathbb{f}(\varphi, \mathbf{q}) \, d\mathbf{x}, \\
&= \frac{1}{2} \int \varphi \varphi^\natural + \langle \mathbf{q}, \mathbf{q}^\natural \rangle_2 + \tilde{\mathbb{f}}(\varphi, \mathbf{q}) \, d\mathbf{x},
\end{aligned}
\tag{3.17}
$$

using the Euclidean norm $\|a\|^2 = \langle a, a \rangle_2$, the Frobenius norm $\|A\|_F^2 = \mathrm{trace}(A^\top A)$, and the differential operator $\vec{\mathbf{\nabla}}$, given by $\vec{\mathbf{\nabla}} \mathbf{q} = \left(\partial_1 q_1 + \partial_2 q_2, \ \partial_1 q_2 - \partial_2 q_1 \right)^\top$. The polynomial parts of the energy are given by

$$
\mathbb{f}(\varphi, \mathbf{q}) = A_1 \varphi^2 - \frac{1}{3} \varphi^3 + \frac{1}{6} \varphi^4 + \left(2D_1 + \frac{1}{2} \varphi(\varphi - 1) \right) \|\mathbf{q}\|^2 + \frac{1}{16} \|\mathbf{q}\|^4
$$

$$
\tilde{\mathbb{f}}(\varphi, \mathbf{q}) = \frac{1}{3} (\varphi^3 - \varphi^4) - \varphi(\varphi - 2) \|\mathbf{q}\|^2.
$$

Dissipative dynamics can be obtained by choosing the dynamical equations (3.10) and the mobility parameters α_1, α_3, and α_4, s.t. $\partial_t F[\varphi, \mathbf{q}] \leq 0$, with

$$
\begin{aligned}
\partial_t F[\varphi, \mathbf{q}] &= \int \partial_t \varphi \varphi^\natural + \langle \partial_t \mathbf{q}, \mathbf{q}^\natural \rangle_2 \, d\mathbf{x} \\
&= -\int 2\alpha_1 \|\nabla \varphi^\natural\|^2 + 4\alpha_3 \langle \nabla \varphi^\natural, \vec{\mathbf{\nabla}} \mathbf{q}^\natural \rangle_2 + 4\alpha_1 \|\vec{\mathbf{\nabla}} \mathbf{q}^\natural\|^2 + 8\alpha_4 \|\mathbf{q}^\natural\|^2 \, d\mathbf{x},
\end{aligned}
$$

Figure 3.3 – *Phase diagram with coexistence regions for the mean density $\bar\varphi \in [-1.6, 0.4]$ and the parameters $A_1 \in [1.3, 3.5]$, $A_2 = 14$, $B_3 = -0.4$, $D_1 = 1$, and $D_2 = 0.8$. Three different liquid-crystalline phases are realized: isotropic, columnar/smectic A (CSA), and plastic triangular crystalline (PTC). The coexistence regions (shaded areas) are calculated using Maxwell's double tangent construction. The black dashed lines in the coexistence regions indicate the intersection lines of the energy curves of the two adjacent phases. Six black circles indicate certain parameter combinations for which detailed calculations were performed (see Figure 3.5–Figure 3.10). The colored crosses correspond to the simulated data to create the diagram.*

where we have used the identity $\int -\langle \vec{\boldsymbol{\nabla}} \mathbf{q}^\natural, \vec{\boldsymbol{\nabla}} \mathbf{q}^\natural \rangle_2 \, d\mathbf{x} = \int \langle \vec{\Delta} \mathbf{q}^\natural, \mathbf{q}^\natural \rangle_2 \, d\mathbf{x}$.

By requiring the Onsager matrix of phenomenological mobility coefficients

$$\begin{bmatrix} 2\alpha_1 & 2\alpha_3 & 0 \\ 2\alpha_3 & 4\alpha_1 & 0 \\ 0 & 0 & 8\alpha_4 \end{bmatrix}$$

to be positive semidefinite, i.e., $\alpha_1, \alpha_4 \geq 0$, and $|\alpha_3| \leq \sqrt{2}\alpha_1$, we get the energy decreasing property.

3.1.4 Results

We first restrict ourselves to certain parameter combinations, which allow for several liquid-crystalline coexistences. In detail, we fix the parameters $A_2 = 14$, $B_3 = -0.4$, $D_1 = 1$, and $D_2 = 0.8$, but vary the parameter A_1 (which corresponds to some formal temperature in the context of mean-field theories) and the reduced mean density $\bar\varphi$.[5] The resulting equilibrium bulk phase diagram is shown in Figure 3.3[6] in consistency with earlier data [3]. In the parameter range of A_1 and $\bar\varphi$ shown, the phase diagram exhibits three stable liquid-crystalline phases, namely, the isotropic phase, a plastic triangular crystal (PTC)[7], and a columnar phase. As we

---

[5]The parameters in the dynamical equations (3.3)–(3.6) are always chosen to be $\alpha_1 = \alpha_3 = \alpha_4 = 1$. Clearly, the stationary results do not depend on their particular values.

[6]A phase diagram that varies also the parameter B_3 was calculated in [250].

[7]The plastic triangular crystal in the phase diagram 3.3 is called "plastic triangular crystal 2" (PTC2) in [3].
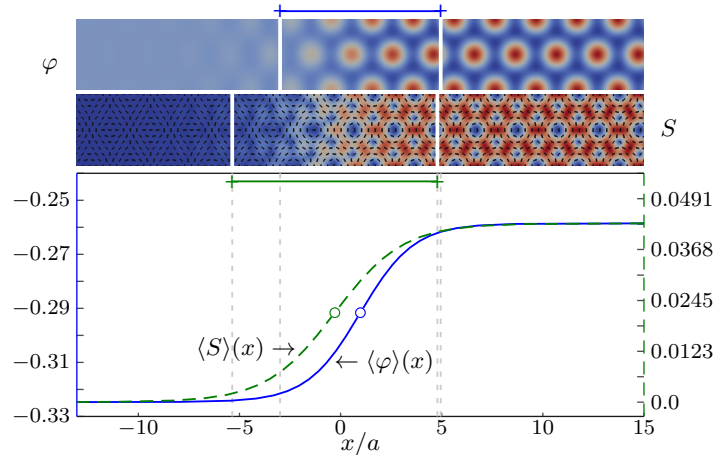
Figure 3.4 – *Top: Two contour plots for $\varphi(x, y)$ and $S(x, y)$ at an isotropic-PTC coexistence with $A_1 = 3.21$ and $\bar{\varphi} = -0.3$ (the other parameters are the same as in Figure 3.3). $\hat{\mathbf{n}}(\mathbf{x})$ is represented by short black lines that are superimposed to the lower contour plot. Bottom: Averaged density $\langle \varphi \rangle(x)$ (left ordinate) and averaged nematic order parameter $\langle S \rangle(x)$ (right ordinate). The x-direction is chosen perpendicular to the interface, while the y-axis is parallel to the interface. The averaged quantities are defined by $\langle f \rangle(x) = \int \mathrm{d}y' \int_{x-a}^{x+a} \mathrm{d}x' \, f(x', y')$ for $f \in \{\varphi, S\}$ with the width of the stripes $2a = 4\pi/(k\sqrt{3})$ and $k = 1/\sqrt{2}$.*

consider two spatial dimensions here, a columnar phase is indistinguishable from a smectic A phase, therefore we call the latter columnar/smectic A (CSA)[8] phase. The coexistence regions, as obtained by a Maxwell double tangent construction, are depicted by the shaded area in Figure 3.3. We selected in total six different coexistence conditions as labeled by black circles in Figure 3.3, which correspond to three isotropic-PTC and three CSA-PTC coexistence situations serving as basic reference situations for our subsequent investigations.

A typical example for an isotropic-PTC interfacial profile is presented in Figure 3.4 for the (10)-orientation of the hexagonal crystal[9]. In the bulk PTC phase, there are periodic peaks in the full density profile $\varphi(x, y)$ at the crystal lattice positions, shown as a contour plot in Figure 3.4. The typical standard deviation of these peaks (the so-called Lindemann parameter) is pretty large with about 27% of the lattice constant. The corresponding orientational ordering as embodied in the nematic tensor is complicated and exhibits topological defects in the Wigner-Seitz cell of the lattice (see [3, 63] for a more detailed discussion). The mean orientational unit vector field $\hat{\mathbf{n}}(x, y)$ as obtained by the direction of the eigenvector of the nematic tensor corresponding to the highest eigenvalue, is sketched by short black lines in Figure 3.4. The largest eigenvalue itself multiplied by 2 – the scalar nematic order-parameter field $S(x, y)$ – is also presented as a contour plot in Figure 3.4. In the isotropic phase, on the other hand, the density field is constant and the nematic order parameter vanishes. In between there is an interfacial region with laterally averaged profiles $\langle \varphi \rangle(x)$ and $\langle S \rangle(x)$ with x denoting the direction perpendicular to the interface (see caption of Figure 3.4).

---

[8]This columnar/smectic A (CSA) phase is called "C/SA phase" in [3].

[9]In our calculations, the one-mode approximation was used to determine the lattice spacing in y-direction. In fact, we found for varied periodicity in y-direction that the free-energy density is minimal for a lattice spacing very close to the one-mode approximation such that the system is practically not strained in y-direction.
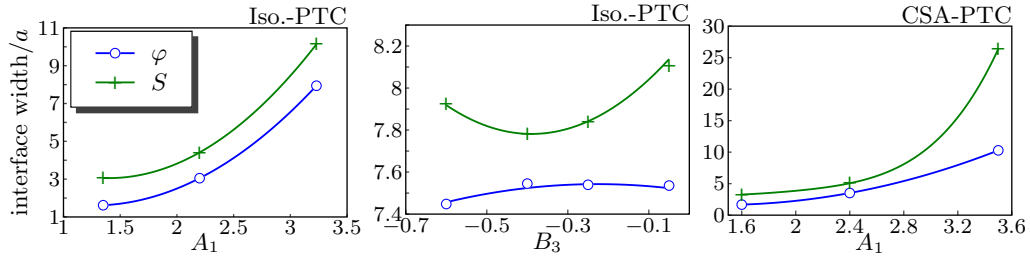
Figure 3.5 – *Left and center: Widths of the isotropic-PTC interfaces of $\varphi(\mathbf{x})$ and $S(\mathbf{x})$ in dependence of A_1 and B_3, respectively. Right: Width of the CSA-PTC interfaces in dependence of A_1. The parameters are (left) $(\bar{\varphi}, A_1) \in \{(-1.2, 1.3), (-0.85, 2.2), (-0.3, 3.21)\}$, (center) $B_3 \in \{-0.6, -0.4, -0.25, -0.05\}$ with fixed $(\bar{\varphi}, A_1) = (-0.3, 3.21)$. The parameters of the right plot are $(\bar{\varphi}, A_1) \in \{(-0.05, 1.6), (0.05, 2.4), (0.31, 3.5)\}$. The remaining parameters are as in Figure 3.3. Notice that the presented data in (left) and (right) correspond to the six points highlighted by black circles in Figure 3.3 and that they are connected by polynomial fitting curves. The stripes of the CSA phase in (right) are oriented perpendicular to the interface (see Figure 3.7).*

We define a typical interface width of an order parameter profile $f(x,y) \in \{\varphi(x,y), S(x,y)\}$ as the distance of the positions, where a `tanh`-approximation of $\langle f \rangle(x)$ attains the values $0.95\langle f\rangle(-\infty) + 0.05\langle f\rangle(\infty)$ and $0.05\langle f\rangle(-\infty) + 0.95\langle f\rangle(\infty)$, respectively. These widths for $\varphi(x,y)$ and $S(x,y)$ are indicated in Figure 3.4. Remarkably, the width of the density profile is significantly smaller than the width of the orientational profile. The position, where the `tanh`-approximation of an averaged field $\langle f \rangle(x)$ with $f \in \{\varphi, S\}$ attains the value $(\langle f\rangle(-\infty) + \langle f\rangle(\infty))/2$ can be taken as a natural location $\xi(f)$ of the interface with respect to this field. Interestingly, as revealed in Figure 3.4, the location of the averaged density profile $\langle\varphi\rangle(x)$ and the averaged orientational profile $\langle S\rangle(x)$ do not coincide. The location of the orientational profile is more shifted towards the isotropic phase than the location of the density profile. This means that coming from the isotropic side, at first the nematic order builds up and then the density follows. This finding is reminiscent to the fluid-crystal interface of systems of spherical particles [162, 110], which can be described by a two-order-parameter description involving the conserved mean density and a non-conserved crystallinity [156, 157]. Coming from the fluid side, also in this case, the non-conserved crystallinity starts to grow first and the density follows.

We have further studied the dependence of the interface widths on the parameters A_1 and B_3. As A_1 is increased, the coexistence comes closer to a critical point where the interfacial widths diverge. This trend is documented in Figure 3.5(left).

Figure 3.5(left) also shows that the width of the orientational order-parameter profile is larger than that of the density interface over the full range of A_1. All trends are the same for different parameter combinations for the isotropic-PTC interface, as documented by Figure 3.6. The dependence of the interface width on the parameter B_3 as shown in Figure 3.5(center) is much less pronounced than the dependence on the parameter A_1. Interestingly, the interface width of the orientational order-parameter profile is again larger than the width of the density interface. The trend of the curves indicates that this behavior holds also for a larger parameter interval of B_3 than plotted in Figure 3.5(center). However, due to the huge parameter space and high computational complexity of the calculations we cannot rule out the possibility that there is a certain combination of the five parameters of the PFC model, where the interface width for

$$\bar{\varphi} = -1.2, \ A_1 = 1.35 \qquad\qquad\qquad \bar{\varphi} = -0.3, \ A_1 = 3.21$$
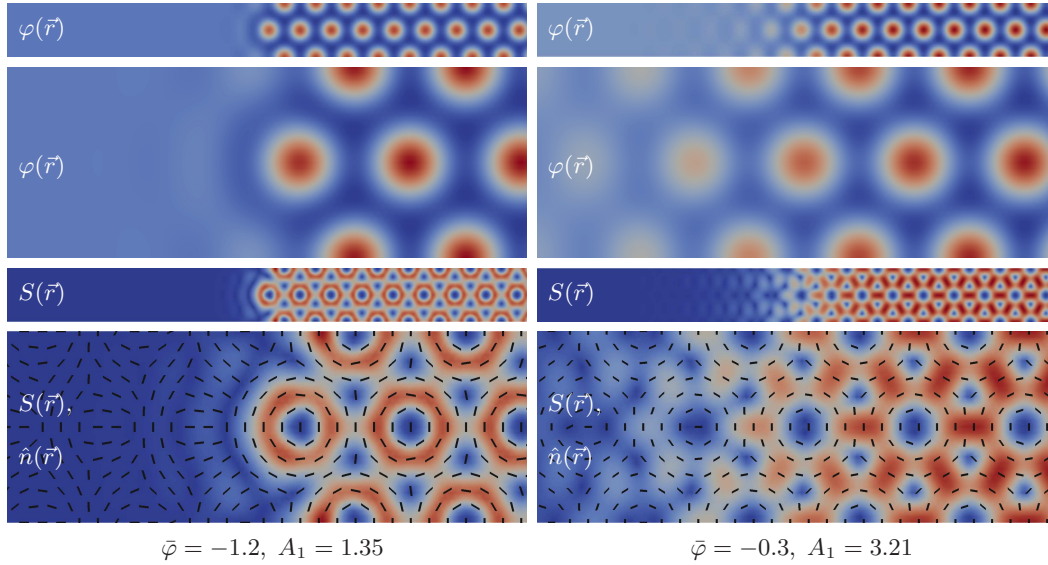
Figure 3.6 – *Interface of the isotropic-PTC phase coexistence for the same parameters as in Figure 3.3. The plots show the translational density $\varphi(\mathbf{x})$ and the nematic order parameter $S(\mathbf{x})$ both for a large area and for a close-up view of the interface, where blue and red indicate low and high values, respectively. In addition, the director field $\hat{\mathbf{n}}(\mathbf{x})$ is represented by short black lines that are superimposed to the lowest plots.*

the orientational order-parameter profile is not larger than for the density profile.

Next, we consider the coexistence between the PTC and the CSA phase. In this case, the interface structure depends on the relative orientations of the two phases. While we fix the orientation of the PTC phase in the (10)-direction, we consider here two different possibilities of the column direction relative to the interface, namely perpendicular and parallel. For these two relative orientations, the order-parameter fields are given in Figure 3.7 and Figure 3.8 for two different parameter combinations of coexistence[10]. For perpendicular column direction (see Figure 3.7), the density field reveals that the columns end at a lattice density peak. This implies that the degeneracy of the column positions is broken by the presence of the crystal, which pins the transversal columnar order by the interface. Along the columns away from the interface, there are still some density undulations in x-direction. For parallel column direction (see Figure 3.8), on the other hand, there is a nontrivial density field across the interface insofar as the columns are significantly bent in the presence of the crystalline peaks, i.e., the crystal induces a systematic undulation of the neighboring columns. The amplitude of this undulation decreases farer away from the interface position. Likewise, along the columns there is a periodic density modulation in y-direction induced by the crystalline peaks nearby.

Results for the interfacial widths, similarly defined as in the previous case, are shown in Figure 3.5(right), where the same trends are observed as for the isotropic-PTC interface (see

---

[10]It is important to note that in Figure 3.7 the interface connects two phases which have in principle different periodicities in y-direction. Therefore, care has to be taken in determining the box size in y-direction, in particular if these two periodicities are incommensurate. We have checked that a doubled system size in y-direction does not affect the results. Nevertheless, a much larger system size could possibly lead to superstructures which are not explored here.

$$\bar{\varphi} = -0.05, \ A_1 = 1.6 \qquad\qquad \bar{\varphi} = 0.31, \ A_1 = 3.5$$
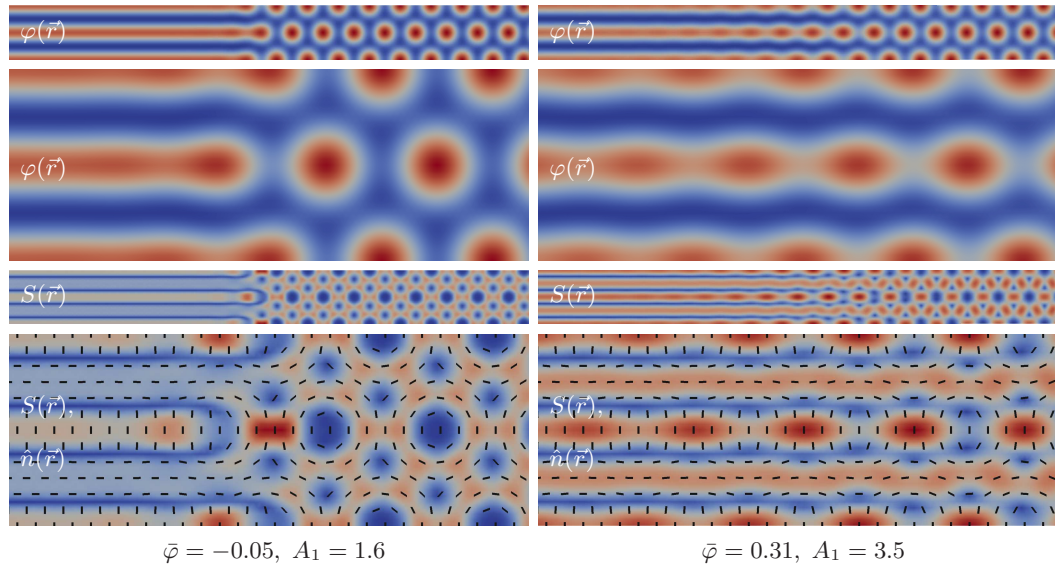
Figure 3.7 – *The same as in Figure 3.6, but now for the CSA-PTC interface. Note that the stripes of the CSA phase are oriented perpendicular to the interface.*

$$\bar{\varphi} = -0.05, \ A_1 = 1.6 \qquad\qquad \bar{\varphi} = 0.31, \ A_1 = 3.5$$
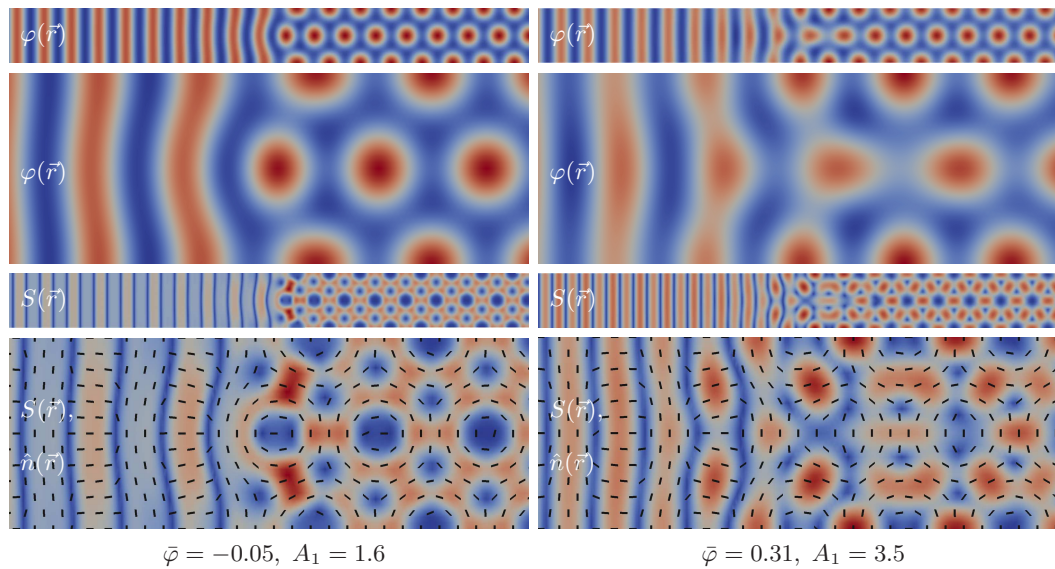
Figure 3.8 – *The same as in Figure 3.7, but now for a CSA-PTC interface, where the stripes of the CSA phase are oriented parallel to the interface.*
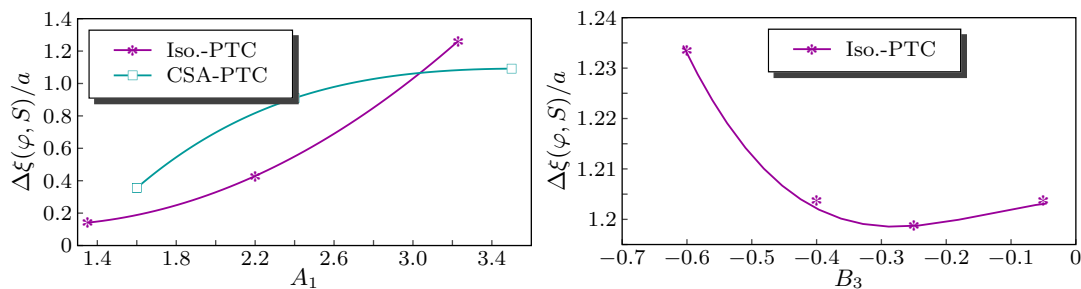
Figure 3.9 – Distance $\Delta\xi(\varphi, S) = \xi(\varphi) - \xi(S)$ of the interfaces of $\varphi(\mathbf{x})$ and $S(\mathbf{x})$ in dependence of (left) A_1 and (right) B_3, where we always consider the transition from the non-crystalline to the crystalline phase. The parameters are the same as in Figure 3.5 and the stripes of the CSA phase are again oriented perpendicular to the interface (see Figure 3.7).

Figure 3.10 – Time evolution of the averaged order parameters (left) $\langle\varphi\rangle(x)$ and (right) $\langle S\rangle(x)$ for an isotropic-PTC coexistence. The parameters are $\alpha_1 = \alpha_3 =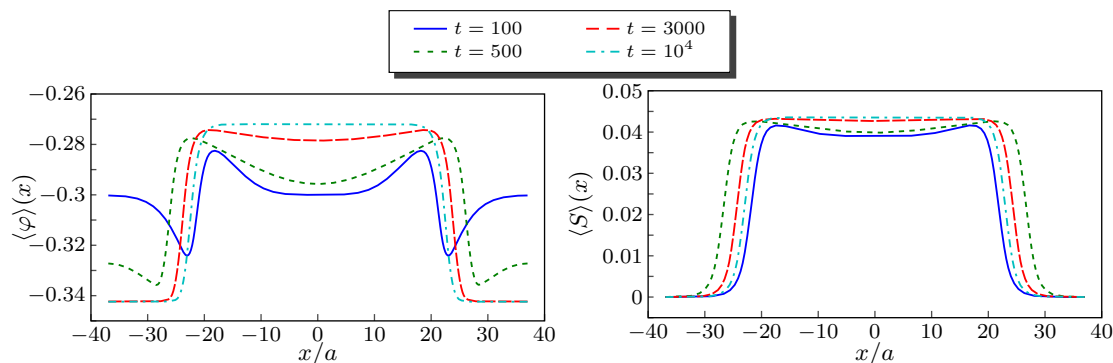 \alpha_4 = 1$, $\bar{\varphi} = -0.3$, $A_1 = 3.21$ and for the rest as in Figure 3.3. Snapshots are taken at times $t = 100, 500, 3000$, and 10000. At time $t = 0$ the averaged translational density is constant ($\langle\varphi\rangle(x) = -0.3$) and the averaged nematic order parameter $\langle S\rangle(x)$ is a smeared Heaviside step function.

Figure 3.5(left)). The width of the orientational interface is considerably larger than that for the density profile and there is a strong dependence on the parameter A_1 with huge interfacial widths, where the parameter is close to criticality. Both for the isotropic-PTC coexistence and for the CSA-PTC coexistence, the interface position of the density profile is more shifted towards the PTC phase than the interface position of the orientational profile, which is more in the coexisting CSA phase (see Figure 3.9). As shown in Figure 3.9, the distance of the two interface positions depends on the parameters A_1 and B_3.

Finally, we show some results on the dynamical evolution of the interfacial profiles based on the physical dynamics described by equations (3.3) and (3.4). It is important to note that the density is a conserved order parameter, while the nematic ordering is non-conserved. We plotted an example of the interface relaxation towards equilibrium for a prescribed starting profile in Figure 3.10. The orientational order-parameter field is a smeared Heaviside step function, while the density is constant. Similar setups for interfacial kinetics have been studied earlier [158]. The density field subsequently takes up the orientational inhomogeneity and both order

parameters relax to their equilibrium profiles. The density develops a marked transient non-monotonic profile and relaxes much slower than the orientational order. It takes quite a long time in units of the basic time scale of the dimensionless dynamical equations (3.3)–(3.6) to end up in the final equilibrium state. These findings show that our dynamical equations (3.3) and (3.4), which reflect the diffusive dynamics of colloidal systems, can in principle be applied to plenty of further growth phenomena in the future.

3.1.5 Conclusions

In conclusion, we have explored the equilibrium structure of interfaces between various coexisting liquid-crystalline phases using a PFC model for liquid crystals. In two spatial dimensions, we have considered explicitly the isotropic-plastic crystalline and the smectic A-plastic crystalline interface, which are both anisotropic, i.e., they depend on the relative orientation of the two coexisting phases. To determine the equilibrium structures numerically, we calculated the relaxation of the dissipative PFC dynamics towards equilibrium (i.e., the minimization of the PFC functional) under the constant-mobility approximation using the finite-element method.

Basically, we have considered a two-order-parameter description of the interfaces containing the conserved (translational) density field and the non-conserved (orientational) nematic tensor. The phase diagram, the typical widths of the interfaces, the order-parameter profiles, and their dynamics were computed. For the isotropic-plastic crystalline interface we found that in approaching the interface from the isotropic side, at first the nematic order builds up and then the density follows. The relative shift of the two profiles is about half the lattice constant of the plastic crystal. This finding is reminiscent to the fluid-crystal interface of systems of spherical particles [162, 110], which can be described by a two-order-parameter description involving the conserved mean density and a non-conserved crystallinity [156, 157]. For the fluid-crystal interface, a similar shift has been found: if the interface is approached from the fluid side, first the (non-conserved) crystallinity increases and then the (conserved) mean density follows [156, 155, 184, 183]. This has to do with the fact that a fluid is more responsive to an oscillatory density wave than to a global density change [155]. For the smectic A-plastic crystalline interface we found a similar behavior as for the isotropic-plastic crystalline interface with a shift of the density interface towards the plastic crystalline phase. Furthermore, our results show that in the whole parameter range we explored the width of the interface with respect to the nematic order parameter is larger than the width of the mean density interface.

Our results can be verified either in particle-resolved computer simulations [121] or in experiments. Particle-resolved computer simulations for rod-like systems have been performed both for structure [61, 46, 6, 167] and dynamics [153, 135] in various situations. So far experiments are concerned, most notably colloidal liquid crystals [276, 69, 143] that are confined to two spatial dimensions are ideal realizations of our model. One important example is a suspension of the tobacco mosaic virus, which can be confined to monolayers [277] and which shows a variety of liquid-crystalline phases [106], but there are more other examples of liquid-crystalline rod-like particle suspensions, which have been prepared in a controlled way (see, e.g., [220, 263, 62]).

Future work should extend the present study to three spatial dimensions [282, 85], which would require more numerical work but promises a richer equilibrium bulk phase diagram. Also the dynamics of a growing crystalline front, which has been studied for spherical particles already in detail [227, 252, 218], should be addressed for liquid crystals as well. If a plastic

crystalline phase grows into an isotropic phase, it would be interesting to follow the origin of topological defects in the director field, which have to grow out of nothing [11]. Moreover, crystal-fluid interfaces in external fields like gravity exhibit unusual effects already for isotropic particles [42, 13] and it would be challenging to explore this for liquid-crystalline interfaces [168]. Finally, our model should be generalized towards liquid crystals on manifolds [181] to describe nematic [77] or smectic bubbles [171].

3.2 The Polar Liquid-Crystal PFC model

In [284, 283] a Phase-Field Crystal model for polar liquid crystals was proposed. In contrast to the apolar liquid crystals considered so far, these systems are described by an additional field variable $\mathbf{p}$, namely the polar order. This is an oriented vector field driven by rotational and translational diffusion of its thermodynamic conjugate $\mathbf{p}^\natural$, given by the functional derivative of a corresponding free-energy functional.

This static free-energy is formulated in dimensionless form [283] following the notation of equation (3.17):

$$
\begin{aligned}
F[\varphi, \mathbf{p}, \mathbf{q}] &= \int A_2 |\Delta\varphi|^2 - A_2 \|\nabla\varphi\|^2 + C_2 \|\nabla\mathbf{p}\|_F^2 - C_2 (\nabla\cdot\mathbf{p})^2 + D_2 \|\nabla\mathbf{q}\|_F^2 \\
&\quad + B_1 \langle\nabla\varphi, \mathbf{p}\rangle_2 + B_2 \langle\mathbf{p}, \vec{\blacktriangledown}\mathbf{q}\rangle_2 + B_3 \langle\nabla\varphi, \vec{\blacktriangledown}\mathbf{q}\rangle_2 + \mathbb{f}(\varphi, \mathbf{p}, \mathbf{q})\, d\mathbf{x} \\
&= \frac{1}{2}\int \varphi\varphi^\natural + \langle\mathbf{p}, \mathbf{p}^\natural\rangle_2 + \langle\mathbf{q}, \mathbf{q}^\natural\rangle_2 + \tilde{\mathbb{f}}(\varphi, \mathbf{p}, \mathbf{q})\, d\mathbf{x}
\end{aligned}
\tag{3.18}
$$

with

$$
\begin{aligned}
\mathbb{f}(\varphi, \mathbf{p}, \mathbf{q}) &= A_1\varphi^2 - \frac{1}{3}\varphi^3 + \frac{1}{6}\varphi^6 + C_1\|\mathbf{p}\|^2 + 2D_1\|\mathbf{q}\|^2 + \frac{1}{16}(\|\mathbf{p}\|^4 + \|\mathbf{q}\|^4) \\
&\quad + \frac{1}{2}(\|\mathbf{p}\|^2 + \|\mathbf{q}\|^2)(\varphi^2 - \varphi) + \frac{1}{4}\mathbf{p}^\top\mathbf{Q}\mathbf{p}(2\varphi - 1) + \frac{1}{4}\|\mathbf{p}\|^2\|\mathbf{q}\|^2\ , \\
\tilde{\mathbb{f}}(\varphi, \mathbf{p}, \mathbf{q}) &= \frac{1}{3}(\varphi^3 - \varphi^4) - \frac{1}{8}(\|\mathbf{p}\|^4 + 4\|\mathbf{p}\|^2\|\mathbf{q}\|^2 + \|\mathbf{q}\|^4) \\
&\quad - \frac{1}{2}(\|\mathbf{p}\|^2 + \|\mathbf{q}\|^2)(2\varphi^2 - \varphi) + \frac{1}{4}\mathbf{p}^\top\mathbf{Q}\mathbf{p}(\varphi - 1).
\end{aligned}
\tag{3.19}
$$

In [283] the dynamical equations for $\varphi, \mathbf{p}$, and $\mathbf{q}$ were formulated to fulfill the Onsager reciprocal relations. In the constant mobility approximation the equations read

$$
\begin{aligned}
\partial_t\varphi &= 2\alpha_1\Delta\varphi^\natural + 2\alpha_3\blacktriangle_i q_i^\natural \\
\partial_t\mathbf{p} &= 2\alpha_2\vec{\Delta}\mathbf{p}^\natural + 4\alpha_3\nabla(\nabla\cdot\mathbf{p}^\natural) - 2\alpha_4\mathbf{p}^\natural \\
\partial_t\mathbf{q} &= 4\alpha_1\vec{\Delta}\mathbf{q}^\natural + 2\alpha_3\blacktriangle\varphi - 8\alpha_4\mathbf{q}^\natural
\end{aligned}
\tag{3.20}
$$

with the thermodynamic conjugates following from functional differentiation of F,

$$
\begin{aligned}
\varphi^\natural &= f_\varphi(\varphi, \mathbf{p}, \mathbf{q}) + 2A_1\varphi + 2A_2(\Delta + \Delta^2)\varphi - B_1(\nabla\cdot\mathbf{p}) - B_3\blacktriangle_i q_i\ , \\
\mathbf{p}^\natural &= f_\mathbf{p}(\varphi, \mathbf{p}, \mathbf{q}) + 2C_1\mathbf{p} + 2C_2\vec{\Delta}\mathbf{p} - 2C_2\nabla(\nabla\cdot\mathbf{p}) + B_1\nabla\varphi + B_2\vec{\blacktriangledown}\mathbf{q}\ , \\
\mathbf{q}^\natural &= f_\mathbf{q}(\varphi, \mathbf{p}, \mathbf{q})i + 4D_1\mathbf{q} - 2D_2\vec{\Delta}\mathbf{q} - B_2\nabla*\mathbf{p} - B_3\blacktriangle\varphi.
\end{aligned}
\tag{3.21}
$$

---

[11]In [250] some of these questions were answered.

The derivative $\nabla*$ denotes the adjoint operator to $\vec{\blacktriangledown}$, i.e., $\nabla * \mathbf{p} := \left(\partial_1 p_1 - \partial_2 p_2, \, \partial_1 p_2 + \partial_2 p_1 \right)^\top$. Nonlinear terms arising from differentiation of the polynomial f and $\tilde{f}$ can be found,

$$\partial_\varphi f =: f_\varphi(\varphi, \mathbf{p}, \mathbf{q}) = -\varphi^2 + \frac{2}{3}\varphi^3 + \frac{1}{2}\mathbf{p}^\top \mathbf{Q}\mathbf{p} + \frac{1}{2}(2\varphi - 1)(\|\mathbf{q}\|^2 + \|\mathbf{p}\|^2) \, ,$$

$$\partial_\mathbf{p} f =: f_\mathbf{p}(\varphi, \mathbf{p}, \mathbf{q}) = \varphi(\varphi - 1)\mathbf{p} + \frac{1}{4}(\|\mathbf{p}\|^2 + 2\|\mathbf{q}\|^2)\mathbf{p} + \frac{1}{2}(2\varphi - 1)\mathbf{Q}\mathbf{p} \, , \qquad (3.22)$$

$$\partial_\mathbf{q} f =: f_\mathbf{q}(\varphi, \mathbf{p}, \mathbf{q}) = \varphi(\varphi - 1)\mathbf{q} + \frac{1}{4}(\|\mathbf{q}\|^2 + 2\|\mathbf{p}\|^2)\mathbf{q} + \frac{1}{4}(2\varphi - 1)\mathbf{p} * \mathbf{p},$$

using the product $*$ defined as $\mathbf{p} * \mathbf{p} := (p_1^2 - p_2^2, \, 2p_1 p_2)^\top$. The $*$ operator relates the differential operator $\blacktriangle$ to the gradient, via $\blacktriangle = \nabla * \nabla$ and the vector Laplacian $\vec{\Delta}$ to the vector gradient $\vec{\blacktriangledown}$, via $\vec{\Delta} = \nabla * \vec{\blacktriangledown}$.

In order to guaranty dissipative dynamics, the parameters $\alpha_1, \alpha_2, \alpha_3$, and α_4 must be chosen to form a positive (semi-) definite Onsager matrix, as in Section 3.1.3. The time-derivative of the energy reads

$$\partial_t F[\varphi, \mathbf{p}, \mathbf{q}] = \int \partial_t \varphi \varphi^\natural + \langle \partial_t \mathbf{p}, \mathbf{p}^\natural \rangle_2 + \langle \partial_t \mathbf{q}, \mathbf{q}^\natural \rangle_2 \, \mathrm{d}\mathbf{x}$$

$$= -\int 2\alpha_1 \|\nabla \varphi^\natural\|^2 + 4\alpha_3 \langle \nabla \varphi^\natural, \vec{\blacktriangledown} \mathbf{q}^\natural \rangle_2 + 4\alpha_1 \|\vec{\blacktriangledown} \mathbf{q}^\natural\|^2 + 8\alpha_4 \|\mathbf{q}^\natural\|^2$$

$$+ 2\alpha_2 \|\vec{\blacktriangledown} \mathbf{p}\|^2 + 4\alpha_3 (\nabla \cdot \mathbf{p}^\natural)^2 + 4\alpha_4 \|\mathbf{p}^\natural\|^2 \, \mathrm{d}\mathbf{x}.$$

Thus, we now require $\alpha_1, \alpha_2, \alpha_3, \alpha_4 \geq 0$, and $\alpha_3 \leq \sqrt{2}\alpha_1$, to ensure $\partial_t F \leq 0$.

3.2.1 Numerical discretization

The evolution equations (3.20) for the three fields $\varphi, \mathbf{p}$, and $\mathbf{q}$ can discretized in time using an operator-splitting approach and a semi-implicit backward Euler discretization. This leads to a three step procedure:

Step 1:

$$\frac{1}{\tau_k}\varphi_{k+1} = \frac{1}{\tau_k}\varphi_k + 2\alpha_1 \Delta \varphi^\natural_{k+1} + 2\alpha_3 \blacktriangle \cdot \mathbf{q}^\natural_k$$

$$\varphi^\natural_{k+1} = f_\varphi(\varphi_{k+1}, \mathbf{p}_k, \mathbf{q}_k) + 2A_1 \varphi_{k+1} + 2A_2(\Delta + \Delta^2)\varphi_{k+1} - B_1(\nabla \cdot \mathbf{p}_k) - B_3 \blacktriangle \cdot \mathbf{q}_k \, ,$$

Step 2:

$$\frac{1}{\tau_k}\mathbf{p}_{k+1} = \frac{1}{\tau_k}\mathbf{p}_k + 2\alpha_2 \vec{\Delta}\mathbf{p}^\natural_{k+1} + 4\alpha_3 \nabla(\nabla \cdot \mathbf{p}^\natural_{k+1}) - 2\alpha_4 \mathbf{p}^\natural_{k+1}$$

$$\mathbf{p}^\natural_{k+1} = f_\mathbf{p}(\varphi_{k+1}, \mathbf{p}_{k+1}, \mathbf{q}_k) + 2C_1 \mathbf{p}_{k+1} + 2C_2 \vec{\Delta}\mathbf{p}_{k+1} - 2C_2 \nabla(\nabla \cdot \mathbf{p}_{k+1}) + B_1 \nabla \varphi_{k+1} + B_2 \vec{\blacktriangledown}\mathbf{q}_k \, ,$$

Step 3:

$$\frac{1}{\tau_k}\mathbf{q}_{k+1} = \frac{1}{\tau_k}\mathbf{q}_k + 4\alpha_1 \vec{\Delta}\mathbf{q}^\natural_{k+1} + 2\alpha_3 \blacktriangle \varphi_{k+1} - 8\alpha_4 \mathbf{q}^\natural_{k+1}$$

$$q^\natural_{k+1} = f_\mathbf{q}(\varphi_{k+1}, \mathbf{p}_{k+1}, \mathbf{q}_{k+1}) + 4D_1 \mathbf{q}_{k+1} - 2D_2 \vec{\Delta}\mathbf{q}_{k+1} - B_2 \nabla * \mathbf{p}_{k+1} - B_3 \blacktriangle \varphi_{k+1} \, ,$$

φ $\|\mathbf{p}\|$, $\mathbf{p}$ S, $\hat{\mathbf{n}}$
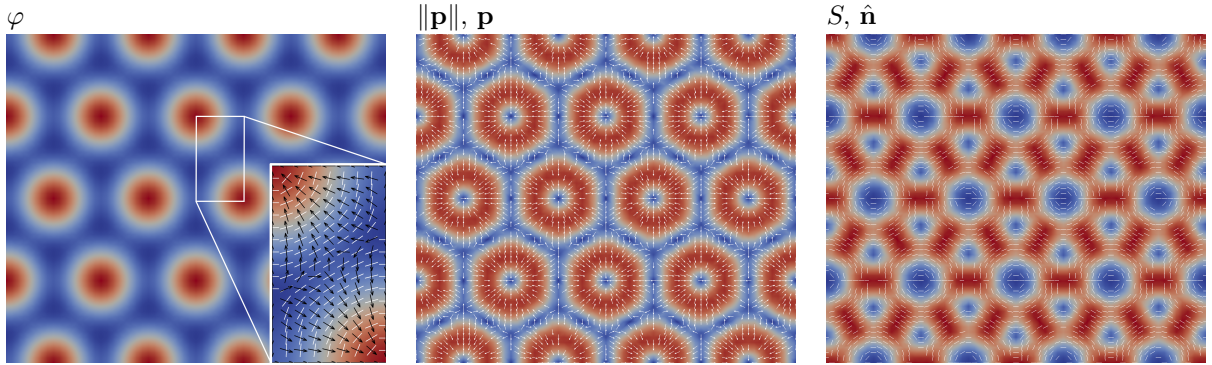
Figure 3.11 – *Order-parameter fields of a plastic triangular phase PTC3. Left: Translational density φ, Center: Norm and direction of the polarization field $\mathbf{p}$. Right: Orientational order-parameter S and director $\hat{\mathbf{n}}$. The polarization points toward the maxima in the density field and is orthogonal to the director field. Parameters used in the simulation: $\bar{\varphi} = 0$, $A_1 = 3$, $A_2 = 14$, $B_1 = -1$, $B_2 = -1$, $B_3 = -0.4$, $C_1 = 0$, $C_2 = -1$, $D_1 = 1$, $D_2 = 0.8$. The inlet in the left image shows the polarization vector (black) and nemati director (white) in detail.*

where the non-linear terms f_φ, $f_\mathbf{p}$ and $f_\mathbf{q}$ can be approximated by a first order Taylor-expansion.

This procedure allows to implement a PFC preconditioner for the solution of the first step, neglecting all coupling terms and the non-linear term. The equations in step 2 and 3 behave better in numerical tests, when a BiCGStab(ℓ) [237] is applied, than the PFC equation in step 1. Thus, we can apply this iterative method directly or use standard precondition-techniques.

3.2.2 Computational results

In order to test the polar liquid crystal PFC model, we have set up a parameter study to find classical phases. Presented in the following are 4 two-dimensional reference phases that involve non-trivial order in all the order-parameters. We have found a plastic triangular phase (PTC3)[12], a plastic square crystal phase (PSC3) and two columnar phases (CSA3 and CSA3a). The phases of the apolar liquid crystal PFC model can be reproduced as well, since by setting the coupling parameters B_1 and B_2 to zero, we obtain basically the apolar model.

In Figure 3.11 the PTC3 configuration is shown. The density builds a stable hexagonal pattern that is also highlighted by the norm of the polarization field in the center image. The polarization vector field is oriented along the gradients of the density field and thus points toward the maxima. There, the vector field forms an aster defect. This gives, in equilibrium, a vanishing effective net polarization. The orientational order-parameter S has the form similar to the PTC2 phase with minima on the density maxima. The director $\hat{\mathbf{n}}$ forms a vortex defect on the density maxima, surrounded by six disclination defects.

Figure 3.12 shows a square crystal phase PSC3. The polarization vector in the center image points to the center of the maxima and forms a sink defect, surrounded by four source defects

---

[12]In Ref. [3] two plastic triangular phases are shown, the PTC1, that involves only translational order, and the PTC2 phase, that has translational and orientational order. The naming PTC3 comes from the fact that we have three involved fields.

φ $\|\mathbf{p}\|$, $\mathbf{p}$ S, $\hat{\mathbf{n}}$
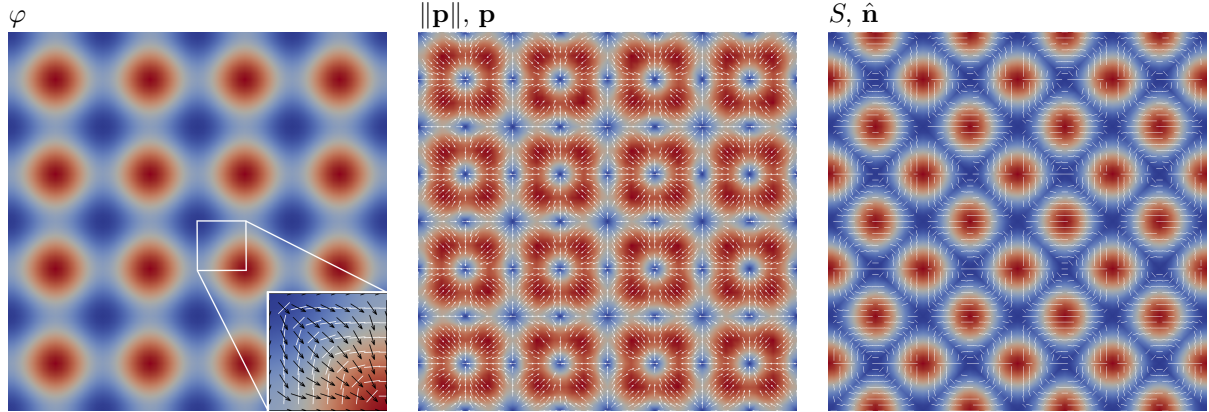
Figure 3.12 – *Order-parameter fields of a plastic square crystal phase PSC3. Left: Translational density φ, Center: Norm and direction of the polarization field $\mathbf{p}$. Right: Orientational order-parameter S and director $\hat{\mathbf{n}}$. The polarization points toward the maxima in the density field. Parameters used in the simulation: $\bar{\varphi} = 0.1$, $A_1 = 1.5$, $A_2 = 14$, $B_1 = -1$, $B_2 = -1$, $B_3 = -4$, $C_1 = 0$, $C_2 = -1$, $D_1 = -0.2$, $D_2 = 8$. The inlet in the left image shows the polarization vector (black) and nemati director (white) in detail.*

and four hedgehog defects. The topological defects of the director $\hat{\mathbf{n}}$ are shown in the right image of Figure 3.12, i.e., a vortex defect on the density maxima, surrounded by four hedgehog defects. The structure of the orientational order-parameter forms a square pattern, but rotated by $\pi/2$ compared to the translational density pattern.

The structure of the polarization field in Figure 3.13 is qualitatively similar to both, the PTC3 and the PSC3 phase, i.e., the polarization vectors point to the maxima in the density field, that is, to the maxima of the density stripes. On the stripes and between stripes the vector field has a line-defect to allow for a flip of the direction. On the stripes the polarization thus forms a sink line-defect and between the stripes a source line-defect. On the stripes the director $\hat{\mathbf{n}}$ is ordered and oriented perpendicular to the stripes direction.

In constrast to the former phases another stripe phase, here called CSA3a, has a different structure in the director and polarization (see Figure 3.14). The vector $\mathbf{p}$ points along the stripes direction, on high density values φ the direction $\mathbf{p}$ points to the left and for low density values $\mathbf{p}$ points to the right. In between, $\mathbf{p}$ switches its direction smoothly. Also the director $\hat{\mathbf{n}}$ changes schmoothly from perpendicular to the stripes direction on high density values to parallel to the stripes direction on low density values. Thus, there is no line defect in the director and the polarization, respectively. The colors in the right image of Figure 3.14 show misleadingly regions with high and low order-parameter S. The scaling of these values shows, that S is nearly constant in the domain.

3.2.3 Conclusion

The polar liquid crystal PFC model was formulated, discretized and solved using finite-elements in space and a time discretization similar to the scheme introduced in Section 3.1.2 for the apolar liquid crystal model. Evolution equations for the polarization as third order-parameter
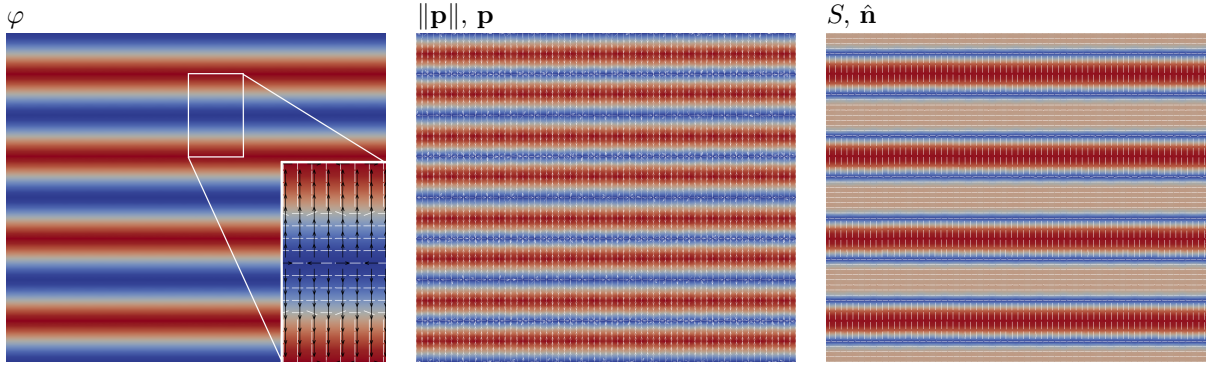
Figure 3.13 – *Order-parameter fields of a columnar and smectic A phase CSA3. Left: Translational density φ, Center: Norm and direction of the polarization field $\mathbf{p}$. Right: Oientational order-parameter S and director $\hat{\mathbf{n}}$. The polarization points toward the maxima-line in the density field. Parameters used in the simulation: $\bar{\varphi} = 0.1$, $A_1 = 1.5$, $A_2 = 14$, $B_1 = -1$, $B_2 = -1$, $B_3 = -0.4$, $C_1 = 0$, $C_2 = -1$, $D_1 = 1$, $D_2 = 0.8$. The inlet in the left image shows the polarization vector (black) and nemati director (white) in detail.*
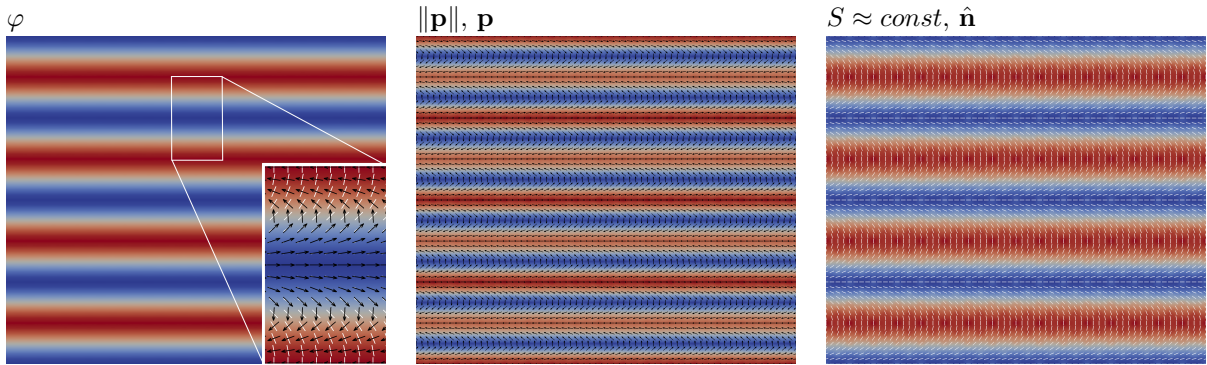
Figure 3.14 – *Order-parameter fields of second columnar phase: CSA3a. Left: Translational density φ, Center: Norm and direction of the polarization field $\mathbf{p}$. Right: Orientational order-parameter S and director $\hat{\mathbf{n}}$. The polarization points in the direction of the stripes in the density field. Thus, on the stripes the polarization is orthogonal to the director and within the stripes its parallel to the director $\hat{\mathbf{n}}$. Parameters used in the simulation: $\bar{\varphi} = 0.1$, $A_1 = 1.5$, $A_2 = 14$, $B_1 = -1$, $B_2 = -1$, $B_3 = -0.4$, $C_1 = 0$, $C_2 = -1$, $D_1 = -2$, $D_2 = 0.8$. The inlet in the left image shows the polarization vector (black) and nemati director (white) in detail.*

field extend the coupled system (3.16) by an additional block for the terms related to $\mathbf{p}$ and $\mathbf{p}^{\natural}$. Similar to the apolar case, the systems were either solved using an operator splitting approach by solving the PFC part, Q-tensor part, and polarization part, in rotation or by assembling a full system that involves all couplings introduced by the polynomials $f_{\varphi}, f_{\mathbf{p}}$, and $f_{\mathbf{q}}$, by the terms with prefactor $B_{1,2,3}$ in the free-energy and by the dynamical equations in the terms with prefactor α_3.

A preconditioner for the PFC part of the linear system can be formulated in a similar fashion as before, by neglecting the coupling terms. This leads to the preconditioner matrix $\mathbf{P}$ in (1.15) or the matrix that involves a mobility parameter $M_0 \equiv 2\alpha_1$ in (2.45) or (2.46) respectively.

We have shown that this solution strategy leads to meaningful solutions of the polar liquid crystal system, by examining three phases, the PTC3 phase, the PSC3 phase, and a CSA3 stripe phase. All these phases have in common, that the polarization vector points toward the density maxima and is often parallel, or perpenticular to the nematic director $\hat{\mathbf{n}}$ on high density values. A fourth phase, here called CSA3a, shows another stripe solution with different orientational and polar order-parameter, i.e., without line-defects as in the CSA phase.

In [176, 177] a simplified polar PFC model was extended by an activity parameter that drives the system out of equilibrium and was shown to act as a minimal model to describe traveling crystals and traveling lamella. More advanced polarization models combined with a density diffusion or a phase-field evolution, cf. [1, 169], have shown to be attractive descriptions for some active systems. A combination of polar order and nematic order for active systems (see e.g. [164, 37]) may be simulated using the polar liquid crystal PFC model combined with an appropriate descriptions of an active source term. Density variations combined with orientational order is also an active field of research, e.g., in the context of active smectics [5, 57]. This may be considered in future work.

Phase-Field Crystal model in non-regular domains

$\mathbb{I}$ N the previous chapters we have solved the Phase-Field Crystal equation and its variants in a rectangular domain. The strength of the finite-element method comes into effect when considering adaptive or non-rectangular domains and for surface triangulations. Thus, we consider these cases and study the impact on the preconditioner. Therefore, two reference problems are solved, a surface PFC problem and the PFC equation in an evolving domain.

The first example in Section 4.1 considers the Phase-Field Crystal equation solved on a spherical surface that acts as a model system to find the optimal distribution of isotropic particles on the sphere. Various discretization methods exist to solve differential equations on manifolds, e.g., surface finite-differences, discrete exterior calculus, surface finite-elements and spherical spectral methods based on spherical harmonics. All these methods use an explicit description of the surface. We focus on the surface finite-element approach. Another ansatz, considered in Section 4.2 is based on an implicit description of the surface, using a phase-field variable. This method was compared to a surface finite-element and a spectral method in the published paper [28]. To numerically solve the arising linear systems in the implicit method, we apply the preconditioner developed in Chapter 1 and analyze the properties depending on some model parameters.

In Section 4.3 we develop a model to describe interacting particles in an evolving confinement. The moving domain is described implicitly by a phase-field variable and the interacting particles by a Navier-Stokes PFC model, as introduced in Section 2.2. A cluster of soft colloidal particles, restricted to a deformable droplet that applies a force on the crystal, shows slip of particle layers along each other. On the other hand, the arranging crystal applies a force to the droplet interface. The coupled system of equations is discretized using finite-elements and solved block-wise, involving the developed PFC preconditioner.

4.1   Discrete Ordering on the sphere

The centennial of Hilbert's announcement of his mathematical problems for the 20th century was the natural occasion to propose a "new set of Hilbert problems". One of these problems proposed by Smale [238] asks about the distribution of N points on a sphere. Let

$$V_N(\vec{\mathbf{x}}) = \sum_{1 \leq i < j \leq N} 1/\|\mathbf{x}_i - \mathbf{x}_j\|^q, \quad \text{and} \quad V_N = \min_{\vec{\mathbf{x}}} V_N(\vec{\mathbf{x}}) \tag{4.1}$$

with $\vec{\mathbf{x}} = (\mathbf{x}_1, \dots, \mathbf{x}_N)$, $\mathbf{x}_i$ distinct points on the 2-sphere $\mathbb{S}^2$, $\|\mathbf{x}_i - \mathbf{x}_j\|$ the distance in $\mathbb{R}^3$, and $q \in \mathbb{N}_+$. The problem is to find

$$\vec{\mathbf{x}}, \quad \text{s.t.} \quad V_N(\vec{\mathbf{x}}) - V_N \leq C \log N \tag{4.2}$$

with C an universal constant. The corresponding problem related to the case $q = 0$ with $V_N(\vec{\mathbf{x}}) = -\sum_{1 \leq i < j \leq N} \log \|\mathbf{x}_i - \mathbf{x}_j\|$ is related to finding a good starting polynomial for a homotopy algorithm for realizing the fundamental theorem of algebra [234]. For $q = 1$, $V_N(\vec{\mathbf{x}})$ is the Coulomb potential and finding the minimal energy configuration for N electrons on $\mathbb{S}^2$ is known as the Thomson problem [255]. But also other values of q are possible, $q = 3$ would model dipole interactions and $q = 12$ could be used to model the repulsive part of a Leonard-Jones potential.

The criteria to be included in the "new set of Hilbert problems" are fulfilled: The problem is easy to formulate but not easy to solve and it is likely that its solution will have a large impact. Various numerical approaches have been applied to find an optimal distribution of N points on a sphere. However, the optimization problem becomes extremely difficult to solve for large N, as the number of local minima growth exponentially in N (see [87] for the Thomson problem). It remains to discuss the potential impact. Besides its importance in mathematics, i.e., for the mentioned application in algebra, ordering of interacting point on a sphere or more generally on curved surfaces, has also applications in different fields, e.g., water droplets in oil, which are coated with colloidal particles [38, 10, 228]. Such coated droplets are potential drug delivery vehicles [206, 68]. Similar configurations occur if a jammed layer of colloidal particles separates two immiscible fluids forming a so-called bijel [243, 11], which has potential applications as an efficient micro-reacting media. A large number of ordered particles on curved surfaces is also required for fabrication of nanostructures on pliable substrates, e.g., to make foldable electronic devices [245]. Also viral capsides, where protein subunits play the role of the particles [151, 293, 292, 12] are possible applications. The same is true for the head groups of lipid bilayers in biological membranes or self-assembled peptide nanostructures (see [47]).

We will introduce a surface Phase-Field Crystal model as continuum description to study the ordering of interacting particles on a sphere and other geometries. Only recently various numerical methods have been proposed to solve a general class of partial differential equations on surfaces. They can be distinguished into direct methods, which require a surface mesh or points on a surface and indirect methods in which the surface is only implicitly described. Within the first approach parametric finite-elements can be used to solve the surface partial differential equation (see, e.g., [75, 81, 76, 273]). Other direct approaches consider finite volume discretizations (see, e.g., [53]), and finite-difference discretization (see, e.g., [223, 261]). Level set methods have been used within the second approach (see, e.g., [41]). Furthermore, also phase-field models can be used to implicitly describe the surface, as used in [210, 211, 159, 253]. In order

for the implicit approach to be efficient, adaptively refined meshes or narrow band approaches are required. For recent approaches in this direction see [230, 223, 82]. [1]

We will here concentrate on the parametric finite-element approach. A discussion of a spectral method based on non-equispaced Fourier transforms on the sphere to solve equations (4.4)–(4.6) is included in the published paper [28]. In Section 4.2 a diffuse-interface approach is introduced and discussed.

4.1.1   A surface PFC model

As introduced in [31, 28] we formulate a free-energy for the one-particle density $\psi : \Gamma \to \mathbb{R}$ on the (smooth and closed) surface $\Gamma \subset \mathbb{R}^3$. Therefore, let Δ_Γ denote the Laplace Beltrami operator on Γ. The free-energy $F_{\mathrm{sh}}[\psi]$ as introduced in (1.1) is transformed into $F_{\mathrm{sh}}^\Gamma[\psi]$, by replacing the standard Laplacian in flat-space by Δ_Γ:

$$F_{\mathrm{sh}}^\Gamma[\psi] := \int_\Gamma -\|\nabla_\Gamma \psi\|_\Gamma^2 + \frac{1}{2}|\Delta_\Gamma \psi|^2 + \mathbb{f}(\psi)\,\mathrm{d}s \tag{4.3}$$

with $\|a\|_\Gamma^2 := g(a, a)$, g a corresponding Riemannian metric on Γ, and $\mathbb{f}(\psi) := \frac{1}{2}(1 + r)\psi^2 + \frac{1}{4}\psi^4$ the free-energy density.

A surface H^{-1}-gradient flow of $F_{\mathrm{sh}}^\Gamma[\psi]$, i.e.,

$$\partial_t \psi = \Delta_\Gamma \frac{\delta F_{\mathrm{sh}}^\Gamma[\psi]}{\delta \psi}\,,$$

leads to a system of three second order equations to be solved on the surface Γ:

$$\begin{aligned}
\partial_t \psi &= \Delta_\Gamma \psi^\natural, &&&(4.4)\\
\psi^\natural &= 2\psi^\flat + \Delta_\Gamma \psi^\flat + f(\psi), && \text{in } \Gamma \times [0, T] &(4.5)\\
\psi^\flat &= \Delta_\Gamma \psi &&&(4.6)
\end{aligned}$$

with $f(\psi) = \mathbb{f}'(\psi)$.

4.1.2   Parametric finite-elements

A direct approach to solve equations (4.4)–(4.6) introduces a triangulation of the surface Γ by flat triangular elements. In a parametric finite-element approach instead of performing the integration on the surface elements S of a surface triangulation $\mathcal{S}_h$ of $\mathbb{S}^2$ directly, a mapping $F_S : \hat{S} \to S$ is used with $\hat{S} = \mathrm{conv\ hull}\{0, \mathbf{e}_1, \mathbf{e}_2\}$ the standard element in $\mathbb{R}^2$. Furthermore, we can define the basis functions on a reference element $\overline{S} = \{(\lambda_1, \lambda_2, \lambda_3) \in \mathbb{R}_+^3 : \sum_k \lambda_k = 1\}$ using barycentric coordinates. These allow to transform all integrations onto the standard element and have the definition of basis functions on the reference element at hand. Both are defined in $\mathbb{R}^2$ and $\mathbb{R}^3$. The parameterization F_S is given by the coordinates of the surface mesh elements and provides the only difference between solving equations on surfaces and on planar domains. For a surface we have to allow $F_S : \mathbb{R}^2 \to \mathbb{R}^3$, whereas for a planar domain $F_S : \mathbb{R}^2 \to \mathbb{R}^2$. With this tiny modification any code to solve partial differential equations on Cartesian grids

---

[1]This introductory section is taken from our published paper [28], up to minor notational adaptions.
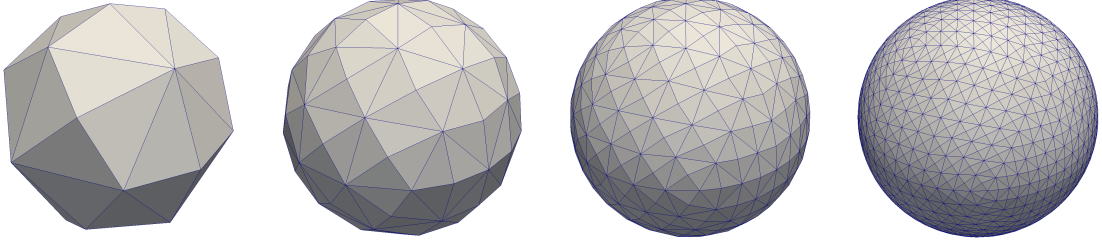
Figure 4.1 – *Sequence of surface meshes approximating* $\mathbb{S}^2$.

can be used to solve the same problem on a surface, providing a surface triangulation is given. Again the approach is therefore not restricted to $\mathbb{S}^2$ but works for any triangulated surface. With this approach all available tools to solve partial differential equations on planar domains, such as adaptive refinement, multigrid algorithms or parallelization approaches, can be used also to solve partial differential equations on surfaces (see, e.g., [273, 140, 275]).

Similar to the the discretization scheme in Section 1.2 used for the flat case, we use a semi-implicit time-discretization and Lagrange finite-elements in space. The time interval $[0, T]$ is split into $N + 1$ timesteps $0 = t_0 < t_1 < \ldots < t_N = T$ with timestep width $\tau_k = t_{k+1} - t_k$. We linearize $f(\psi_{k+1}) \approx f(\psi_k) + f'(\psi_k)(\psi_{k+1} - \psi_k)$ and treat all other terms implicitly. To discretize in space, let Γ_h be a conforming triangulation of Γ. We use the finite-element space of globally continuous, piecewise linear elements $V_h := P^1(\Gamma_h)$. We thus obtain: For $k = 0, 1, \ldots, N-1$ find $\psi_{k+1}, \psi_{k+1}^\sharp, \psi_{k+1}^\flat \in V_h$, such that

$$\left(\psi_{k+1}^\sharp - f'(\psi_k)\psi_{k+1}, \vartheta_h\right)_{\Gamma_h} + \left(2\nabla\psi_{k+1} + \nabla\psi_{k+1}^\flat, \nabla\vartheta_h\right)_{\Gamma_h} = \left(f(\psi_k) - f'(\psi_k)\psi_k, \vartheta_h\right)_{\Gamma_h},$$

$$\left(\psi_{k+1}, \vartheta_h'\right)_{\Gamma_h} + \tau_k\left(\nabla\psi_{k+1}^\sharp, \nabla\vartheta_h'\right)_{\Gamma_h} = \left(\psi_k, \vartheta_h'\right)_{\Gamma_h}, \qquad (4.7)$$

$$\left(\psi_{k+1}^\flat, \vartheta_h''\right)_{\Gamma_h} + \left(\nabla\psi_{k+1}, \nabla\vartheta_h''\right)_{\Gamma_h} = 0, \qquad \forall \vartheta_h, \vartheta_h', \vartheta_h'' \in V_h.$$

This leads to a linear system of equations for $\boldsymbol{\psi}_{k+1}$, $\boldsymbol{\psi}_{k+1}^\sharp$ and $\boldsymbol{\psi}_{k+1}^\flat$

$$\mathbf{M}^\Gamma \boldsymbol{\psi}_{k+1}^\sharp + 2\mathbf{K}^\Gamma \boldsymbol{\psi}_{k+1} + \mathbf{K}^\Gamma \boldsymbol{\psi}_{k+1}^\flat - \mathbf{F}^\Gamma \boldsymbol{\psi}_{k+1} = \mathbf{f}^\Gamma,$$

$$\mathbf{M}^\Gamma \boldsymbol{\psi}_{k+1} + \tau_k\mathbf{K}^\Gamma \boldsymbol{\psi}_{k+1}^\sharp = \mathbf{M}^\Gamma \boldsymbol{\psi}_k, \qquad (4.8)$$

$$\mathbf{M}^\Gamma \boldsymbol{\psi}_{k+1}^\flat + \mathbf{K}^\Gamma \boldsymbol{\psi}_{k+1} = 0$$

with

$$\mathbf{M}^\Gamma = \left((\theta_j, \theta_i)_{\Gamma_h}\right)_{ij}, \qquad\qquad \mathbf{K}^\Gamma = \left((\nabla\theta_j, \nabla\theta_i)_{\Gamma_h}\right)_{ij},$$

$$\mathbf{F}^\Gamma = \left((f'(\psi_k)\theta_j, \theta_i)_{\Gamma_h}\right)_{ij}, \qquad\qquad \mathbf{f}^\Gamma = \left(((f(\psi_k) - f'(\psi_k))\psi_k, \theta_i)_{\Gamma_h}\right)_i,$$

where $(\cdot, \cdot)_{\Gamma_h}$ denotes the L^2-scalar product on Γ_h. We use a surface mesh, which results from adaptive refinement by bisection and projection of the inserted nodes on $\mathbb{S}^2$, starting from a cube with 12 triangular elements, see Figure 4.1 for a sequence of refined meshes.
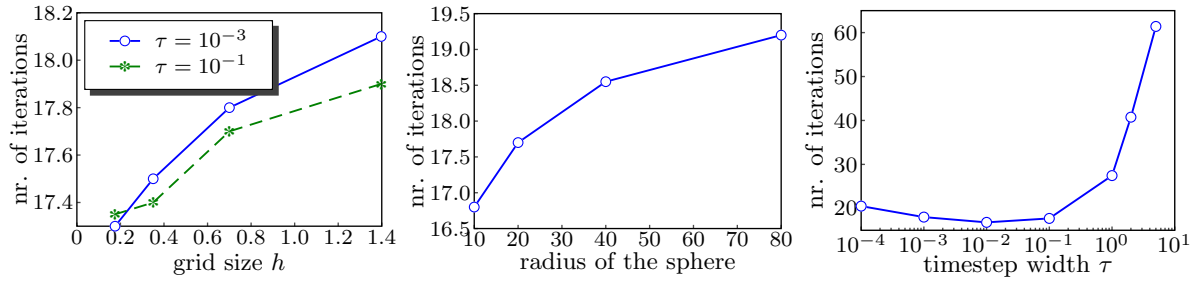
Figure 4.2 – *Number of solver iterations, depending of various system parameters. Left: Depending on grid size h for fixed radius $r = 20$. Center: Depending on the radius of the sphere, for fixed grid width $h = 0.7$ and timestep width $\tau = 10^{-3}$. Right: Depending on the timestep width τ, for fixed radius $r = 20$ and grid size $h = 0.7$.*

Preconditioner for the linear system

In order to solve the linear system of equations (4.8) we apply a preconditioned FGMRES solver to the system. Thereby, the preconditioner matrix $\mathbf{P}$ of Section 1.3 is used with $\mathbf{M}$ replaced by $\mathbf{M}^\Gamma$ and $\mathbf{K}$ replaced by $\mathbf{K}^\Gamma$:

$$\mathbf{P}^\Gamma := \begin{bmatrix} \mathbf{M}^\Gamma & 2\mathbf{K}^\Gamma - \mathbf{K}^\Gamma(\mathbf{M}^\Gamma)^{-1}\mathbf{K}^\Gamma & 0 \\ \tau_k\mathbf{K}^\Gamma & \mathbf{M}^\Gamma + \sqrt{\tau_k}\big(-\mathbf{K}^\Gamma + \mathbf{K}^\Gamma(\mathbf{M}^\Gamma)^{-1}\mathbf{K}^\Gamma\big) & 0 \\ 0 & \mathbf{K}^\Gamma & \mathbf{M}^\Gamma \end{bmatrix}.$$

In Figure 4.2 the influence of some system parameters to the number of FGMRES iterations is studied, namely the size of the surface triangles h, the overall size of a spherical surface, i.e., the radius of the sphere and the timestep width τ that is chosen constant over all timesteps in this study. It is found that a change in the grid size h and in the radius of the sphere has only a little influence on the solver iterations. On the other hand we have a big change in the solver iterations, when increasing the timestep width. This is found also in the flat case in Chapter 1.

Numerical examples

In [28] we have studied the arrangement of N particles on the sphere. For $N < 100$ the results are in perfect agreement with other numerical and theoretical results published in literature. Additionally the occurrence of grain boundary scars, as expected for larger particle numbers, i.e., $N > 360$, is analyzed and a comparison of parametric finite-elements with a spectral approach based on spherical harmonics is done. Both methods show similar configurations and energy decreasing properties, whereas the final configuration has only a slightly larger value than the global minimum. Thus, the surface PFC model is a reliable tool to calculate these optimal point configurations.

The second example considers an elastic instability of a growing crystal on a sphere, similar to the experimental results for colloidal crystals in [175]. The observed branching of the crystal minimizes the curvature induced elastic energy, see Figure 4.3. A crystalline layer on a minimal surface, the 'Schwarz P surface', is shown in Figure 4.4, which might be an approach to stabilize such surfaces by colloidal particles, see [120]. Both examples can be solved efficiently up to

a large number of unknowns using the developed preconditioner and can be combined with domain-decomposition techniques for parallel calculations.
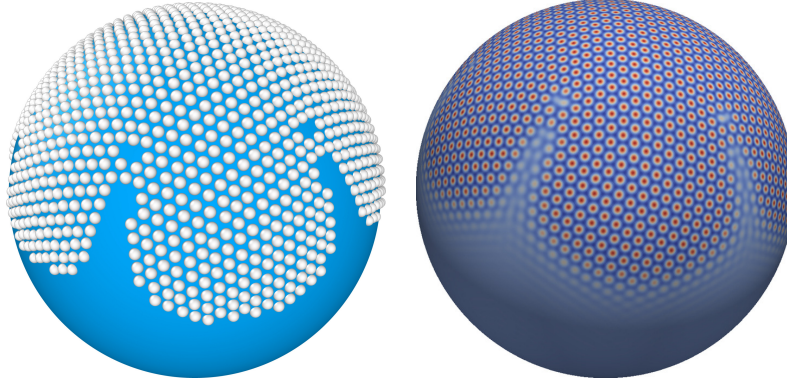
Figure 4.3 – *Crystallization on a sphere $\mathcal{S}_{120}(0)$. Left: Visualization using OVITO [244], indicating each wave as a colloidal particle. Right: Order parameter field ψ. Number of DOFs: 397,584, calculated on 8 processors.*
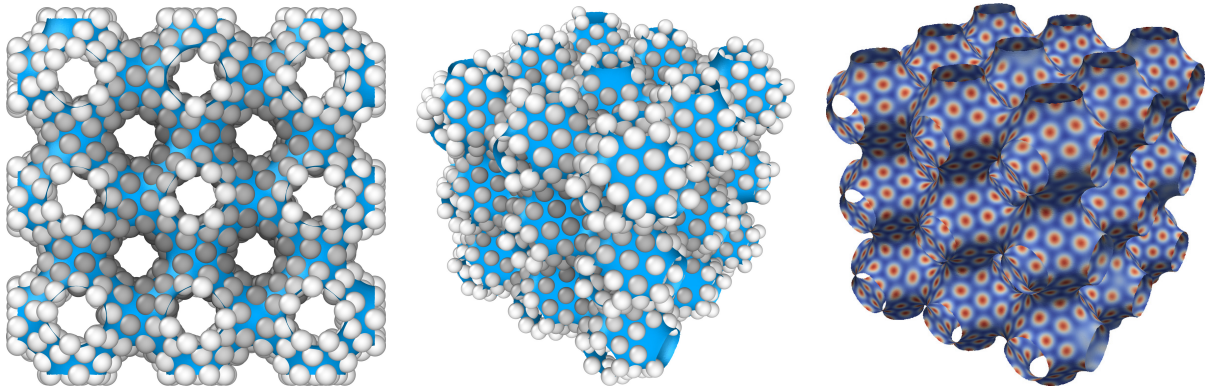
Figure 4.4 – *Crystal structure on a 'Schwarz P surface'. Left and Center: Visualization using OVITO [244] in two different perspectives, indicating each wave as a colloidal particle. Right: Order parameter field ψ. Number of DOFs: 250,000, calculated on one processor.*

4.2 Phase-Field Crystal model in implicitly described geometries

Complex geometries can easily be handled in finite-element discretizations, if a suitable triangulation of the complicated domain is available. This is not always easily achievable, when an bounded aspect ratio of the element, i.e., angle between two adjacent pairs of edges in a tetrahedron, is required for stability reasons. In case of adaptive refinement of the mesh, based on error estimators or information about the structure of the solution, the quality of an initially generated optimal mesh (with respect to some optimality criterion for the chosen discretization) may be violated when a bisection or red-green refinement procedure is applied. Thus an expensive remeshing may be necessary that drops the performance of the finite-element method drastically.

In the context of moving and deforming meshes the task of an adaptive optimal triangulation of the domain gets even more complicated and expensive. Therefore, alternative descriptions of the complex geometries are developed. One such description is based on an implicit representation of the domain by levelsets of a higher-dimensional function.

4.2.1 Phase-Field methods

Let Ω be embedded in a bigger and simpler domain $\Omega \subset \widehat{\Omega}$, with $\partial\Omega \cap \partial\widehat{\Omega} = \emptyset$.

Definition 2. *A mapping* $\mathrm{d} : \widehat{\Omega} \to \mathbb{R}$, *defined by*

$$\mathrm{d}(\mathbf{x}) := \pm \operatorname{dist}(\mathbf{x}, \partial\Omega)$$

with sign negative in Ω *and positive in* $\widehat{\Omega} \setminus \Omega$, *is called* signed distance function.

The domain Ω may now be represented by the negative levelsets of d, i.e.,

$$\Omega = \{\mathbf{x} \in \widehat{\Omega} \,:\, \mathrm{d}(\mathbf{x}) \leq 0\}.$$

For a smooth representation of the characteristic function χ_Ω that takes the value 1 inside of Ω and 0 outside, the signed distance function can be transformed into a phase-field function:

Definition 3. *A mapping* $\phi : \widehat{\Omega} \to [0,1]$, *defined by*

$$\phi(\mathbf{x}) := \frac{1}{2}\big(1 - \tanh(3\mathrm{d}(\mathbf{x})/\epsilon)\big)$$

with $\epsilon \ll 1$ *a parameter that defines the width of the interface between* 0 *and* 1, *is called* phasephield function.

Diffuse-domain approach

In [145] the transformation of differential equations from a domain Ω to the bigger domain $\widehat{\Omega}$ is explained and is basically based on the idea to replace the integrals in the weak formulation of the PDEs by integrals over the bigger domain, restricted to Ω by multiplication with the smeared out characteristic function ϕ. Various different boundary conditions on $\partial\Omega$ are implemented using a weak representation in terms of the phase-field variable ϕ. This approach is called *diffuse-domain formulation*. An analysis of convergence of the implicit equations to the equations in

explicit domain in the sense of matched asymptotic analysis is given in [145] and a more rigorous justification of the approach is given in [93]. Various applications are based on this approach, cf. [9, 91, 232, 139]

Taking $\widehat{\Omega}$ to be a rectangular domain, a simple triangulation based on right triangles/ tetrahedra can be constructed that conserves the initial aspect ratio of the elements during local refinement of the mesh [229, 273, 272].

Diffuse-interface approach

In [210] an approach was proposed how to solve partial differential equations on implicitly defined surfaces. Thereby, the surface is represented by the 1/2-level set of a phase-field variable ϕ, which is defined in a domain $\widehat{\Omega} \subset \mathbb{R}^3$ containing the surface $\mathbb{S}^2$. However, the approach is not restricted to approximate partial differential equations on a sphere, but works for any surface Γ, which can be represented implicitly. Formally, the approach results from an extension of the partial differential equation to $\widehat{\Omega}$ and multiplication of all terms in their weak formulation by a surface delta function δ_Γ, that can be approximated by

$$\delta_\Gamma \approx \delta_\epsilon(\phi) := \frac{3\sqrt{2}}{\epsilon} B(\phi)$$

with $B(\phi) = 36\phi^2(1 - \phi)^2$ and ϕ as above.

It can easily be shown, that δ_ϵ is a nascent delta function with respect to Definition 1. Since all terms in a PDE-system are multiplied with δ_ϵ, the prefactor can be neglected.

4.2.2   Phase-Field Crystal equation in diffuse-interface formulation

The PFC equations (1.4) restricted to a surface $\Gamma \subset \Omega$, can formally be written as

$$\begin{aligned}
\delta_\Gamma \partial_t \psi &= \nabla \cdot (\delta_\Gamma \nabla \psi^\natural), \\
\delta_\Gamma \psi^\natural &= 2\nabla \cdot (\delta_\Gamma \nabla \psi) + \nabla \cdot (\delta_\Gamma \nabla \psi^\flat) + \delta_\Gamma f(\psi), \qquad \text{in } \widehat{\Omega} \times [0, T] \qquad (4.9) \\
\delta_\Gamma \psi^\flat &= \nabla \cdot (\delta_\Gamma \nabla \psi)
\end{aligned}$$

with zero-flux boundary conditions on $\partial\widehat{\Omega}$ for ψ, $\psi^\natural$, and $\psi^\flat$, and appropriate initial conditions for ψ. Within a next step we approximate δ_Γ by δ_ϵ. The system to solve now reads

$$\begin{aligned}
B(\phi)\partial_t \psi &= \nabla \cdot (B(\phi)\nabla \psi^\natural), \\
B(\phi)\psi^\natural &= 2\nabla \cdot (B(\phi)\nabla \psi) + \nabla \cdot (B(\phi)\nabla \psi^\flat) + B(\phi)f(\psi), \qquad \text{in } \widehat{\Omega} \times [0, T] \qquad (4.10) \\
B(\phi)\psi^\flat &= \nabla \cdot (B(\phi)\nabla \psi).
\end{aligned}$$

Matched asymptotic analysis can be performed along the same lines as discussed in [210] for general parabolic systems of second order equations, to show the convergence to the original problem as $\epsilon \to 0$, cf. [28].

In order to solve equations (4.10) we use a semi-implicit backward Euler time-discretization and Lagrange finite-elements in space. We linearize $f(\psi_{k+1}) \approx f(\psi_k) + f'(\psi_k)(\psi_{k+1} - \psi_k)$ and treat all other terms implicit. To discretize in space, let $\mathcal{T}_h$ be a conforming triangulation of $\widehat{\Omega}$. We

use the finite-element space of globally continuous, piecewise linear elements V_h as introduced in Section 1.2. We thus obtain a sequence of problem: For $k = 0, 1, \ldots, N-1$ find $\psi_{k+1}, \psi_{k+1}^{\natural}, \psi_{k+1}^{\flat} \in V_h(\widehat{\Omega})$, such that

$$\left(B(\phi)[\psi_{k+1}^{\natural} - f'(\psi_k)\psi_{k+1}], \vartheta_h\right)_{\widehat{\Omega}} + \left(B(\phi)[2\nabla\psi_{k+1} + \nabla\psi_{k+1}^{\flat}], \nabla\vartheta_h\right)_{\widehat{\Omega}}$$
$$= \left(B(\phi)[f(\psi_k) - f'(\psi_k)\psi_k], \vartheta_h\right)_{\widehat{\Omega}},$$
$$\left(B(\phi)\psi_{k+1}, \vartheta_h'\right)_{\widehat{\Omega}} + \tau_k\left(B(\phi)\nabla\psi_{k+1}^{\natural}, \nabla\vartheta_h'\right)_{\widehat{\Omega}} = \left(B(\phi)\psi_k, \vartheta_h'\right)_{\widehat{\Omega}}, \quad (4.11)$$
$$\left(B(\phi)\psi_{k+1}^{\flat}, \vartheta_h''\right)_{\widehat{\Omega}} + \left(B(\phi)\nabla\psi_{k+1}, \nabla\vartheta_h''\right)_{\widehat{\Omega}} = 0, \qquad \forall \vartheta_h, \vartheta_h', \vartheta_h'' \in V_h.$$

This leads to a linear system of equations for $\boldsymbol{\psi}_{k+1}$, $\boldsymbol{\psi}_{k+1}^{\natural}$ and $\boldsymbol{\psi}_{k+1}^{\flat}$ with $\psi_{k+1} = \sum_i \boldsymbol{\psi}_{i,k+1}\theta_i$, $\psi_{k+1}^{\natural} = \sum_i \boldsymbol{\psi}_{i,k+1}^{\natural}\theta_i$ and $\psi_{k+1}^{\flat} = \sum_i \boldsymbol{\psi}_{i,k+1}^{\flat}\theta_i$, with $\{\theta_i\}$ a basis of V_h:

$$\widehat{\mathbf{M}}\boldsymbol{\psi}_{k+1}^{\natural} + 2\widehat{\mathbf{K}}\boldsymbol{\psi}_{k+1} + \widehat{\mathbf{K}}\boldsymbol{\psi}_{k+1}^{\flat} - \widehat{\mathbf{F}}(\psi_k)\boldsymbol{\psi}_{k+1} = \widehat{\mathbf{f}}(\psi_k),$$
$$\widehat{\mathbf{M}}\boldsymbol{\psi}_{k+1} + \tau_k\widehat{\mathbf{K}}\boldsymbol{\psi}_{k+1}^{\natural} = \widehat{\mathbf{M}}\boldsymbol{\psi}_k,$$
$$\widehat{\mathbf{M}}\boldsymbol{\psi}_{k+1}^{\flat} + \widehat{\mathbf{K}}\boldsymbol{\psi}_{k+1} = 0$$

with

$$\widehat{\mathbf{M}} = \left((B(\phi)\theta_j, \theta_i)_{\widehat{\Omega}}\right)_{ij}, \qquad\qquad \widehat{\mathbf{K}} = \left((B(\phi)\nabla\theta_j, \nabla\theta_i)_{\widehat{\Omega}}\right)_{ij},$$
$$\widehat{\mathbf{F}}(\psi) = \left((B(\phi)f'(\psi)\theta_j, \theta_i)_{\widehat{\Omega}}\right)_{ij}, \qquad \widehat{\mathbf{f}}(\psi) = \left((B(\phi)(f(\psi) - f'(\psi))\psi, \theta_i)_{\widehat{\Omega}}\right)_i,$$
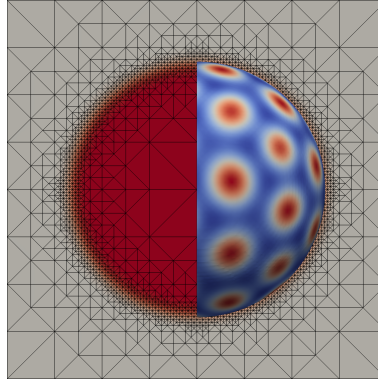
where $(\cdot, \cdot)_{\widehat{\Omega}}$ denotes the L^2-scalar product in $\widehat{\Omega}$. The resulting linear system needs to be solved. Small and coarse discretized systems may be solver iteratively using a BiCGStab(ℓ) Krylov-subspace method [237] or using a direct solver, as before for the flat case. In order for the approach to be efficient we use an adaptively refined mesh along the 1/2-level set of the phase-field function ϕ. Within the diffuse interface we require $h < \epsilon$ with approximately 10 grid points across the interface. We further require $\epsilon < d$ with d the equilibrium lattice constant in the Phase-Field Crystal model. Figure 4.5 shows a typical mesh together with the phase-field variable ϕ describing the surface and the solution for ψ on the 1/2-level set of ψ in $\widehat{\Omega}$.

Small values of ϵ require small values of h and thus a find grid and large linear systems. More advances solvers are needed to solve the arising linear systems. We apply the preconditioner developed in Section 1.3 to the system, where $\mathbf{M}$ is replaced by $\widehat{\mathbf{M}}$ and $\mathbf{K}$ by $\widehat{\mathbf{K}}$. The preconditioner matrix $\mathbf{P}$ then leads to the diffuse-interface preconditioner matrix

$$\widehat{\mathbf{P}} := \begin{bmatrix} \widehat{\mathbf{M}} & 2\widehat{\mathbf{K}} - \widehat{\mathbf{K}}\widehat{\mathbf{M}}^{-1}\widehat{\mathbf{K}} & 0 \\ \tau_k\widehat{\mathbf{K}} & \widehat{\mathbf{M}} + \sqrt{\tau_k}\left(-\widehat{\mathbf{K}} + \widehat{\mathbf{K}}\widehat{\mathbf{M}}^{-1}\widehat{\mathbf{K}}\right) & 0 \\ 0 & \widehat{\mathbf{K}} & \widehat{\mathbf{M}} \end{bmatrix}, \qquad (4.12)$$

or as in equation (1.20)

$$\widehat{\mathbf{P}}_{\mathrm{CH}} := \begin{bmatrix} \widehat{\mathbf{M}} & -2\tau_k^{1/4}\widehat{\mathbf{K}} - \widehat{\mathbf{K}}\widehat{\mathbf{M}}^{-1}\widehat{\mathbf{K}} & 0 \\ \tau_k\widehat{\mathbf{K}} & \widehat{\mathbf{M}} + (\tau_k^{1/2} + 2\tau_k^{1/4})\widehat{\mathbf{K}} + \tau_k^{1/2}\widehat{\mathbf{K}}\widehat{\mathbf{M}}^{-1}\widehat{\mathbf{K}} & 0 \\ 0 & \widehat{\mathbf{K}} & \widehat{\mathbf{M}} \end{bmatrix}, \qquad (4.13)$$

Figure 4.5 – *Adaptively refined mesh along the 1/2-level set of ϕ representing $\mathbb{S}^2$, solution for ψ in on 1/2-level set and phase-field variable.*

respectively.

In Figure 4.6 the influence of ϵ and grid refinement to the number of solver iterations of a FGMRES Krylov-subspace solver is shown. All four plots in Figure 4.6 (a), (b), (c), and (d) show decreasing number of solver iterations for increasing interface width ϵ. Except for the plot (d), a higher refinement level needs larger number of solver iterations. For small ϵ an interplay between interface width and grid size shows small fluctuations in the number of solver iterations. The minimal iteration count is achieved for $\tau_k = 0.01$.

4.2.3   The Vacancy PFC model in diffuse-domain formulation

The classical PFC model introduced in Section 1.1 combined with the penalty term given in Section 2.2.2 leads to the Vacancy PFC (VPFC) equations

$$
\begin{aligned}
\partial_t \psi &= \nabla \cdot \left(M(\psi)\nabla\psi^{\natural} \right), \\
\psi^{\natural} &= \psi^3 + (r + (1+\Delta)^2)\psi + b(\psi), \qquad \text{in } \Omega \times [0, T]
\end{aligned}
\tag{4.14}
$$

with $b(\psi) = 3\omega_2\psi^2(\text{sign}(\psi) - 1)$ and $\omega_2 \gg 1$. Combined with the Navier-Stokes equations, this model is used in Chapter 2 to describe individual particles in a flowing environment.

Representing this environment/domain implicitly by a phase-field variable leads to the diffuse-domain VPFC model that can formally be written as

$$
\begin{aligned}
\phi\partial_t \psi &= \nabla \cdot \left(\phi M(\psi)\nabla\psi^{\natural} \right), \\
\phi\psi^{\natural} &= \phi\psi^3 + \phi(r + 1)\psi + 2\nabla \cdot \phi\nabla\psi + \nabla \cdot \phi\nabla\psi^{\flat} + \phi b(\psi) + BC(\phi), \qquad \text{in } \widehat{\Omega} \times [0, T] \quad (4.15) \\
\phi\psi^{\flat} &= \nabla \cdot \phi\nabla\psi,
\end{aligned}
$$

where BC is a boundary condition term that needs to be specified. Restricting the particles to the domain Ω corresponds to the condition that the particle density ψ vanishes outside of Ω, i.e., a homogeneous Dirichlet boundary condition on $\partial\Omega$. The corresponding diffuse representation of this boundary condition, as formulated in [145] and widely used in the context of other implicit methods, can be written as

$$
BC(\phi) = \frac{1}{\epsilon^3}(1 - \phi)\psi,
$$
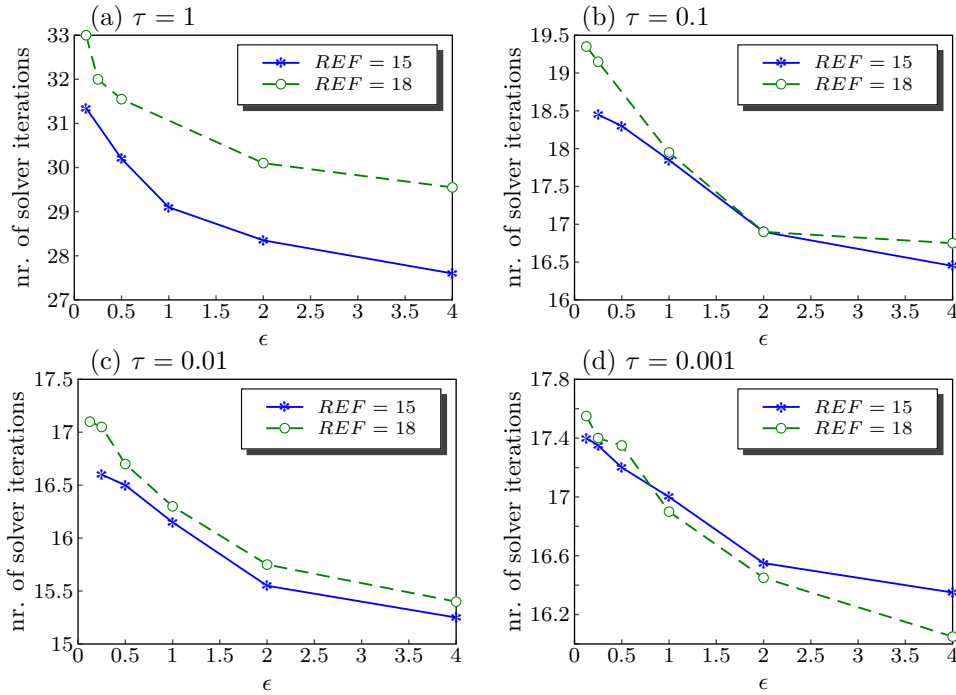
Figure 4.6 – *Dependence of the number of solver iterations on the interface width ϵ, the refinement level REF of the interface, and on the timestep width τ. Refinement level REF = 15 corresponds to grid-size $h \in [1.5708, 20.5208]$ and REF = 18 to grid-size $h \in [0.7854, 20.5208]$. For $\epsilon = 0.5$ these refinements correspond to a system size of 17,365 DOFs per component and 97,113 DOFs per component, respectively.*

where the exponent ϵ^3 can be justified by asymptotic analysis. An exponent > 2 was considered in [93] and convergence of the boundary value was analyzed.

Since $\psi \equiv 0$ in $\widehat{\Omega} \setminus \Omega$, also the Laplacian $\Delta\psi$ vanishes outside of Ω. Thus, the equations (4.15) can be simplified to the original equations (4.14), solved in the extended domain $\widehat{\Omega}$, and equipped with the boundary term BC,

$$\begin{aligned} \partial_t \psi &= \nabla \cdot \left(M(\psi) \nabla \psi^\natural \right), \\ \psi^\natural &= \psi^3 + (r + (1 + \Delta)^2)\psi + b(\psi) + BC(\phi), \qquad \text{in } \widehat{\Omega} \times [0, T]. \end{aligned} \tag{4.16}$$

4.2.4 Numerical experiments

We consider a configuration of initial density peaks $\psi_0^{(i)}$, as introduced in equation (2.41) in form of a hexagonal lattice, restricted to the domain Ω, by using the phase-field function ϕ:

$$\psi_0(\mathbf{x}) := \phi(\mathbf{x}) \sum_{i=1}^{N_p} \psi_0^{(i)}(\mathbf{x}).$$

As test domains we have chosen two circular shapes, that is, a regular circular disc and a perturbed disc by a cosine variation of the radius, see Figure 4.7.

In equation (4.16) the mobility function is restricted to the particles, by defining $M(\psi)$ as

$$M(\psi) := M_0 \max \left(\psi / \max_{\mathbf{x} \in \Omega}(\psi(\mathbf{x})), \delta \right)$$

with $\delta, M_0 > 0$. In the following we have set $\delta := 10^{-2}$.

A linearization of the nonlinear terms, that is, $b(\psi)$, $M(\psi)$, and ψ^3, combined with a simple backward Euler time-discretization, leads to the variational form: For $k = 0, 1, \ldots, N-1$ find $\psi_{k+1}, \psi_{k+1}^\natural, \psi_{k+1}^\flat \in V_h(\widehat{\Omega})$, s.t.

$$(\psi_{k+1}^\natural - (1 + r + 3\psi_k^2 + b'(\psi_k) + \epsilon^{-3}(1 - \phi))\psi_{k+1}, \vartheta_h)_{\widehat{\Omega}} + (2\nabla\psi_{k+1} + \nabla\psi_{k+1}^\flat, \nabla\vartheta_h)_{\widehat{\Omega}}$$
$$= (-2\psi_k^3 + b(\psi_k) - b(\psi_k)'\psi_k, \vartheta_h)_{\widehat{\Omega}},$$
$$\left(\psi_{k+1}, \vartheta_h'\right)_{\widehat{\Omega}} + (\tau_k M(\psi_k)\nabla\psi_{k+1}^\natural, \nabla\vartheta_h')_{\widehat{\Omega}} = \left(\psi_k, \vartheta_h'\right)_{\widehat{\Omega}},$$
$$(\psi_{k+1}^\flat, \vartheta_h'')_{\widehat{\Omega}} + (\nabla\psi_{k+1}, \nabla\vartheta_h'')_{\widehat{\Omega}} = 0, \qquad \forall\vartheta_h, \vartheta_h', \vartheta_h'' \in V_h(\widehat{\Omega}).$$

This leads to a linear system

$$\begin{bmatrix} \mathbf{M} & -\mathbf{F}(\psi_k) + 2\mathbf{K} & \mathbf{K} \\ \tau_k\mathbf{K}_M(\psi_k) & \mathbf{M} & 0 \\ 0 & \mathbf{K} & \mathbf{M} \end{bmatrix} \begin{pmatrix} \boldsymbol{\psi}_{k+1}^\natural \\ \boldsymbol{\psi}_{k+1} \\ \boldsymbol{\psi}_{k+1}^\flat \end{pmatrix} = \begin{pmatrix} \mathbf{f}(\psi_k) \\ \mathbf{M}\boldsymbol{\psi}_k \\ 0 \end{pmatrix} \qquad (4.17)$$

with $\mathbf{M}$ and $\mathbf{K}$ as in Section 1.2 and

$$\mathbf{F}(\psi) := \left((1 + r + 3\psi^2 + b'(\psi) + \epsilon^{-3}(1 - \phi))\theta_j, \theta_i)_{\widehat{\Omega}}\right)_{ij},$$
$$\mathbf{f}(\psi) := \left((-2\psi^3 + b(\psi) - b(\psi)'\psi, \theta_i)_{\widehat{\Omega}}\right)_i,$$

and $\mathbf{K}_M(\psi) := \left((M(\psi)\nabla\theta_j, \nabla\theta_i)_{\widehat{\Omega}}\right)_{ij}$.

A preconditioner that incorporates the mobility function $M(\psi)$ can be constructed by neglecting the nonlinearity matrix $\mathbf{F}$ and perturbing the diagonal entry,

$$\mathbf{P} := \begin{bmatrix} \mathbf{M} & 2\mathbf{K} - \mathbf{K}\mathbf{M}^{-1}\mathbf{K} & 0 \\ \tau_k\mathbf{K}_M(\psi_k) & \mathbf{M} + \sqrt{\tau_k}\left(\mathbf{K}_M(\psi_k) - 2\mathbf{K} + \mathbf{K}\mathbf{M}^{-1}\mathbf{K}\right) & 0 \\ 0 & \mathbf{K} & \mathbf{M} \end{bmatrix},$$

as in (2.45). Analogously, a preconditioner involving the Cahn-Hilliard subpreconditioner, as in (2.46), can be constructed and is used throughout the numerical studies.

The preconditioner is combined with a Krylov-subspace solver FGMRES to solve the linear system (4.17) for both geometries visualized in Figure 4.7, for various mobility factors M_0 and interface widths ϵ. The results of such a benchmark calculation can be found in Figure 4.8. Initially, the particles overlap the diffuse interface, but due to the diffuse Dirichlet boundary condition the particles are pushed towards the inside of Ω, where they remain fixed.

The preconditioner study in Figure 4.9 shows that the number of solver iterations is not much larger than that for exactly the same system without an implicit boundary. This is visualized in the left plot of Figure 4.9 by red cross curve. The mobility on the other hand, has a big influence on the solver iterations. Increasing M_0 increases the number of iterations a lot. Mobilities with $M_0 \gg 100$ lead to a non-converging method. For both geometries the slightly more complicated geometric shape leads to slightly more iterations. Increasing the interface width ϵ mainly increases the band width of fine grid size. This may lead to the increase in solver iterations, as visualized in the right plot of Figure 4.9.
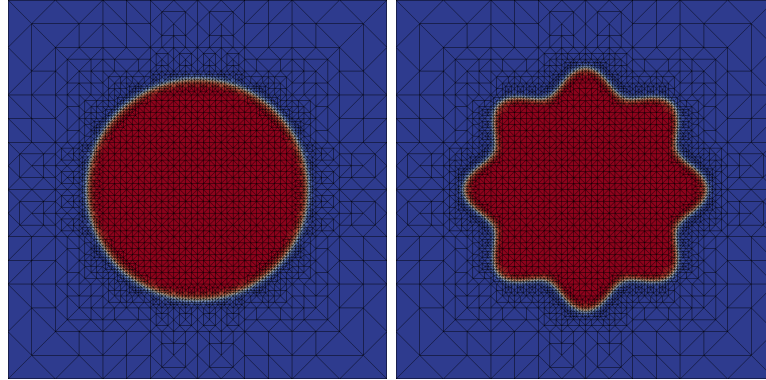
Figure 4.7 – *Phase-field representations of a circular (left) and perturbed circular (right) domain Ω. The color blue (outside of the domain) corresponds to the value 0 and red (inside the domain) to the value 1. Grid lines are shown that are coarse outside of Ω, fine on the interface, and with an intermediate refinement level inside the domain, so that the individual particles can be resolved accordingly.*
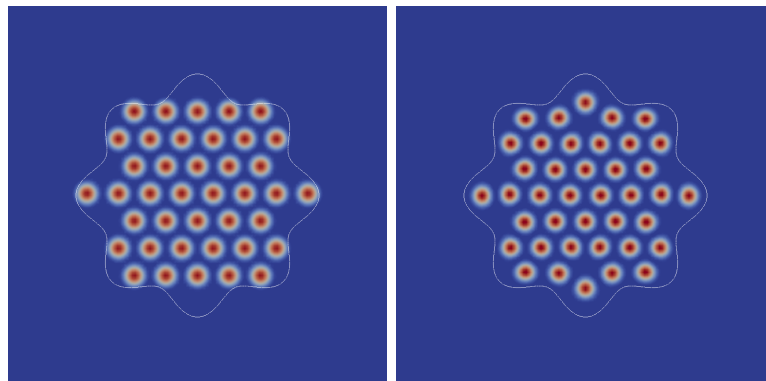
Figure 4.8 – *Left: Initial solution $\psi_0(\mathbf{x})$ with 1/2-levelset of phase-field function ϕ. Right: Stationary solution with particles shifted symmetrically inside the domain Ω.*
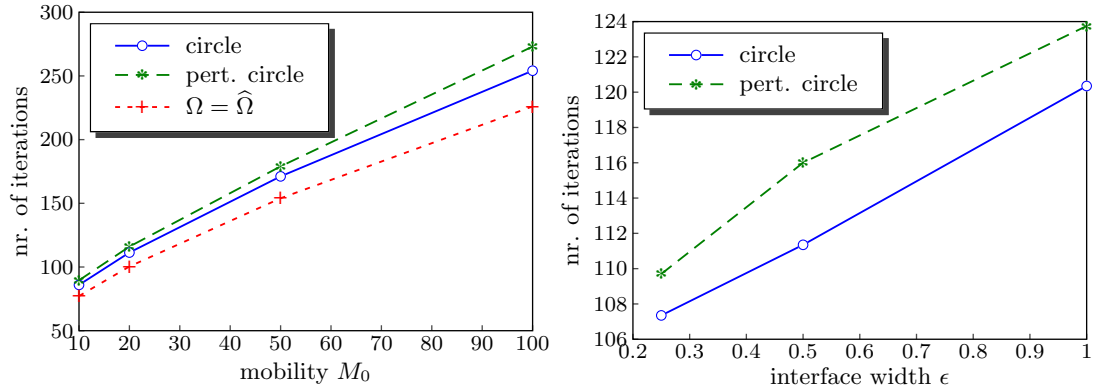
Figure 4.9 – *Number of solver iterations depending on the mobility parameter M_0 (left) and on the interface width ϵ (right). Two geometries (see Figure 4.7) are compared and show just a little difference in the number of iterations. Left: Parameter $\epsilon := 0.5$ for circle and pert. circle, compared to a non-diffuse-domain calculation. Right: Parameter $M_0 := 20$.*

4.3 Navier-Stokes Cahn-Hilliard (Vacancy) Phase-Field Crystal model

Colloidal particles suspended in a two-phase fluid, e.g., a mixture of oil and water, may arrange at the interface between the fluid-phases, when partially coated with a hydrophilic and a hydrophobic layer. Depending on the contact angles between the three phase, the water and oil phase and the solid phase – the colloidal particle – it may happen that the particles concentrate completely in one of the fluid phases [163].

An evolution of the particle phase pushes the individual colloids out of their position, i.e., the arrangement is disturbed. If the droplet with the particles shrinks, e.g., due to evaporation of the fluid, a highly compressed supraparticle can be formed [163, 60, 287], which may be used as building blocks for new materials.

Particles moving in an evolving domain and interacting with the domain boundaries are modeled by a vacancy PFC model. An evolving domain is described by a Navier-Stokes Cahn-Hilliard/Allen-Cahn model. Coupling both approaches results in a continuous model introduced in this chapter.

We follow here the approach of [10, 11], extended by a contribution to freely moving particles, i.e., the Vacancy PFC model. The authors proposed a diffuse-interface model for the Phase-Field Crystal equation, where the phase-field, describing the diffuse interface, is given by the solution of a Cahn-Hilliard equation. Instead of restricting the particles to the interface, we propose a model to restrict the particles to one of the phases given by the Cahn-Hilliard solution. The interaction of the particles with the phase-interface is given by a wall potential depending on the phase-field.

Thus, we combine the ideas of particles in a flowing solvent (see Section 2.1) for the colloid-wall interaction, the Navier-Stokes PFC model (see Section 2.2) to have interacting freely moving particles, and the diffuse-domain description (see Section 4.2) for complex domains. The evolution of the domain is driven by a Cahn-Hilliard equation, cf. [52, 9, 49, 24, 7].

4.3.1 Energy of the system and the balance equations

In order to derive constitutive equations for the velocity $\mathbf{u}$, the PFC density modulation ψ and the phase-field ϕ, we start with the energy contributions and formulate an energy dissipative dynamical equation for all the parameters.

Consider the sum of three energies, kinetic energy F_{kin}, surface energy F_{ch} and a contribution to the interaction of (colloidal) particles F_{sh}, i.e., the elastic part of the energy:

$$F[\mathbf{u}, \psi, \phi] = F_{\text{kin}}[\mathbf{u}] + F_{\text{ch}}[\phi] + F_{\text{sh}}[\psi, \phi] \,, \tag{4.18}$$

$$F_{\text{kin}}[\mathbf{u}] = \int \frac{1}{2} \|\mathbf{u}\|^2 \, d\mathbf{x} \,, \tag{4.19}$$

$$F_{\text{ch}}[\phi] = \int \frac{\epsilon^2}{2} \|\nabla\phi\|^2 + f_{\text{ch}}(\phi) \, d\mathbf{x} \,, \tag{4.20}$$

$$F_{\text{sh}}[\psi, \phi] = \frac{1}{\text{El}} \int \frac{1}{4}\psi^4 + \frac{1}{2}\psi\big(r + U(\phi) + (1 + \Delta)^2\big)\psi + b(\psi) \, d\mathbf{x} \,, \tag{4.21}$$

where ϵ, r are system parameters, and El an elasticity number to weight the elastic energy related to the surface energy. The function U acts as a wall potential that restricts the particles to the domain described by the 1-phase of ϕ, and is defined by

$$U(\phi) = \omega_1(1 - \phi) \,,$$

where $\omega_1 \gg 1$ is a scaling factor. The double-well function f_{ch} is simply given by

$$f_{\text{ch}}(\phi) = \frac{1}{4}\phi^2(1 - \phi)^2$$

and enforces the values of the concentration ϕ to the range $[0, 1]$.

To have particles restricted to a subdomain of the domain and to conserve the particle number rather than the particle density, the Vacancy-PFC model enforces the density to have positive value, i.e. we add the constraint $\psi \geq 0$. In Refs. [55, 40], Section 2.2.2, and Section 4.2.3, this es achieved by adding a penalty term $b(\psi)$ to the energy, given by

$$b(\psi) = \omega_2(|\psi|^n - \psi^n)$$

with $\omega_2 \gg 1$ and $n = 3$. This modification allows for the occurrence of stable vacancies or the treatment of individual particles.

4.3.2 Thermodynamically consistent dynamic equations

We consider a system where the particles live in a heat bath, i.e. an incompressible fluid with constant density. To model the dynamics of the particles and the domain surface, including hydrodynamic interactions between particles and surface, we assume the evolution/ balance equations

$$\begin{aligned}
\nabla \cdot \mathbf{u} &= 0 \,, \\
\partial_t \mathbf{u} + \mathbf{u} \cdot \nabla \mathbf{u} &= \nabla \cdot \mathbf{T} \,, \\
\partial_t \psi + \mathbf{u} \cdot \nabla \psi &= -\nabla \cdot \mathbf{J}_{\text{sh}} \,, \\
\partial_t \phi + \mathbf{u} \cdot \nabla \phi &= -\nabla \cdot \mathbf{J}_{\text{ch}} \,,
\end{aligned} \tag{4.22}$$

where $\mathbf{T} = -p\mathbf{I} + \eta(\nabla\mathbf{u} + \nabla\mathbf{u}^\top) + \mathbf{T}_0$ describes the stress tensor with determinable force $\mathbf{F} := \nabla \cdot \mathbf{T}_0$. The PFC and Cahn-Hiliard fluxes $\mathbf{J}_{\mathrm{sh}}$ and $\mathbf{J}_{\mathrm{ch}}$ also need to be determined. These dynamic equations correspond to the Navier-Stokes equations for the velocity $\mathbf{u}$ and generalized diffusion equations for the concentration field ϕ and particle density ψ. To get expressions for the force and fluxes we consider the time-evolution of the energy and expect the energy to decrease over time, i.e., $\partial_t F \leq 0$.

Let $\widehat{\Omega}$ be a fixed domain with Lipschitz-boundary. The time-evolution of the energy $\partial_t F = \partial_t F_{\mathrm{kin}} + \partial_t F_{\mathrm{ch}} + \partial_t F_{\mathrm{sh}}$ can be split into

$$
\begin{aligned}
\partial_t F_{\mathrm{kin}} &= \int_{\widehat{\Omega}} \mathbf{u} \cdot \partial_t \mathbf{u} \,\mathrm{d}\mathbf{x} = \int_{\widehat{\Omega}} \mathbf{u} \cdot (-\mathbf{u} \cdot \nabla\mathbf{u} + \nabla \cdot \mathbf{T}) \,\mathrm{d}\mathbf{x}, \\
\partial_t F_{\mathrm{ch}} &= \int_{\widehat{\Omega}} \frac{\delta F[\mathbf{u}, \psi, \phi]}{\delta\phi} \cdot \partial_t\phi \,\mathrm{d}\mathbf{x}, \\
\partial_t F_{\mathrm{sh}} &= \int_{\widehat{\Omega}} \frac{\delta F[\mathbf{u}, \psi, \phi]}{\delta\psi} \cdot \partial_t\psi \,\mathrm{d}\mathbf{x}
\end{aligned}
\tag{4.23}
$$

with

$$
\begin{aligned}
\frac{\delta F[\mathbf{u}, \psi, \phi]}{\delta\phi} &=: \phi^\natural = -\epsilon^2\Delta\phi + f(\phi) - \frac{\omega_1}{2}\psi^2, \\
\mathsf{El}\frac{\delta F[\mathbf{u}, \psi, \phi]}{\delta\psi} &=: \psi^\natural = \psi^3 + (r + (1+\Delta)^2)\psi + \psi\, U(\phi) + b(\psi),
\end{aligned}
\tag{4.24}
$$

with the penalty term

$$
\begin{aligned}
b(\psi) &:= \mathbb{b}'(\psi) = n\,\omega_2\psi^{n-1}(\mathrm{sign}(\psi) - 1), \\
f(\phi) &:= \mathbb{f}'_{\mathrm{ch}}(\phi) = \frac{1}{2}\phi \cdot \left(1 - 3\phi + 2\phi^2\right),
\end{aligned}
$$

where the signum function $\mathrm{sign}(\psi)$ gives 1 for positive densities and -1 for negative ones.

To obtain energy dissipative dynamics, the condition $\partial_t F \leq 0$ can be fulfilled by inserting the time derivatives with respect to the balance equations (4.22) into (4.23) and defining $\mathbf{J}_{\mathrm{ch}}$, $\mathbf{J}_{\mathrm{sh}}$, and $\mathbf{F}$ accordingly.

Using incompressibility of the fluid and integration by parts, where we assume that the boundary integrals vanish by introducing appropriate boundary conditions, we get for the kinetic part of the energy

$$
\partial_t F_{\mathrm{kin}} = \int_{\widehat{\Omega}} -\eta\nabla\mathbf{u} : (\nabla\mathbf{u} + \nabla\mathbf{u}^\top) + \mathbf{u} \cdot \mathbf{F} \,\mathrm{d}\mathbf{x}.
$$

The derivation of the Cahn-Hilliard and Phase-Field Crystal part of the energy read

$$
\begin{aligned}
\partial_t F_{\mathrm{ch}} &= \int_{\widehat{\Omega}} \mathbf{J}_{\mathrm{ch}} \cdot \nabla\phi^\natural - \mathbf{u} \cdot \phi^\natural\nabla\phi \,\mathrm{d}\mathbf{x}, \\
\partial_t F_{\mathrm{sh}} &= \frac{1}{\mathsf{El}} \int_{\widehat{\Omega}} \mathbf{J}_{\mathrm{sh}} \cdot \nabla\psi^\natural - \mathbf{u} \cdot \psi^\natural\nabla\psi \,\mathrm{d}\mathbf{x}.
\end{aligned}
$$

Putting all together yields an expression, where we can derive fluxes and a force, which define a thermodynamical consistent system. We use the notation $\mathbf{D}(\mathbf{u}) := \frac{1}{2}(\nabla\mathbf{u} + \nabla\mathbf{u}^\top)$ and the

relation

$$
\begin{aligned}
(\mathbf{D}(\mathbf{u}), \nabla\mathbf{u})_{\widehat{\Omega}} &= (\mathbf{D}(\mathbf{u}), \frac{\nabla\mathbf{u}}{2})_{\widehat{\Omega}} + (\mathbf{D}(\mathbf{u})^\top, \frac{\nabla\mathbf{u}^\top}{2})_{\widehat{\Omega}} \\
&= (\mathbf{D}(\mathbf{u}), \frac{\nabla\mathbf{u}}{2})_{\widehat{\Omega}} + (\mathbf{D}(\mathbf{u}), \frac{\nabla\mathbf{u}^\top}{2})_{\widehat{\Omega}} \\
&= (\mathbf{D}(\mathbf{u}), \mathbf{D}(\mathbf{u}))_{\widehat{\Omega}}
\end{aligned}
\tag{4.25}
$$

with $(\mathbf{A}, \mathbf{B})_{\widehat{\Omega}} := \int_{\widehat{\Omega}} \mathbf{A}(\mathbf{x}) : \mathbf{B}(\mathbf{x}) \, \mathrm{d}\mathbf{x}$, to obtain

$$
\partial_t F = \int_{\widehat{\Omega}} \mathbf{u} \cdot (\mathbf{F} - \phi^\natural \nabla\phi - \mathsf{El}^{-1}\psi^\natural \nabla\psi) + \mathbf{J}_{\mathrm{ch}}\nabla\phi^\natural + \mathsf{El}^{-1}\mathbf{J}_{\mathrm{sh}}\nabla\psi^\natural - 2\eta(\mathbf{x})\mathbf{D}(\mathbf{u}) : \mathbf{D}(\mathbf{u}) \, \mathrm{d}\mathbf{x}.
$$

For the unknowns we choose

$$
\mathbf{F} = \phi^\natural \nabla\phi + \mathsf{El}^{-1}\psi^\natural \nabla\psi, \quad \mathbf{J}_{\mathrm{ch}} = -M_{\mathrm{ch}}\nabla\phi^\natural, \quad \mathbf{J}_{\mathrm{sh}} = -M_{\mathrm{sh}}\nabla\psi^\natural,
$$

with the mobilities $M_{\mathrm{ch}}, M_{\mathrm{sh}} > 0$. Finally, the energy dissipation holds, since

$$
\partial_t F = -M_{\mathrm{ch}}\|\nabla\phi^\natural\|_{\widehat{\Omega}}^2 - M_{\mathrm{sh}}\|\nabla\psi^\natural\|_{\widehat{\Omega}}^2 - (2\eta\mathbf{D}(\mathbf{u}), \mathbf{D}(\mathbf{u}))_{\widehat{\Omega}} \leq 0,
$$

using $\eta(\mathbf{x}) > 0$.

Friction

In [176] a simple form of a friction term is added. Defining

$$
\mathbf{F} := \mathbf{F} - \alpha\mathbf{u}, \quad \text{or} \quad \mathbf{F} := \mathbf{F} - \mathbb{A}\mathbf{u},
$$

with positive friction coefficient $\alpha > 0$, and positive definite friction tensor $\mathbb{A} \succ 0$, respectively, we still have a thermodynamic consistent system, since

$$
\partial_t F = -\alpha\|\mathbf{u}\|_{\widehat{\Omega}}^2 - M_{\mathrm{ch}}\|\nabla\phi^\natural\|_{\widehat{\Omega}}^2 - M_{\mathrm{sh}}\|\nabla\psi^\natural\|_{\widehat{\Omega}}^2 - (2\eta\mathbf{D}(\mathbf{u}), \mathbf{D}(\mathbf{u}))_{\widehat{\Omega}} \leq 0,
$$

and

$$
\partial_t F = -\|\mathbf{u}\|_{\mathbb{A},\widehat{\Omega}}^2 - M_{\mathrm{ch}}\|\nabla\phi^\natural\|_{\widehat{\Omega}}^2 - M_{\mathrm{sh}}\|\nabla\psi^\natural\|_{\widehat{\Omega}}^2 - (2\eta\mathbf{D}(\mathbf{u}), \mathbf{D}(\mathbf{u}))_{\widehat{\Omega}} \leq 0,
$$

respectively, with $\|\mathbf{u}\|_{\mathbb{A},\widehat{\Omega}}^2 := \int_{\widehat{\Omega}} \mathbf{u}^\top \mathbb{A}\mathbf{u} \, \mathrm{d}\mathbf{x}$.

4.3.3   System of equations

The derived system of evolution equations for the Navier-Stokes Cahn-Hilliard Vacancy-PFC system, inserting all the functions, fluxes, and forces, reads

$$
\begin{aligned}
\nabla \cdot \mathbf{u} &= 0, \\
\partial_t\mathbf{u} + \mathbf{u} \cdot \nabla\mathbf{u} &= -\nabla p + \nabla \cdot \left[\eta(\psi)(\nabla\mathbf{u} + \nabla\mathbf{u}^\top) \right] + \phi^\natural\nabla\phi + \mathsf{El}^{-1}\psi^\natural\nabla\psi - \alpha\mathbf{u}, \\
\partial_t\psi + \mathbf{u} \cdot \nabla\psi &= \nabla \cdot (M_{\mathrm{pfc}}\nabla\psi^\natural), \\
\psi^\natural &= \psi^3 + (1+r)\psi + 2\Delta\psi + \Delta^2\psi + \omega_1\psi(1-\phi) + 3\omega_2\psi^2(\mathrm{sign}(\psi) - 1), \\
\partial_t\phi + \mathbf{u} \cdot \nabla\phi &= \nabla \cdot (M_{\mathrm{ch}}\nabla\phi^\natural), \\
\phi^\natural &= -\epsilon^2\Delta\phi + \frac{1}{2}\phi \cdot (1 - 3\phi + 2\phi^2) - \frac{\omega_1}{2}\psi^2, \qquad \text{in } \widehat{\Omega} \times [0, T].
\end{aligned}
\tag{4.26}
$$

It can be solved using a sequential operator splitting approach [25] and linearization of all nonlinear terms [29, 7]. The viscosity η is non-constant in our simulations, to control the rigidity of the particles, i.e., we have implemented the expression

$$\eta(\psi) = \bar{\eta}_f + (\bar{\eta}_p - \bar{\eta}_f)\frac{\psi}{\max_\Omega(\psi)}\,,$$

similar to the approach (2.32).

4.3.4 Numerical discretization

The evolution equations (4.26) are discretized using continuous finite-elements in space and a semi-implicit backward Euler discretization in time. Therefore, we choose Taylor-Hood elements P^2/P^1 for the Navier-Stokes equations and P^2 element for the Phase-Field Crystal and Cahn-Hilliard part. A splitting of the time-interval $[0, T]$ into timesteps $0 = t_0 < t_1 < \ldots < t_N = T$ with the timestep width $\tau_k = t_{k+1} - t_k$ leads to a three step procedure.

Let $\phi_0, \psi_0 \in L_2(\Omega)$ and $\mathbf{u}_0 \in \left[L_2(\Omega)\right]^m$ be given. For $k = 0, 1, \ldots, N-1$ solve

Step 1:

$$\nabla \cdot \mathbf{u}_{k+1} = 0\,,$$
$$\frac{1}{\tau_k}\mathbf{u}_{k+1} + \mathbf{u}_k \cdot \nabla \mathbf{u}_{k+1} = \frac{1}{\tau_k}\mathbf{u}_k - \nabla p + \nabla \cdot \left[\eta(\psi_k)(\nabla \mathbf{u}_{k+1} + \nabla \mathbf{u}_{k+1}^\top)\right]$$
$$+ \phi_k^\natural \nabla \phi_k + \mathsf{El}^{-1}\psi_k^\natural \nabla \psi_k - \alpha \mathbf{u}_{k+1}\,,$$

Step 2:

$$\psi_{k+1}^\natural - (1+r)\psi_{k+1} - 2\Delta\psi_{k+1} - \Delta\psi_{k+1}^\flat = 3\psi_k^2\psi_{k+1} - 2\psi_k^3 + \omega_1\psi_{k+1}(1-\phi_k)$$
$$+ b(\psi_k) + b'(\psi_k)(\psi_{k+1} - \psi_k)\,,$$
$$\psi_{k+1} + \tau_k\mathbf{u}_{k+1} \cdot \nabla\psi_{k+1} = \psi_k + \tau_k\nabla \cdot (M_{\text{pfc}}\nabla\psi_{k+1}^\natural)\,,$$
$$\psi_{k+1}^\flat - \Delta\psi_{k+1} = 0$$

Step 3:

$$\phi_{k+1}^\natural + \epsilon^2\Delta\phi_{k+1} = f(\phi_k) + f'(\phi_k)(\phi_{k+1} - \phi_k) - \frac{\omega_1}{2}\psi_{k+1}^2\,,$$
$$\phi_{k+1} + \tau_k\mathbf{u}_{k+1} \cdot \nabla\phi_{k+1} = \phi_k + \tau_k\nabla \cdot (M_{\text{ch}}\nabla\phi_{k+1}^\natural).$$

Each system can be solved separately using an individual solver. We use a preconditioned MINRES Krylov-subspace method for the Navier-Stokes equations, a FGMRES solver with the PFC preconditioner, as developed in Section 4.2.4, for the Vacancy PFC equation, and a FGMRES solver with the Cahn-Hilliard preconditioner, as introduced in [49] and used as subpreconditioner through this work, for the solution of step 3.

This leads to an overall efficient solution procedure that can be implemented in a highly parallel environment.
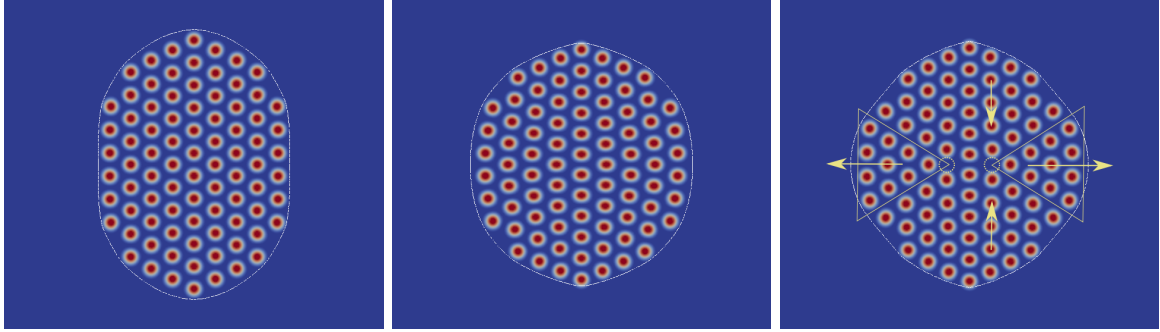
Figure 4.10 – *Particles in an ellipsoidal domain. Top-Left: Initial configuration, particles no not fit in the ellipse. Left: Phase-field is adapted to particle-distribution. Center: Surface-tension drives the interface to relax. Optimal form of the interface would be a circle. Due to the interaction with the particles a faceted interface is build up. Right: Particle-layers slide over each other to fit better into the deformed ellipse.*

4.3.5 First results

In Figure 4.10 the evolution of an ellipsoidal fluid interface, indicated by a white line, is shown with particles confined in the inner phase. An ellipse would relax to a circular shape if no external force inhibits this evolution. The particles, on the other hand, may be compressed to hexagonal shape and are slightly deformable, depending on the mobility parameter M_{pfc}, i.e., a small mobility allows larger deformations than larger mobilities. Thus, we see a stretching of the initial crystal configuration that breaks up for large enough forces from the interface. In the right image of Figure 4.10 a triangular domain within the crystal is moved out to the left and right. Particle layers are slid over each other in order to allow the motion of a sub-crystal. This gives a shape that is more circular than before with less stretched particle shapes.

Replacing the Cahn-Hilliard equation by a simpler Allen-Cahn equation would allow for the study of a shrinking phase instead of having volume conservation as in the Cahn-Hilliard model. This may be a tool to study the development of supraparticles using the Navier-Stokes PFC model.

4.3.6 Conclusion and outlook

The Vacancy PFC model combined with a description of an evolving domain by a Cahn-Hilliard-Navier-Stokes model is analyzed and a simple model system is simulated to study the interplay between these three equations. It shows that the model may be a reasonable way to describe evolving (and also shrinking) droplets filled with confined colloidal particles and may be used to simulate supramolecules.

In [161, 262] spherical and ellipsoidal particles are confined in a spherical disc in order to study the formation of patterns in the domain. Therefore, the authors have considered active particles instead of passive ones, as in this chapter. The activity allows to form particle vortices and shows circular collective motion. A modification of the disc towards ellipsoidal shape shows a change in the motion patterns. It would be interesting to study the interplay between the emergence of collective motion and the evolution of the domain, interacting with the moving particles. This can be modeled by extending the Navier-Stokes Vacancy PFC model by a particle

polarization, as it is done in [176] and Section 3.2 for the classical PFC model and an activity similar to [256, 257].

CHAPTER 5

Block-Preconditioner for conserved gradient-flow approaches

$\mathbb{I}$ N *the previous sections a preconditioner for the Phase-Field Crystal equation was developed, analyzed and applied to various model systems, which incorporate small modifications to the classical PFC model. Part of the PFC preconditioner is a preconditioner for the Cahn-Hilliard equation. Both equations are H^{-1}-gradient flows of a Ginzburg-Landau type energy, i.e., a gradient-expansions plus a polynomial part. In order to develop preconditioners for higher order expansions a generalization of the PFC/CH preconditioner approach is proposed in this chapter that allows to formulate preconditioners for various H^{-1}-gradient flow models.*

We propose and analyze a discretization of a conserved Lifshitz-Petrich model in Section 5.2, which describes the crystallization of quasicrystals and acts as a model system for a higher order gradient-flow model. Results are shown for quasicrystals with 5-fold and 12-fold symmetry in domains that exploit the symmetry of the structure. Additionally, the crystallization of a 12-fold symmetric quasicrystal in the flat two-dimensional space, as well as on the surface of a sphere, is investigated.

5.1 Preconditioner for gradient-flow approaches

All the analyzed models in this thesis have in common, that they are based on a dynamic density functional theory that minimizes an approximation of a Helmholtz free-energy F_{H}. This functional arises from a functional Taylor expansion of an excess-free part the energy, F_{exc}, and a Fourier-expansion, i.e., a gradient-expansion, of the second variational derivative of the energy, that is, the two-point direct correlation function (for details see Section 2.1.1). Thereby, the Cahn-Hilliard energy can be seen as a first-order expansion, whereas the Phase-Field Crystal and Swift-Hohenberg energy as a second-order expansion. Higher-order expansions were explained in [123, 123, 122], i.e., an eighth-order PFC model. A second-mode (multi-mode) PFC model was introduced in [2, 178, 21, 22] and is analyzed in Section 5.2.

For the development of a preconditioner for all of those models a more general approach than the preconditioner of Section 1.3 needs to be formulated. This generalization includes the

PFC and Cahn-Hilliard preconditioner as special cases.

We start with a free-energy that all introduced models are based on, in an abstract form

$$F[\psi] = \int_\Omega \frac{1}{2}\psi p(\Delta)\psi + \mathbb{f}(\psi)\,\mathrm{d}\mathbf{x}\;,$$

where p is a polynomial of the differential operator Δ. Examples that fit into this form of the energy include the Cahn-Hilliard energy [52, 49]

$$F_{\mathrm{ch}}[\psi] = \int_\Omega -\frac{1}{2}\epsilon^2\psi\Delta\psi + \mathbb{f}_{\mathrm{ch}}(\psi)\,\mathrm{d}\mathbf{x}\;\;\text{with}\;\mathbb{f}_{\mathrm{ch}}(\psi) = \frac{1}{4}\psi^2(1-\psi)^2$$
$$\Rightarrow\; p(\Delta) = -\epsilon^2\Delta\;,$$

the Swift-Hohenberg energy [247, 78]

$$F_{\mathrm{sh}}[\psi] = \int_\Omega \frac{1}{2}\psi(1+\Delta)^2\psi + \mathbb{f}_{\mathrm{sh}}(\psi)\,\mathrm{d}\mathbf{x}\;\;\text{with}\;\mathbb{f}_{\mathrm{sh}}(\psi) = r\psi^2 + \frac{1}{4}\psi^4$$
$$\Rightarrow\; p(\Delta) = (1+\Delta)^2\;,$$

the eighth-order PFC energy [123]

$$F_{\mathrm{eof}}[\psi] = \int_\Omega \frac{1}{2}\psi\big(A_0(1+\Delta)^2 + A_1(1+\Delta)^4\big)\psi + \mathbb{f}_{\mathrm{eof}}(\psi)\,\mathrm{d}\mathbf{x}\;\;\text{with}\;\mathbb{f}_{\mathrm{eof}}(\psi) = a_2\psi^2 + a_3\psi^3 + a_4\psi^4$$
$$\Rightarrow\; p(\Delta) = A_0(1+\Delta)^2 + A_1(1+\Delta)^4\;,$$

and the Lifshitz-Petrich energy [149, 34, 2]

$$F_{\mathrm{lp}}[\psi] = \int_\Omega \frac{1}{2}c\psi(1+\Delta)^2(q_0^2+\Delta)^2\psi + \mathbb{f}_{\mathrm{lp}}(\psi)\,\mathrm{d}\mathbf{x}\;\;\text{with}\;\mathbb{f}_{\mathrm{lp}}(\psi) = r\psi^2 - \frac{1}{3}\psi^3 + \frac{1}{4}\psi^4$$
$$\Rightarrow\; p(\Delta) = c(1+\Delta)^2(q_0^2+\Delta)^2.$$

All those energies are based on a gradient expansion of the unknown excess free-energy F_{exc}.

The corresponding H^{-1}-gradient-flow of the energies can be formulated as

$$\partial_t\psi - \Delta\big(p(\Delta)\psi + f(\psi)\big) = 0$$

with $f = \mathbb{f}'$. A simple backward Euler discretization, using a linearization of f around the old timestep, leads to the time-discrete system with timestep width τ

$$\psi_{k+1} - \tau\Delta\big(p(\Delta)\psi_{k+1} + f'(\psi_k)\psi_{k+1}\big) = \psi_k - \tau\Delta\big(f'(\psi_k)\psi_k - f(\psi_k)\big)$$

that can be formulated as 2x2 block system

$$\underbrace{\begin{bmatrix} 1 & -p_2(\Delta) \\ \tau p_1(\Delta) & 1-\tau\Delta f' \end{bmatrix}}_{A}\begin{pmatrix} \mu \\ \psi_{k+1} \end{pmatrix} = \begin{pmatrix} 0 \\ \psi_k - \tau\Delta\big(f'(\psi_k)\psi_k - f(\psi_k)\big) \end{pmatrix}$$

with $p_1(\Delta)p_2(\Delta) = -\Delta p(\Delta)$ a regular splitting of the polynomial p.

Following the ideas of [25, 49], an approximation of A can be formulated that has a simple triangular factorization, by adding a perturbation to the diagonal element,

$$A \approx P := \begin{bmatrix} 1 & -p_2(\Delta) \\ \tau p_1(\Delta) & 1 + \delta(\alpha p_1(\Delta) + \frac{1}{\alpha} p_2(\Delta)) \end{bmatrix} = \begin{bmatrix} 1 & 0 \\ \tau p_1(\Delta) & 1 + \delta \alpha p_1(\Delta) \end{bmatrix} \begin{bmatrix} 1 & -p_2(\Delta) \\ 0 & 1 + \frac{\delta}{\alpha} p_2(\Delta) \end{bmatrix}$$
(5.1)

with $\delta = \sqrt{\tau}, \alpha > 0$, where we require that $1 + \delta \alpha p_1(\Delta)$ and $1 + \frac{\delta}{\alpha} p_2(\Delta)$ are invertible. In terms of a finite-element discretization, using the shortcuts $\mathbf{M}$ and $\mathbf{K}$, introduced in Section 1.2, the block systems read

$$\mathbf{A} = \begin{bmatrix} \mathbf{M} & -\mathbf{P}_2 \\ \tau \mathbf{P}_1 & \mathbf{M} + \tau \mathbf{K} \mathbf{M}^{-1} \mathbf{N} \end{bmatrix}, \quad \mathbf{P} = \begin{bmatrix} \mathbf{M} & -\mathbf{P}_2 \\ \tau \mathbf{P}_1 & \mathbf{M} + \delta(\alpha \mathbf{P}_1 + \frac{1}{\alpha} \mathbf{P}_2) \end{bmatrix},$$

where $\mathbf{N}$ corresponds to a discretization and assembling of the linearized polynomial term and $\mathbf{P}_1$, $\mathbf{P}_2$ to a discretization of the differential operators p_1 and p_2 respectively, with

$$-\Delta \rightsquigarrow \mathbf{K}, \quad \Delta^2 \rightsquigarrow \mathbf{K} \mathbf{M}^{-1} \mathbf{K}.$$

Example 5.1. *The Cahn-Hilliard preconditioner of [49] implements the polynomial factorization $p_1(\Delta) = -\Delta$ and $p_2(\Delta) = -\epsilon^2 \Delta$. Using the factor $\alpha := \epsilon$, we obtain the proposed preconditioner*

$$\mathbf{P}_{\mathrm{ch}} = \begin{bmatrix} \mathbf{M} & -\epsilon^2 \mathbf{K} \\ \tau \mathbf{K} & \mathbf{M} + 2\epsilon\delta \mathbf{K} \end{bmatrix}.$$

◁

Example 5.2. *In the Phase-Field Crystal preconditioner of Section 1.3 we have used the factorization $p_1(\Delta) = -\Delta$ and $p_2(\Delta) = 2\Delta + \Delta^2$, where we have put the lowest order (constant) term of $p(\Delta)$ into the function f. This leads to $\mathbf{P}_1 = \mathbf{K}$ and $\mathbf{P}_2 = -2\mathbf{K} + \mathbf{K}\mathbf{M}^{-1}\mathbf{K}$. Using the factor $\alpha := 1$, we obtain the preconditioner-matrix*

$$\mathbf{P}_{\mathrm{pfc}} = \begin{bmatrix} \mathbf{M} & 2\mathbf{K} - \mathbf{K}\mathbf{M}^{-1}\mathbf{K} \\ \tau \mathbf{K} & \mathbf{M} - \delta \mathbf{K} + \delta \mathbf{K}\mathbf{M}^{-1}\mathbf{K} \end{bmatrix}.$$

◁

Applying the precondition operator $\mathbf{P}$ to a vector $(\mathbf{b}_0, \mathbf{b}_1)^\top$, i.e., solving $\mathbf{P}\mathbf{x} = \mathbf{b}$, can be carried out in a sequence of simple to perform steps,

(1) $\mathbf{M}\mathbf{y}_0 = \mathbf{b}_0$,   (2) $(\mathbf{M} + \delta\alpha\mathbf{P}_1)\mathbf{y}_1 = \mathbf{b}_1 - \tau\mathbf{P}_1\mathbf{y}_0$,

(3) $(\mathbf{M} + \frac{\delta}{\alpha}\mathbf{P}_2)\mathbf{x}_1 = \mathbf{M}\mathbf{y}_1$,   (4) $\mathbf{x}_0 = \mathbf{y}_0 + \frac{\alpha}{\delta}(\mathbf{y}_1 - \mathbf{x}_1)$,   (5.2)

where we can simplify step (2) to

(2a) $(\mathbf{M} + \delta\alpha\mathbf{P}_1)\mathbf{z} = \mathbf{b}_1 + \frac{\tau}{\delta\alpha}\mathbf{b}_0$,   (2b) $\mathbf{y}_1 = \mathbf{z} - \frac{\tau}{\delta\alpha}\mathbf{y}_0$.

Nevertheless, in step (2) and (3) a nontrivial linear system must be solved. In the case of the PFC equation a Δ^2 term is involved in $1 + \frac{\delta}{\alpha}p_2(\Delta)$. By applying the approximation idea (5.1)

recursively, i.e., factorizing the polynomials, until a simple to solve system is reached, an overall preconditioner can be formulated. Therefore, we have to write $1 + \delta\alpha p_1(\Delta)$ and $1 + \frac{\delta}{\alpha}p_2(\Delta)$ as H^{-1}-gradient flow systems, i.e.,

$$
\begin{aligned}
1 + \delta\alpha p_1(\Delta) &= 1 - \tau_1\Delta\big(C_1 + p'_1(\Delta)\big) \text{ and} \\
1 + \frac{\delta}{\alpha}p_2(\Delta) &= 1 - \tau_2\Delta\big(C_2 + p'_2(\Delta)\big),
\end{aligned}
\tag{5.3}
$$

respectively, with C_1, C_2 some constante, $\tau_1 = \delta\alpha$, $p'_1 \in \mathbb{P}_0$, and $\tau_2 = \frac{\delta}{\alpha}$, $p'_2 \in \mathbb{P}_0$. The polynomial space $\mathbb{P}_0$ denotes the set of polynomials that vanishes at the origin, i.e.,

$$
\mathbb{P}_0 := \{p \in \mathbb{P} \mid p(0) = 0\}.
$$

This can be achieved, if we have $p_1, p_2 \in \mathbb{P}_0$. The constants C_i are neglected in the preconditioners, as it is done for the f' term in (5.1).

Example 5.3. *In the case of the PFC preconditioner, we have $p_2 = 2\Delta + \Delta^2$ and thus $p'_2(\Delta) = -\Delta \Rightarrow C_2 = -2$. A factorization similar to (5.1) leads to*

$$
\mathbf{P}' = \begin{bmatrix} \mathbf{M} & -\mathbf{K} \\ \tau_2\mathbf{K} & \mathbf{M} + 2\sqrt{\tau_2}\mathbf{K}, \end{bmatrix}
$$

with $\tau_2 = \frac{\delta}{\alpha} = \sqrt{\tau}$ and thus the Cahn-Hilliard preconditioner.   ◁

Spectral analysis of the preconditioner

For estimating the properties of the preconditioner we follow the approach of Section 1.5 and analyze the symbols of the operators A and P. Let $\mathbf{k} = (k_1, k_2, k_3)$ be the wave vector and denote $\mathcal{A}$ the symbol of A and $\mathcal{P}$ the symbol of P with

$$
\mathcal{A} = \begin{bmatrix} 1 & -p_2(-\mathbf{k}^2) \\ \tau p_1(-\mathbf{k}^2) & 1 \end{bmatrix}, \quad \mathcal{P} = \begin{bmatrix} 1 & -p_2(-\mathbf{k}^2) \\ \tau p_1(-\mathbf{k}^2) & 1 + \sqrt{\tau}\big(\alpha p_1(-\mathbf{k}^2) + \frac{1}{\alpha}p_2(-\mathbf{k}^2)\big) \end{bmatrix},
$$

respectively. Calculating the eigenvalues of the preconditioned symbol $\mathcal{Q} := \mathcal{A}\mathcal{P}^{-1}$ gives the set

$$
\sigma(\mathcal{Q}) = \left\{1, \frac{1 + \tau p_1(-\mathbf{k}^2)p_2(-\mathbf{k}^2)}{1 + \tau p_1(-\mathbf{k}^2)p_2(-\mathbf{k}^2) + \sqrt{\tau}(\alpha p_1(-\mathbf{k}^2) + \frac{1}{\alpha}p_2(-\mathbf{k}^2))} \; \middle| \; \mathbf{k} \in \mathbb{R}^m \right\}.
\tag{5.4}
$$

The following theorem shows, that for an appropriate splittings of the polynomial p an overall good preconditioner $\mathcal{P}$, in the sense of spectral similarity to the operator $\mathcal{A}$, is constructed.

Theorem 6. *For the eigenvalues λ of the preconditioned operator $\mathcal{Q}$ the following statements hold true:*

1. *If $p_1(-\mathbf{k}^2), p_2(-\mathbf{k}^2) \geq 0 \; \forall \mathbf{k} \in \mathbb{R}^m$, then $0 < \lambda \leq 1$.*

2. *If $p_1, p_2 \in \mathbb{P}_0 \Rightarrow \lambda \xrightarrow{|\mathbf{k}| \to 0} 1$.*

3. Let the requirements of Statement 1. be fulfilled and let $C_1, C_2 > 0$ with $p_1 = C_1 + \tilde{p}_1$, $\tilde{p}_1 \in \mathbb{P}_0$ and $p_2 = C_2 + \tilde{p}_2$, $\tilde{p}_2 \in \mathbb{P}_0$. Then Statement 2. can be generalized to

$$\lambda \xrightarrow{|\mathbf{k}| \to 0} \frac{1 + \tau C_1 C_2}{(1 + \sqrt{\tau}\alpha C_1)(1 + \sqrt{\tau}\frac{1}{\alpha}C_2)} \leq 1.$$

4. $\lambda \xrightarrow{\tau \to 0} 1$.

5. If $p_1 = p_2$, with $\left[\alpha p_1(-\mathbf{k}^2) + \frac{1}{\alpha}p_2(-\mathbf{k}^2)\right] \geq 0$, then the eigenvalues are bounded from below, i.e., $\lambda \in \left[\frac{2\alpha}{(1+\alpha)^2}, 1\right]$ with optimal $\alpha = 1$.

Proof. Statements 1, 2, 3, and 4 follow directly from the structure of the rational function

$$\lambda = \frac{1 + \tau p_1 p_2}{1 + \tau p_1 p_2 + \sqrt{\tau}(\alpha p_1 + \frac{1}{\alpha}p_2)}$$

when ignoring the argument $-\mathbf{k}^2$. Statement 5. can easily be verified, by setting $p := p_1 = p_2$ and analyzing the critical points with $\partial_p \lambda = 0$:

$$\partial_p \lambda = \frac{\alpha(1 + \alpha^2)\sqrt{\tau}(\tau p^2 - 1)}{\left(\alpha(1 + \tau p^2) + (1 + \alpha^2)\sqrt{\tau}p\right)^2}.$$

It follows $\partial_p \lambda = 0 \Leftrightarrow p = p^* := \pm 1/\sqrt{\tau}$ and $\partial_p^2 \lambda(p^*) = \pm 2\tau\alpha(1 + \alpha^2)/(1 \pm \alpha)^4$. Thus, the minimal eigenvalue is achieved at p_+^*, that is $\lambda_{\min} = \lambda(p_+^*) = 2\alpha/(1 + \alpha)^2$.

The critical point with respect to α can be calculated, by

$$\partial_\alpha \lambda(p^*) = \frac{2(1 - \alpha)}{(1 + \alpha)^3} = 0 \Leftrightarrow \alpha = \alpha^* := 1$$

with $\partial_\alpha^2 \lambda(p^*, \alpha^*) = -\frac{1}{4}$. $\square$

Remark 7. *A simple modification of Statement 5. of Theorem 6 recapitulates Proposition 2 in [49] and Proposition 4.1. in [25], for the special case, that $\epsilon^2 p_1 = p_2 = -\epsilon^2\Delta$. We obtain the eigenvalue bounds $\lambda \in [\frac{1}{2}, 1]$.* ◁

5.2 A Quasi-Crystal Phase-Field Crystal model

Historically, crystals were seen as structures with a periodic order. The macroscopic shape is thereby determined by its internal periodic microstructure. Periodicity implies a limited choice of allowed rotational symmetries in the crystalline patterns, i.e., 2-, 3-, 4-, and 6-fold symmetry. A long period of time it was assumed, that there exist no other crystallographic structures in nature, especially no aperiodic tilings in the crystalline patterns.

In the middle of the 20th century this historic assumption broke down. Shechtman and coworkers [233] observed in electron diffraction patterns of a rapidly cooled alloy of Al-Mn a five-fold symmetry. Later Levine and Steinhardt [144] named these crystalline structures with those aperiodic patterns *Quasi-Crystals*. Mathematically, these structures were analyzed and

published by Penrose [196, 197]. These pioneering works have lead to many experimentally observed and reported Quasi-Crystals.

Starting from the research of Lifshitz and Petrich [149, 148, 147] a free-energy for systems with higher order symmetry was formulated. This free-energy is similar to the Swift-Hohenberg functional introduced in equation (1.1) and named later *Liftshitz-Petrich energy*. Minimizing the free-energy, using an L_2-gradient flow, Zhang [127] and others have shown patterns with the proposed symmetries. Here we analyze an extension to conserved evolutions, applying the H^{-1}-gradient flow to the free-energy minimization. This was investigated recently in [2] to analyze the growth of a quasicrystalline patterns in two spatial dimensions. A discretization with finite-elements has been applied to the resulting dynamical equations. We analyze stability and the properties of a preconditioner for the linear system arising from the FEM-discretization of the system and show simulations that exploit the symmetry already in the discretization of the grid.

5.2.1   Modelling

We consider the Liftshitz-Petrich (LP) energy [149, 33, 34]

$$F_{\mathrm{lp}}[\psi] = \int_\Omega \frac{1}{4}\psi^4 - \frac{1}{3}\psi^3 + \frac{1}{2}\psi\big(r + c(1+\Delta)^2(q_0^2 + \Delta)^2\big)\psi\,\mathrm{d}\mathbf{x} \qquad (5.5)$$

with phenomenological parameters r, q_0, and c. In contrast to the Swift-Hohenberg energy (1.1) a cubic term is included in the original LP-energy. In [2] and others this term is neglected, as it can be eliminated by rescaling and shifting of the order-parameter field ψ. This is shown in Section 2.2.5 for the non-dimensionalization of the PFC model.

Achim et al. [2] have introduced a H^{-1}-gradient flow of the LP-energy,

$$\begin{aligned}
\partial_t\psi &= M_0\Delta\frac{\delta F_{\mathrm{lp}}[\psi]}{\delta\psi} \\
&= M_0\Delta\big\{c(1+\Delta)^2(q_0^2+\Delta)^2\psi + r\psi - \psi^2 + \psi^3\big\}
\end{aligned} \qquad (5.6)$$

with a constant mobility M_0. This may be extended towards non-constant mobilities, but this is not subject of this chapter.

Linear stability analysis of the equations shows parameter regimes, where (quasi-)crystalline structure can be expected.

Theorem 7. *The H^{-1}-Quasi-Crystals (QPFC) equation (5.6) is unstable with respect to small perturbations of a constant phase $\bar\psi$, if*

$$3\bar\psi - 2\bar\psi + r < 0\,,$$

for the system parameters $r, \bar\psi$, and $M_0 > 0$.

Proof. Let $\psi = \bar\psi + \eta$ be the density expansion around $\bar\psi$ for perturbations $\eta \ll 1$. Inserting this into the QPFC-equation (5.6) and neglecting higher order powers of η, we obtain an evolution equation for the perturbation,

$$\partial_t\eta = \nabla \cdot M_0\nabla\big\{c(1+\Delta)^2(q_0^2+\Delta)^2\eta + r\eta + (3\bar\psi^2 - 2\bar\psi)\eta\big\}. \qquad (5.7)$$

The Fourier transform of equation (5.7) with $\hat{\eta} := \mathcal{F}(\eta)(\mathbf{k}, t)$, leads to

$$\partial_t \hat{\eta} = -M_0 \mathbf{k}^2 \big\{ c(1 - \mathbf{k}^2)^2 (q_0^2 - \mathbf{k}^2)^2 + r + 3\bar{\psi}^2 - 2\bar{\psi} \big\} \hat{\eta} =: -A\hat{\eta}.$$
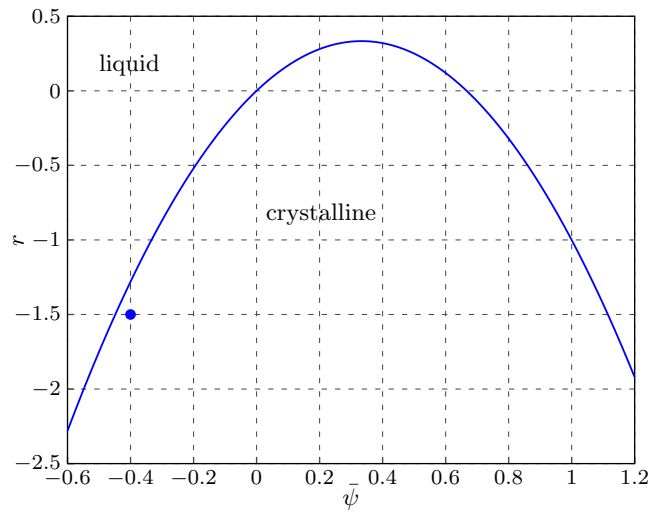
Stability can be achieved for

$$A = M_0 \mathbf{k}^2 \big\{ c(1 - \mathbf{k}^2)^2 (q_0^2 - \mathbf{k}^2)^2 + r + 3\bar{\psi}^2 - 2\bar{\psi} \big\} > 0.$$

A necessary condition for stability is $r + 3\bar{\psi}^2 - 2\bar{\psi} > 0$ (i.e., for the limiting cases $\mathbf{k} \to \{1, q_0\}$) and thus instability can be found for r and $\bar{\psi}$ that fulfill the relation

$$r + 3\bar{\psi}^2 - 2\bar{\psi} < 0.$$

$\square$

Figure 5.1 – *Linear stability diagram for the QPFC equation. The blue dot corresponds to the simulation parameter for the preconditioner studies ($\bar{\psi} = -0.4, r = -1.5$). In [2] a more detailed phase-diagram was published. There, a separation of phases and coexistence regions were shown.*

The parameter r in the energy can be interpreted as distance to a critical temperature of the system and the parameter c is a simple scaling parameter that can be eliminated by rescaling of the energy. The third parameter q_0 controls the symmetry of the system, as it is explained in [33, 127], among others. Therefore, we choose q_0 of the form

$$q_0 = 2\cos\Big(\frac{\pi}{SYM}\Big),$$

where SYM names the integral symmetry number, i.e., 12-fold symmetry is achieved by $q_0 = 2\cos(\pi/12) = \sqrt{2 + \sqrt{3}}$ and 4-fold symmetry by $q_0 = \sqrt{2}$.

5.2.2   Solving the QPFC-equation

In order to solve the partial differential equation (5.6) we show a variational formulation discretized using finite-elements. Therefore, the higher-order derivatives are split into a sequence of second-order derivatives:

$$
\begin{aligned}
\psi^{\natural} &= (1 + 2\Delta)\mu + \Delta\mu^{\flat} + r\psi - \psi^2 + \psi^3 \ , \\
\partial_t \psi &= M_0 \Delta\psi^{\natural} \ , \\
\mu &= cq_0^2(q_0^2 + 2\Delta)\psi + c\Delta\psi^{\flat} \ , \\
\mu^{\flat} &= \Delta\mu \ , \\
\psi^{\flat} &= \Delta\psi \ .
\end{aligned}
\tag{5.8}
$$

A backward Euler discretization in time, a linearization of the nonlinear term $\psi^3 - \psi^2$ around the old timestep and a finite-element discretization in space lead to a sequence of linear problems that need to be solved in rotation: Let $\psi_0 \in L_2(\Omega)$ be given. For $k = 0, 1, \ldots, N - 1$ find $\psi_{k+1}, \psi_{k+1}^{\natural}, \psi_{k+1}^{\flat}, \mu_{k+1}, \mu_{k+1}^{\flat} \in V_h$, s.t.

$$
\begin{aligned}
(\psi_{k+1}^{\natural} - \mu_{k+1} - \big(r + 3\psi_k^2 - 2\psi_k\big)\psi_{k+1}, \vartheta_h)_{\Omega} + (2\nabla\mu_h + \nabla\mu_{k+1}^{\flat}, \nabla\vartheta_h)_{\Omega} &= (-2\psi_k^3 + \psi_k^2, \vartheta_h)_{\Omega} \ , \\
\big(\psi_{k+1}, \vartheta_h'\big)_{\Omega} + \tau_k(M_0\nabla\psi_{k+1}^{\natural}, \nabla\vartheta_h')_{\Omega} &= \big(\psi_k, \vartheta_h'\big)_{\Omega} \ , \\
(\mu_{k+1} - cq_0^4\psi_{k+1}, \vartheta_h'')_{\Omega} + c(2q_0^2\nabla\psi_{k+1} + \nabla\psi_{k+1}^{\flat}, \nabla\vartheta_h'')_{\Omega} &= 0 \ , \\
(\mu_{k+1}^{\flat}, \vartheta_h''')_{\Omega} + (\nabla\mu_h, \nabla\vartheta_h''')_{\Omega} &= 0 \ , \\
(\psi_{k+1}^{\flat}, \vartheta_h^{(iv)})_{\Omega} + (\nabla\psi_{k+1}, \nabla\vartheta_h^{(iv)})_{\Omega} &= 0 \ ,
\end{aligned}
\tag{5.9}
$$

for all $\vartheta_h, \vartheta_h', \vartheta_h'', \vartheta_h''', \vartheta_h^{(iv)} \in V_h$. Using the shortcuts $\mathbf{M}$ and $\mathbf{K}$ for mass-matrix and stiffness-matrix, $\mathbf{F}(\psi) := \big((-3\psi^2\theta_j + 2\psi\theta_j, \theta_i)_{\Omega}\big)_{ij}$ and $\mathbf{f}(\psi) := \big((-2\psi^3 + \psi^2, \theta_i)_{\Omega}\big)_i$ for the nonlinear terms, we can write the system matrix $\mathbf{A}$ and right-hand-side vector $\mathbf{b}$ as

$$
\mathbf{A} = \begin{bmatrix}
\mathbf{M} & \mathbf{F}(\psi_k) - r\mathbf{M} & -\mathbf{M} + 2\mathbf{K} & \mathbf{K} & 0 \\
\tau M_0\mathbf{K} & \mathbf{M} & 0 & 0 & 0 \\
0 & -cq_0^4\mathbf{M} + 2cq_0^2\mathbf{K} & \mathbf{M} & 0 & c\mathbf{K} \\
0 & 0 & \mathbf{K} & \mathbf{M} & 0 \\
0 & \mathbf{K} & 0 & 0 & \mathbf{M}
\end{bmatrix}, \quad
\mathbf{b} = \begin{pmatrix}
\mathbf{f}(\psi_k) \\
\mathbf{M}\psi_k \\
0 \\
0 \\
0
\end{pmatrix}
\tag{5.10}
$$

with $x = (\boldsymbol{\psi}_{k+1}^{\natural}, \boldsymbol{\psi}_{k+1}, \boldsymbol{\mu}_{k+1}, \boldsymbol{\mu}_{k+1}^{\flat}, \boldsymbol{\psi}_{k+1}^{\flat})^{\top}$.

Preconditioner for the QPFC-system

We follow the general approach developed in the last section and provide a splitting of the polynomial $-\Delta p(\Delta) = -c\Delta(1 + \Delta)^2(q_0^2 + \Delta)^2$, corresponding to the splitting in equations (5.8), that is,

$$
p_1(\Delta) = -\Delta(1 + \Delta)^2, \quad p_2(\Delta) = c(q_0^2 + \Delta)^2.
\tag{5.11}
$$

Introducing the sub H^{-1}-gradient flows, as in equation (5.3), we get the PFC equation and the Cahn-Hilliard equation as part of the QPFC preconditioner, i.e.,
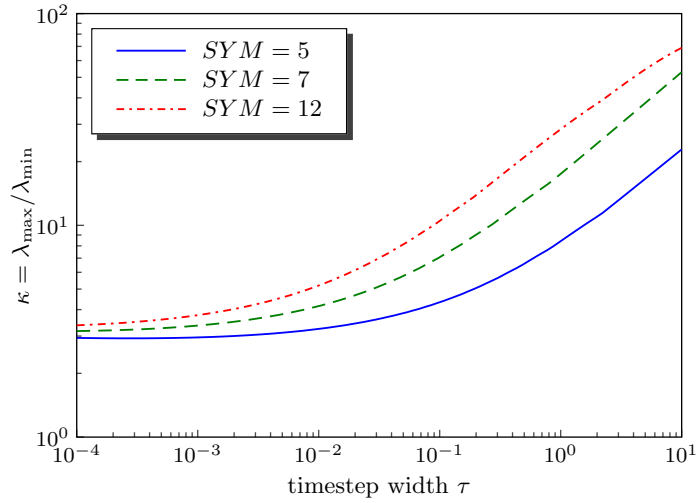
$$
\begin{aligned}
1 + \tau_1 p_1(\Delta) &= 1 - \tau_1\Delta\big(1 + 2\Delta + \Delta^2\big) \rightsquigarrow 1 - \tau_1\Delta\big(2\Delta + \Delta^2\big), \\
1 + \tau_2 p_2(\Delta) &= (1 + \tau_2 cq_0^4) - \tau_2\Delta\big(-2cq_0^2 - \Delta\big) \rightsquigarrow 1 - \tau_2\Delta\big(-c\Delta\big),
\end{aligned}
\tag{5.12}
$$

where again we have negelected the lowest order terms. In order to precondition a QPFC equation we have to apply the PFC preconditioner followed by a Cahn-Hilliard preconditioner. Writing this as a sequence of solver steps, we obtain:

$$
\text{(1) } \mathbf{M}\mathbf{y}_2 = \mathbf{b}_2, \qquad\qquad \text{(2.1) } (\mathbf{M} + \tau_1^{1/2}\mathbf{K})\mathbf{u}_0 = \mathbf{b}_1 - \frac{\tau}{\tau_1}\mathbf{b}_2,
$$

$$
\text{(2.2) } (\mathbf{M} + \tau_1^{1/4}\mathbf{K})\mathbf{u}_1 = \mathbf{M}\mathbf{u}_0, \qquad \text{(2.3) } (\mathbf{M} + \tau_1^{1/4}\mathbf{K})\mathbf{u}_2 = \mathbf{M}\mathbf{u}_1, \qquad (5.13)
$$

$$
\text{(3.1) } (\mathbf{M} + (c\tau_2)^{1/2}\mathbf{K})\mathbf{u}_3 = \mathbf{M}\mathbf{u}_2 - \frac{\tau}{\tau_1}\mathbf{b}_2, \qquad \text{(3.2) } (\mathbf{M} + (c\tau_2)^{1/2}\mathbf{K})\mathbf{x}_1 = \mathbf{M}\mathbf{u}_3,
$$

$$
\text{(4) } \mathbf{x}_2 = \mathbf{y}_2 + \tau_2^{-1}(\mathbf{u}_2 - \frac{\tau}{\tau_1}\mathbf{y}_2 - \mathbf{x}_1)
$$

with the solution components $\mathbf{x} = (\boldsymbol{\psi}^{\natural}, \boldsymbol{\psi}, \boldsymbol{\mu}, \boldsymbol{\mu}^{\flat}, \boldsymbol{\psi}^{\flat})$. In order to precondition all block-vector components we have to solve the additional steps

$$
\text{(5) } \mathbf{M}\mathbf{x}_4 = \mathbf{b}_4 - \mathbf{K}\mathbf{x}_1, \qquad\qquad \text{(6) } \mathbf{M}\mathbf{x}_3 = \mathbf{b}_3 - \mathbf{K}\mathbf{x}_2,
$$

$$
\text{(7.1) } \mathbf{M}\mathbf{y}_0 = \mathbf{b}_0 - \mathbf{K}\mathbf{x}_3, \qquad\qquad \text{(7.2) } \mathbf{x}_0 = \mathbf{y}_0 + \mathbf{x}_2 + 2\mathbf{x}_3.
$$

Figure 5.2 – *The condition number $\kappa := \frac{\lambda_{\max}}{\lambda_{\min}}$ of the preconditioner symbol $\mathcal{Q}$ for three different symmetry numbers SYM, depending on the timestep width τ.*

In Figure 5.2 the spectral representation of the QPFC preconditioner is analyzed. Therefore, the eigenvalues of $\mathcal{Q}$ in (5.4) are examined and it is found, that $\lambda \in \sigma(\mathcal{Q})$ is real and positive, and since $p_1, p_2 \geq 0$ we have by Theorem 6 that $\lambda \in (0, 1]$. Thus, a meaningful value that describes the convergence of a Krylov subspace methods is the condition number $\kappa := \frac{\lambda_{\max}}{\lambda_{\min}}$. In Section 1.4.2 the asymptotic convergence factor ρ is given in terms of κ, see (1.29). For increasing timestep width τ the condition number also increases and we have greater condition numbers for greater symmetry numbers.
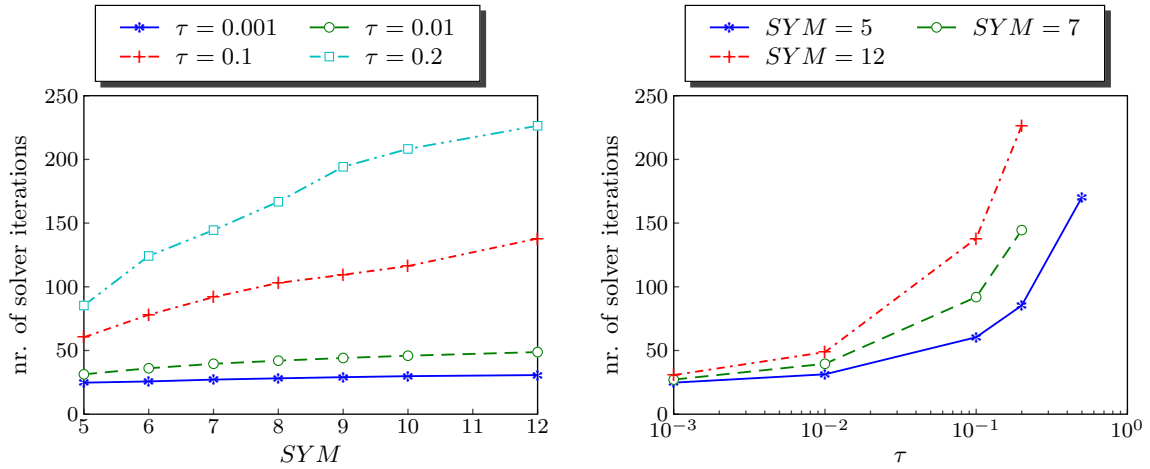
Figure 5.3 – *Left: Number of solver iterations versus symmetry number SYM, shown for various timestep widths τ. We see an increase in the solver iterations for larger second mode $q = 2\cos(\pi/SYM)$. Right: Number of solver iterations versus timestep widths τ. For larger τ the solver iterations increases nearly linearly.*

Numerically, this behavior can be proven, by looking at a small setup with a symmetric positioning of SYM initial particles around the domain center, as it can be seen in the crystallization example in Figure 5.5. Running a simulation for 20 timesteps with timestep width τ and averaging the number of solver iterations over all these timesteps, shows an increase in the iteration number for increasing timestep width and increasing symmetry number. This is visualized in Figure 5.3.

5.2.3   Conclusion

We have formulated a finite-element discretization for a higher-order PFC model, based on an H^{-1}-gradient flow of the Lifshitz-Petrich energy. The system can be solved in non-rectangular domains, by exploiting the symmetric structure of the solution already in the setup of the problem. This can be seen in Figure 5.4, where the QPFC equation is solve on a triangular mesh with inner angle that conforms with the symmetry number SYM. Thus, the cost for assembling and inverting the linear system can be reduced a lot.

The numerical inversion of the arising linear system is performed using the gradient-flow preconditioner developed in general in the last section. Applied to the QPFC system we have analyzed a splitting of the polynomial derivative operator, with respect to a variation in timestep width and symmetry number. The theoretical results are conform to the numerical results and show reasonable performance, in terms of solver iterations, when using the preconditioned Krylov-subspace method FGMRES.
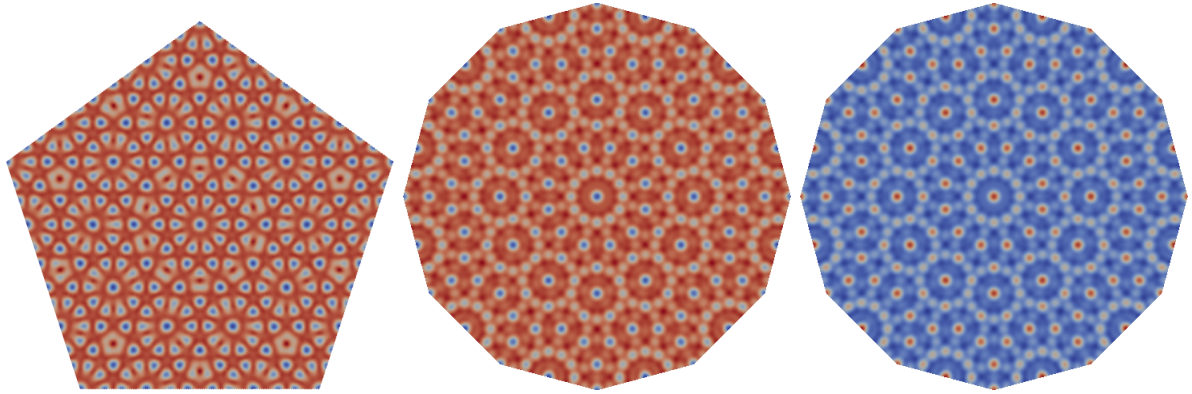
Figure 5.4 – *Quasi-Crystal pattern in a domain that enforces symmetry. Left: Honeycomb phase in 5-fold symmetry, Center: Honeycomb phase in 12-fold symmetry, Right: Plastic crystal in 12-fold symmetry. All simulations are performed in a triangular domain with inner angle $2\pi/SYM$ for the SYM-fold symmetry.*
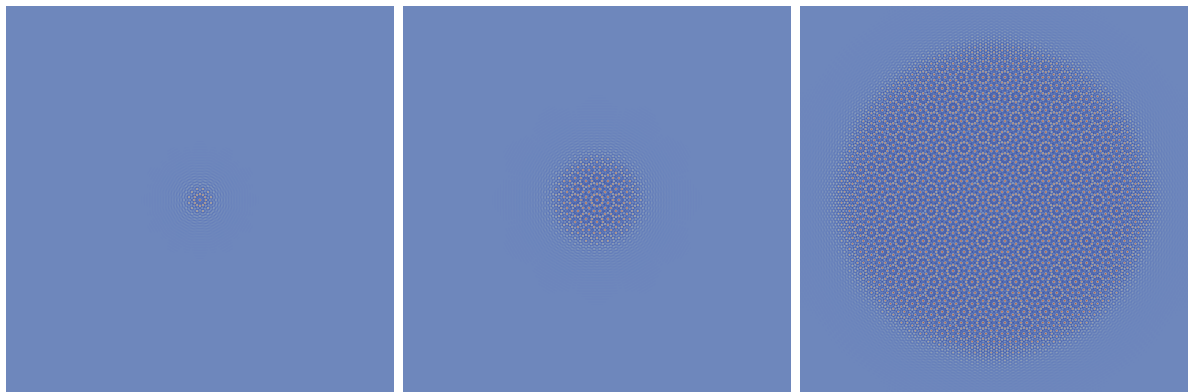
Figure 5.5 – *Crystallization of a quasicrystalline structure from a grain with 12-fold symmetry in the center of a domain. Total number of DOFs per component: 2,144,191. The simulation is parallelized and run using 96 cores.*

Alternative solution methods

$\mathbb{T}$HE *problem dependent block-preconditioners as developed in* Chapter 1 *and generalized in* Chapter 5 *are not the only way to solve the linear systems arising from a discretization of the Phase-Field Crystal equation. We summarize some methods introduced in the literature and tested in numerical experiments, which are alternative solution methods for the linear systems.*

We start from optimized direct solvers and continue with domain decomposition methods. Finally a combination of both approaches could be accomplished.

6.1 Accelerated multi-frontal solvers

Multi-frontal solvers like MUMPS [16] or UMFPACK [65] build a class of direct linear solvers, which calculate an LU-factorization of a sparse matrix $\mathbf{A}$. The algorithm was introduced in 1983 in the work of Duff and Reid [74]. Despite the numerical robustness and reliability, direct solvers are known to require a big amount of memory during their factorization procedure. This is due to the fact that, although the matrix is sparse, the triangular factors L and U might not be sparse, because of fill-in that is produced in the elimination process.

In order to reduce fill-in direct solvers perform a reordering of the unknowns. Let $\mathcal{G}$ be the adjacency graph of $\mathbf{A}$ (we assume a symmetric sparsity pattern of $\mathbf{A}$ and thus an undirected graph $\mathcal{G}$) and $\mathcal{S}$ a connected subgraph that separates two parts of $\mathcal{G}$, i.e., when $\mathcal{S}$ is removed from $\mathcal{G}$ two disjoint graphs remain. We call $\mathcal{S}$ a separator of $\mathcal{G}$. The three subsets of the vertices on $\mathcal{G}$, i.e., two unconnected subsets $\mathcal{D}_1$ and $\mathcal{D}_2$ and the separator $\mathcal{S}$, are numbered one after the other, starting with $\mathcal{D}_1$, then $\mathcal{D}_2$ and finally $\mathcal{S}$ (see Figure 6.1 (left) for a sketch of the graph structure).

This renumbering of the vertices and of the unknowns results, correspondingly, in a block
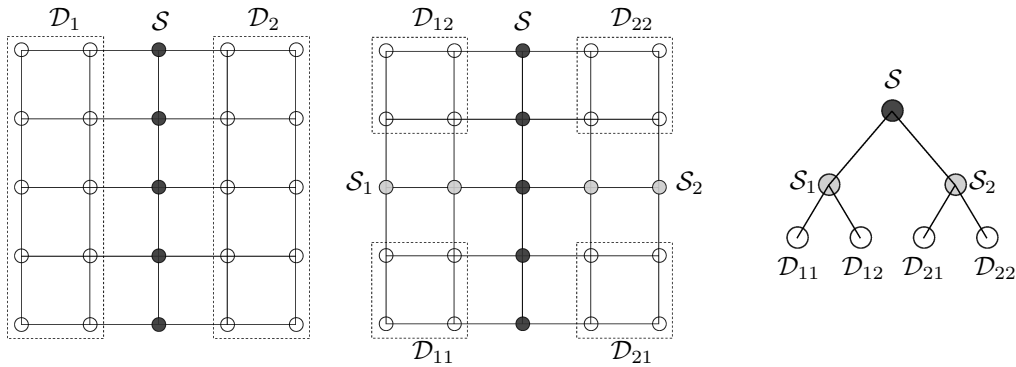
Figure 6.1 – *Left: First step of nested dissection procedure generates a separator $\mathcal{S}$ and two disjoint subgraphs $\mathcal{D}_1$ and $\mathcal{D}_2$. Center: The left and right subgraph are separated again by the separators $\mathcal{S}_1$ and $\mathcal{S}_2$, respectively. Right: The corresponding elimination tree.*

structure of $\mathbf{A}$ with a bottom-right-arrow pattern, which is preferable for the elimination process:

$$\mathbf{A} = \begin{bmatrix} A_{11} & & A_{1,S} \\ & A_{22} & A_{2,S} \\ A_{S,1} & A_{S,2} & A_{SS} \end{bmatrix}.$$

Since the factorization of the diagonal blocks A_{11} and A_{22} may also produce a lot of fill-in, the renumbering procedure is repeated recursively on these blocks. The recursive renumbering algorithms is called nested dissection ordering [225]. It is repeated until small enough blocks remain. The order of the elimination is now represented by an elimination tree, whose nodes correspond to the graph separators and the children of the nodes to the left and right subgraph $\mathcal{D}_1$ and $\mathcal{D}_2$, sketched in Figure 6.1 for a simple hexagonal grid arising from a finite-difference discretization.

Multi-frontal solvers build dense matrices $F^{(k)}$ in each level k of the elimination tree, composed of 2x2 blocks corresponding to the vertices of a separator $\mathcal{S}_k$ and some of its neighbor vertices $\mathcal{N}_k$, e.g.,

$$F^{(k=0)} = \begin{bmatrix} A_{\mathcal{S}_k \mathcal{S}_k} & A_{\mathcal{S}_k, \mathcal{N}_k} \\ A_{\mathcal{N}_k, \mathcal{S}_k} & 0 \end{bmatrix}$$

for the leaf level and $F^{(k)}$ build in the same way, combined with the Schur complements of the lower level frontal matrices, for $k > 0$ (see, e.g., [17]).

In classical approaches these matrices $F^{(k)}$ are factorized, e.g., by using a Schur complement approach and a factorization of the diagonal blocks. In the recent development of accelerated multi-frontal algorithms, the off-diagonal blocks of $F^{(k)}$ are approximate by a low-rank approximation, or the total matrix $F^{(k)}$ is approximated by an easier to factorize structure.

Various approaches were developed for matrices arising from different applications, e.g., approximating the frontal matrix by a hierarchically semiseparable (HSS) matrix [56], by a block low-rank (BLR) matrix [15], or by a hierarchically off-diagonal low-rank (HODLR) matrix [17, 18]. All those approaches lead to approximate solutions $\tilde{\mathbf{x}}$ of the linear system $\mathbf{Ax} = \mathbf{b}$

$n \approx 824,000$	factorization time [s]	memory [GB]	#iterations
Conventional	$2,259.23$	34.04	—
HODLR1	$1,590.44$	24.03	16
HODLR2	$2,506.32$	17.55	17

Table 6.1 – *Comparison of a conventional factorization procedure, i.e., without an approximation of the frontal matrices, to the HODLR approximation with two different levels of approximation.*

$n \approx 3,417,000$	factorization time [s]	memory [GB]	#iterations
Conventional	$42,137.3$	205	—
HODLR1	$19,368$	60	21

Table 6.2 – *Comparison of a conventional factorization procedure to the HODLR approximation for a large benchmark matrix.*

and are combined with an appropriate iterative solver for the residual equation $\mathbf{A}\delta\tilde{\mathbf{x}} = \mathbf{b} - \mathbf{A}\tilde{\mathbf{x}}$, $\mathbf{x} = \tilde{\mathbf{x}} + \delta\tilde{\mathbf{x}}$.

We analyze the HODLR approach for the Phase-Field Crystal system (1.8), by factorizing assembled matrices for a 3D test case as in Section 1.6 for the crystallization from an initial seed in one corner of the domain. The direct solver is not sensitive to variations in timestep width τ or grid resolution h, only the sparsity pattern and number of unknowns n are relevant. Thus, we set up two systems with different refinement level, both with finite-element Lagrange basis-function with polynomial degree $p = 4$, producing different matrix sizes. We compare an accelerated multi-frontal solver to the classical multi-frontal approach, i.e., without approximating the frontal matrices $F^{(k)}$. The outer iterative method is a GMRES method, solved up to an absolute tolerance of 10^{-7}.

In Table 6.1 and Table 6.2 the results, obtained in corporation with AmirHossein Aminfar from Stanford University cf. [17, 18], are summarized. It shows, that the factorization time can be reduced a lot, up the half of the conventional method, especially for larger matrices. Also the amount of memory, necessary to perform the factorization, drops down to the half or a third of the conventional method. Thus, using the accelerated multi-front solver larger systems can be solved. Combined with domain-decomposition methods, as also benchmarked in [18], huge setups can be handled.

The advantage of *LU*-factorization methods is clearly the ability of repeated solutions of the linear system with different right-hand-side vectors, as it is the case when used as a preconditioner in a Krylov-subspace iterations or in combination with a Rosenbrock time discretization, where all stages are solved with the same Jacobi-matrix and thus the factorization can be reused in the whole Rosenbrock procedure of one timestep.

Since the system matrix $\mathbf{A}$ (1.8) changes only in one block from timestep to timestep, namely in the discretization of the nonlinear term, a Schur complement approach could be implemented that holds the factorization of all time-constant matrices in memory and just updates the factorization of the changing block. Thus, a reduction of the size of the matrix to factorize reduces to one third of the full matrix size. Hence, the memory requirements and the factorization time

might be reduced correspondingly.

6.2 Block-jacobi preconditioners

Classical preconditioners for symmetric positive systems are based on a splitting of the system matrix $\mathbf{A} = \mathbf{D} - \mathbf{L} - \mathbf{U}$ with $\mathbf{D}$ the diagonal of $\mathbf{A}$, and $\mathbf{L}, \mathbf{U}$ the lower and upper triangular part of $\mathbf{A}$, respectively. Reformulating the linear system $\mathbf{Ax} = \mathbf{b}$ as fixed point problem,

$$\mathbf{Ax} = \mathbf{b} \Leftrightarrow \mathbf{Mx} = \mathbf{Nx} + \mathbf{b} \Leftrightarrow \mathbf{x} = \mathbf{x} + \mathbf{M}^{-1}(\mathbf{b} - \mathbf{Ax})$$

with $\mathbf{M}$ an invertible matrix and $\mathbf{A} = \mathbf{M} - \mathbf{N}$, leads to a simplified Newton method,

$$\mathbf{x}^{k+1} = \mathbf{x}^k + \mathbf{M}^{-1}(\mathbf{b} - \mathbf{Ax}^k)$$

that can be solved for a few iterations to approximately solve the linear system. The Jacobi-method chooses $\mathbf{M}$ to be the diagonal-matrix, i.e., $\mathbf{M} = \mathbf{D}$. This leads to a separate relaxation of the individual components of the residual vector $\mathbf{r} = \mathbf{b} - \mathbf{Ax}$.

A generalization of the point-relaxation toward a relaxation of multiple components at the same time leads to a block-relaxation method [225]. Therefore, let the set of all indices be denoted by $S = \{1, 2, \dots, n\}$ partitioned into subsets $S_1, S_2, \dots, S_p$, s.t.

$$S_i \subseteq S, \quad \bigcup_{i=1,\dots,p} S_i = S.$$

If $S_i \cap S_j = \emptyset$ the splitting is called *non-overlapping decomposition*, otherwise *overlapping decomposition*. In the following, let $n_i = |S_i|$ be the size of the index-set S_i, defined by

$$S_i = \{m_{i1}, m_{i2}, \dots, m_{in_i}\}.$$

To restrict the rows and columns of the matrix $\mathbf{A}$ to a subset S_i we introduce the projection matrices $\mathbf{V}_i$, build from the columns of the unit-matrix $\mathbf{I} \in \mathbb{R}^{n \times n}$, $\mathbf{I} = [\mathbf{e}_1, \mathbf{e}_2, \dots, \mathbf{e}_n]$, corresponding to the indices in S_i, i.e.

$$\mathbf{V}_i = [\mathbf{e}_{m_{i1}}, \mathbf{e}_{m_{i2}}, \dots, \mathbf{e}_{m_{in_i}}] \in \mathbb{R}^{n \times n_i}.$$

Furthermore, the matrices $\mathbf{W}_i$ are introduced, s.t. $\sum_i \mathbf{V}_i \mathbf{W}_i^\top = \mathbf{I}$, with

$$\mathbf{W}_i = [\eta_{m_{i1}} \mathbf{e}_{m_{i1}}, \eta_{m_{i2}} \mathbf{e}_{m_{i2}}, \dots, \eta_{m_{in_i}} \mathbf{e}_{m_{in_i}}].$$

The factors $\eta_{m_{ij}}$ are chosen appropriately. A natural choice for the scaling factors is $\eta_i = 1/s_i$, with $s_i := |\{l \,|\, i \in S_l\}|$.

To introduce the sub-matrices of $\mathbf{A}$ corresponding to the index-sets S_i, we define the $n_i \times n_j$ block-matrices $\mathbf{A}_{ij}$ and the corresponding sub-vectors $\boldsymbol{\xi}_i$ and $\boldsymbol{\beta}_i$ of the solution and right-hand-side vector, respectively, according to

$$\mathbf{A}_{ij} = \mathbf{W}_i^\top \mathbf{A} \mathbf{V}_j, \quad \boldsymbol{\xi}_i = \mathbf{W}_i^\top \mathbf{x}, \quad \boldsymbol{\beta}_i = \mathbf{W}_i^\top \mathbf{b}.$$

With this definition we can represent the solution vector $\mathbf{x}$ as $\mathbf{x} = \sum_{i=1}^p \mathbf{V}_i \boldsymbol{\xi}_i$.

#processors p	$\mathbf{P}_{\text{CH}}$		bjacobi	
	time [sec]	#iterations	time [sec]	#iterations
48	13.62	24	32.47	25
96	13.57	24	32.11	25
192	13.83	25	30.30	27
384	14.97	25	33.69	25

Table 6.3 – *Average number of iterations and solution time in the first 20 timesteps for approximately 25,000 DOFs per partition.*

In the context of projection methods we search for an $\mathbf{x}^{k+1} \in \tilde{\mathbf{x}} + \mathcal{K}_i$, with the initial solution $\tilde{\mathbf{x}}$ and a subspace $\mathcal{K}_i$ spanned by the columns of $\mathbf{V}_i$, such that the corresponding residual is orthogonal to a subspace $\mathcal{L}_i$ spanned by the columns of $\mathbf{W}_i^\top$. Thus, for $\mathbf{x}^{k+1} := \tilde{\mathbf{x}} + \mathbf{V}\boldsymbol{\delta}$ and $\tilde{\mathbf{r}} = \mathbf{b} - \mathbf{A}\tilde{\mathbf{x}}$, the residual vector can be written as

$$\mathbf{r}^{k+1} = \mathbf{b} - \mathbf{A}\mathbf{x}^{k+1} = \mathbf{b} - \mathbf{A}(\tilde{\mathbf{x}} + \mathbf{V}_i\boldsymbol{\delta}) = \tilde{\mathbf{r}} - \mathbf{A}\mathbf{V}_i\boldsymbol{\delta}.$$

The orthogonality condition to he subspace $\mathcal{L}_i$ translates into

$$\mathbf{W}_i^\top \mathbf{r}^{k+1} = \mathbf{W}_i^\top (\tilde{\mathbf{r}} - \mathbf{A}\mathbf{V}_i\boldsymbol{\delta}) \overset{!}{=} 0$$

and thus, we obtain the representation $\mathbf{x}^{k+1} = \tilde{\mathbf{x}} + \mathbf{V}_i\mathbf{A}_{ii}^{-1}\mathbf{W}_i^\top \tilde{\mathbf{r}}$.

One step of the block-jacobi method applies this formula to the starting vector $\tilde{\mathbf{x}} = \mathbf{x}^k$ for all i. This leads to Algorithm 1.


Algorithm 1 Block-jacobi method

1: Choose initial solution $\mathbf{x}^0$
2: **for** $k = 0, 1, \ldots$ **do**
3:     **for** $i = 1, 2, \ldots, p$ **do**
4:         Solve $\mathbf{A}_{ii}\hat{\boldsymbol{\delta}}_i = \mathbf{W}_i^\top (\mathbf{b} - \mathbf{A}\mathbf{x}^k)$
5:     Update $\mathbf{x}^{k+1} = \mathbf{x}^k + \sum_i \mathbf{V}_i\hat{\boldsymbol{\delta}}_i$

This algorithm can be applied to non-positive definite systems, if the diagonal blocks $\mathbf{A}_{ii}$ are invertible. The approach described here is similar to a multisplitting-block-jacobi method [185]. In the context of domain-decomposition approaches the index-sets S_i correspond to the unknowns in local partitions of the domain. For the Phase-Field Crystal model the equations can easily be restricted to parts of the domain with homogeneous Neumann boundary conditions on the inner domain boundaries. This allows to invert the local problems separately.

We have analyzed the block-jacobi preconditioner using a local direct solver, such as MUMPS [16] or UMFPACK [65], to invert the matrices $\mathbf{A}_{ii}$. Therefore, the 3D setup of Section 1.6 is investigated with a homogeneous partitioning of the computational domain Ω in p subdomains.

In Table 6.3 the block-jacobi approach (bjacobi) is compared to the preconditioner developed in Chapter 1 ($\mathbf{P}_{\text{CH}}$). An equal setup with approximately 25,000 DOFs per subdomain and the same number of used processors is considered. While the average number of solver iterations
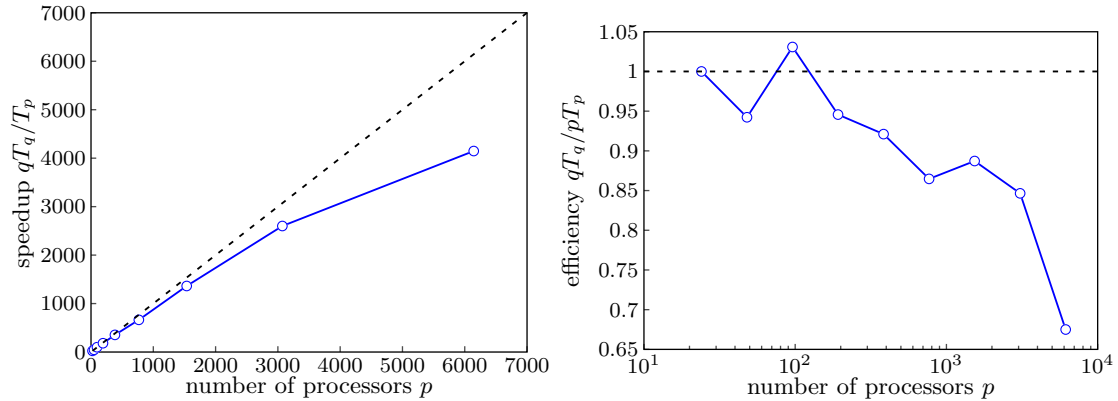
Figure 6.2 – *Left: Speedup of weak scaling computations using the block-jacobi preconditioner in a 3D PFC setup. Right: Corresponding efficiency curve. Reference calculations are performed with $q = 24$, corresponding to one compute node with 24 cores.*

is approximately equal, the solution time for one linear system, i.e., time for one timestep, is about half the time for the PFC preconditioner as for the block-jacobi preconditioner. This clearly shows an advantage of the problem dependent approach.

In Figure 6.2 a large scale computation for up to 6,144 processors is visualized. The weak-scaling speedup and efficiency curves show, that up to about 3,000 cores the computations scale well with more than 85% efficiency and then drop down to less than 70%. A calculation with more than 12,000 cores (not plotted) shows an even worse scaling that needs to be analyzed in more detail.

In [291] an additive Schwarz preconditioner was formulated. This is a generalization of the non-overlapping block-jacobi approach that allows overlap of the subdomains. It was shown that an approximate local solver, such as an incomplete LU factorization, leads to no convergence in the outer GMRES iteration, while with a direct solver they have obtained convergence for large overlap regions. In their benchmarks they have required more than 100–1,000 GMRES iterations to converge to an acceptable tolerance. Finally, they have shown scaling results for up to 2,300 processors.

Compared to their results the block-jacobi preconditioner used in our studies seems to perform much better and more stable. This discrepancy needs to be analyzed in more detail.

A combination of the block-jacobi with the HODLR-direct solver could be an reasonable improvement that may be comparable in speed and memory requirements to the PFC preconditioner.

Conclusion and outlook

$\mathbb{I}$N this thesis we have analyzed solution methods for the classical Phase-Field Crystal equation arising as an approximated dynamic density functional theory. Discretizing the nonlinear partial differential equation in space using a finite-element method and using various time-discretizations, such as semi-implicit Euler or Rosenbrock discretization, has led to linear systems that turned out to be hard to solve with classical method.

For small systems direct solvers, based on a sparse LU factorization, could be applied, but numerical experiments have shown that these methods do not scale well with increasing system size. Recently, the classical multi-frontal approach or super-nodal approach, which lead to an exact factorization of the matrix up to rounding errors, were modified to allow some approximations in the procedure. Basically, the dense frontal matrices, arising in these multi-frontal approaches, were approximated with an off-diagonal low-rank matrix structure. Various different approaches were developed in the recent years, cf. [15, 17, 18, 290], and were combined with outer iterative solver to improve the approximate inverse solutions. One such approach [18] was successfully applied to the PFC equation as a preconditioner for an FGMRES method and has relaxed the memory restrictions of classical direct solvers slightly.

Larger linear systems were handled using iterative Krylov-subspace solvers, like FGMRES. We have shown by analytical and numerical arguments that the developed preconditioner can be applied to the classical PFC equation successfully and reduces the estimated asymptotic convergence factor a lot. A spectral analysis has shown possible timestep limitations for the initial approach and the lack of these limitations for the inner Cahn-Hilliard preconditioner. This has been numerically verified.

In the following chapters we have added various modifications to the classical PFC model, like an advection term in Section 2.1 and a density penalization to allow vacancies in the density field in Section 2.2. In Section 3.1 an additional order-parameter field was introduced and the evolution was coupled to the PFC equation. In Chapter 4 the model was restricted to complex geometries using a diffuse-interface model and a wall potential similar to a diffuse-domain approach. All those modifications had an influence on the preconditioner. Larger flow velocities increased the number of solver iterations and also larger mobilities in the Vacancy PFC model made the solver less efficient. The orientational order-parameter had only little influence on the preconditioner, whereas the diffuse-interface approach has reduced its efficiency, depending on the width of the interface and its resolution.

Finally, in Chapter 5 a generalization of the PFC preconditioner was postulated that might

be applicable to a wider range of PFC-like models. As an example we have studied the two-mode PFC model, i.e., Quasi-Crystal PFC model. Although the number of solver iterations were larger than those of the classical PFC equation, a convergence of the iterative Krylov-subspace method could be achieved.

In summary, we have developed the problem depended PFC preconditioner as efficient solution method for the PFC equation. Only for the Vacancy PFC and diffuse-domain PFC approach the number of solver iterations were increased. The other analyzed modifications of the classical equation seem to be less problematic. Although a block-jacobi preconditioner with direct local solver is more stable with respect to problem variations, it is in total less efficient with respect to memory requirement and solver time.

Efficiency of the solver is shown, i.e. it can easily be implemented with standard finite-element techniques and reduces the overall solution time by orders of magnitude, in comparison with direct solver approaches and non-preconditioned krylov-subspace methods. The solver is widely applicable to setups of various geometries, in two-dimension, three-dimensions, and on surfaces. Additionally, minor problem modifications can be handled with only little modification in the preconditioner. The method scales well in highly parallel simulations.

Nevertheless, the developed preconditioner cannot compete in performance against finite-difference methods combined with specialized nonlinear multigrid solvers, as described in [119, 279, 36, 35], and against spectral methods, especially in periodic rectangular domains. The derivation of the PFC preconditoner, on the other hand, has given an insight into the structure of this gradient flow problem and it is worth to apply the method in various situations, where the other methods may fail or are too complicated to implement.

In all the chapters of this thesis we have given outlooks to future work, interesting questions that need to be considered, and open problems. Some of the questions were already answered in the subsequent sections or in publications listed at the beginning of this work. Basically, all the numerical examples were performed in 2D, except the benchmark cases in the first chapter. As already stated in the conclusion of Section 3.1, three dimensional setups are of practical interest and are expected to show interesting phenomena. Also for the flowing particles, 3D simulations would be challenging. There the preconditioner might be a valuable tool to solve the arising linear systems.

It was shown in Section 4.1 that equations on manifolds can easily be solved using surface finite-element methods combined with the developed preconditioner for the linear system. An extension of the liquid-crystal PFC model (and the polar LC-PFC model) to surfaces is an interesting problem and techniques, based on a tangentiality penalization for the director fields and polarization fields, might lead to an efficient numerical tool for these equations.

The diffuse-domain approach is a widely used numerical technique to solve partial differential equations in complex geometries, also in 3D domains. More physically relevant examples for the particles restricted to an evolving domain, than set up in Section 4.3, should be implemented to see the quantitative properties of the propesed approach. There, also the coupling of moving particles to a polarization field, in the sense of a particle orientation extended by a particle activity in this direction, could be an interesting example. The setups in [161, 262] are restricted to stationary domains. An evolution of the geometry in combination with the motion of the particles inside of the geometry give rise to interesting phenomena.

Finally, the generalied preconditioner in Section 5.1 could be applied to a wider range of problems of the form of a H^{-1}-gradient flow of a Helmholtz free-energy expansion and maybe

also to problems not directly related to this gradient-flow approach. We have in mind equations coming from problems in image processing and biology, like a (conserved) Willmore flow equation, which has similar difficulties with the linear equations, as the PFC equation.

We have just started to examine the accelerated multi-frontal approach in Section 6.1 and also modified incomplete LU-factorizations that allow an amount of fill-in, as direct solver approaches. A combination with the preconditioner or as part of the block-jacobi preconditioner, this could be an efficient solution method for the PFC equation.

Bibliography

[1] Carl A. Whitfield, D. Marenduzzo, R. Voituriez, and R. J. Hawkins, *Active polar fluid flow in finite droplets*, Eur. Phys. J. E, 37 (2014).

[2] C. V. Achim, M. Schmiedeberg, and H. Löwen, *Growth modes of quasicrystals*, Phys. Rev. Lett., 112 (2014), p. 255501.

[3] C. V. Achim, R. Wittkowski, and H. Löwen, *Stability of liquid crystalline phases in the phase-field-crystal model*, Phys. Rev. E, 83 (2011), p. 061712.

[4] S. Adams, N. Dirr, M. Peletier, and J. Zimmer, *Large deviations and gradient flows*, Phil. Trans. Royal Soc. A, 371 (2013).

[5] T. C. Adhyapak, S. Ramaswamy, and J. Toner, *Live soap: Stability, order, and fluctuations in apolar active smectics*, Phys. Rev. Lett., 110 (2013), p. 118102.

[6] N. Akino, F. Schmid, and M. P. Allen, *Molecular-dynamics study of the nematic-isotropic interface*, Phys. Rev. E, 63 (2001), p. 041706.

[7] Sebastian Aland, *Time integration for diffuse interface models for two-phase flow*, J. Comput. Phys., 262 (2014), pp. 58 – 71.

[8] S. Aland, H. Hatzikirou, J. Lowengrub, and A. Voigt, *Time integration for diffuse interface models for two-phase flow*, Biophys. J., 109 (2015).

[9] S. Aland, J. Lowengrub, and A. Voigt, *Two-phase flow in complex geometries: A diffuse domain approach*, Comp. Model. Eng. Sci., 57 (2010), pp. 77–108.

[10] ——, *A continuum model of colloid-stabilized interfaces*, Physics of Fluids, 23 (2011), p. 062103.

[11] ——, *Particles at fluid-fluid interfaces: A new navier-stokes-cahn-hilliard surface-phase-field-crystal model*, Phys. Rev. E, 86 (2012), p. 046321.

[12] S. Aland, A. Rätz, M. Röger, and A. Voigt, *Buckling instability of viral capsids – a continuum approach*, Multiscale Model. Sim., 10 (2012), pp. 82–110.

[13] E. Allahyarov and H. Löwen, *Huge broadening of the crystal-fluid interface for sedimenting colloids*, Eur. Phys. Lett., 95 (2011), p. 38004.

[14] L. Almenar and M. Rauscher, *Dynamics of colloids in confined geometries*, J. Phys.-Condens. Mat., 23 (2011), p. 184115.

[15] P. Amestoy, C. Ashcraft, O. Boiteau, A. Buttari, J.-Y. L'Excellent, and C. Weisbecker, *Improving multifrontal methods by means of block low-rank representations*, SIAM J. Sci. Comp., 37 (2015), pp. A1451–A1474.

[16] P. R. Amestoy, I. S. Duff, J. Koster, and J.-Y. L'Excellent, *A fully asynchronous multifrontal solver using distributed dynamic scheduling*, SIAM J. Matrix Ana. Appl., 23 (2001), pp. 15–41.

[17] A. Aminfar, S. Ambikasaran, and E. Darve, *A fast block low-rank dense solver with applications to finite-element matrices*, ArXiv e-prints, (2014).

[18] A. Aminfar and E. Darve, *A fast and memory efficient sparse solver with applications to finite-element matrices*, ArXiv e-prints, (2014).

[19] S. V. Apte, M. Martin, and N. A. Patankar, *A numerical method for fully resolved simulation (FRS) of rigid particle-flow interactions in complex flows*, J. Comput. Phys., 228 (2009), pp. 2712–2738.

[20] Andrew J. Archer, *Dynamical density functional theory for molecular and colloidal fluids: a microscopic approach to fluid mechanics.*, J. Chem. Phys., 130 (2009), p. 014509.

[21] E. Asadi and M. Asle Zaeem, *A modified two-mode phase-field crystal model applied to face-centered cubic and body-centered cubic orderings*, Commun. Math. Sci., 105 (2015), pp. 110–113.

[22] ——, *Quantifying a two-mode phase-field crystal model for BCC metals at melting point*, Commun. Math. Sci., 105 (2015), pp. 101–109.

[23] ——, *A review of quantitative phase-field crystal modeling of solid-liquid structures*, JOM, 67 (2015), pp. 186–201.

[24] O. Axelsson, P. Boyanova, M. Kronbichler, M. Neytcheva, and X. Wu, *Numerical and computational efficiency of solvers for two-phase problems*, Comp. Math. Appl., 65 (2013), pp. 301–314.

[25] O. Axelsson and M. Neytcheva, *Operator splittings for solving nonlinear, coupled multiphysics problems with an application to the numerical solution of an interface problem*, Tech. Report 2011-009, Department of Information Technology, Uppsala University, 2011.

[26] E. Backofen and A. Voigt, *A phase-field-crystal approach to critical nuclei*, J. Phys.-Condens. Mat., 22 (2010), p. 364104.

[27] R. Backofen, K. Barmak, K. E. Elder, and A. Voigt, *Capturing the complex physics behind universal grain size distributions in thin metallic films*, Acta Mater., 64 (2014), pp. 72–77.

[28] R. Backofen, M. Gräf, D. Potts, S. Praetorius, A. Voigt, and T. Witkowski, *A continuous approach to discrete ordering on $\mathbb{S}^2$*, Multiscale Model. Sim., 9 (2011), pp. 314–334.

[29] R. Backofen, A. Rätz, and A. Voigt, *Nucleation and growth by a phase field crystal (PFC) model*, Philos. Mag. Lett., 87 (2007), pp. 813–820.

[30] R. Backofen and A. Voigt, *A phase field crystal study of heterogeneous nucleation – application of the string method*, Eur. Phys. J. Special Topics, 223 (2014), pp. 497–509.

[31] R. Backofen, A. Voigt, and T. Witkowski, *Particles on curved surfaces: A dynamic approach by a phase-field-crystal model*, Phys. Rev. E, 81 (2010), p. 025701.

[32] A. Balay, M. F. Adams, J. Brown, P. Brune, K. Buschelman, V. Eijkhout, W. D. Gropp, D. Kaushik, M. G. Knepley, L. C. McInnes, K. Rupp, B. F. Smith, and H. Zhang, *PETSc.* http://www.mcs.anl.gov/petsc, 2014.

[33] Kobi Barkan, *Stability of quasicrystals composed of soft isotropic particles*, PhD thesis, Tel Aviv University, September 2009.

[34] K. Barkan, H. Diamant, and R. Lifshitz, *Stability of quasicrystals composed of soft isotropic particles*, Phys. Rev. B, 83 (2011), p. 172201.

[35] A. Baskaran, Z. Hu, J. S. Lowengrub, C. Wang, S. M. Wise, and P. Zhou, *Energy stable and efficient finite-difference nonlinear multigrid schemes for the modified phase field crystal equation*, J. Comput. Phys., 250 (2013), pp. 270–292.

[36] A. Baskaran, J. S. Lowengrub, C. Wang, and S. M. Wise, *Convergence analysis of a second order convex splitting scheme for the modified phase field crystal equation*, SIAM J. Numer. Anal., 51 (2013), pp. 2851–2873.

[37] A. Baskaran and M. C. Marchetti, *Self-regulation in self-propelled nematic fluids*, Eur. Phys. J. E, 35 (2012).

[38] A. R. Bausch, M. J. Bowick, A. Cacciuto, A. D. Dinsmore, M. F. Hsu, D. R. Nelson, M. G. Nikolaides, A. Travesset, and D. A. Weitz, *Grain boundary scars and spherical crystallography*, Science, 299 (2003), pp. 1716–1718.

[39] J. Berry, K. R. Elder, and M. Grant, *Melting at dislocations and grain boundaries: A phase field crystal study*, Phys. Rev. B, 77 (2008), p. 224114.

[40] J. Berry and M. Grant, *Modeling multiple time scales during glass formation with phase-field crystals*, Phys. Rev. Lett., 106 (2011), p. 175702.

[41] M. Bertalmio, L. T. Cheng, S. Osher, and G. Sapiro, *Variational problems and partial differential equations on implicit surfaces*, J. Comput. Phys., 174 (2001), pp. 759–780.

[42] T. Biben, R. Ohnesorge, and H. Löwen, *Crystallization in sedimentation profiles of hard spheres*, Eur. Phys. Lett., 28 (1994), pp. 665–670.

[43] M. BIER, L. HARNAU, AND S. DIETRICH, *Bulk and interfacial properties of binary hard-platelet fluids*, Phys. Rev. E, 69 (2004), p. 021506.

[44] K. BINDER AND M. MÜLLER, *Computer simulation of profiles of interfaces between co-existing phases*, Int. J. Mod. Phys. C, 11 (2000), pp. 1093–1113.

[45] CHRISTOPHE BLANC, *Measurement of the anisotropy of the energy of an isotropic-smectic interface in a smectic cylinder: application to the L_3-L_α interface*, Phys. Rev. E, 64 (2001), p. 011702.

[46] P. BOLHUIS AND D. FRENKEL, *Tracing the phase boundaries of hard spherocylinders*, J. Chem. Phys., 106 (1997), pp. 666–687.

[47] M. J. BOWICK AND L. GIOMI, *Two-dimensional matter: order, curvature and defects*, Adv. Phys., 58 (2009), pp. 449–563.

[48] P. BOYANOVA, M. DO-QUANG, AND M. NEYTCHEVA, *Block-preconditioners for conforming and non-conforming fem discretizations of the cahn-hilliard equation*, in Large-Scale Scientific Computing, vol. 7116 of Lecture Notes in Computer Science, Springer Berlin Heidelberg, 2012, pp. 549–557.

[49] ——, *Efficient preconditioners for large scale binary cahn-hilliard models.*, Comput. Meth. Appl. Math., 12 (2012), pp. 1–22.

[50] J. F. BRADY AND G. BOSSIS, *Stokesian Dynamics*, Annu. Rev. Fluid Mech., 20 (1988), pp. 111–157.

[51] W. L. BRIGGS, S. F. MCCORMICK, AND V. E. HENSON, *A Multigrid Tutorial: Second Edition*, Siam, 2000.

[52] J. W. CAHN AND J. E. HILLIARD, *Free energy of a nonuniform system. i. interfacial free energy*, J. Chem. Phys., 28 (1958), pp. 258–267.

[53] D. A. CALTHOUN, C. HELZEL, AND R. J. LEVEQUE, *Logically rectangular grids and finite volume methods for pdes in circular and spherical domains*, SIAM Rev., 50 (2008), pp. 723–752.

[54] H. CAO AND Z. SUN, *Two finite difference schemes for the phase field crystal equation*, Science China Mathematics, (2015), pp. 1–20.

[55] P. Y. CHAN, N. GOLDENFELD, AND J. DANTZIG, *Molecular dynamics on diffusive time scales from the phase-field-crystal equation*, Phys. Rev. E, 79 (2009), p. 035701.

[56] S. CHANDRASEKARAN, M. GU, AND T. PALS, *A fast ulv decomposition solver for hierarchically semiseparable representations*, SIAM J. Matrix Ana. Appl., 28 (2006), pp. 603–622.

[57] L. CHEN AND J. TONER, *Universality for moving stripes: A hydrodynamic theory of polar active smectics*, Phys. Rev. Lett., 111 (2013), p. 088701.

[58] L. Q. CHEN, *Phase-field models for microstructure evolution*, Annu. Rev. Mat. Res., 32 (2002), pp. 113–140.

[59] M. Cheng and J. A. Warren, *An efficient algorithm for solving the phase field crystal model*, J. Comput. Phys., 227 (2008), pp. 6241–6248.

[60] Y.-S. Cho, S.-H. Kim, G.-R. Yi, and S.-M. Yang, *Self-organization of colloidal nanospheres inside emulsion droplets: Higher-order clusters, supraparticles, and supraballs*, Coll. Surf. A, 345 (2009), pp. 237–245.

[61] D. J. Cleaver, C. M. Care, M. P. Allen, and M. P. Neal, *Extension and generalization of the gay-berne potential*, Phys. Rev. E, 54 (1996), pp. 559–567.

[62] J. J. Crassous, H. Dietsch, P. Pfleiderer, V. Malik, A. Diaz, L. A. Hirshi, M. Drechsler, and P. Schurtenberger, *Preparation and characterization of ellipsoidal-shaped thermosensitive microgel colloids with tailored aspect ratios*, Soft Matter, 8 (2012), pp. 3538–3548.

[63] P. Cremer, M. Marechal, and H. Löwen, *Director field in plastic crystals*, Eur. Phys. Lett., 99 (2012), p. 38005.

[64] R. L. Davidchack, J. R. Morris, and B. B. Laird, *The anisotropic hard-sphere crystal-melt interfacial free energy from fluctuations*, J. Chem. Phys., 125 (2006), p. 094710.

[65] Timothy A. Davis, *A column pre-ordering strategy for the unsymmetric-pattern multifrontal method*, ACM Trans. Math. Softw., 30 (2004), pp. 196–199.

[66] P.-G. de Gennes and J. Prost, *The Physics of Liquid Crystals*, vol. 83 of International Series of Monographs on Physics, Oxford University Press, 2 ed., 1995.

[67] D. Demidov, K. Ahnert, K. Rupp, and P. Gottschling, *Programming cuda and opencl: A case study using modern c++ libraries*, SIAM J. Sci. Comp., 35 (2013), pp. C453–C472.

[68] A. D. Dinsmore, M. F. Hsu, M. G. Nikolaides, A. R. Marquez, M. amd Bausch, and D. A. Weitz, *Colloidosomes: selectively permeable capsules composed of colloidal particles*, Science, 298 (2002), pp. 1006–1009.

[69] Z. Dogic and S. Fraden, *Smectic phase in a colloidal suspension of semiflexible virus particles*, Phys. Rev. Lett., 78 (1997), pp. 2417–2420.

[70] ——, *Development of model colloidal liquid crystals and the kinetics of the isotropic-smectic transition*, Phil. Trans. Royal Soc. A, 359 (2001), pp. 997–1014.

[71] T. Driscoll, K. Toh, and L. Trefethen, *From potential theory to matrix iterations in six steps*, SIAM Rev., 40 (1998), pp. 547–578.

[72] T. Driscoll and S. Vavasis, *Numerical conformal mapping using cross-ratios and delaunay triangulation*, SIAM J. Sci. Comp., 19 (1998), pp. 1783–1803.

[73] Toby A. Driscoll, *Algorithm 756: A matlab toolbox for schwarz-christoffel mapping*, ACM Trans. Math. Softw., 22 (1996), pp. 168–186.

[74] I. S. Duff and J. K. Reid, *The multifrontal solution of indefinite sparse symmetric linear*, ACM Trans. Math. Softw., 9 (1983), pp. 302–325.

[75] G. Dziuk and C. M. Elliott, *Surface finite elements for parabolic equations*, J. Comput. Math., 25 (2007), pp. 385–407.

[76] G. Dziuk and C. M. Elliott, *Finite element methods for surface pdes*, Acta Num., 22 (2013), pp. 289–396.

[77] J. Dzubiella, M. Schmidt, and H. Löwen, *Topological defects in nematic droplets of hard spherocylinders*, Phys. Rev. E, 62 (2000), pp. 5081–5091.

[78] K. Elder, M. Katakowski, M. Haataja, and M. Grant, *Modeling Elasticity in Crystal Growth*, Phys. Rev. Lett., 88 (2002), p. 245701.

[79] K. R. Elder and M. Grant, *Modeling elastic and plastic deformations in nonequilibrium processing using phase field crystals*, Phys. Rev. E, 70 (2004), p. 051605.

[80] K. R. Elder, N. Provatas, J. Berry, P. Stefanovic, and M. Grant, *Phase-field crystal modeling and classical density functional theory of freezing*, Phys. Rev. B, 75 (2007), p. 064107.

[81] C. M. Elliott and G. Dziuk, *Finite elements on evolving surfaces*, IMA J. Num. Ana., 27 (2007), pp. 262–292.

[82] C. M. Elliott and B. Stinner, *Analysis of a diffuse interface approach to an advection diffusion equation on a moving surface*, Math. Model. Meth. Appl. Sci., 19 (2009), pp. 787–802.

[83] M. Elsey and B. Wirth, *A simple and efficient scheme for phase field crystal simulation*, ESAIM: Math. Model. Num., 47 (2013), pp. 1413–1432.

[84] Mark Embree, *How descriptive are gmres convergence bounds?*, tech. report, Oxford University Computing Laboratory, 1999.

[85] H. Emmerich, H. Löwen, R. Wittkowski, T. Gruhn, G. I. Tòth, G. Tegze, and L. Gránásy, *Phase-field-crystal models for condensed matter dynamics on atomic length and diffusive time scales: an overview*, Adv. Phys., 61 (2012), pp. 665–743.

[86] B. Engquist, A. Tornberg, and R. Tsai, *Discretization of dirac delta functions in level set methods*, J. Comput. Phys., 207 (2005), pp. 28–51.

[87] T. Erber and G. M. Hockney, *Equilibrium configurations of n equal charges on a sphere*, J. Phys. A-Math. Gen., 24 (1991), pp. L1369–L1377.

[88] P. Español and M. Revenga, *Smoothed dissipative particle dynamics*, Phys. Rev. E, 67 (2003), p. 026705.

[89] Robert Evans, *The nature of the liquid-vapour interface and other topics in the statistical mechanics of non-uniform, classical fluids*, Adv. Phys., 28 (1979), pp. 143–200.

[90] V. Fallah, N. Ofori-Opoku, J. Stolle, N. Provatas, and S. Esmaeili, *Simulation of early-stage clustering in ternary metal alloys using the phase-field crystal method*, Acta Mater., 61 (2013), pp. 3653–3666.

[91] F. H. Fenton, E. M. Cherry, A. Karma, and W.-J. Rappel, *Modeling wave propagation in realistic heart geometries using the phase-field method*, Chaos, 15 (2005).

[92] A. F. Fortes, D. D. Joseph, and T. S. Lundgren, *Nonlinear mechanics of fluidization of beds of spherical particles*, j. Fluid Mech., 177 (2006), pp. 467–483.

[93] S. Franz, R. Gärtner, H. Roos, and A. Voigt, *A Note on the Convergence Analysis of a Diffuse-domain Approach*, Comput. Meth. Appl. Math., 12 (2012), pp. 121–240.

[94] Daan Frenkel, *Course 9: Statistical mechanics of liquid crystals*, in Liquids, Freezing and Glass Transition, J.-P. Hansen, D. Levesque, and J. Zinn-Justin, eds., vol. 2 of Proceedings of the Les Houches Summer School, Course LI, 3–28 July 1989, 1991, pp. 689–762.

[95] M. Fujita and Y. Yamaguchi, *Mesoscale modeling for self-organization of colloidal systems*, Curr. Opin. Coll. Int. Sci., 15 (2010), pp. 8–12.

[96] A. Furukawa and H. Tanaka, *Key Role of Hydrodynamic Interactions in Colloidal Gelation*, Phys. Rev. Lett., 104 (2010), p. 245702.

[97] P. K. Galenko, H. Gomez, N. V. Kropotin, and K. R. Elder, *Unconditionally stable method and numerical solution of the hyperbolic phase-field crystal equation*, Phys. Rev. E, 88 (2013), p. 013310.

[98] L. Gerardo-Giorda and L. Mirabella, *Spectral analysis of a block-triangular preconditioner for the bidomain system in electrocardiology*, E. Trans. Num. Ana., 39 (2012), pp. 186–201.

[99] R. Glowinski, T-W. Pan, T. I. Hesla, and D. D. Joseph, *A distributed lagrange multiplier/fictitious domain method for particulate flows*, Int. J. MultiPhase Fl., 25 (1999), pp. 755–794.

[100] R. Glowinski, T. W. Pan, T. I. Hesla, D. D. Joseph, and J. Périaux, *A Fictitious Domain Approach to the Direct Numerical Simulation of Incompressible Viscous Flow past Moving Rigid Bodies: Application to Particulate Flow*, J. Comput. Phys., 169 (2001), pp. 363–426.

[101] B. D. Goddard, A. Nold, N. Savva, P. Yatsyshin, and S. Kalliadasis, *Unification of dynamic density functional theory for colloidal fluids to include inertia and hydrodynamic interactions: derivation and numerical experiments*, J. Phys.-Condens. Mat., 25 (2013), p. 035101.

[102] H. Gomez and X. Nogueira, *An unconditionally energy-stable method for the phase field crystal equation*, Comp. Meth. Appl. Mech. Eng., 249-252 (2012), pp. 52–61.

[103] P. Gottschling and A. Lumsdaine, *MTL4*. http://www.simunova.com/en/node/24, 2014.

[104] P. Gottschling, T. Witkowski, and A. Voigt, *Integrating object-oriented and generic programming paradigms in real-world software environments: Experiences with AMDiS and MTL4*, in POOSC 2008 workshop at ECOOP08, Paphros, Cyprus, 2008.

[105] H. Graf and H. Löwen, *Density functional theory for hard spherocylinders: phase transitions in the bulk and in the presence of external fields*, J. Phys.-Condens. Mat., 11 (1999), pp. 1435–1452.

[106] H. Graf and H. Löwen, *Phase diagram of tobacco mosaic virus solutions*, Phys. Rev. E, 59 (1999), pp. 1932–1942.

[107] Y. Guo, J. Wang, Z. Wang, S. Tang, and Y. Zhou, *Phase field crystal model for the effect of colored noise on homogenerous nucleation*, Acta Phys. Sin., 61 (2012), p. 146401.

[108] C. Gutsche, F. Kremer, M. Krüger, M. Rauscher, R. Weeber, and J. Harting, *Colloids dragged through a polymer solution: experiment, theory and simulation*, J. Chem. Phys., 129 (2008), p. 084902.

[109] E. Hairer, S. S. P. Nørsett, and G. Wanner, *Solving Ordinary Differential Equations II: Stiff and Differential-Algebraic Problems*, vol. 14 of Springer Series in Computational Mathematics, Springer, 1993.

[110] A. Härtel, M. Oettel, R. E. Rozas, S. U. Egelhaaf, J. Horbach, and H. Löwen, *Tension and stiffness of the hard sphere crystal-fluid interface*, Phys. Rev. Lett., 108 (2012), p. 226101.

[111] Y. He and K. Li, *Stability analysis of nonlinear galerkin & galerkin methods for nonlinear evolution equations*, Applied Mathematics, 11 (1996), pp. 137–152.

[112] J. S. Hesthaven, S. Gottlieb, and D. Gottlieb, *Spectral methods for time-dependent problems*, vol. 21 of Cambridge Monographs on Applied and Computational Mathematics, Cambridge University Press, Cambridge, 2007.

[113] T. Hirouchi, T. Takaki, and Y. Tomita, *Development of numerical scheme for phase field crystal deformation simulation*, Comput. Mater. Sci., 44 (2009), pp. 1192–1197.

[114] P. Hohenberg and B. Halperin, *Theory of dynamic critical phenomena*, Rev. Mod. Phys., 49 (1977), pp. 435–479.

[115] P. Holmqvist, M. P. Lettinga, J. Buitenhuis, and J. K. G. Dhont, *Crystallization kinetics of colloidal spheres under stationary shear flow*, Langmuir, 21 (2005), pp. 10976–10982.

[116] P. J. Hoogerbrugge and J. M. V. A. Koelman, *Simulating microscopic hydrodynamic phenomena with dissipative particle dynamics*, Eur. Phys. Lett., 19 (1992), p. 155.

[117] J. J. Hoyt, M. Asta, and A. Karma, *Method for computing the anisotropy of the solid-liquid interfacial free energy*, Phys. Rev. Lett., 86 (2001), pp. 5530–5533.

[118] H. H. Hu, D. D. Joseph, and M. J. Crochet, *Direct Simulation of Fluid Particle Motions*, Theor. Comp. Fluid. Dyn., 3 (1992), pp. 285–306.

[119] Z. Hu, S. M. Wise, C. Wang, and J. S. Lowengrub, *Stable and efficient finite-difference nonlinear-multigrid schemes for the phase field crystal equation*, J. Comput. Phys., 228 (2009), pp. 5323–5339.

[120] W. T. M. Irvine, V. Vitelli, and P. M. Chaikin, *Pleats in crystals on curved surfaces*, Nature, 468 (2010), pp. 947–951.

[121] A. V. Ivlev, H. Löwen, G. E. Morfill, and C. P. Royall, *Complex Plasmas and Colloidal Dispersions: Particle-Resolved Studies of Classical Liquids and Solids*, vol. 5 of Series in Soft Condensed Matter, World Scientific Publishing, 1 ed., 2012.

[122] Akusti Jaatinen, *Modeling materials with phase field crystal models*, PhD thesis, Aalto University School of Science and Technology, December 2010.

[123] A. Jaatinen and T. Ala-Nissila, *Eighth-order phase-field-crystal model for two-dimensional crystallization*, Phys. Rev. E, 82 (2010), p. 061602.

[124] ——, *Extended phase diagram of the three-dimensional phase field crystal model*, J. Phys.-Condens. Mat., 22 (2010), p. 205402.

[125] David Jacqmin, *Calculation of two-phase navier-stokes flows using phase-field modeling*, J. Comput. Phys., 155 (1999), p. 32.

[126] I. M. Jánosi, T. Tél, D. E. Wolf, and J. A. C. Gallas, *Chaotic particle dynamics in viscous flows: The three-particle stokeslet problem*, Phys. Rev. E, 56 (1997), pp. 2858–2868.

[127] K. Jiang and P. Zhang, *Numerical methods for quasicrystals*, J. Comput. Phys., 256 (2014), pp. 428–440.

[128] V. John, G. Matthies, and J. Rang, *A comparison of time-discretization/linearization approaches for the incompressible Navier-Stokes equations*, Comp. Meth. Appl. Mech. Eng., 195 (2006), pp. 5995–6010.

[129] V. John and J. Rang, *Adaptive time step control for the incompressible Navier-Stokes equations*, Comp. Meth. Appl. Mech. Eng., 199 (2010), pp. 514–524.

[130] R. Jordan, D. Kinderlehrer, and F. Otto, *Free energy and the Fokker-Planck equation*, Physica D, 107 (1997), pp. 265–271.

[131] ——, *The variational formulation of the fokker–planck equation*, SIAM J. Math. Anal., 29 (1998), pp. 1–17.

[132] A. S. Joshi and Y. Sun, *Multiphase lattice boltzmann method for particle suspensions*, Phys. Rev. E, 79 (2009), p. 066703.

[133] Winfried Kaballo, *Einfhrung in die Analysis III*, Spektrum-Akademischer Vlg, 1999.

[134] T. Kempe and J. Fröhlich, *An improved immersed boundary method with direct forcing for the simulation of particle laden flows*, J. Comput. Phys., 231 (2012), pp. 3663–3684.

[135] Th. Kirchhoff, H. Löwen, and R. Klein, *Dynamical correlations in suspensions of charged rodlike macromolecules*, Phys. Rev. E, 53 (1996), pp. 5011–5022.

[136] Denis C. Kovacs, *Inertial manifolds and nonlinear Galerkin methods*, PhD thesis, Virginia Polytechnic Institute and State University, 2005.

[137] Arno B. J. Kuijlaars, *Convergence analysis of krylov subspace iterations with methods from potential theory*, SIAM Rev., 48 (2006), pp. 3–40.

[138] J. Kundin, M. A. Choudhary, and H. Emmerich, *Bridging the phase-field and phase-field crystal approaches for anisotropic material systems*, Eur. Phys. J. Special Topics, 223 (2014), pp. 363–372.

[139] C. Landsberg, F. Stenger, A. Deutsch, M. Gelinsky, A. Rösen-Wolff, and A. Voigt, *Chemotaxis of mesenchymal stem cells within 3d biomimetic scaffolds-a modeling approach*, J. Biomech., 44 (2011), pp. 359–364.

[140] C. Landsberg and A. Voigt, *A multigrid finite element method for reaction-diffusion systems on surfaces*, Comput. Vis. Sci., 13 (2010), pp. 177–185.

[141] Jens Lang, *Adaptive Multilevel Solution of Nonlinear Parabolic PDE Systems: Theory, Algorithm, and Applications*, Lecture Notes in Computational Science and Engineering, Springer, 2010.

[142] J. Lang and J. Verwer, *Ros3p–an accurate third-order rosenbrock solver designed for parabolic problems*, BIT Num. Math., 41 (2001), pp. 731–738.

[143] M. P. Lettinga, J. K. G. Dhont, Z. Zhang, S. Messlinger, and G. Gompper, *Hydrodynamic interactions in rod suspensions with orientational ordering*, Soft Matter, 6 (2010), pp. 4556–4562.

[144] D. Levine and P. J. Steinhardt, *Quasicrystals: A new class of ordered structures*, Phys. Rev. Lett., 53 (1984), pp. 2477–2480.

[145] X. Li, J. Lowengrub, A. Rätz, and A. Voigt, *Solving Pdes in Complex Geometries: a Diffuse Domain Approach.*, Commun. Math. Sci., 7 (2009), pp. 81–107.

[146] X. S. Li and J. W. Demmel, *SuperLU_DIST: A scalable distributed-memory sparse direct solver for unsymmetric linear systems*, ACM Trans. Math. Softw., 29 (2003), pp. 110–140.

[147] Ron Lifshitz, *Symmetry breaking and order in the age of quasicrystals*, Israel J. Chem., 51 (2011), pp. 1156–1167.

[148] R. Lifshitz and H. Diamant, *Soft quasicrystals – why are they stable?*, Philos. Mag., 87 (2007), pp. 3021–3030.

[149] R. Lifshitz and D. M. Petrich, *Theoretical model for faraday waves with multiple-frequency forcing*, Phys. Rev. Lett., 79 (1997), pp. 1261–1264.

[150] S. Lin, Y. Chin, J. Hu, and Y. Chen, *A pressure correction method for fluid-particle interaction flow: Direct-forcing method and sedimentation flow*, Int. J. Numer. Meth. Fl., 67 (2011), pp. 1771–1798.

[151] J. Lindmar, L. Mirny, and D. R. Nelson, *Virus shapes and buckling transitions in spherical shells*, Phys. Rev. E, 68 (2003), p. 051910.

[152] S. Litvinov, M. Ellero, X. Hu, and N. A. Adams, *Smoothed dissipative particle dynamics model for polymer molecules in suspension*, Phys. Rev. E, 77 (2008), p. 066703.

[153] Hartmut Löwen, *Brownian dynamics of hard spherocylinders*, Phys. Rev. E, 50 (1994), pp. 1232–1242.

[154] ——, *A phase-field-crystal model for liquid crystals*, J. Phys.-Condens. Mat., 22 (2010), p. 364105.

[155] H. Löwen and T. Beier, *Crystallinity in liquid films*, Phys. Rev. B, 41 (1990), pp. 4435–4440.

[156] H. Löwen, T. Beier, and H. Wagner, *Van der Waals theory of surface melting*, Eur. Phys. Lett., 9 (1989), pp. 791–796.

[157] ——, *Multiple order parameter theory of surface melting: a van der Waals approach*, Z. Phys. B Con. Mat., 79 (1990), pp. 109–118.

[158] H. Löwen and D. W. Oxtoby, *An exactly soluble model for interfacial kinetics*, J. Chem. Phys., 93 (1990), pp. 674–678.

[159] J. Lowengrub, A. Rätz, and A. Voigt, *Phase-field approximation of the dynamics of multicomponent vesicles: spinodal decomposition, coarsening, budding, and fission*, Phys. Rev. E, 79 (2009), p. 031926.

[160] Ch. Lubich and M. Roche, *Rosenbrock methods for differential–algebraic systems with solution-dependent singular matrix multiplying the derivative*, Computing, 43 (1990), pp. 325–342.

[161] E. Lushi, H. Wioland, and R. E. Goldstein, *Fluid flows created by swimming bacteria drive self-organization in confined suspensions*, Proc. Nat. Acad. Sci., 111 (2014), pp. 9733–9738.

[162] James F. Lutsko, *Recent developments in classical density functional theory*, Adv. Chem. Phys., 144 (2010), pp. 1–92.

[163] Vinothan N. Manoharan, *Colloidal spheres confined by liquid droplets: Geometry, physics, and physical chemistry*, Solid State Comm., 139 (2006), pp. 557 – 561.

[164] M. C. Marchetti, J. F. Joanny, S. Ramaswamy, T. B. Liverpool, J. Prost, M. Rao, and R. A. Simha, *Hydrodynamics of soft active matter*, Rev. Mod. Phys., 85 (2013), pp. 1143–1189.

[165] U. M. B. MARCONI AND P. TARAZONA, *Dynamic density functional theory of fluids*, J. Phys.-Condens. Mat., 12 (2000), p. A413.

[166] K.-A. MARDAL AND R. WINTHER, *Preconditioning discretizations of systems of partial differential equations*, Num. Lin. Alg. w. Appl., 18 (2011), pp. 1 – 40.

[167] M. MARECHAL AND M. DIJKSTRA, *Stability of orientationally disordered crystal structures of colloidal hard dumbbells*, Phys. Rev. E, 77 (2008), p. 061405.

[168] ——, *Colloidal hard dumbbells under gravity: structure and crystallization*, Soft Matter, 7 (2011), pp. 1397–1408.

[169] W. MARTH, S. PRAETORIUS, AND A. VOIGT, *A mechanism for cell motility by active polar gels*, J. R. Soc. Interface, 12 (2015).

[170] Y. MATSUOKA, T. FUKASAWA, K. HIGASHITANI, AND R. YAMAMOTO, *Effect of hydrodynamic interactions on rapid Brownian coagulation of colloidal dispersions*, Phys. Rev. E, 86 (2012), p. 051403.

[171] K. MAY, K. HARTH, T. TRITTEL, AND R. STANNARIUS, *Dynamics of freely floating smectic bubbles*, Eur. Phys. Lett., 100 (2012), p. 16003.

[172] A. J. MCDONALD, M. P. ALLEN, AND F. SCHMID, *Surface tension of the isotropic-nematic interface*, Phys. Rev. E, 63 (2001), p. 010701.

[173] L. MEDEROS AND D. E. SULLIVAN, *Smectic-A ordering at a liquid-vapor interface*, Phys. Rev. A, 46 (1992), pp. 7700–7707.

[174] J. MELLENTHIN, A. KARMA, AND M. PLAPP, *Phase-field crystal study of grain-boundary premelting*, Phys. Rev. B, 78 (2008), p. 184110.

[175] G. MENG, J. PAULOSE, D. R. NELSON, AND V. N. MANOHARAN, *Elastic instability of a crystal growing on a curved surface*, Science, 343 (2014), pp. 634–637.

[176] A. M. MENZEL AND H. LÖWEN, *Traveling and Resting Crystals in Active Systems*, Phys. Rev. Lett., 110 (2013), p. 055702.

[177] A. M. MENZEL, T. OHTA, AND H. LÖWEN, *Active crystals and their stability*, Phys. Rev. E, 89 (2014), p. 022301.

[178] S. K. MKHONTA, K. R. ELDER, AND Z. HUANG, *Exploring the complex world of two-dimensional ordering with three modes*, Phys. Rev. Lett., 111 (2013), p. 035501.

[179] C. MÜLLER, *Spherical Harmonics*, Springer, Aachen, 1966.

[180] Y. NAKAYAMA AND R. YAMAMOTO, *Simulation method to resolve hydrodynamic interactions in colloidal dispersions*, Phys. Rev. E, 71 (2005), p. 036707.

[181] I. NITSCHKE, A. VOIGT, AND J. WENSCH, *A finite element approach to incompressible two-phase flow on manifolds*, j. Fluid Mech., 708 (2012), pp. 418–438.

[182] S. NORDHOLM, M. JOHNSON, AND B. C. FREASIER, *Generalized van der waals theory. iii. the prediction of hard sphere structure*, Aust. J. Chem., 33 (1980), pp. 2139 – 2150.

[183] MARTIN OETTEL, *Mode expansion for the density profiles of crystal-fluid interfaces: hard spheres as a test case*, J. Phys.-Condens. Mat., 24 (2012), p. 464124.

[184] M. OETTEL, S. DOROSZ, M. BERGHOFF, B. NESTLER, AND T. SCHILLING, *Description of hard-sphere crystals and crystal-fluid interfaces: a comparison between density functional approaches and a phase-field crystal model*, Phys. Rev. E, 86 (2012), p. 021404.

[185] D. P. O'LEARY AND R. E. WHITE, *Multi-splittings of matrices and parallel solution of linear systems*, SIAM J. Alg. Discr. Meth., 6 (1985), pp. 630–640.

[186] S. T. T. OLLILA, C. J. SMITH, T. ALA-NISSILA, AND C. DENNISTON, *The hydrodynamic radius of particles in the hybrid lattice boltzmann–molecular dynamics method*, Multiscale Model. Sim., 11 (2013), pp. 213–243.

[187] J. ONISHI, A. KAWASAKI, Y. CHEN, AND H. OHASHI, *Lattice boltzmann simulation of capillary interactions among colloidal particles*, Comp. Math. Appl., 55 (2008), pp. 1541–1553.

[188] M. A. OSIPOV, J. R. SAMBLES, AND L. RUAN, *Theory of nematic-smectic phase separation in thin twisted liquid crystal cells*, Liquid Crystals, 30 (2003), pp. 823–830.

[189] R. OSSERMAN, *A survey of minimal surfaces*, Courier Corporation, 2002.

[190] A. OSTERMANN AND M. ROCHE, *Rosenbrock methods for partial differential equations and fractional orders of convergence*, SIAM J. Numer. Anal., 30 (1993), pp. 1084–1098.

[191] J. PADDING AND A. LOUIS, *Hydrodynamic interactions and Brownian forces in colloidal suspensions: Coarse-graining over time and length scales*, Phys. Rev. E, 74 (2006), p. 031402.

[192] T. PALBERG, *Crystallization kinetics of colloidal model suspensions: recent achievements and new perspectives*, J. Phys.-Condens. Mat., 26 (2014), p. 333101.

[193] J. W. PEARSON AND A. J. WATHEN, *A new approximation of the schur complement in preconditioners for pde-constrained optimization*, Num. Lin. Alg., 19 (2012), pp. 816–829.

[194] M. A. PELETIER, D. R. M RENGER, AND M. VENERONI, *Variational formulation of the fokker-planck equation with decay: A particle approach*, Commun. Contemp. Math., 15 (2013), p. 1350017.

[195] F. PENNA, J. DZUBIELLA, AND P. TARAZONA, *Dynamic density functional study of a driven colloidal particle in polymer solutions*, Phys. Rev. E, 68 (2003), p. 061407.

[196] ROGER PENROSE, *The role of aesthetics in pure and applied mathematical research*, Bull. Inst. Math. Appl., 10 (1974), pp. 266–271.

[197] ——, *Pentaplexity a class of non-periodic tilings of the plane*, The Mathematical Intelligencer, 2 (1979), pp. 32–37.

[198] CHARLES S. PESKIN, *The immersed boundary method*, Acta Num., 11 (2002), pp. 479–517.

[199] SIMON PRAETORIUS, *Interacting particles in flowing solvents – modeling, numerics and high-performance computing*, master's thesis (Diplomarbeit), Technische Universität Dresden, Germany, Dezember 2010.

[200] S. PRAETORIUS AND A. VOIGT, *A Phase Field Crystal Approach for Particles in a Flowing Solvent*, Macromol. Theor. Sim., 20 (2011), pp. 541–547.

[201] ——, *Development and analysis of a block-preconditioner for the phase-field crystal equation*, SIAM J. Sci. Comp., 37 (2015), pp. B425–B451.

[202] ——, *A navier-stokes phase-field crystal model for colloidal suspensions*, J. Chem. Phys., 142 (2015), p. 154904.

[203] S. PRAETORIUS, A. VOIGT, R. WITTKOWSKI, AND H. LÖWEN, *Structure and dynamics of interfaces between two coexisting liquid-crystalline phases*, Phys. Rev. E, 87 (2013), p. 052406.

[204] T. RAMAKRISHNAN AND M. YUSSOUFF, *First-principles order-parameter theory of freezing*, Phys. Rev. B, 19 (1979), pp. 2775–2794.

[205] SRIRAM RAMASWAMY, *Issues in the statistical mechanics of steady sedimentation*, Adv. Phys., 50 (2001), pp. 297–341.

[206] L. RAMOS, T. C. LUBENSKY, N. DAN, P. NELSON, AND D. A. WEITZ, *Surfactant-mediated two-dimensional crystallization of colloidal crystals*, Science, 286 (1999), pp. 2325–2328.

[207] J. RANG AND L. ANGERMANN, *New Rosenbrock W-Methods of Order 3 for Partial Differential Algebraic Equations of Index 1*, BIT Num. Math., 45 (2005), pp. 761–787.

[208] ROLF RANNACHER, *Finite element methods for the incompressible navier-stokes equations*, in Fundamental Directions in Mathematical Fluid Mechanics, G. P. Galdi, J. G. Heywood, and R. Rannacher, eds., Advances in Mathematical Fluid Mechanics, Birkhäuser Basel, 2000, pp. 191–293.

[209] THOMAS RANSFORD, *Potential Theory in the Complex Plane*, London Mathematical Society Student Texts, Cambridge University Press, 1995.

[210] A. RÄTZ AND A. VOIGT, *Pde's on surfaces - a diffuse interface approach*, Commun. Math. Sci., 4 (2006), pp. 575–590.

[211] ——, *A diffuse-interface approximation for surface diffusion including adatoms*, Nonlin., 20 (2007), pp. 177–192.

[212] MARKUS RAUSCHER, *DDFT for brownian particles and hydrodynamics*, J. Phys.-Condens. Mat., 22 (2010), p. 364109.

[213] M. RAUSCHER, A. DOMINGUEZ, M. KRUGER, AND F. PENNA, *A dynamic density functional theory for particles in a flowing solvent*, J. Chem. Phys., 127 (2007), p. 244906.

[214] H. Reich, M. Dijkstra, R. van Roij, and M. Schmidt, *Entropic wetting and the free isotropic-nematic interface of hard colloidal platelets*, J. Phys. Chem. B, 111 (2007), pp. 7825–7835.

[215] M. Rex and H. Löwen, *Dynamical density functional theory with hydrodynamic interactions and colloids in unstable traps*, Phys. Rev. Lett., 101 (2008), p. 148302.

[216] A. Ribalta, C. Stoecker, S. Vey, and A. Voigt, *Amdis – adaptive multidimensional simulations: Parallel concepts*, in Domain Decomposition Methods in Science and Engineering XVII, U. Langer, M. Discacciati, D. E. Keyes, O. B. Widlund, and W. Zulehner, eds., vol. 60 of Lecture Notes in Computational Science and Engineering, Springer Berlin Heidelberg, 2008, pp. 615–621.

[217] J. B. Ritz and J. P. Caltagirone, *A numerical continuous model for the hydrodynamics of fluid particle systems*, Int. J. Numer. Meth. Fl., 30 (1999), pp. 1067–1090.

[218] M. J. Robbins, A. J. Archer, U. Thiele, and E. Knobloch, *Modeling the structure of liquids and crystals using one- and two-component modified phase-field crystal models*, Phys. Rev. E, 85 (2012), p. 061408.

[219] Michel Roche, *Rosenbrock methods for differential algebraic equations*, Numerische Mathematik, 52 (1987), pp. 45–63.

[220] S. Roorda, T. van Dillen, A. Polman, C. Graf, A. van Blaaderen, and B. J. Kooi, *Aligned gold nanorods in silica made by ion irradiation of core-shell colloidal particles*, Adv. Mat., 16 (2004), pp. 235–237.

[221] Y. Rosenfeld, M. Schmidt, H. Löwen, and P. Tarazona, *Fundamental-measure free-energy density functional for hard spheres: Dimensional crossover and freezing*, Phys. Rev. E, 55 (1997), pp. 4245–4263.

[222] R. E. Rozas and J. Horbach, *Capillary wave analysis of rough solid-liquid interfaces in nickel*, Eur. Phys. Lett., 93 (2011), p. 26006.

[223] S. J. Ruuth and B. Merriman, *A simple embedding method for solving partial differential equations on surfaces*, J. Comput. Phys., 227 (2008), pp. 2118–2129.

[224] Yousef Saad, *A flexible inner-outer preconditioned gmres algorithm*, SIAM J. Sci. Comp., 14 (1993), pp. 461–469.

[225] ——, *Iterative Methods for Sparse Linear Systems: Second Edition*, Society for Industrial and Applied Mathematics, 2003.

[226] Y. Saad and M. H. Schultz, *Gmres: A generalized minimal residual algorithm for solving nonsymmetric linear systems*, SIAM J. Sci. Stat. Comp., 7 (1986), pp. 856–869.

[227] K. Sandomirski, E. Allahyarov, H. Löwen, and S. Egelhaaf, *Heterogeneous crystallization of hard-sphere colloids near a wall*, Soft Matter, 7 (2011), pp. 8050–8055.

[228] V. Schmid and A. Voigt, *Crystalline order and topological charges on capillary bridges*, Soft Matter, 10 (2014), pp. 4694–4699.

[229] A. Schmidt and K. G. Siebert, *Design of Adaptive Finite Element Software, The Finite Element Toolbox ALBERTA*, vol. 42 of Lecture Notes in Computational Science and Engineering, Springer, 2005.

[230] P. Schwartz, D. Adalsteinsson, P. Coletta, A. P. Arkin, and M. Onsum, *Numerical computation of diffusion on a sphere*, Proc. Nat. Acad. Sci., 102 (2005), pp. 11151–11156.

[231] A. Segal, M. ur Rehman, and C. Vuik, *Preconditioners for incompressible Navier-Stokes solvers*, Numer. Math. Theor. Meth. Appl., 3 (2010), pp. 245 – 275.

[232] D. Shao, W.-J. Rappel, and H. Levine, *A computational model for cell morphodynamics*, Phys. Rev. Lett., 105 (2010), p. 108104.

[233] D. Shechtman, I. Blech, D. Gratias, and J. W. Cahn, *Metallic phase with long-range orientational order and no translational symmetry*, Phys. Rev. Lett., 53 (1984), pp. 1951–1953.

[234] M. Shub and S. Smale, *Complexity of bezout's theorem, iii: condition number and packing*, J. Complexity, 9 (1993), pp. 4–14.

[235] E. Siggia, B. Halperin, and P. Hohenberg, *Renormalization-group treatment of the critical dynamics of the binary-fluid and gas-liquid transitions*, Phys. Rev. B, 13 (1976), pp. 2110–2123.

[236] V. Simoncini and D. B. Szyld, *Recent computational developments in krylov subspace methods for linear systems*, Num. Lin. Alg., 14 (2007), pp. 1–59.

[237] G. L. G. Sleijpen and D. R. Fokkema, *BiCGstab (ℓ) for linear equations involving unsymmetric matrices with complex spectrum*, E. Trans. Num. Ana., 1 (1993), pp. 11–32.

[238] Steve Smale, *Mathematical problems for the next century*, Math. Intelligencer, 20 (1998), pp. 7–15.

[239] A. M. Somoza, L. Mederos, and D. E. Sullivan, *Wetting and layering transitions in liquid crystals*, Phys. Rev. E, 52 (1995), pp. 5017–5027.

[240] E. J. Stancik, G. T. Gavranovic, M. J. O. Widenbrant, A. T. Laschitsch, J. Vermant, and G. G. Fuller, *Structure and dynamics of particle monolayers at a liquid-liquid interface subjected to shear flow*, Faraday Discuss., 123 (2003), pp. 145–156.

[241] M. J. O. Stancik, E. J. Widenbrant, A. T. Laschitsch, J. Vermant, and G. G. Fuller, *Structure and dynamics of particle monolayers at a liquid-liquid interface subjected to extensional flow*, Langmuir, 18 (2002), pp. 4372–4375.

[242] T. Steihaug and A. Wolfbrandt, *An attempt to avoid exact jacobian and nonlinear equations in the numerical solution of stiff differential equations*, Math. Comp., 33 (1979), pp. 521–534.

[243] K. STRATFORD, R. ADHIKARI, I. PAGONABARRAGA, J. C. DESPLAT, AND M. E. CATES, *Colloidal jamming at interfaces: a route to fluid-bicontinuous gels*, Science, 309 (2005), pp. 2198–2201.

[244] ALEXANDER STUKOWSKI, *Visualization and analysis of atomistic simulation data with ovito–the open visualization tool*, Model. Sim. Mater. Sci., 18 (2010), p. 015012.

[245] Y. G. SUN, W. M. CHOI, H. Q. JIANG, Y. Y. HUANG, AND J. A. ROGERS, *Controlled buckling of semiconductor nanoribbons for strechable electronics*, Nature Nano., 1 (2007), pp. 201–207.

[246] M. SUSSMAN, P. SMEREKA, AND S. OSHER, *A level set approach for computing solutions to incompressible two-phase flow*, J. Comput. Phys., 114 (1994), pp. 146–159.

[247] J. SWIFT AND P. C. HOHENBERG, *Hydrodynamic fluctuations at the convective instability*, Phys. Rev. A, 15 (1977), pp. 319–328.

[248] H. TANAKA AND T. ARAKI, *Simulation method of colloidal suspensions with hydrodynamic interactions: Fluid particle dynamics*, Phys. Rev. Lett., 85 (2000), pp. 1338–1341.

[249] S. TANG, R. BACKOFEN, J. WANG, Y. ZHOU, A. VOIGT, AND Y. YU, *Three-dimensional phase-field crystal modeling of fcc and bcc dendritic crystal growth*, J. Cryst. Growth, 334 (2011), pp. 146–152.

[250] S. TANG, S. PRAETORIUS, R. BACKOFEN, A. VOIGT, Y.-M. YU, AND J. WANG, *Two-dimensional liquid crystalline growth within a phase-field-crystal model*, Phys. Rev. E, 92 (2015), p. 012504.

[251] G. TEGZE, G. BANSEL, G.I. TÒTH, T. PUSZTAI, Z. FAN, AND L. GRÁNÁSY, *Advanced operator splitting-based semi-implicit spectral method to solve the binary phase-field crystal equations with variable coefficients*, J. Comput. Phys., 228 (2009), pp. 1612–1623.

[252] G. TEGZE, G. I. TÓTH, AND L. GRÁNÁSY, *Faceting and branching in 2D crystal growth*, Phys. Rev. Lett., 106 (2011), p. 195502.

[253] K. E. TEIGEN, X. LI, J. LOWENGRUB, F. WANG, AND A. VOIGT, *A diffuse-interface approach for modelling transport, diffusion and adsorption/desorption of material quantities on a deformable interface*, Commun. Math. Sci., 7 (2009), pp. 1009–1037.

[254] U. THIELE, A. J. ARCHER, M. J. ROBBINS, H. GOMEZ, AND E. KNOBLOCH, *Localized states in the conserved swift-hohenberg equation with cubic nonlinearity*, Phys. Rev. E, 87 (2013), p. 042915.

[255] JOSEPH J. THOMSON, *On the structure of the atom: an investigation of the stability and periods of oscillation of a number of corpuscles arranged at equal intervals around the circumference of a circle; with application of the results on the theory of atomic structure*, Philos. Mag., 7 (1904), pp. 237–265.

[256] J. TONER AND Y. TU, *Flocks, herds, and schools: A quantitative theory of flocking*, Phys. Rev. E, 58 (1998), pp. 4828–4858.

[257] J. TONER, Y. TU, AND S. RAMASWAMY, *Hydrodynamics and phases of flocks*, Ann Phys., 318 (2005), pp. 170 – 244.

[258] G. I. TÓTH, L. GRÁNÁSY, AND G. TEGZE, *Nonlinear hydrodynamic theory of crystallization*, J. Phys.-Condens. Mat., 26 (2014), p. 055001.

[259] JOHN D. TOWERS, *Two methods for discretizing a delta function supported on a level set*, J. Comput. Phys., 220 (2007), pp. 915–931.

[260] L. N. TREFETHEN AND M. EMBREE, *Spectra and pseudospectra: the behavior of nonnormal matrices and operators*, Princeton University Press, 2005.

[261] U. TROTTENBERG, C. W. OOSTERLEE, AND A. SCHÜLLER, *Multigrid*, Academic Press, 2001.

[262] A. C. H. TSANG AND E. KANSO, *Circularly confined microswimmers exhibit multiple global patterns*, Phys. Rev. E, 91 (2015), p. 043008.

[263] A. TURKOVIĆ, P. DUBČEK, AND N. D. FOX, *Self-organization of nanoparticles in a TiO_2 thin film on a glass substrate*, Vacuum, 80 (2005), pp. 108–112.

[264] MARKUS UHLMANN, *An immersed boundary method with direct forcing for the simulation of particulate flows*, J. Comput. Phys., 209 (2005), pp. 448–476.

[265] B. ULLRICH, G. K. AUERNHAMMER, E. M. SAM, AND D. VOLLMER, *Tracer colloids close to an isotropic-nematic domain interface with phase transition-induced solute transport*, Coll. Surf. A, 354 (2010), pp. 298–307.

[266] M. UR REHMAN, T. GEENEN, C. VUIK, G. SEGAL, AND S. P. MACLACHLAN, *On iterative methods for the incompressible stokes problem*, Int. J. Numer. Meth. Fl., 65 (2011), pp. 1180 – 1200.

[267] D. VAN DER BEEK, H. REICH, P. VAN DER SCHOOT, M. DIJKSTRA, T. SCHILLING, R. VINK, M. SCHMIDT, R. VAN ROIJ, AND H. LEKKERKERKER, *Isotropic-nematic interface and wetting in suspensions of colloidal platelets*, Phys. Rev. Lett., 97 (2006), p. 087801.

[268] S. VAN TEEFFELEN, R. BACKOFEN, A. VOIGT, AND H. LÖWEN, *Derivation of the phase-field-crystal model for colloidal solidification*, Phys. Rev. E, 79 (2009), p. 051404.

[269] E. VELASCO, L. MEDEROS, AND D. E. SULLIVAN, *Density-functional study of the nematic-isotropic interface of hard spherocylinders*, Phys. Rev. E, 66 (2002), p. 021708.

[270] A. A. VERHOEFF, R. H. J. OTTEN, P. VAN DER SCHOOT, AND H. N. W. LEKKERKERKER, *Magnetic field effects on tactoids of plate-like colloids*, J. Chem. Phys., 134 (2011), p. 044904.

[271] J. VERMANT AND M. J. SOLOMON, *Flow-induced structure in colloidal suspensions*, J. Phys.-Condens. Mat., 17 (2005), p. R187.

[272] SIMON VEY, *Adaptive Finite Elements for Systems of PDEs: Software Concepts, Multi-level Techniques and Parallelization*, PhD thesis, Technische Universität Dresden, November 2007.

[273] S. VEY AND A. VOIGT, *AMDiS: adaptive multidimensional simulations*, Comput. Vis. Sci., 10 (2007), pp. 57–67.

[274] R. L. C. VINK AND T. SCHILLING, *Interfacial tension of the isotropic-nematic interface in suspensions of soft spherocylinders*, Phys. Rev. E, 71 (2005), p. 051716.

[275] A. VOIGT AND T. WITKOWSKI, *Hybrid parallelization of an adaptive finite element code*, Kybernetika, 46 (2010), pp. 316–327.

[276] G. J. VROEGE AND H. N. W. LEKKERKERKER, *Phase transitions in lyotropic colloidal and polymer liquid crystals*, Rep. Prog. Phys., 55 (1992), pp. 1241–1309.

[277] S. P. WARGACKI, B. PATE, AND R. A. VAIA, *Fabrication of 2D ordered films of tobacco mosaic virus (tmv): processing morphology correlations for convective assembly*, Langmuir, 24 (2008), pp. 5439–5444.

[278] ANDREW J. WATHEN, *Realistic eigenvalue bounds for the galerkin mass matrix*, IMA J. Num. Ana., 7 (1987), pp. 449–457.

[279] S. M. WISE, C. WANG, AND J. S. LOWENGRUB, *An Energy-Stable and Convergent Finite-Difference Scheme for the Phase Field Crystal Equation*, SIAM J. Numer. Anal., 47 (2009), pp. 2269–2288.

[280] T. WITKOWSKI, S. LING, S. PRAETORIUS, AND A. VOIGT, *Software concepts and numerical algorithms for a scalable adaptive parallel finite element method*, Adv. Comput. Math., (2015), pp. 1–33.

[281] R. WITTKOWSKI AND H. LÖWEN, *Dynamical density functional theory for colloidal particles with arbitrary shape*, Mol. Phys., 109 (2011), pp. 2935–2943.

[282] R. WITTKOWSKI, H. LÖWEN, AND H. R. BRAND, *Derivation of a three-dimensional phase-field-crystal model for liquid crystals from density functional theory*, Phys. Rev. E, 82 (2010), p. 031708.

[283] ——, *Microscopic and macroscopic theories for the dynamics of polar liquid crystals*, Phys. Rev. E, 84 (2011), p. 041708.

[284] ——, *Polar liquid crystals in two spatial dimensions: the bridge from microscopic to macroscopic modeling*, Phys. Rev. E, 83 (2011), p. 061706.

[285] S. WOLFSHEIMER, C. TANASE, K. SHUNDYAK, R. VAN ROIJ, AND T. SCHILLING, *Isotropic-nematic interface in suspensions of hard rods: mean-field properties and capillary waves*, Phys. Rev. E, 73 (2006), p. 061703.

[286] DAVID P. WOODRUFF, *The Solid-Liquid Interface*, vol. 1 of Cambridge Solid State Science Series, Cambridge University Press, London, 1 ed., 1980.

[287] M. Woźniak, G. Derkachov, K. Kolwas, J. Archer, T. Wojciechowski, D. Jakubczyk, and M. Kolwas, *Formation of highly ordered spherical aggregates from drying microdroplets of colloidal suspension*, Langmuir, 31 (2015), pp. 7860–7868.

[288] Thomas G. Wright, *Eigtool.* http://www.comlab.ox.ac.uk/pseudospectra/eigtool, 2002.

[289] K. Wu and P. W. Voorhees, *Phase field crystal simulations of nanocrystalline grain growth in two dimensions*, Acta Mater., 60 (2012), pp. 407–419.

[290] Jianlin Xia, *Randomized sparse direct solvers*, SIAM J. Matrix Ana. Appl., 34 (2013), pp. 197–227.

[291] C. Yang and X.-C. Cai, *A scalable implicit solver for phase field crystal simulations*, in Parallel and Distributed Processing Symposium Workshops PhD Forum (IPDPSW), 2013 IEEE 27th International, 2013, pp. 1409–1416.

[292] R. Zandi and D. Reguera, *Mechnical properties of viral capsids*, Phys. Rev. E, 72 (2005), p. 021917.

[293] R. Zandi, D. Reguera, R. F. Bruisma, W. M. Gelbart, and J. Rudnick, *Origin of icosahedral symmetry in viruses*, Proc. Nat. Acad. Sci., 101 (2004), pp. 15556–15560.

[294] Z. Zhang, Y. Ma, and Z. Qiao, *An adaptive time-stepping strategy for solving the phase field crystal model*, J. Comput. Phys., 249 (2013), pp. 204–215.

[295] O. C. Zienkiewicz, R. L. Taylor, and P. Nithiarasu, *The Finite Element Method for Fluid Dynamics*, Elsevier Science, 2013.

[296] T. Zykova-Timan, J. Horbach, and K. Binder, *Monte Carlo simulations of the solid-liquid transition in hard spheres and colloid-polymer mixtures*, J. Phys.-Condens. Mat., 133 (2010), p. 014705.

[297] T. Zykova-Timan, R. E. Rozas, J. Horbach, and K. Binder, *Computer simulation studies of finite-size broadening of solid-liquid interfaces: from hard spheres to nickel*, J. Phys.-Condens. Mat., 21 (2009), p. 464102.